

**DATA-DRIVEN MODELLING OF DAYLIGHT  
REDIRECTING FENESTRATION AT VARIABLE  
DIRECTIONAL RESOLUTION**

**A Thesis Submitted to  
the Graduate School of Engineering and Sciences of  
İzmir Institute of Technology  
in Partial Fulfillment of the Requirements for the Degree of**

**DOCTOR OF PHILOSOPHY**

**in Architecture**

**by  
Lars O. GROBE**

**October 2019  
İZMİR**

We approve the thesis of **Lars O. GROBE**

**Examining Committee Members:**

---

**Prof. Dr. Zehra Tuğçe KAZANASMAZ**  
Department of Architecture, Izmir Institute of Technology

---

**Prof. Dr. Serdar KALE**  
Department of Architecture, Izmir Institute of Technology

---

**Assoc. Prof. Dr. Mustafa Emre İLAL**  
Department of Architecture, Izmir Institute of Technology

---

**Assoc. Prof. Dr. Mehlika İNANICI**  
Department of Architecture, University of Washington

---

**Assoc. Prof. Dr. Başak KUNDAKÇI KOYUNBABA**  
Department of Architecture, Yaşar University

**1 October 2019**

---

**Prof. Dr. Zehra Tuğçe KAZANASMAZ**  
Supervisor, Department of Architecture  
Izmir Institute of Technology

---

**Prof. Dr. Stephen WITTKOPF**  
Co-Supervisor, Lucerne School of  
Engineering and Architecture

---

**Prof. Dr. Koray KORKMAZ**  
Head of the Department of  
Architecture

---

**Prof. Dr. Aysun SOFUOĞLU**  
Dean of the Graduate School of  
Engineering and Sciences

## ACKNOWLEDGMENTS

I would not have been able to conduct this research without the supportive environments that I enjoyed in Izmir as well as in Lucerne. I am grateful to my professors, fellow students, and the administrative staff at İYTE, who more than once saved my venturesome attempt of combining an appointment in Switzerland with my studies in Turkey by their flexibility, commitment and readiness to help. In Lucerne, I benefited from the remarkable tolerance level of my colleagues toward my frequent absences and related irregular working hours, as well as the university's generous funding scheme for doctoral studies.

I express my gratitude to my supervisor, Prof. Dr. Zehra Tuğçe Kazanasmaz, who encouraged me to start my studies and reliably guided me through it, and who was always accessible to discuss my findings, doubts, and progress. I am thankful to my co-supervisor, Prof. Dr. Stephen Wittkopf, who always had the right question at hand to keep my research targeted, and who encouraged me to aim at a career in research years ago when I was all in architectural practice. Thanks to all members of the committee for accompanying my research with critical and constructive feedback, and their readiness to adapt working hours to the many time zones that the committee spans.

From the group of daylighting experts and enthusiasts that have, over long periods and often without a permanent academic affiliation, guided many developments and careers in research by their readiness to share their expertise, I want to acknowledge two who stand for many. Greg Ward, for developing, continuously extending, and even more so for maintaining the software that is driving this research, as well as for patiently providing guidance through the algorithms. And Dr. Peter Apian-Bennewitz, for generously sharing of his expertise in the theoretical and experimental aspects of light scattering, always coupled with a distinct interest in architecture and daylighting.

I am thankful to my colleague Dr. Roland Schregle, without whom I would have been lost in the implementation of the PHOTON MAP, and to Andreas Noback, with whom I have in common the late decision for a doctoral program, for discussing theoretical aspects of daylight simulation as much as experimental results. The many other contributions to particular aspects of this research are acknowledged in the respective chapters.

# ABSTRACT

## DATA-DRIVEN MODELLING OF DAYLIGHT REDIRECTING FENESTRATION AT VARIABLE DIRECTIONAL RESOLUTION

Daylight Redirecting Fenestration (DRF) aims at the optimal utilisation of daylight in buildings striving for high visual comfort standards. Daylight simulation allows to assess whether this objective is met in architectural context, and guides decisions in building design as well as the development of DRF. The daylight simulation suite *RADIANCE* allows to employ data-driven models of variable resolution to accurately replicate the irregular light scattering by DRF.

In this context, this research provides methods to improve DRFs' integration in daylight assessments. The thesis consolidates a series of publications that address particular problems in the generation and application of data-driven models, with a focus on accurate image synthesis for visual comfort assessments. First, the parametrisation of model generation from gonio-photometric measurements is tested. Second, a novel extension of the instrumentation allows to characterise and subsequently model retro-reflection by an innovative coating. Applied in DRF, the coating controls solar gains and glare, while maintaining a view to the outside. Third, to assemble accurate data-driven models of fenestration layers into descriptions of the entire DRF, an approach employing matrix calculations is adapted and tested. Finally, the *PHOTON MAP* implementation in *RADIANCE* is modified for efficient image synthesis with data-driven models, and employed in a simplified but accurate approach to Climate-Based Daylight Modelling that demonstrates the potential of retro-reflection to efficiently control glare and maintain view with static DRF.

The research contributes to the applicability of data-driven models, and confirms the potential of DRF to reconcile diverging daylight performance targets such as glare control and view.

## ÖZET

### GÜNIŞIĞI YÖNLENDİRMELİ PENCERENİN DEĞİŞKEN YÖNLÜ ÇÖZÜNÜRLÜKTE VERİ DAYALI MODELLENMESİ

Günişığı Yönlendirmeli Pencere (GYP), yüksek görsel konfor standartlarını sağlamak için çaba sarfeden binalarda günişığın en iyi şekilde kullanılmasını amaçlar. Günişığı benzetimi mimari bağlamda bu hedefin sağlanıp sağlanmadığının değerlendirilmesine imkan tanır. Bina tasarımında ve aynı zamanda GYP'lerin geliştirilmesinde alınacak kararları yönlendirir. Böyle bir benzetim aracı olan RADIANCE, GYP'nin düzensiz optik özelliklerini tekrarlayarak değişken yönlü çözünürlükte veri dayalı modeller kullanabilir.

Bu tez, bu bağlamda, GYP'lerin doğal aydınlatma analizine katılmasını geliştirmek için yeni bir yöntem önermektedir. Metin, görsel konfor değerlendirmelerinde, özellikle görüntülerin doğru sentezlenmesine odaklanarak, veri dayalı modellerin oluşturulması ve uygulanması hakkındaki problemleri işaret eden makaleleri birleştirmektedir. İlk olarak, gonio-fotometrik ölçümlerden oluşturulan parametrik model test edilmektedir. İkinci olarak, bu ölçüm cihazına yeni bir eklenti ile yeni bir kaplamanın geri yansıtma özelliklerinin modellenmesi ve karakterizasyonu sağlanır. GYP'lere uygulanan bu kaplama, dışarıya olan görüşü koruyarak ısı kazançlarını ve kamaşmayı kontrol eder. Üçüncü olarak, pencere katmanlarının değişken yönlü çözünürlükte modellerinin kombine edilmesi için matris hesaplamaları uyarlayan bir yaklaşım oluşturulup test edilmiştir. Sonra, RADIANCE programına katılan PHOTON MAP uygulaması, veri dayalı modeller ile etkin bir görsel sentez için modifiye edilip geliştirilmiştir. PHOTON MAP İklima Dayalı Günişığı Modellemesi yöntemini basitleştirmekte; görüşü kapatmayan ve görsel konforu artıran statik/hareket etmeyen GYP'lerin geri yansıtma potansiyelini göstermektedir.

Bu araştırma, değişken yönlü çözünürlükte, veri dayalı modellerin uygulanmasına katkıda bulunur ve GYP'nin kamaşma kontrolü ve manzara gibi günişığı performansı hedeflerini yakalama potansiyelini kesinleştirir.

# CONTENTS

LIST OF FIGURES	x
LIST OF TABLES	xiii
LIST OF ABBREVIATIONS	xiv
CHAPTER 1: INTRODUCTION	1
1.1 Background: Daylight in architectural design . . . . .	1
1.2 Visual comfort as a criteria for daylight performance . . . . .	2
1.3 Daylight Redirecting Fenestration for increased visual comfort .	3
1.4 Assessing visual comfort achieved by DRF . . . . .	6
1.4.1 The new European daylight standard . . . . .	6
1.4.2 Daylight provision: Supply and distribution of daylight . . .	7
1.4.3 Glare protection . . . . .	8
1.5 Problem statement . . . . .	9
1.6 Research questions and objectives . . . . .	10
1.7 Scope of this research . . . . .	11
1.8 Structure of the thesis . . . . .	12
CHAPTER 2: MEASUREMENT OF THE BSDF	14
2.1 Instrumentation . . . . .	14
2.1.1 Fundamentals . . . . .	14
2.1.2 Illumination system . . . . .	15
2.1.2.1 Light sources . . . . .	15
2.1.2.2 Focus and beam shape . . . . .	18
2.1.3 Detectors . . . . .	19
2.1.4 Detector types and spectral response . . . . .	20
2.1.5 Geometry of detector movement . . . . .	21
2.1.6 Sample mounts . . . . .	21
2.2 Data acquisition procedures . . . . .	23
2.2.1 Beam characterization . . . . .	23
2.2.2 Measurement of scattered light . . . . .	24
2.3 Derivation of BSDF from measurements . . . . .	26
CHAPTER 3: HIGH-RESOLUTION DATA-DRIVEN MODELS OF DRCs	28
3.1 Introduction . . . . .	29
3.2 Methodology . . . . .	31
3.2.1 Two cases of Daylight Redirecting Components . . . . .	31
3.2.1.1 Measurement . . . . .	31
3.2.2 Model generation . . . . .	33
3.2.3 Comparison of transmission distributions . . . . .	34
3.2.4 Evaluation of the effects of interpolation and extrapolation .	34
3.2.5 Evaluation of the effects of resolution and data-reduction . .	35

3.3	Results and discussion	35
3.3.1	Measurement	35
3.3.2	Interpolation effects	37
3.3.3	Extrapolation effects	37
3.3.4	Effects of resolution and data-reduction	37
3.4	Conclusions and outlook	41
3.5	Acknowledgments	42
CHAPTER 4: MEASUREMENT AND DATA-DRIVEN MODELLING OF RETRO-REFLECTION		43
4.1	Introduction	43
4.1.1	Retro-reflection	44
4.1.2	Measurement techniques	44
4.1.3	Modelling retro-reflection	46
4.2	Materials and method	46
4.2.1	Exemplary sample of a retro-reflective coating	46
4.2.2	Measurement of the BSDF	47
4.2.3	Extension of the gonio-photometer to measure retro-reflection	48
4.2.4	Testing of the extended gonio-photometer	51
4.2.5	Measurement of the sample's BSDF	51
4.2.6	Generation of a data-driven model from the measured BSDF	52
4.2.7	Modeling the effect of retro-reflection in Venetian blinds	53
4.2.8	Testing the model in an exemplary test room	56
4.3	Results and discussion	58
4.3.1	Extension of the gonio-photometer	58
4.3.2	Testing of the measurement method	59
4.3.3	Measured Bidirectional Scattering Distribution Function (BSDF) of the coating	59
4.3.4	Data-driven reflection model from measured BSDF	62
4.3.5	Effects of retro-reflection in Venetian blinds	62
4.3.6	Daylight performance with different coatings in an exemplary office	66
4.4	Conclusion	68
4.5	Acknowledgements	69
4.6	Role of the funding source	69
CHAPTER 5: COMBINING THE BSDFs OF FENESTRATION LAYERS AT HIGH DIRECTIONAL RESOLUTION		70
5.1	Introduction	70
5.1.1	Modeling CFSs with BSDFs	71
5.1.2	Computational combination of BSDFs	72
5.1.3	Data-driven models of the BSDF in daylight simulation	74
5.2	Objectives	75
5.3	Method	76
5.3.1	Matrix formalism employing a subdivision algorithm of variable resolution	76
5.3.2	Pair-wise combination of BSDFs at variable resolution	78
5.3.3	Combination of BSDFs of different resolutions	78

5.3.4	Testing the method and its impact on the predicted performance of multilayer fenestration systems . . . . .	79
5.3.4.1	Cases and computational generation of BSDFs . . . . .	79
5.3.4.2	Comparison of the results of the extended matrix formalism and ray-tracing . . . . .	81
5.3.4.3	Comparing the performance of the matrix formalism to ray-tracing . . . . .	82
5.3.4.4	Testing the down-sampling of BSDFs . . . . .	83
5.3.4.5	Impact of directional resolution on the predicted performance of fenestration systems . . . . .	83
5.4	Results . . . . .	83
5.4.1	Computed BSDFs of the fenestration layers . . . . .	85
5.4.2	Re-sampling of the BSDF . . . . .	85
5.4.3	Combined BSDFs and comparison to results of ray-tracing . . . . .	86
5.4.4	Evaluating the performance of the matrix formalism . . . . .	87
5.4.5	Evaluating the impact of directional resolution . . . . .	88
5.5	Discussion and conclusion . . . . .	89

**CHAPTER 6: THE RADIANCE PHOTON MAP FOR IMAGE-BASED VISUAL COMFORT ASSESSMENTS WITH DATA-DRIVEN BSDF MODELS OF HIGH RESOLUTION** 94

6.1	Introduction . . . . .	94
6.1.1	Daylight simulation with data-driven BSDF models in Radiance . . . . .	95
6.1.2	Daylight simulation with the Radiance Photon Map . . . . .	96
6.1.3	Objectives . . . . .	98
6.2	Method . . . . .	99
6.2.1	Modification of the Photon Map implementation in Radiance . . . . .	99
6.2.2	Testing validity for image generation . . . . .	100
6.2.3	Exemplary glare assessments . . . . .	103
6.3	Results . . . . .	104
6.3.1	Visual inspection and comparison of imagery . . . . .	104
6.3.2	Quantitative comparison of imagery . . . . .	107
6.3.3	Results of exemplary glare assessments . . . . .	109
6.3.4	Initial benchmark . . . . .	112
6.4	Discussion . . . . .	113
6.5	Acknowledgements . . . . .	114
6.6	Funding . . . . .	114

**CHAPTER 7: PHOTON-MAPPING IN CBDM WITH HIGH-RESOLUTION BSDFs** 115

7.1	Introduction . . . . .	115
7.1.1	Climate-Based Daylight Modelling in visual comfort assessments . . . . .	115
7.1.2	Data-driven modeling of CFSs . . . . .	117
7.1.3	Daylight simulation with the PHOTON MAP . . . . .	118
7.1.4	Objectives . . . . .	119
7.2	Method . . . . .	120
7.2.1	Refined computation of the solar component . . . . .	120
7.2.2	Three-Phase Method calculation of diffuse sky . . . . .	121
7.2.3	Adding fenestration’s visual detail . . . . .	122

7.2.4	Composition of hourly images . . . . .	122
7.2.5	Cases to test and demonstrate the method . . . . .	123
7.2.5.1	FS1: Static retro-reflecting fenestration . . . . .	124
7.2.5.2	FS2: Redirecting film with operated shading . . . . .	124
7.2.6	Testing the validity of the method with geometric and data-driven fenestration models . . . . .	125
7.2.7	Demonstration of the method . . . . .	126
7.2.7.1	Exemplary glare assessment . . . . .	126
7.2.7.2	Comparison with the Five Phase Method . . . . .	127
7.3	Results and discussion . . . . .	127
7.3.1	Results of CBDM with geometric modelling for one time-step	127
7.3.2	Results of CBDM with data-driven modelling for one time-step	128
7.3.3	Testing validity for one time-step . . . . .	129
7.3.3.1	Identification of a problematic time-step . . . . .	130
7.3.3.2	CBDM with geometric modelling of FS1 . . . . .	132
7.3.3.3	CBDM with data-driven modelling of FS1 . . . . .	134
7.3.3.4	CBDM with data-driven modelling of FS2 . . . . .	135
7.3.3.5	Comparison with 3PM and 5PM . . . . .	136
7.3.4	Exemplary application of the method in the comparison of FS1 and FS2 . . . . .	137
7.4	Conclusions . . . . .	139
7.5	Sequence of simulation steps comprising the Five-Phase-Method (5PM) . . . . .	141
7.6	Model generation parameters . . . . .	142
7.7	Image generation parameters . . . . .	143
<b>CHAPTER 8: CONCLUSIONS AND FUTURE RESEARCH DIRECTIONS</b>		<b>144</b>
8.1	Main research questions and objectives . . . . .	144
8.2	Limitations of this research . . . . .	147
8.3	Recommendations . . . . .	147
8.4	Main contributions . . . . .	148
8.5	Scientific and non-scientific impact . . . . .	148
8.6	Further research directions . . . . .	149

## LIST OF FIGURES

Figure 1.1	Hierarchy of daylight performance. . . . .	3
Figure 1.2	Effects of DRF on the supply and distribution of daylight. . . . .	4
Figure 1.3	Exemplary DRCs. . . . .	5
Figure 1.4	Performance indicators for visual comfort according to EN 17037. . . . .	7
Figure 1.5	Chapters of the thesis. . . . .	13
Figure 2.1	Scanning gonio-photometer employed in this research. . . . .	15
Figure 2.2	Halogen lamp and its emission spectrum. . . . .	17
Figure 2.3	Xenon lamp and its emission spectrum. . . . .	17
Figure 2.4	Green lasern diode and its beam. . . . .	17
Figure 2.5	Focus on detector. . . . .	18
Figure 2.6	Focus on sample plane. . . . .	19
Figure 2.7	Focus at infinity. . . . .	19
Figure 2.8	Detector head with sensors for different wavelength ranges. . . . .	20
Figure 2.9	Scan paths of the gonio-photometer. . . . .	22
Figure 2.10	Large sample mount. . . . .	22
Figure 2.11	Reference measurement. . . . .	23
Figure 2.12	Measurement of light scattered by a sample. . . . .	24
Figure 2.13	Predefined sets of incident directions in the measurements. . . . .	24
Figure 2.14	Width of collimated beam exceeding sample size at oblique incidence. . . . .	25
Figure 2.15	Constraining the width of the sampling aperture. . . . .	25
Figure 2.16	Valid ranges of incident directions with collimated illumination. . . . .	25
Figure 2.17	Beam shaping with two crossed cylindrical lenses $L_{2a}$ and $L_{2b}$ . . . . .	26
Figure 3.1	Samples DRC1 (daylight redirecting film) and DRC2 (micro-grid). . . . .	32
Figure 3.2	Gonio-photometer seen from control work-station. . . . .	32
Figure 3.3	Three sets of incident directions: coarse, refined, high. . . . .	33
Figure 3.4	Measured DSF of daylight redirecting film DRC1. . . . .	36
Figure 3.5	Measured DSF of micro-grid DRC2. . . . .	36
Figure 3.6	Measured and interpolated DSF of daylight redirecting film DRC1. . . . .	38
Figure 3.7	Measured and interpolated DSF of micro-grid DRC2. . . . .	38
Figure 3.8	Measured and extrapolated DSF of daylight redirecting film DRC1. . . . .	39
Figure 3.9	Measured and extrapolated DSF of micro-grid DRC2. . . . .	39
Figure 3.10	Effect of resolution and data-reduction on model of daylight redirecting film DRC1 . . . . .	40

Figure 3.11	Effect of resolution and data-reduction on model of micro-grid DRC2.	40
Figure 4.1	Shading of the sample by the detector. . . . .	45
Figure 4.2	Measurement of retro-reflection employing one beam-splitter. . . . .	45
Figure 4.3	Sample with retro-reflective coating. . . . .	47
Figure 4.4	Gonio-photometer with incident- and outgoing directions. . . . .	48
Figure 4.5	Measurement of retro-reflection employing two beam-splitters. . . . .	49
Figure 4.6	Effect of extended optical path due to beam-splitter on outgoing direction. . . . .	50
Figure 4.7	Cellular office as a test case for the performance of the retro-reflective coating. . . . .	57
Figure 4.8	Prototype of the gonio-photometer's extension for retro-reflection.	58
Figure 4.9	Profile of the mirror's DSF in the scatter plane. . . . .	60
Figure 4.10	Profile of the retro-reflecting sample's DSF in the scatter plane, Vis.	61
Figure 4.11	Profile of the retro-reflecting sample's DSF in the scatter plane, NIR.	61
Figure 4.12	Modelled DSF of the retro-reflecting sample in the scatter plane, Vis.	63
Figure 4.13	Modelled DSF of the retro-reflecting sample in the scatter plane, NIR.	63
Figure 4.14	Transmission through the fenestration system . . . . .	65
Figure 4.15	Reflection by the fenestration system. . . . .	65
Figure 4.16	Illuminance maps with retro-reflecting, mirror-like, and diffuse blinds. . . . .	66
Figure 4.17	Luminance maps with retro-reflecting, mirror-like, and diffuse blinds.	67
Figure 4.18	Glare sources with retro-reflecting, mirror-like, and diffuse blinds.	68
Figure 5.1	Klems basis and square-to-disk mapping by Shirley-Chiu. . . . .	75
Figure 5.2	Re-sampling BSDF to lower directional resolution. . . . .	79
Figure 5.3	Flat mirror blinds and DGU-embedded tilted light-shafts. . . . .	80
Figure 5.4	Transmission through scattering layers CFS1 and CFS2. . . . .	85
Figure 5.5	Comparison of ray-traced and down-sampled BSDFs. . . . .	86
Figure 5.6	Comparison of results by ray-tracing and matrix formalism. . . . .	87
Figure 5.7	Local accordance of BSDF combination by ray-tracing and matrix-formalism. . . . .	88
Figure 5.8	Direct-hemispherical transmission of two CFSs. . . . .	89
Figure 5.9	View toward fenestration modelled by high-resolution BSDF and Klems basis. . . . .	90
Figure 5.10	Distribution of directional transmission predicted by high-resolution BSDF and Klems basis. . . . .	90
Figure 5.11	BSDFs by ray-tracing and matrix formalism for CFS1 and varying incident directions. . . . .	92

Figure 5.12	BSDFs by ray-tracing and matrix formalism for CFS2 and varying incident directions. . . . .	93
Figure 6.1	Paths leading to photon deposition. . . . .	97
Figure 6.2	Modified deposition of caustic photons. . . . .	100
Figure 6.3	Office model and CFS as an exemplary test-case. . . . .	101
Figure 6.4	Luminance maps for view $v1$ . . . . .	105
Figure 6.5	Luminance maps for view $v2$ . . . . .	106
Figure 6.6	Effect of PM modification and peak extraction on appearance of light sources. . . . .	107
Figure 6.7	Relative differences by modified PHOTON MAP and BRT, $v1$ . . .	108
Figure 6.8	Relative differences by modified PHOTON MAP and BRT, $v2$ . . .	108
Figure 6.9	Glare sources in $v1$ as detected by evalglare. . . . .	111
Figure 6.10	Glare sources in $v2$ as detected by evalglare. . . . .	111
Figure 7.1	Office model employed in the evaluation of the proposed method. .	123
Figure 7.2	Profile of the blinds comprising $FS1$ . . . . .	124
Figure 7.3	Dense fabric of $CFS4$ as employed in $FS2$ . . . . .	125
Figure 7.4	Component images comprising the resulting imagery. . . . .	128
Figure 7.5	Component images employing data-driven modelling. . . . .	129
Figure 7.6	Results of the proposed method with geometric and data-driven modelling. . . . .	129
Figure 7.7	Annual distribution of DGP by geometric modeling of $FS1$ . . . .	131
Figure 7.8	Annual distribution of DGP by data-driven modeling of $FS1$ . . . .	131
Figure 7.9	Hourly values of Daylight Glare Probability (DGP) on March 12th by geometric (geo, geo+os) and data-driven modelling of $FS1$ . . .	131
Figure 7.10	Comparison of results by proposed method with ray-tracing. . . .	132
Figure 7.11	Geometric model, oversampling. . . . .	134
Figure 7.12	DSF of $CFS1$ and $CFS2$ . . . . .	134
Figure 7.13	Data-driven modelling of $FS2$ and impact on pixel noise. . . . .	136
Figure 7.14	Comparison of the proposed method with 5PM and 3PM. . . . .	136
Figure 7.15	Histograms of, and 95 percentile DGP compared to results by 5PM and 3PM. . . . .	137
Figure 7.16	95 percentile DGP and Daylight Glare Index (DGI) by $FS1$ and $FS2$ . .	137
Figure 7.17	Operation of sun-shade with $FS2$ (black: closed). . . . .	138
Figure 7.18	Histograms of, and 95 percentiles of $FS1$ and $FS2$ . . . . .	138

## LIST OF TABLES

Table 4.1	Reflection properties of the blinds. . . . .	54
Table 4.2	genBSDF parameters. . . . .	55
Table 4.3	Computed solar-optical properties. . . . .	56
Table 4.4	Computed solar gains. . . . .	64
Table 4.5	Results of glare assessment comparing effects by retro-reflection with specular and diffuse reflection. . . . .	68
Table 5.1	Matrix representation of BSDF components. . . . .	72
Table 5.2	genBSDF parameters in the computation of BSDFs. . . . .	80
Table 5.3	genBSDF parameters in the combination of BSDFs. . . . .	81
Table 5.4	Parameters for <i>rpict</i> in the generation of imagery. . . . .	84
Table 5.5	GA of results from matrix formalism with <i>Shirley-Chiu algorithm</i> and ray-tracing. . . . .	86
Table 5.6	Duration of BSDF combination by ray-tracing and matrix-formalism. . . . .	88
Table 6.1	Ray notation for scattering phenomena. . . . .	97
Table 6.2	Parameters for image generation by BRT and PM. . . . .	102
Table 6.3	Glare classification thresholds for DGP and DGI. . . . .	103
Table 6.4	Photometric quantities computed from the imagery by <i>evalglare</i> . . . . .	103
Table 6.5	Photometric quantities computed for views $v1$ and $v2$ . . . . .	109
Table 6.6	Glare evaluation, views $v1$ and $v2$ . . . . .	110
Table 6.7	Effect of PM on simulation times. . . . .	112
Table 7.1	Configurations of fenestration systems <i>FS1</i> and <i>FS2</i> . . . . .	123
Table 7.2	Optical properties of the fabric employed in <i>CFS4</i> . . . . .	126
Table 7.3	Thresholds applied to DGP and DGI. . . . .	126
Table 7.4	Sky conditions for Izmir on 12th March, 11:30 am. . . . .	131
Table 7.5	Results of single time-step analysis by <i>evalglare</i> . . . . .	133
Table 7.6	Parameters for model generation by <i>genBSDF</i> . . . . .	142
Table 7.7	Parameters for model generation by <i>bsdf2tree</i> . . . . .	142
Table 7.8	Parametrisation of the computation of the solar component. . . . .	143
Table 8.1	DRF modelled as part of this research. . . . .	146

## LIST OF ABBREVIATIONS

<b>ASE</b>	Annual Sunlight Exposure .....	7
<b>BPS</b>	Building Performance Simulation .....	148
<b>BRT</b>	Backward Ray-Tracing .....	145
<b>BS</b>	Beam Splitter .....	45
<b>BSDF</b>	Bidirectional Scattering Distribution Function .....	144
<b>BSDF<sub>L</sub></b>	BSDF of one fenestration layer or a subsystem .....	72
<b>BSDF<sub>S</sub></b>	BSDF of an entire fenestration system .....	72
<b>CBDM</b>	Climate-Based Daylight Modelling .....	145
<b>CFS</b>	Complex Fenestration System .....	116
<b>CGDB</b>	Complex Glazing Database .....	72
<b>CCT</b>	Correlated Color Temperature .....	16
<b>DC</b>	Daylight Coefficient .....	116
<b>DGI</b>	Daylight Glare Index .....	119
<b>DGP</b>	Daylight Glare Probability .....	145
<b>DGU</b>	Double Glazing Unit	
<b>DM</b>	Daylight Metric .....	8
<b>DR</b>	Daylight Redirection .....	11
<b>DRC</b>	Daylight Redirecting Component .....	144
<b>DRF</b>	Daylight Redirecting Fenestration .....	144
<b>DSF</b>	Differential Scattering Function .....	135
<b>EPFL</b>	École Polytechnique Fédérale de Lausanne .....	42
<b>5PM</b>	Five-Phase-Method .....	145
<b>GA</b>	Global Accordance .....	81
<b>GPGPU</b>	General Purpose Graphics Processing Unit .....	94
<b>IEA</b>	International Energy Agency .....	74
<b>IES</b>	Illuminating Engineering Society .....	2
<b>IGDB</b>	International Glazing Database .....	56
<b>InGaAs</b>	Indium Gallium Arsenide .....	20

<b>LA</b>	Local Accordance .....	81
<b>LBL</b>	Lawrence Berkeley National Laboratory .....	30
<b>LCP</b>	Laser Cut Panel .....	145
<b>LESO-PB</b>	Solar Energy and Building Physics Laboratory .....	42
<b>NIr</b>	Near Infrared light 780 nm to 2500 nm .....	50
<b>OoC</b>	Out-of-Core .....	119
<b>PM</b>	Photon Mapping .....	145
<b>RAM</b>	random-access memory .....	82
<b>sDA</b>	spatial Daylight Autonomy .....	7
<b>SHGC</b>	Solar Heat Gain Coefficient .....	56
<b>Si</b>	Silicon .....	20
<b>SNR</b>	Signal to Noise Ratio .....	16
<b>3PM</b>	Three-Phase-Method .....	116
<b>UDI</b>	Useful Daylight Illuminance .....	8
<b>Vis</b>	Visible light 380 nm to 780 nm .....	50
<b>XML</b>	Extensible Markup Language .....	52

# CHAPTER 1

## INTRODUCTION

### 1.1 Background: Daylight in architectural design

The interplay between the man-made substance of buildings, and the intangible daylight it both effects and is exposed to, shapes our perception of architecture. As the design of a building effects the supply and distribution of daylight in its interior, the latter determines the appearance and utilization of the building, as well as the attribution of meaning to architectural design. However, due to the continuously changing nature of sky conditions, there is no means to exactly achieve, maintain or predict any desired spatial and directional distribution of daylight in a building. Daylight is a resource that the architect aims to influence but can never fully control. And yet, due to its role as a medium through which we visually grasp our environment, qualitative knowledge about daylight is driving architects in their design decisions. Le Corbusier, who studies the historic role and utilization of daylight and reflects it by experimenting with light-guiding building elements extensively, considers this an act of composition:

I use light abundantly, as you may have suspected; Light for me is the fundamental basis of architecture. I compose with light.<sup>1</sup>

Besides its importance for perception and aesthetics, functional aspects of the mutual dependence of daylight supply and building design have been one of the primary concerns of architects. It was not before the advent of gas and, later, cheap electrical lighting, that the architect was no more exclusively determining the lighting conditions within, and therefore the utilization of buildings. With the availability of artificial lighting, the hard to tame and ever changing daylight changed its role from a valuable resource to an expendable factor of uncertainty in design. But the idea of the fully controlled building interior found its end soon with the energy crisis of the 70ies, and the observation of negative impacts on occupants referred to as the “sick building syndrome”. Expectations that the utilization of daylight would not only reduce energy demand, but also fulfill the new desire for a more natural, pleasant built environment, for *visual comfort*, motivated technological innovation that still forms the most-part of available daylighting technologies. Yet it remains a task of system integration to fully leverage the potential benefits of these technologies.<sup>2</sup>

## 1.2 Visual comfort as a criteria for daylight performance

Daylight in buildings is essential for the physical and psychological well-being of occupants, and is inevitable in spaces with a view to the outside. Yet it can lead to discomfort, and as a continuously changing factor triggers occupant response that may be unexpected and contradict the intentions of the planner.<sup>3,4</sup> The design of daylighted buildings must therefore moderate the beneficial and negative effects of a continuously changing environment.<sup>5-7</sup> The Illuminating Engineering Society (IES) Lighting Handbook stresses the challenge to balance comfort with efficiency:

Daylighting involves the delivery and distribution of light from the sun and sky to a building interior to provide ambient and/or task lighting to meet the visual and biological requirements of the occupants. The design of a daylit building is a challenging task demanding an integrated design approach to simultaneously address occupant comfort, lighting quality, and energy efficiency across a wide range of daylight and weather conditions.<sup>8</sup>

Daylight performance can assess the characteristics of devices, such as shading systems or glazing assemblies, or their performance in conjunction with a given attached interior.<sup>9-13</sup> Visual comfort assessments take the perspective of the occupant of such spaces. The evaluation of visual comfort is a challenge due to the multitude of its aspects and often conflicting objectives. A systematic approach to relate the functional expectations on the utilization of daylight to measurable indicators is achieved by the application of a hierarchical structure to the evaluated performance criteria. It is proposed to distinguish main performance characteristics from criteria and indicators, as illustrated by Figure 1.1.<sup>14</sup> The approach has been adopted to the field of daylight in buildings and has been applied in the performance evaluation of Venetian blinds. Accordingly, four indicators are listed for visual comfort as a performance characteristic (marked yellow in Figure 1.1).<sup>11</sup>

**Supply of daylight** and room darkening address the amount of daylight admitted into a building by apertures such as windows or skylights.

**Light distribution** describes propagation of daylight admitted into the interior spaces. Resulting from varying sky conditions, the distribution of daylight changes continuously in the building interior.

**Glare protection** aims at the minimization of disability and discomfort glare conditions experiences by an occupant.

**Room darkening** in particular in residential building.

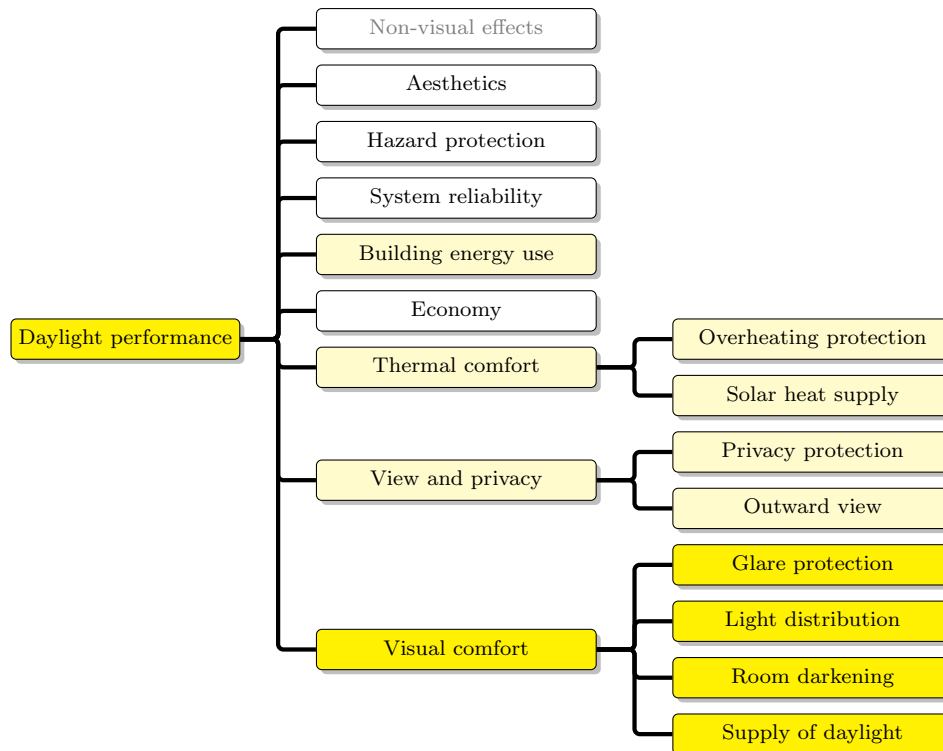


Figure 1.1: Hierarchy of daylight performance (with addition of non-visual effects not considered in the original work).<sup>11</sup> While this thesis addresses visual comfort (yellow), the proposed modelling technique can be applied to other aspects (light yellow).

### 1.3 Daylight Redirecting Fenestration for increased visual comfort

In urban settings, daylight is commonly admitted into multi-storey buildings horizontally through the façade. Such side-lighting designs lead to an uneven distribution of light, and to potential conflicts between the perimeter and core zones of buildings. Vertical apertures provide view and thereby maintain a visual connection to the exterior as well as ample supply of daylight to the perimeter zone of buildings. However, occupants in the core (e.g. located >6.0 m from the façade) experience high contrast in their field of view between near, interior surfaces and the distant, bright façade.<sup>15</sup> Due to the fall-off in the illuminance distribution as a function of distance to the façade, set points for shading devices either favour occupants in the perimeter zone, which are potentially affected by thermal discomfort due to excessive daylight supply, or occupants in the core.

Daylight Redirecting Fenestration (DRF) aims to increase visual comfort by controlling the admission and distribution of daylight. Guiding daylight from the building perimeter, where its abundance can cause discomfort and glare, deeper into the building core, DRF decreases contrast and provides an even distribution of illuminance. Daylight can be supplied to zones without direct access to daylight which would otherwise require constant artificial lighting with the related negative effects on occupants' well-being,

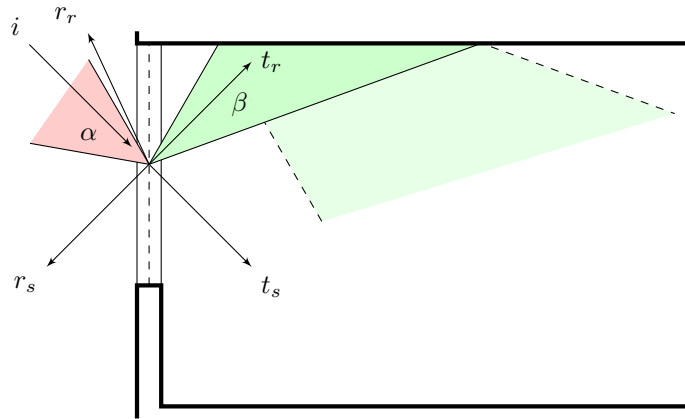


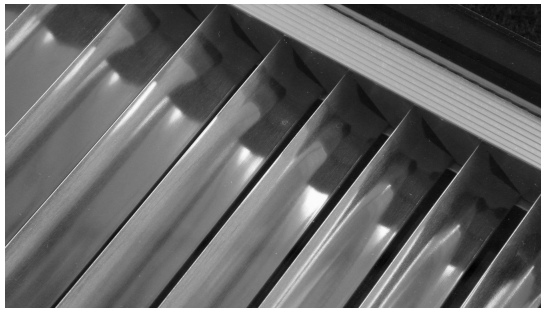
Figure 1.2: Effects of DRF on the supply and distribution of daylight: Minimized specular transmission  $\tau_s$ , maximized redirected transmission  $\tau_r$  from incident light direction  $\vec{i}$ . Directional selectivity blocking incident directions not within admittance angle  $\alpha$ . Directionality of admitted light according to angle  $\beta$ . Retro-reflection  $\rho_r$  for particular systems, specular reflection  $\rho_s$  e.g. due to glazing.

comfort and performance. While primarily addressing visual comfort, DRF also positively effects other aspects of daylight performance (Figure 1.1). Positive effects on building energy use, when artificial lighting is supplemented, stand in contrast with the impact on the outward view depending on the DRF’s optical properties and its location within the façade. Shading DRF further extends its impact on thermal comfort, reducing solar gains and thereby effects of overheating and energy demand for cooling.<sup>16–18</sup>

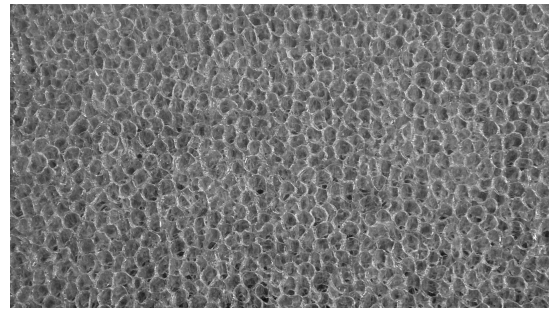
Defined as “façade systems that can alter transmitted light direction”,<sup>19</sup> DRF is a dichotomy to non-redirecting Complex Fenestration System (CFS) that maintains regular light transmission, including many adaptive (also dynamic or switchable) systems.<sup>20,21</sup> The deflection of light that maintains its directionality constitutes the irregular transmission property that all DRF has in common and allows to control the distribution of light in the building interior. It is typically accompanied by irregular reflection properties, e.g. to directions other than the mirror direction, with retro-reflection toward the incident direction being the most prominent case as a means to control solar gains. Figure 1.2 illustrates the geometry of regular and irregular light scattering by DRF.

Applications of DRF combine multiple, typically co-planar fenestration layers. These comprise Daylight Redirecting Components (DRCs), transparent glazing layers, and often operable shading that may introduce a significant amount of diffuse scattering. Only the DRC cause the irregularity of the reflection and transmission properties of DRF, employing refracting or reflecting periodical<sup>1</sup> structures that may be visible, or appear as a uniform surface property. A selection of exemplary DRCs is shown in Figure 1.3. The effective characteristics of the DRF are then a convolution of the regular and irregular properties, including inter-reflection between these layers.<sup>22</sup>

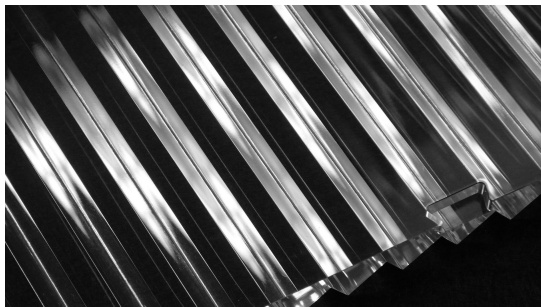
<sup>1</sup>Note that it is the periodicity that causes the directionality.



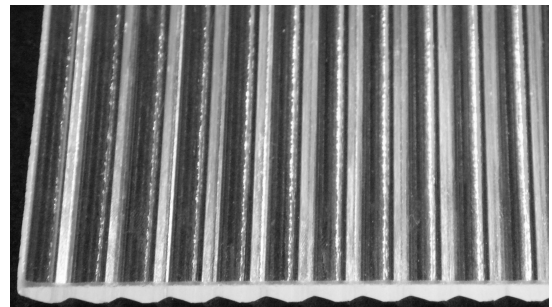
a)



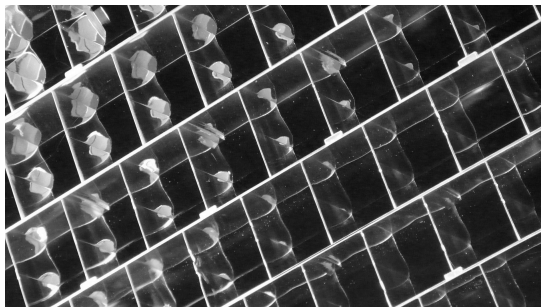
b)



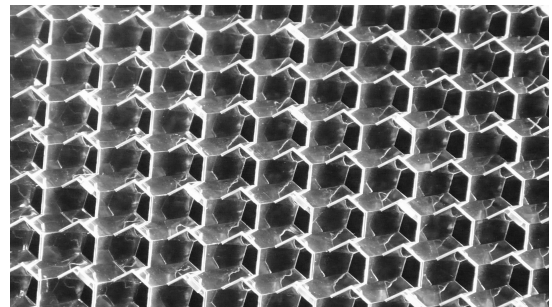
c)



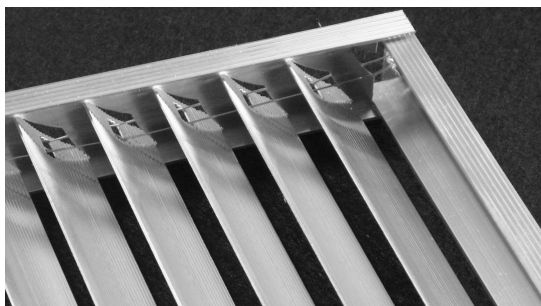
d)



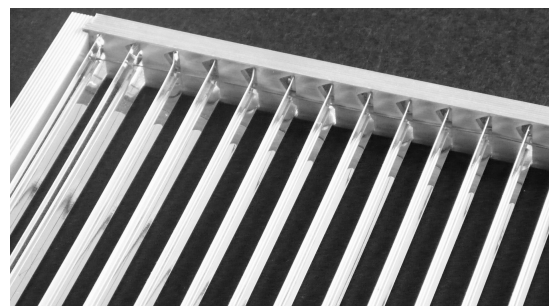
e)



f)



g)



h)

Figure 1.3: Exemplary DRCs: Mirror blinds (a), translucent insulation (b), prism glass with (c) and without (d) reflective coating, micro-grids blocking direct sunlight (e, f), retro-reflection by prismatic surface structures (g) and profiles (h).

## 1.4 Assessing visual comfort achieved by DRF

The quantitative assessment of visual comfort allows to compare and optimize variants and to integrate daylight as a factor into performance driven design.

### 1.4.1 The new European daylight standard

The new European daylight standard EN 17037<sup>23</sup> for the first time provides a unified body of requirements for daylight in buildings. It exclusively addresses the performance criteria of visual comfort by four indicators:

**Daylight provision** covers the supply and spatial distribution of daylight in terms of illuminance on a horizontal reference plane  $E_h$ .

**Protection from glare** requires acceptable glare conditions to be maintained over a given fraction of usage time.

**View out** accounts for the geometric extent of an aperture, and the visual information covered by it, seen from given reference positions.

**Exposure to sunlight** is applicable to residential and healthcare building, and measures the hours when a room receives sunlight for a defined reference day.

This set of indicators slightly differs from that introduced with the hierarchy of daylight performance in section 1.2 (Figure 1.1). It includes the “Outward view” indicator<sup>2</sup> and omits “room darkening”. Sunlight exposure is included as a new indicator. The resulting attribution of indicators to the “visual comfort” criteria according to the new standard is shown in Figure 1.4. In face of the development of Climate-Based Daylight Modelling (CBDM) and corresponding metrics, “supply of daylight” and “light distribution” form the spatio-temporal indicator “daylight provision”.

For the assessment of DRF, not all of these indicators can be assumed to be of equal importance. Maximizing daylight provision is, compared to other CFSs, the main characteristic of DRF. Protection from glare is a common requirement especially in office environments, and one main design target of many DRFs. Consequently, the sections of the standard covering these two indicators are assumed to be most relevant with regards to DRF in this research. On the other hand, the view out indicator addresses an important

---

<sup>2</sup>The “Outward view” indicator was part of the original hierarchy, but attributed to “view and privacy”.

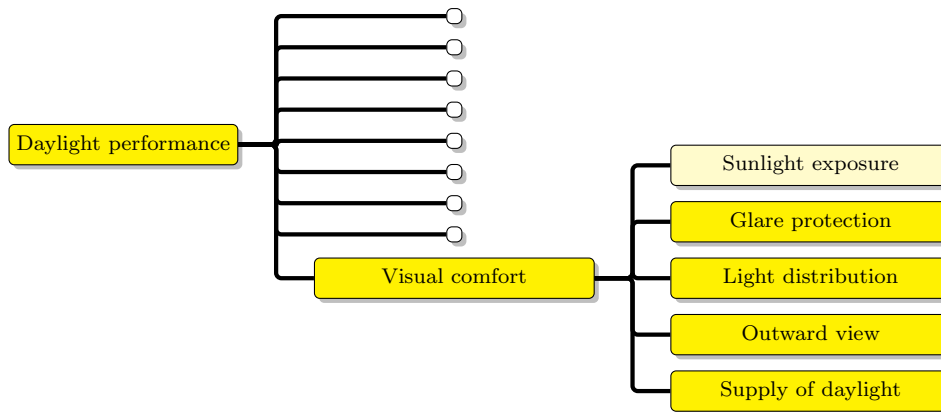


Figure 1.4: Indicators for the performance criteria of visual comfort according to EN 17037. Sunlight exposure is a requirement e.g. for residential and health-care buildings.

target of many DRF designs and should be accounted for, but is defined by the standard in a way that applies to the building geometry rather than the fenestration.

### 1.4.2 Daylight provision: Supply and distribution of daylight

The formulation of minimum target for horizontal illuminance  $E_h$ , defined according to activities or visual tasks, can be considered the least common denominator in regulations addressing lighting requirements in non-residential buildings. However, this target has not been static. Since its peak at  $1500 \text{ lm/m}^2$  before the energy crisis in the 1970's, the IES's recommendation for offices has continuously decreased down to a range of  $50 \text{ lm/m}^2$  to  $1000 \text{ lm/m}^2$ .<sup>24</sup> The current recommendation differentiates between office zones reserved for different activities, allowing for strategies aiming at a low *ambient* illuminance that is locally enhanced according to task requirements. Besides task requirements, occupant-related factors such as age, and the importance of tasks are considered<sup>8,25</sup> as well as targets for vertical illuminance  $E_v$ , and uniformity  $E_{max}/E_{min}$ .<sup>24</sup> Optimization is achieved by matching individually and locally varying lighting requirements.

EN 17037 adopts spatial Daylight Autonomy (sDA) and defines a minimum target  $E_h$  of  $300 \text{ lm/m}^2$ , in line e.g. with EN 12646-1,<sup>26</sup> for at least 50 % of the space. In the temporal domain, it sets the target to 50 % of the annual daylight hours. This distinguishes the standard from e.g. the IES recommendation, which relates the target to the occupied hours.<sup>27-29</sup> EN 17037 here aims to differentiate between external conditions, e.g. due to local climate, from the capability of a chosen building design to utilize the available daylight. EN 17037 however does not couple the assessment of daylight supply with Annual Sunlight Exposure (ASE) to identify potentially negative effects of sunlight. The distribution of daylight, as well as its potential role as a supplement for artificial lighting, in

analogy to Useful Daylight Illuminance (UDI),<sup>30,31</sup> is accounted for by a second target of  $100 \text{ lm/m}^2$  for the entire evaluated area. The two different targets aim at a well-balanced design that does not mislead the designer to maximize the glazed area and accepts the utilization of artificial lighting as a supplement, but not as a replacement for daylight.

The application of illuminance-based Daylight Metric (DM) such as sDA has been supported by the development of efficient CBDM techniques.<sup>32,33</sup> The data-driven fenestration model employed by the Three-Phase-Method (3PM) achieves moderate directional resolution,<sup>34</sup> and allows to replicate arbitrary light scattering properties, including those of DRF, in such simulations.<sup>35–37</sup> The Complex Glazing Database (CGDB) and software such as WINDOW provide access to a models covering a wide range of CFSs, including DRF.

### 1.4.3 Glare protection

Assessing visual comfort solely based on horizontal illuminance shows poor agreement with subjective assessments, and can lead to reductionistic design decisions aiming only at maximized daylight provision.<sup>38,39</sup> In particular the use of ASE, being a by-product of evaluations of daylight supply, to detect glare has been criticized.<sup>40</sup> Using e.g. vertical illuminance, and DMs based on the luminance distribution in the field of view, has been proposed.<sup>40,41</sup> Dedicated contrast-based metrics of discomfort glare have been in use in lighting design,<sup>42</sup> and have been developed for daylight.<sup>43,44</sup>

EN 17037 avoids the problematic application of illuminance-based metrics to glare. It measures glare by Daylight Glare Probability (DGP), a metric combining the established glare formulae with a vertical illuminance term  $E_v$ . The metric can be evaluated based imagery,<sup>45</sup> that can be generated e.g. by daylight simulation.<sup>46</sup> Due to the computational effort of annual image synthesis by daylight simulation, e.g. RADIANCE, acceleration techniques by the use of General Purpose Graphics Processing Units (GPGPUs),<sup>47,48</sup> and variants of the metric such as simplified and enhanced simplified DGP, have been proposed. The latter is implemented in DAYSIM.<sup>49</sup> Based on hourly evaluations, the standards sets requirements for the 95 percentile DGP depending on the level of glare control. Other than in the assessment of daylight provision, not daylight hours but the time when the space is used are considered.

For common daylighting devices such as opaque shutters (including blinds that can be fully closed), shading that exhibits regular direct-direct and direct-diffuse transmission (e.g. fabrics, perforated screens), and clear glazing layers (e.g. electrochromic glazing), the elaborate application of the DGP metric can be substituted by a simplified approach. The simplified approach recommends glare protection classes according to EN 14501,<sup>50</sup>

which are based only on the normal-normal and normal-diffuse transmission of visible light. However, the simplified method of EN 17037 is not applicable to DRF, since a glare classification based on normal-normal transmission is contradicted by the characteristic deflection of transmitted light.

Unfortunately, the techniques to accelerate annual DGP assessments are of limited applicability to DRF. DGP is highly sensitive to the size and intensity of potential glare sources. Data-driven models of moderate resolution, as successfully applied in illuminance-based assessments, effectively increase the width and decrease the intensity of glare sources and thereby effect the accuracy of glare assessments.<sup>36,37</sup> A data-driven Bidirectional Scattering Distribution Function (BSDF) model of variable directional resolution address this shortcoming and has been implemented in RADIANCE.<sup>51</sup> This model can be employed in refined CBDM techniques to increase the accuracy of visual comfort assessments. The Five-Phase-Method (5PM) refines the directional resolution of sky and fenestration models and can be employed to compute time-series of illuminance and image data,<sup>52,53</sup> but is challenging to apply due to the complex sequence of simulation steps it comprises.<sup>54</sup> Mixing geometric models with *BSDF proxies*, and the detection of regular transmission by *peak extraction*, increase accuracy and potentially performance of the method, but are not of general applicability.

## 1.5 Problem statement

Understanding the effects of DRF on visual comfort requires a modelling technique that accounts for the characteristic irregular light scattering, and assessment methods, that can measure performance indicators in context of a building and its utilization.

Data-driven modelling of DRF promises general applicability, since it accounts for arbitrary light scattering properties. An advanced model has been implemented in RADIANCE that offers variable, and locally high, directional resolution, that can be generated from measurements. The impact of the parametrization of measurement and model generation is, however, not fully understood. Other than models of moderate resolution as distributed with the CGDB, models of variable resolution representing fenestration layers cannot be efficiently combined, hindering reuse and thereby sharing of model libraries.

The new European daylighting standard EN 17037 provides a unified framework to assess the daylight performance of building with regards to visual comfort. Applied to DRF and its typical use case in non-residential building, the standard defines targets for *daylight provision*, protection from glare, and view out. These three performance indicators can guide research on the effects of DRF on visual comfort, but only the requirement for daylight provision can be tested using established CBDM techniques such as the 3PM.

Due to the characteristic irregular light scattering properties of DRF, the elaborate annual glare assessment based on DGP cannot be substituted by the glare classification of EN 14501 in practical applications. For the same reason, glare assessments with DRF should not rely on simplified methods such as simplified DGP. The 5PM, which addresses image synthesis for annual assessments of visual comfort, achieves high accuracy, but is challenging due to its complexity. It is computationally demanding in particular with data-driven models of DRF, when accelerations techniques such as the use of BSDF proxies or peak extraction cannot be applied.

CFS aiming to control glare typically obstruct the view out. DRF employing retro-reflection either by macro-structures, e.g. deliberately designed profiles of blinds, and macro-structures, e.g. applied as coating, addresses this by blocking sun-light even with almost horizontal inclination of Venetian blinds. In particular retro-reflective micro-structures ask for a detailed characterization to account for effects that cannot be predicted from their geometry, e.g. stray-light, to guide development and to assess their impact on visual comfort. Such characterization has not been performed, and requires modifications of the instrumentation used in light scatter measurements.

## 1.6 Research questions and objectives

This research focusses on the modelling of DRF by data-driven models, and the application of such models in daylight simulation for visual comfort assessments. The methodological questions are motivated by the aim to better understand the effects of DRF on visual comfort.

Model generation includes the measurement of light scattering by DRF or its components, and computational methods:

**Parametrization of measurement and model generation:** What are the effects of the parametrization of the measurement, and the subsequent generation of data-driven models of variable resolution by interpolation and data-reduction, and how do these effects relate to the characteristics of different DRCs?

**Measuring and modelling retro-reflection:** How can distinct retro-reflection by an innovative coating be captured in measurements of light scattering, and how can it be modelled to assess the effects on visual comfort prior to the availability of prototypes?

**Efficient combination of layer properties:** Can the matrix-calculations to combine the light scattering properties of fenestration layers be adapted to data-driven models of high resolution, so that model libraries could be build up, re-used and shared?

The research questions related to the application of data-driven models of DRF address the efficiency of daylight simulation as a limiting factor for applications in research and practice, and the potential simplification of CBDM techniques employing such models:

**Sampling of data-driven models:** How can the efficiency of daylight simulation with data-driven models of variable resolution be increased?

**Reducing the complexity in CBDM:** Can image synthesis by CBDM, compared to the 5PM, be simplified while maintaining accuracy?

Besides these questions, that primarily aim for methodological advancements, the developed techniques shall allow to test the potential of one particular Daylight Redirection (DR) technique:

**Retro-reflecting micro-structures:** To what extent can retro-reflective micro-structures in DRF control glare without obstructing the view?

## 1.7 Scope of this research

The research leverages recent developments in *RADIANCE* to model DRF or its components by its BSDF. Since the BSDF is averaged over the area, non-uniformity is not accounted for. The BSDF originates either from computational methods, or from measurements on samples. Methods to achieve high directional resolution in the measurement, modelling and application of data-driven BSDF models are developed. The methods are applied to exemplary DRF, that asks for high directional resolution to account for its particular angular selectivity and directional transmission in visual comfort assessments.

DR techniques are employed in overhead glazing, in light guiding and tracking systems, as well as in vertical fenestration. Since the latter is considered to have the largest potential for implementations, including all floors in multi-storey buildings, the research focuses only on DRF, e.g. for integration into the façade. Nevertheless, the methods are applicable to any type of DR that can be adequately described by the BSDF as an average surface property. This condition excludes e.g. heliostats, light-pipes, as well as macro-structured CFS as a whole, although data-driven modelling is demonstrated as a means to describe the components of such devices.

While the approach is applicable to model any short-wave radiative transfer through fenestration, the research focuses on applications in visual comfort assessments and therefore aims at photometric models. This is justified by the assumed particularly high impact of directional resolution on visual comfort. However, the method lends itself also to assess solar gains through highly selective CFS.

## 1.8 Structure of the thesis

The research is presented in the form of a *article thesis*. It comprises a collection of articles, addressing particular aspects of data-driven modelling of DRF for visual comfort assessments, framed by introductory and concluding chapters that are considered essential to put the article into a common research context.

Following this introduction (chapter 1) and a description of the instrumentation and measurement technique employed in this research (chapter 2), the thesis comprises a body of five core chapters. These were written and are either published or accepted for publication as articles in peer-reviewed journals:

**Chapter 3** “High-resolution data-driven models of Daylight Redirection Components”

Grobe, L. O. et al. *Journal of Facade Design and Engineering* **2017**, 5, 101–113

The parametrization of the model generation from measured BSDF as implemented in RADIANCE is evaluated. The tool-chain for interpolation, discretization and data-reduction is employed on measured BSDFs of two DRCs. The lack of an extrapolation method for arbitrary BSDF is discussed.

**Chapter 4** “Characterization and data-driven modeling of a retro-reflective coating in Radiance” Grobe, L. O. *Energy and Buildings* **2018**, 162, 121–133

An extension of the instrumentation is developed and applied to characterize the irregular reflection properties of an innovative retro-reflective coating. The measurements are compiled into a data-driven model, which is used to assess its effects on visual comfort when applied to the slats of Venetian blinds.

**Chapter 5** “Computational combination of the optical properties of fenestration layers at high directional resolution” Grobe, L. O. *Buildings* **2017**, 22

The matrix-based technique to combine the BSDF of one fenestration layer or a subsystems ( $BSDF_L$ s) of fenestration layers into a system BSDF of an entire fenestration system ( $BSDF_S$ ) is extended to models of variable directional resolution, allowing to efficiently model fenestration variants or states.

**Chapter 6** “The Radiance Photon Map for image-based visual comfort assessments with data-driven BSDF models of high resolution” Grobe, L. O. *Journal of Building Performance Simulation* **2019**, DOI: 10.1080/19401493.2019.1653994

Stochastic sampling of data-driven models of high directional resolution is inefficient in backward ray-tracing and limits applications in daylight simulation. A modification of the PHOTON MAP is proposed for efficient image generation employing data-driven

models, and its application is demonstrated in exemplary glare assessments for a single time-step.

**Chapter 7** “The Radiance Photon Map for image-based visual comfort assessments with data-driven BSDF models of high resolution” Grobe, L. O. *Energy and Buildings* accepted

The application of the PHOTON MAP is extended to annual simulations to simplify image synthesis with CBDM.

The relation between these chapters, that form the main contributions of this research and that are associated to the main research fields of data-driven modelling of DRF, and its application in daylight simulation, is illustrated by Figure 1.5.

Chapter 8 presents the main conclusions drawn from the core chapters and provides a set of recommendations based on the research. The main research contributions, scientific and non-scientific impact are reported. Finally, an outlook into possible future research emerging from the presented work given.

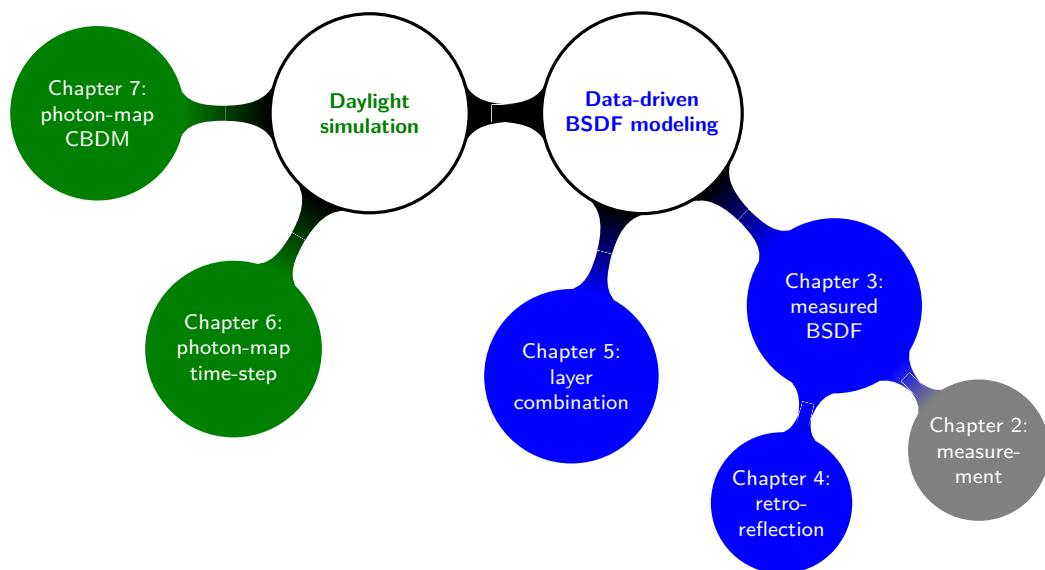


Figure 1.5: Relation between the core chapters of this thesis (green, blue). Each chapter covers a particular aspect of the two main research fields of data-driven BSDF modelling and daylight simulation.

## CHAPTER 2

### MEASUREMENT OF THE BSDF

#### 2.1 Instrumentation

The gonio-photometric acquisition of Bidirectional Scattering Distribution Function (BSDF) by measurement is of central importance for data-driven modeling. The measured BSDF can either be directly compiled into models, or be employed in the validation of models generated by computational means. Therefore, this chapter is dedicated to a brief description of the measurement method and the instrumentation. It extends a summary of the relevant literature on the instrument<sup>60–63</sup> and its experimental predecessor<sup>64</sup> by a description of the configuration and measurement protocol applied in this research.

##### 2.1.1 Fundamentals

The BSDF is a multidimensional, continuous function of – at least – four independent variables  $\theta_i, \phi_i, \theta_s, \phi_s$ . In this research, the photometric BSDF is averaged over

1. the wavelength range of visible light – weighted by  $v(\lambda)$ , the spectral response of human photopic vision – or the near infrared spectrum,
2. a representative area, the sampling aperture,
3. the apparent size of the light source and the detector.

The gonio-photometer employed in this research is shown in Figure 2.1. It implements the out-of-plane measurement of the BSDF by sequential recording – or scanning – of light scattered by a sample under known illumination. The incident light direction  $\theta_i, \phi_i$  is controlled by rotation of the sample with regard to the invariant position of the light source. The detector is mounted on a robotic arm, and continuously rotates around the sample while aiming at it, effectively varying  $\theta_s, \phi_s$ .

Since the instrument is set up so that the field of view of the detectors exceeds the sample size, the sampling aperture is constraint sole by the boundaries of the illuminating

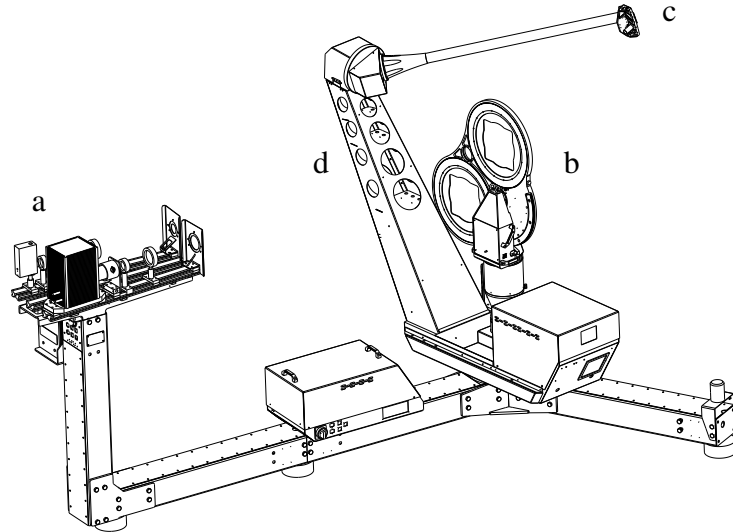


Figure 2.1: Scanning gonio-photometer employed in this research, comprising illumination system (a), sample holder (b) and detectors (c) mounted on robotic arm (d). (Source: pab advanced technologies Ltd.)

beam. This allows to freely configure the size of the sampling aperture by refocusing of the beam. The illumination system and its effects on the measurement are elaborated in subsection 2.1.2.

The detector's spectral response defines the wavelength range covered by the measurement. The geometry of the detector and its movement, together with the configuration of the illumination system, constrain the directional resolution that can be achieved. subsection 2.1.3 introduces the employed detectors and the scan strategy to represent a maximum directional resolution with a compact set of data-points.

## 2.1.2 Illumination system

The illumination system comprises an optical bench equipped with a set of light sources and optical elements to shape the beam. The open layout allows a high degree of flexibility in the configuration.

### 2.1.2.1 Light sources

For this research, three light sources with their respective optics are installed:

**Halogen lamp:** The 35 W incandescent lamp (Osram Halostar ES) lends itself to measurements in the wavelength range of visible light. Its continuous spectrum corresponds to a Correlated Color Temperature (CCT) of  $\approx 2700$  K<sup>1</sup>. The lamp with the optical elements forming its beam, and the resulting spectrum, are shown in Figure 2.2. To increase the optical output, a condenser lens concentrates the emitted light on a pin-hole, that acts as a spatial filter and controls the divergence of the illuminating beam. A subsequent short-pass filter blocks wavelengths  $> 700$  nm. This filter effectively balances the spectral sensitivity when a Silicon detector is employed, since both the maximum detector response and – unfiltered – lamp emission reach their maximum at  $\approx 900$  nm. The last element in the optical path of the illuminator is an achromatic focus lens with a focal length of  $f = 200$  mm, that allows to collimate or focus the beam and thereby sets the boundary of the sampling aperture.

**Xenon lamp:** The 150 W arc lamp (Osram XBO 150 W/CR OFR) emits a dense line spectrum effectively covering the entire solar spectrum, corresponding to a CCT of  $\approx 6000$  K. Figure 2.3 shows the lamp housing with the attached condenser tube, spatial filter and focus lens, and the effective spectrum clipped to the wavelength range of visible light<sup>1</sup>. Emitted light is collected by a back-mirror installed in the lamp housing, as well as by the condenser lens sliding in the attached tube. The original pin-hole was replaced by a variable iris diaphragm to allow for either low beam divergence or increased optical output power. The latter is of importance to increase the Signal to Noise Ratio (SNR) e.g. in spectrally resolved measurements, or when the BSDF is low such as with highly absorptive or highly specular samples. The focal length of  $f = 300$  mm allows to illuminate a large sampling aperture of up to  $\varnothing \approx 65$  mm with a collimated beam at normal incidence, equal to the diameter of the lens. This is of relevance when a large representative area of a sample has to be covered, e.g. in the case of macro-structures and non-uniform samples. BSDF measurements can be spectrally resolved by the introduction of filter stacks into the optical path between iris and focus lens.

**Laser diode:** The recently added 4 mW diode (Infiniter / Quarton VLM-520-02 LPA), as shown in Figure 2.4, emits green light in the range 505 nm to 530 nm, close to the peak sensitivity of the human eye. For maximum stability, it is operated at the lower end of its rated voltage range of 7 V to 10 V. The tunable lens attached to the diode focuses the beam on the sample. This results in a narrow sampling aperture of  $\varnothing \approx 1$  mm, allowing to measure oblique incident directions on very small samples. Due to interference effects, the coherent light source cannot be employed in measurements on very fine structures.

---

<sup>1</sup>Emission spectra and CCT were measured with a Sekonic Spectromaster C-700 spectrometer.

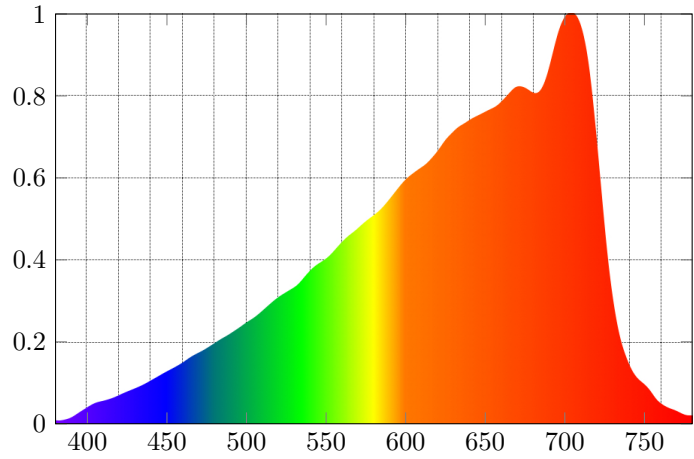
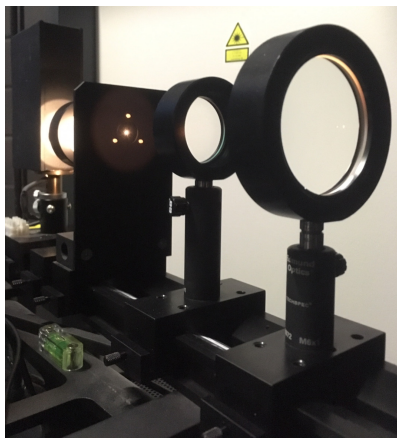


Figure 2.2: Halogen lamp with condenser, spatial filter, short-pass filter, and focus lens, and its normalized effective emission spectrum.

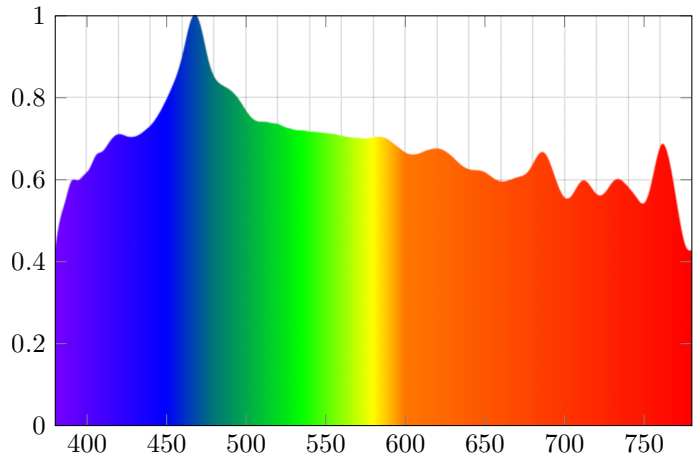
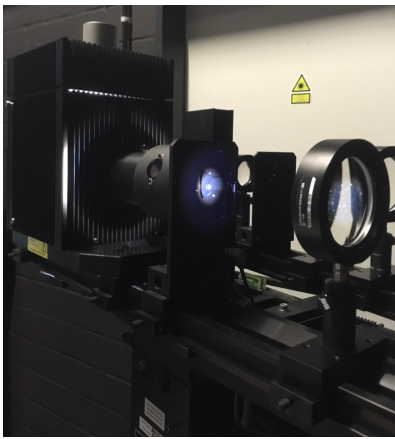


Figure 2.3: Xenon lamp with condenser, iris (in attached tube) and focus lens, and its normalized effective emission spectrum clipped to the wavelength range of visible light.

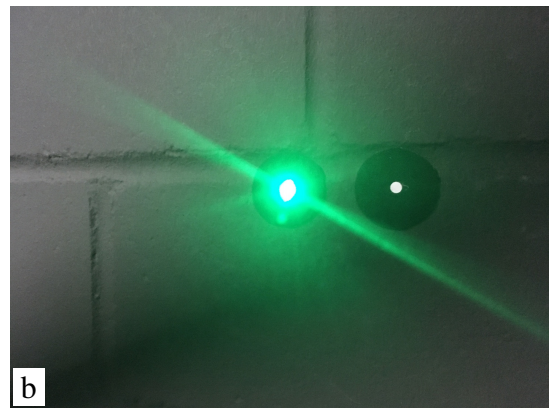
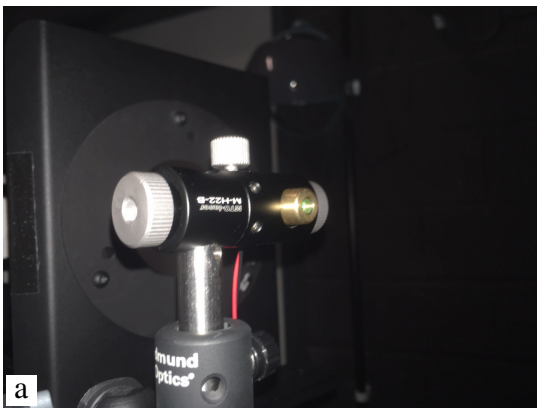


Figure 2.4: Green laser diode with built-in focus lens (a) and its beam on the back-wall of the laboratory(b).

### 2.1.2.2 Focus and beam shape

For any of the light sources, the beam diameter, and thereby the size of the sampling aperture as well as the apparent size of the light source, can be configured. Typical configurations are shown in Figure 2.5, Figure 2.6, and Figure 2.7. While the positions of the condenser lens  $L_1$  and the spatial filter, implemented by a pin-hole or variable iris diaphragm  $PH$ , are invariant, the distance of the focus lens  $L_2$  to  $PH$  is varied:

**Focus on detector:** Focusing the illuminating beam on the detector, as shown in Figure 2.5, minimizes the apparent size of the light source, and therefore achieves the highest directional resolution of  $\approx 0.7^\circ$ . This is the default configuration when the resulting, moderate size of the sampling aperture is acceptable, and allows the characterization of samples with highly directional, e.g. "peakish", transmission and reflection properties.

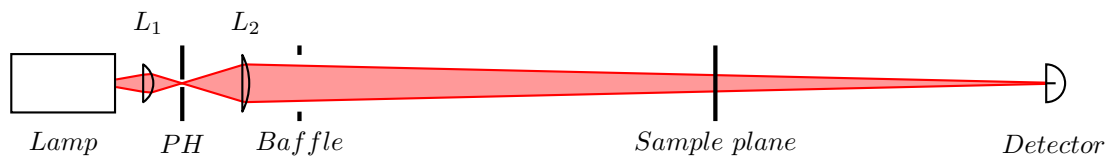


Figure 2.5: Focus on detector.

**Focus on sample:** This configuration, illustrated by Figure 2.6, minimizes the sampling aperture. This effect is desirable with small samples, when otherwise the illuminated area would exceed the sample size for oblique incident directions, or when particular regions on a non-uniform sample shall be characterized separately. The apparent diameter of the light source at the detector is moderately increased, the maximum directional resolution is  $\approx 1.0^\circ$ .

**Focus at infinity:** The collimated beam achieved by the configuration shown in Figure 2.7 best approximates the ideal of parallel light, and increases the sampling aperture to the size of the focus lens  $L_2$  of  $\approx 65$  mm. While the achievable directional resolution degrades to  $\approx 2.0^\circ$ , this configuration allows to cover a representative area on samples featuring large periodical structures, such as blinds assemblies, or spatially non-uniform properties. To avoid the width of the beam exceeding the size at the sample at oblique incident directions, a baffle can be introduced into the optical path. However, this

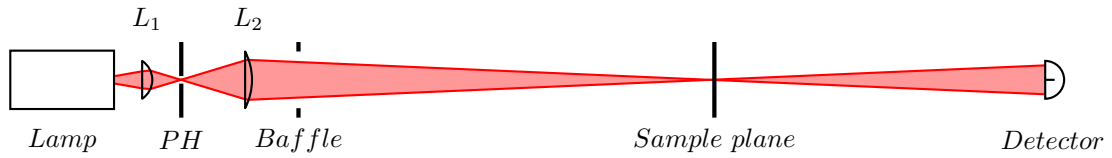


Figure 2.6: Focus on sample plane.

results in high losses by shading most of the power contained in the beam, and therefore decreases the SNR.



Figure 2.7: Focus at infinity.

The setup for the laser source differs in that only a focus lens is coupled to the diode. A spatial filter would improve the quality of the beam in terms of axial symmetry and stray-light close to the peak, but cause a loss of the integral power. Since the main motivation to extend the instrument by a coherent source is the minimization of the sampling aperture, not the increase of directional resolution, the current setup lacks a spatial filter. To avoid excessive stress for the measurement electronics, focus on the detector is avoided.

### 2.1.3 Detectors

The gonio-photometer features three detectors mounted to a robotic arm allowing a spherical rotation over the sample (Figure 2.8). All three detectors are directly coupled to circuitry supporting four amplifier levels to achieve quasi-linear response over a dynamic range of  $\approx 7$  decades.



Figure 2.8: Si (a), Si photometric (b), and InGaAs (c) detectors employed in this research. The outer two positions are unused and available for future extensions.

### 2.1.4 Detector types and spectral response

Two of detectors are based on a Silicon (Si) photodiode, the third features an Indium Gallium Arsenide (InGaAs) diode:

**Silicon:** This solar cell has a response in the range  $\approx 300$  nm to 1100 nm peaks at  $\approx 900$  nm, and achieves the highest sensitivity. It lends itself to measurements where the SNR is critical and a flat spectrum can be assumed, as well as to measurement configurations that define wavelength bands on the illuminator's side by the use of filters.

**Photometric:** A Si diode equipped with a  $v(\lambda)$  filter mimics human photopic response according to a standard observer. The weighted response 380 nm to 780 nm has its peak at about 550 nm and allows photometric measurements.

**Indium Gallium Arsenide:** The spectral response covers the near infrared wavelengths in the range 1200 nm to 2500 nm. The detector is not cooled and sensitive to the room temperature.

To avoid a signal drift due to changing room temperature, and to minimize thermal noise especially in measurements in the near infrared, the laboratory's air temperature is kept constant at 20 °C and is monitored for stratification at several heights.

The – weighted – combination of the measurements by Si and InGaAs detectors allows to forge a solar BSDF. The weighing factors differ for the various solar standard spectra in use. If the spectral power distribution is known to be flat, a weighted combination of photometric and near infrared can approximate the solar properties. However, due to the weighting of the  $v(\lambda)$  curve and the resulting gap 780 nm to 1200 nm, the combination of the unfiltered Si and the InGaAs measurements is preferred.

## 2.1.5 Geometry of detector movement

The measurement of the continuous BSDF by discrete sampling implies the application of a directional basis to any of its independent variables. The scanning gonio-photometer employed in this research allows to program the distribution of sampled directions by programming the movement of the detector in terms of scan paths. This flexibility distinguishes the scanning gonio-photometer from typical instrumentation employing image-based acquisition techniques with an invariant directional resolution. Four basic path types, as illustrated by Figure 2.9, can be parametrized and combined to form a complex scan geometry of adaptive directional resolution:

**Spherical:** This path describes a full spherical scan around the sample by continuous rotation of both segments of the robotic arm. The spherical scan lends itself to an overall, coarse characterization of the scattering properties. Given that the initial scan is fine enough to locate all distinct features of the distribution, subsequent refinements can be guided.

**Concentric peak:** The detector moves on a spiral path starting at a central direction that can be either defined as ideal reflection and transmission, or automatically derived by analysis of a preceding spherical scan. Currently, only one peak direction can be identified automatically.

**Scanline peak:** An alternative scan pattern for refinements of peaks covers a rectangular region by parallel line-scans. Compared to the concentric peak scan, the stability of the detector movement is improved.

**In-plane:** The scan covers a band centred at the scatter plane for  $\phi = 0^\circ$ . It lends itself to in-plane characterization, e.g. for an accurate acquisition of the profile of the BSDF for comparisons, and to linear structures, such as prism arrays and blinds, causing a deflecting by multiple peaks or over a widened angle.

## 2.1.6 Sample mounts

A set of interchangeable holders allows to mount samples of different sizes in a range from  $\approx 50 \text{ mm} \times 50 \text{ mm}$  to  $1000 \text{ mm} \times 900 \text{ mm}$  (Figure 2.10 a). The latter is relevant e.g. if samples cannot be cut to size, such as assemblies comprising tempered glass layers,

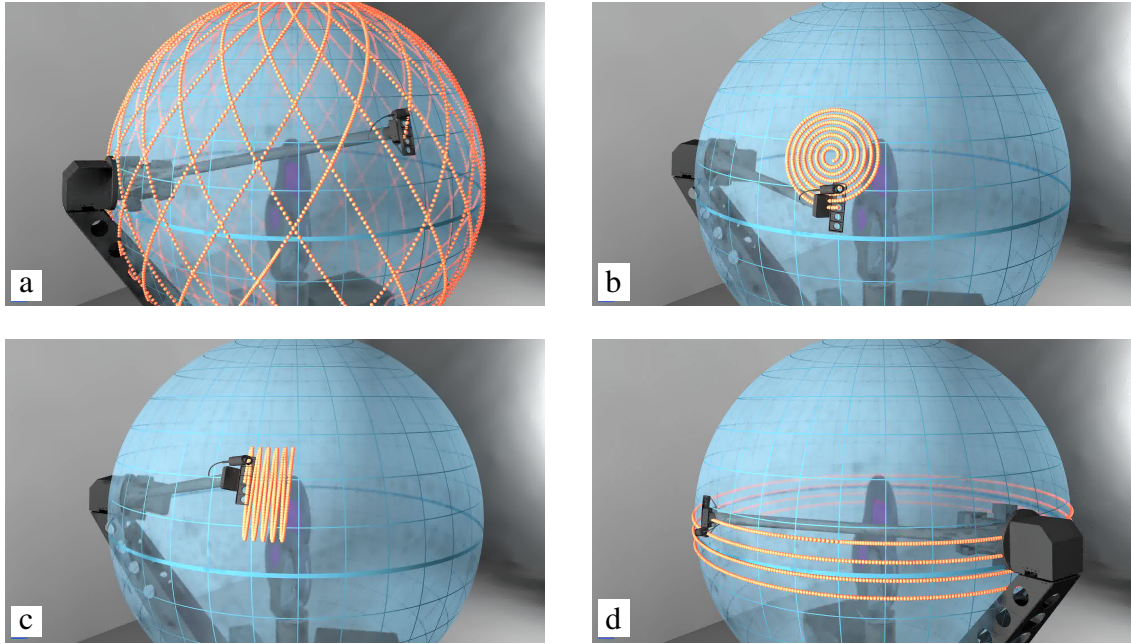


Figure 2.9: Spherical (a), concentric (b) and scanline peak (c), and in-plane (d) scan paths. Image courtesy pab advanced technologies Ltd.

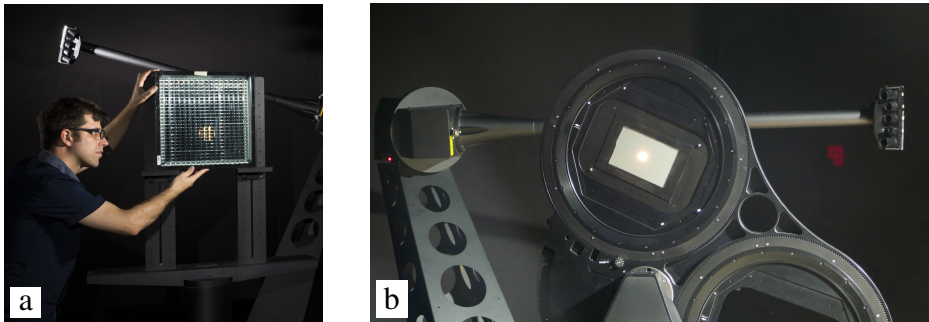


Figure 2.10: Large mount for samples up to 1000 mm  $\times$  900 mm (a) and automated holder and positioner for two A4 sized samples (b).

or if a large sampling aperture shall be covered in measurements of macro-structured Complex Fenestration System (CFS).

All sample holders allow to automatically vary the incident direction by rotation over the vertical axis, effectively defining  $\theta_i$ .  $\phi_i$  is set by manual rotation in the sample plane. An automated holder (Figure 2.10 b) positions two A4 sized samples in the beam path, removes them for the characterization of the unobstructed beam, and allows to program arbitrary orientation of the samples toward the light source by two-axis rotation. This extension is of particular importance if samples are not only to be characterized by measurements for few, selected incident directions, but when data-driven models are generated by interpolation between a large amount of measurements.

For specular measurements on retro-reflective samples, an experimental extension is developed that supports small samples up to  $\approx 50$  mm  $\times$  50 mm. The extension, and its application, are presented in detail in chapter 4.

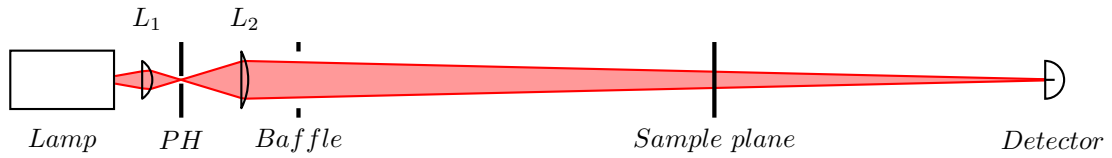


Figure 2.11: Reference measurement.

## 2.2 Data acquisition procedures

The gonio-photometer measures the BSDF relative to the differential irradiance on the sample, which is acquired by a characterization of the unobstructed beam. This design avoids dependencies on a fixed instrument calibration in favor of a built-in calibration step, and thereby supports the reconfiguration of the instrument. Measurements take place in a dark environment.

### 2.2.1 Beam characterization

The unobstructed beam measurement, also referred to as the reference beam, accounts for all effects of changes in the illumination system, as well as detector response. These can be intended, such as the reconfiguration of the optical elements, or unintended, such as instability of the light sources. While, in practice, the beam power does not change over the course of weeks, a frequent beam characterization is a reliable indicator for instabilities as well as misalignment.

The beam measurement is performed with the intended configuration of the latter sample characterization, but prior to the introduction of the sample into the optical path (Figure 2.11). Assuming that the optical setup is effective in shaping the beam, the beam measurement can rely on one of the peak paths introduced in subsection 2.1.5. The path has to be configured so that the entire beam, including stray-light by the optical elements of the illumination system, is covered at sufficient directional resolution.

The integral of the measured beam distribution corresponds to the power reaching the sample, equal to the exitance from the empty sample aperture. This integral is used later in the derivation of the BSDF, which is described in section 2.3.

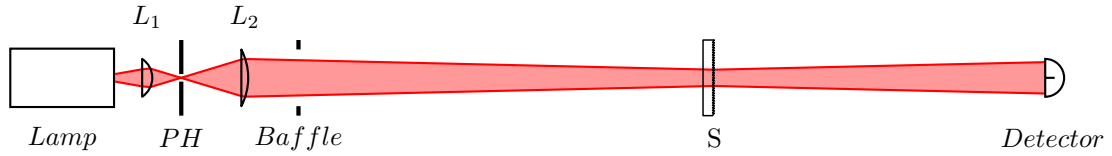


Figure 2.12: Measurement of light scattered by a sample.

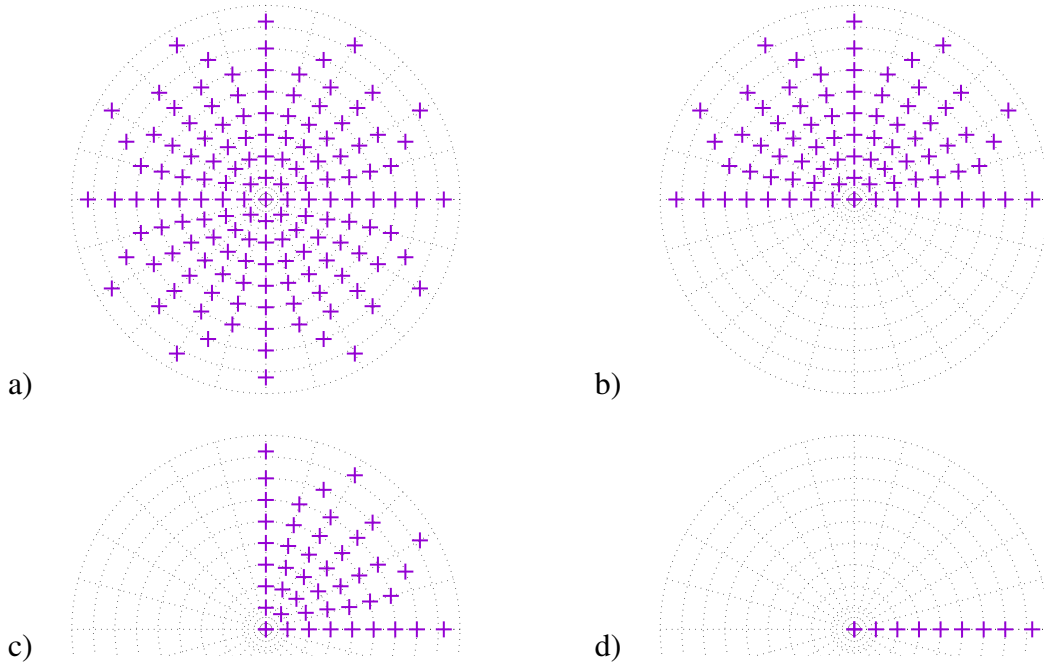


Figure 2.13: Incident directions: 145 directions by Klemm basis (a), half set assuming one-axis symmetry (b), quarter set for two-axis symmetry (c), and slice for isotropic scattering (d).

## 2.2.2 Measurement of scattered light

After completion of the beam characterization, the sample is introduced into the light path by manually installing it on a sample mount, or by switching the position of the programmable sample holder. The latter is implemented by rotation of a disk with three apertures, two for samples and one for the unobstructed beam characterization. In this configuration, light can reach the detector only by reflection, for cases when the detector is on the side of the sample facing the illumination system, or by transmission as illustrated by Figure 2.12).

The incident light direction is configured by rotation of the sample holder. The Klemm directional basis and, according to symmetry of the scatter properties, its subsets are chosen as incident directions in this research (Figure 2.13).

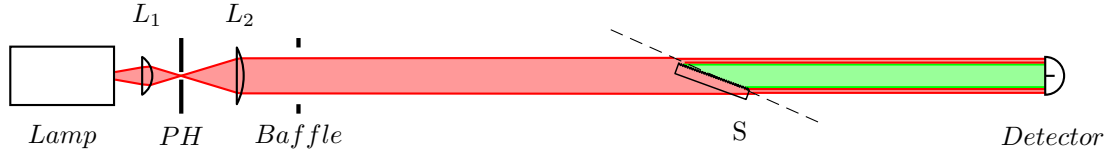


Figure 2.14: Width of collimated beam exceeding sample size at oblique incidence.

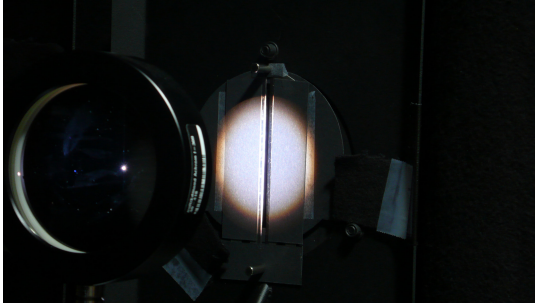


Figure 2.15: An improvised baffle, comprising two razor blades, constrains the effective width of the collimated beam.

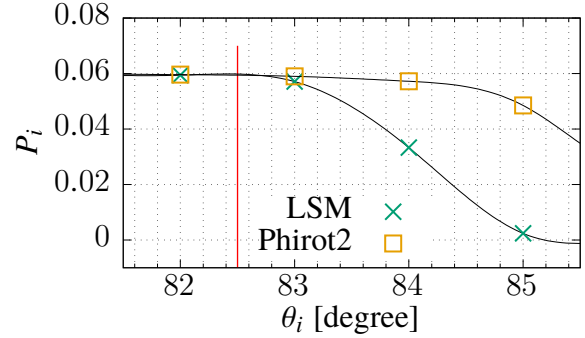


Figure 2.16: Integral  $P_i$  of the collimated beam under oblique incidence with slit baffle and two different sample holders.

The Klems basis defines a range of incident off-normal angles of  $\theta_i = 0^\circ$  to  $82.5^\circ$  for the front, and  $\theta_i = 97.5^\circ$  to  $180^\circ$  for the back measurements. Since the effective sampling aperture's width increases with the cosine of  $\theta_i$ , it may exceed the sample area if a collimated beam is employed to cover a representative area on macro-structured samples (Figure 2.14). e.g. in the case of the automated holder supporting up to A4 size. The introduction of a slit baffle, as shown in Figure 2.15, mitigates this limitation but results in a significant loss of the illumination system's output power. Figure 2.16 shows the effectiveness of this measure, achieving a constant beam integral  $P_i$  even for directions exceeding the maximum  $\theta_i$  defined by the Klems basis (red line) when a manually operated large sample holder (LSM), or the automated sample holder and selector (Phiro2) are employed in measurements with oblique, collimated beam.

An alternative approach to minimize the width of the sampling aperture with any non-coherent light source was devised, but could not be implemented yet. As illustrated in Figure 2.17, the focus lens  $L_2$  is replaced by a rod lens  $L_{2a}$  ( $\varnothing = 4$  mm) and a cylindrical lens  $L_{2b}$  ( $\varnothing = 70$  mm) in a cross configuration, each with the pin-hole in their focal points. The setup would shape an elliptical rather than a circular beam diameter to constrain the beam size in only one direction. The proposed design would theoretically produce a narrow elliptical beam of 70 mm height (y) and 4 mm width (x in Figure 2.17) at normal incidence. For a maximum oblique incidence of  $\theta_i = 82.5^\circ$ , this would result in an effective width of the sampling aperture of  $\cos 82.5^\circ \cdot 4$  mm = 52 mm. The design would avoid the interference effects of the laser with small structures, as well as the losses caused by the use of slit-baffles.

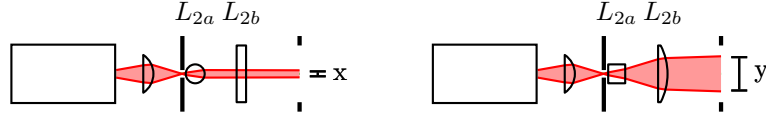


Figure 2.17: Beam shaping with two crossed cylindrical lenses  $L_{2a}$  and  $L_{2b}$ .

For each incident light direction the distribution of scattered light is recorded sequentially along scan paths defined by parametrization and combination of the basic types as introduced in subsection 2.1.5. During its continuous movement, the detector samples irradiance  $E_s$  at a frequency of 1 kHz. To extend the dynamic range of the measurement, the scan sequence is repeated with varying signal amplification levels up to four times.

### 2.3 Derivation of BSDF from measurements

The measurement for each incident direction  $\theta_i, \phi_i$  results in a dense distribution of data-points  $E_s(\theta_s, \phi_s)$  scattered on a spherical surface. Typical data-sets comprise 100 000 to 500 000 data-points per incident direction. The following passage briefly summarizes the derivation of the BSDF from the measured signal.<sup>62,64</sup>

To derive the BSDF first the integral of the beam characterization is calculated:

$$P_i = \int_{\theta_s=90}^{\theta_s=180} \int_{\phi_s=0}^{\phi_s=90} E_s(\theta_s, \phi_s) d\theta_s d\phi_s \quad (2.1)$$

With  $P_i$  being known, the Differential Scattering Function (DSF) for each data-point can be computed:

$$DSF(\theta_i, \phi_i, \theta_s, \phi_s) = \frac{E_s(\theta_i, \phi_i, \theta_s, \phi_s)}{P_i} \quad (2.2)$$

The BSDF is equivalent and calculated by scaling the DSF with the inverse of  $\cos(\theta_s)$ :

$$BSDF(\theta_i, \phi_i, \theta_s, \phi_s) = \frac{DSF(\theta_i, \phi_i, \theta_s, \phi_s)}{\cos(\theta_s)} \quad (2.3)$$

All measured data is stored in a relational data-base, and accessed through the software MOUNTAIN. MOUNTAIN implements the above calculations and performs all relevant post-processing on the data, in particular:

**Interpolation:** The scattered data-points are connected by triangulation to reconstruct the continuous distribution from the samples. The software implements the Delaunay algorithm in two dimensions.<sup>65</sup>

**Interactive visualization:** The resulting triangle mesh, as well as the data-points, are visualized in an interactive environment allowing to zoom, rotation and translation. This functionality is important for the visual inspection of the results, and allow to identify errors such as misalignment, drift, noise and other inconsistencies.

**Integration:** The triangulated mesh allows the hemispherical integration of the distributions. This is of particular importance to find the illuminating beam integral  $P_i$ , but can also be used to compute integrals sample properties such as direct-hemispherical transmission and reflection,  $\tau_{d,h}, \rho_{d,h}$ .

**Export:** The dataset representing each measured incident direction can be exported in a tabular format following the recommendations of ASTM E-2387-05. Each such file comprises a header section, reporting sample and measurement conditions, and a table with three columns  $\theta_s$ ,  $\phi_s$ , and either BSDF or DSF. Sections through the triangle mesh can be exported for any given  $\phi_s$ , allowing to extract profiles of the BSDF or DSF.

## CHAPTER 3

### HIGH-RESOLUTION DATA-DRIVEN MODELS OF DRCs

*This section expands a previously published article based on a conference paper:*  
“High-resolution data-driven models of Daylight Redirection Components” Grobe, L. O. et al. *Journal of Facade Design and Engineering* **2017**, 5, 101–113  
“High-resolution data-driven models of daylight redirecting components” Grobe, L. O. et al. In *ICBEST Istanbul: Interdisciplinary perspectives for future building envelopes*, ed. by Tavit, A.; Çelik, O. C., Istanbul Technical University: Istanbul, 2017, pp 84–93

---

The data-driven model in Radiance is a general means to model Daylight Redirecting Components (DRCs) in daylight simulation. Rather than internal optical mechanisms, their resulting Bidirectional Scattering Distribution Functions (BSDFs) are replicated. Models of two DRCs are generated from measurements. The impact of three necessary steps in the generation of data-driven models from measured BSDF is evaluated:

**interpolation** between measurements at sparse sets of incident directions,

**extrapolation** for directions that cannot be measured, and the application of a

**directional basis** of given directional resolution and subsequent data-reduction.

It is shown that data-driven models can provide a realistic representation of both DRCs. The sensitivity to effects from interpolation differ for the two DRCs due to the different complexity of their BSDFs. Due to the irregularity of the measured BSDFs, extrapolation is not reliable and fails for both tested DRCs. Different measurement and modelling protocols should be applied to different classes systems, rather than aiming at a common low-resolution discretization.

### 3.1 Introduction

DRCs control the admission and directional distribution of daylight in buildings. The application of DRCs aims at the optimized utilization of daylight for visual and thermal comfort, well-being and energy efficiency [7, 17]. Typical applications of DRCs are the upward deflection of daylight transmitted through the facade, to achieve even illumination, or the directional selective transmission only of diffuse daylight through horizontal glazing [16, 18]. Deflection and directional selectivity are examples for the irregular optical properties of DRCs that can be utilized for optimized daylight performance, but are beyond the capabilities of typical simulation tools employed in building design [67, pp. 579-580]. To address this lack of predictability as a barrier for the wide-spread and successful application of the technique, different modelling approaches have been demonstrated for the application in daylight simulation.

Software algorithms such as forward ray-tracing or the bidirectional combination of backward ray-tracing and forward photon-mapping can replicate the light propagation through DRCs based on geometric models. Photon mapping has been implemented in the daylight simulation software *RADIANCE* [68–70] and was extended to support even advanced simulation techniques such as Climate-Based Daylight Modelling (CBDM). However, this explicit approach demands highly detailed simulation models in cases where the micro-structures in the scale of millimetres comprising DRCs covering entire building facades shall be modelled geometrically.

Models of the Bidirectional Scattering Distribution Function replicate the effective light scattering characteristics of DRCs rather than the comprised geometric structures causing it. Such models describe light propagation as a function of incident and outgoing light direction through a surface. The two directions, relative to a coordinate system attached to the surface of the DRC, are typically expressed as pairs of elevation and azimuth angles  $\theta, \phi$ . The BSDF approximates light scattering as a uniform, average property of a thin surface. Analytic models of the BSDFs of DRCs have been developed and validated [71–73]. However, the development of such custom models for particular devices and applications is elaborate and of limited generalizability.

A general approach is the use of data-driven models of the BSDF. Such models comprise a discrete set of luminous coefficients, evaluating to the light propagation through the device for incident and outgoing directions merged into regions according to a given directional basis. They can be generated by computational simulation as well as from measurements [74, 75]. As a “black box”, data-driven models hide the complexity of the internal optical mechanisms effecting light propagation through the device from simulations employing the model [76, 77]. A symmetric directional basis of 145 incident and 145 outgoing directions is in wide-spread use and supported by a set of software tools mainly

developed by Lawrence Berkeley National Laboratory (LBL), such as `RADIANCE` and `WINDOW`. The latter allows to combine the BSDFs of co-planar fenestration layers into that of an entire glazing assembly, and provides an interface to the Complex Glazing Database (CGDB). The directional basis is employed in multiple domains of building simulation and backs advanced CBDM methods such as the Three-Phase-Method (3PM) [34, 78]. An asymmetric directional basis of 145 incident and 1297 outgoing directions was recommended by the International Energy Agency (IEA) and can be employed to pre-compute the transmission through DRCs with `mkillum` in `RADIANCE` [79, 80].

The highest directional resolution can be achieved by the locally adaptive tensor-tree format of `RADIANCE`, allowing up to 16 384 incident and 16 384 outgoing directions. To be applicable in simulation, and to allow sharing and re-use such as in model libraries, a compact representation for the data-driven model is required. Starting from a four-dimensional tensor of initially constant directional resolution, a data-reduction algorithm selectively merges cells representing adjacent directions with little variance in the BSDF to generate the compact tensor-tree [81, 82]. The combination of the optical properties of fenestration layers described by the tensor-tree format has been demonstrated in analogy to the method implemented in `WINDOW` [57].

The use of a discrete data to describe the continuous BSDF introduces problems of resolution into the generation, storing and application of models. Measurements sample the BSDF for a finite set of incident and outgoing directions. This set of directions is bound to geometric constraints of the instrument, excluding e.g. directions close to grazing and retro-reflection [83]. While their underlying dataset is necessarily incomplete, models must provide coefficients for any pair of directions in and therefore rely on interpolation and extrapolation. Data-reduction such as the merging of directions leads to a loss of information in the model.

In this chapter, the impact of both the interpolation and extrapolation in the generation of models from measurements, and the effect of directional resolution and data-reduction applied to the data-driven model shall be assessed for two exemplary DRCs.

A better understanding of the parameters defining measurement and model generation will guide the generation and application of data-driven BSDF models. Such models would provide a general means to better predict the daylight performance of DRCs in buildings, supporting both practitioners and researchers in the field of daylighting.

## 3.2 Methodology

The effects of the parametrisation of BSDF measurements, and the model generation process implemented in `RADIANCE`, are evaluated for two exemplary Daylight Redirecting Fenestrations (DRFs).

### 3.2.1 Two cases of Daylight Redirecting Components

The selection cases aims at typical examples of shading and non-shading DRCs for applications in vertical and horizontal glazing. The examples employ the optical mechanisms of reflection and refraction on periodic structures. Due to the small size of these structures, their scattering properties are perceived as uniform when seen from a typical observer position. It is therefore possible to model both DRCs by their effective BSDFs rather than explicit modelling of the geometrical structures causing their irregular transmission characteristics.

**DRC1** (Figure 3.1 left) is glazing unit with applied films. A prismatic film is laminated on the inward-facing surface of an outer pane and shall deflect incident light. A diffusing film is applied on the inner pane to achieve a smooth light distribution. The system improves daylight supply by deflection without but provides no shading effects [75, 84]. It can be employed e.g. in the upper zone of windows. The exact geometry of the micro-structures on both films is not known. The utilization of a data-driven model, based on measured BSDF data, allows to replicate its transmission characteristics even without detailed knowledge of the system's composition.

**DRC2** (Figure 3.1 right), a grid of tilted anidolic light-shafts, reflects direct sun-light but transmits and evenly distributes diffuse sky-light. It can control solar gains and glare when applied in sky-lights. The geometry of its highly reflective structure is known in detail [85].

#### 3.2.1.1 Measurement

The BSDFs of the DRCs are measured on a scanning gonio-photometer as shown in Figure 4.4. The characterization of each DRC comprises measurements of the illuminator's

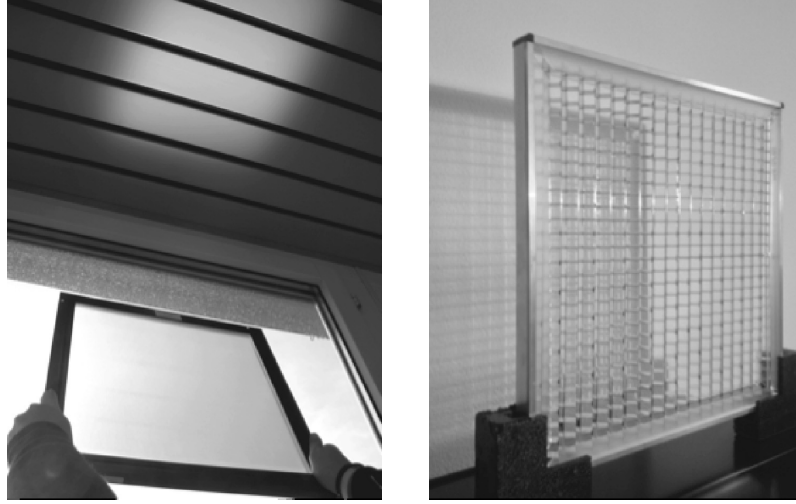


Figure 3.1: Samples of DRC1 (left) and DRC2 (right) provided for the measurement.

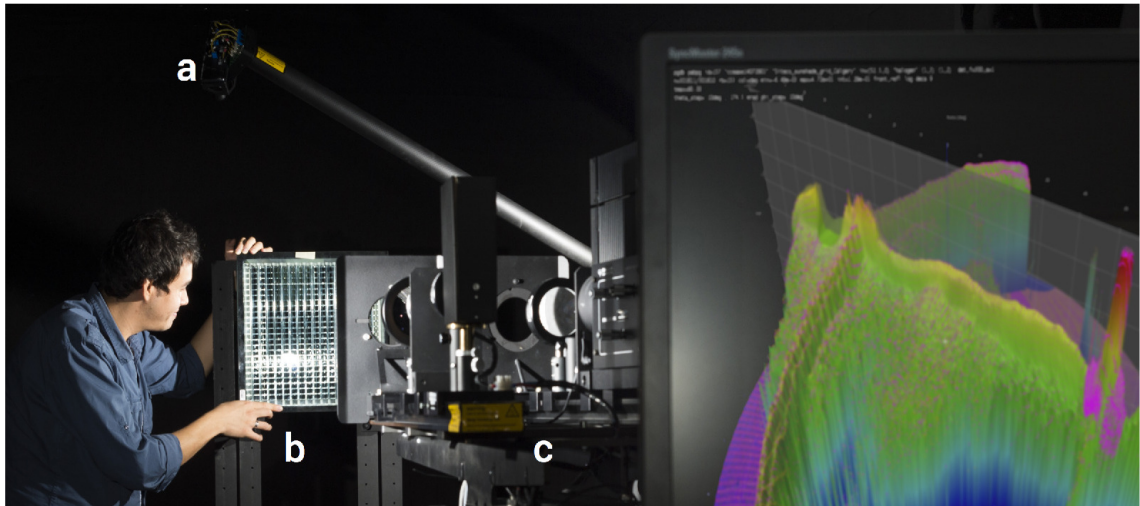


Figure 3.2: Gonio-photometer, comprising detector (a) moving around rotatable sample (b), and illuminator (c). Photograph: Martin Vogel.

intensity distribution followed by the recording of light scatter for each given incident direction. The latter is set by rotation of the sample, and the detector subsequently performs a continuous scan around the sampling aperture while recording illuminance  $E_s$ . The scan path is adaptive to the measurement and allows refinement e.g. for regions where transmission peaks occur.

Due to the prior beam characterization, the BSDF can be computed without photometric calibration from  $E_s$ , the power of the incident beam  $P_i$  (the integral of the unobstructed measurement) and the cosine of the outgoing elevation angle  $\theta_s$ :  $BSDF = E_s \cdot P_i^{-1} \cdot \cos(\theta_s)^{-1}$  [60].

The fine structures of DRC1 allow to set the focus of the illuminator on the detector for maximum directional resolution. The BSDF of DRC2 is measured under collimated illumination, leading to a widened illuminated sampling aperture covering a representative number of periodical structures.

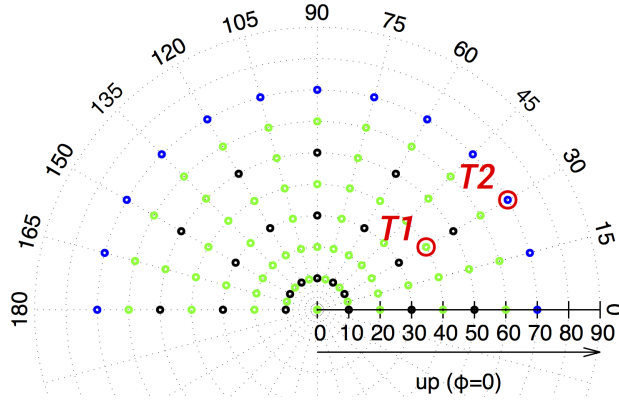


Figure 3.3: Incident directions Coarse (black), Refined (green), High (blue), T1 and T2 (red).

An asymmetric resolution of coarse incident directions  $\theta_i, \phi_i$  and dense outgoing scattered light directions  $\theta_s, \phi_s$  is chosen, assuming that features in the BSDFs require dense sampling of outgoing directions, but change only gradually between adjacent incident directions [63]. Due to the symmetry of both DRCs incident azimuth angles are varied as  $\phi_i = 0^\circ$  to  $180^\circ$ . For DRC1,  $\phi = 0^\circ$  corresponds to up, for DRC2 to North in typical applications.

Three sets of incident directions are distinguished (Figure 3.3):

**Coarse** (black): Low resolution with  $\theta_i = 10^\circ$  to  $50^\circ$  in increments of  $20^\circ$ ,  $\phi_i = 0^\circ$  to  $180^\circ$  in increments of  $30^\circ$ .

**Refined** (green): Refining Coarse with  $\theta_i = 0^\circ$  to  $60^\circ$  in increments of  $10^\circ$ ,  $\phi_i = 0^\circ$  to  $180^\circ$  in increments of  $15^\circ$ .

**High** (blue): Complementing Coarse and Refined, this dataset comprise incident elevation angles above  $60^\circ$ .

To test interpolation and extrapolation, the BSDFs for additional two incident directions T1  $\theta_i = 40^\circ, \phi_i = 30^\circ$  and T2  $\theta_i = 70^\circ, \phi_i = 30^\circ$  (red) are measured. In the results, these directions are shown mirrored as red circles.

### 3.2.2 Model generation

Three data-driven models are generated from the three data-sets. The process comprises three passes:

1. **pabopto2bsdf** fits a set of radial basis functions as interpolants to the four components (reflection front/back and transmission front/back) of the measurement.

2. These interpolants are subsequently sampled by the command `bsdf2ttree`<sup>1</sup> into a four-dimensional tensor of  $2^{4 \cdot 7} = 268\,435\,456$  elements. Higher resolutions are not possible on typical hardware due to memory constraints.
3. `bsdf2ttree` internally calls `rttree_reduce` to reduce this vast amount of data by merging adjacent directions of low local variance until 90 % of the initial data-set are eliminated, and saves the resulting tensor tree into a Extensible Markup Language (XML)-formatted file.

The method provides a set of three BSDF-models of adaptive resolution for each DRC:

**M1DRC1, M1DRC2** comprise BSDF from Coarse.

**M2DRC1, M2DRC2** comprise data-sets Coarse and Refined.

**M3DRC1, M3DRC2** comprise Coarse, Refined and High.

### 3.2.3 Comparison of transmission distributions

To evaluate the effect of parameters in the measurement and model-generation, pairs of the BSDF for a given direction are compared. We evaluate only transmission to the interior, which is of particular importance in building applications.

To maintain readability up to high outgoing directions, the Differential Scattering Function (DSF), equal to  $\text{BSDF}(\theta_i, \phi_i, \theta_s, \phi_s) \cdot \cos \theta_s$ , is plotted rather than the BSDF. The latter, due to the division by  $\cos \theta_s$ , tends to exaggerate data at measurement points close to grazing. The transmission distributions are plotted in polar coordinates, the center being  $\theta = 180^\circ$  and  $\phi = 0^\circ$  aiming right.

### 3.2.4 Evaluation of the effects of interpolation and extrapolation

The BSDFs of both DRCs for direction T1 as predicted by M1 and M2 are compared to the measurements. Predictions by M1, are result of interpolation, while M2 rely on measured data.

---

<sup>1</sup>The command is called as `bsdf2ttree -t4 -g 7 -t 90` for a four-dimensional tensor of initial directional resolution  $2^{4 \cdot 7}$ . The target for the data reduction is 90 %.

The measured BSDFs of DRC1 and DRC2 for T2 are compared to the extrapolated BSDFs from M2 and M3. As no data for incident directions above  $\theta_i = 60^\circ$  is employed in the generation of M2, these models provide results based on extrapolation. M3 comprise measured data for the queried incident direction.

### 3.2.5 Evaluation of the effects of resolution and data-reduction

For both DRCs, variants of M3 of reduced resolution (tensor of  $2^{4 \cdot 6} = 16\,777\,216$  elements representing  $2^{6 \cdot 2}$  incident and  $2^{6 \cdot 2}$  outgoing directions) without data-reduction are generated <sup>2</sup>. These are compared to variants of high resolution ( $2^{7 \cdot 2}$  incident and  $2^{7 \cdot 2}$  outgoing directions), but data-reduction by 97% applied leading to comparable model sizes <sup>3</sup>.

## 3.3 Results and discussion

For both DRCs, the generated BSDF models are compared to the corresponding measurements to assess the impact of interpolation, extrapolation and data-reduction.

### 3.3.1 Measurement

Figure 3.4 and Figure 3.5 show the DSF of DRC1 and DRC2 measured for T1 and T2. The prismatic structure of DRC1 spreads the scattered light to a rim with an upward peak for T1. DRC2 shows two forward peaks for T1 and a pattern of scattered light on the opposite side of the  $\phi_i = 0^\circ, 180^\circ$  plane. These peaks disappear at direction T2 with a remaining distribution of diffused light.

---

<sup>2</sup>Generated by `bsdf2ttree -t4 -g 6 -t -1`

<sup>3</sup>Generated by `bsdf2ttree -t4 -g 7 -t 97`.

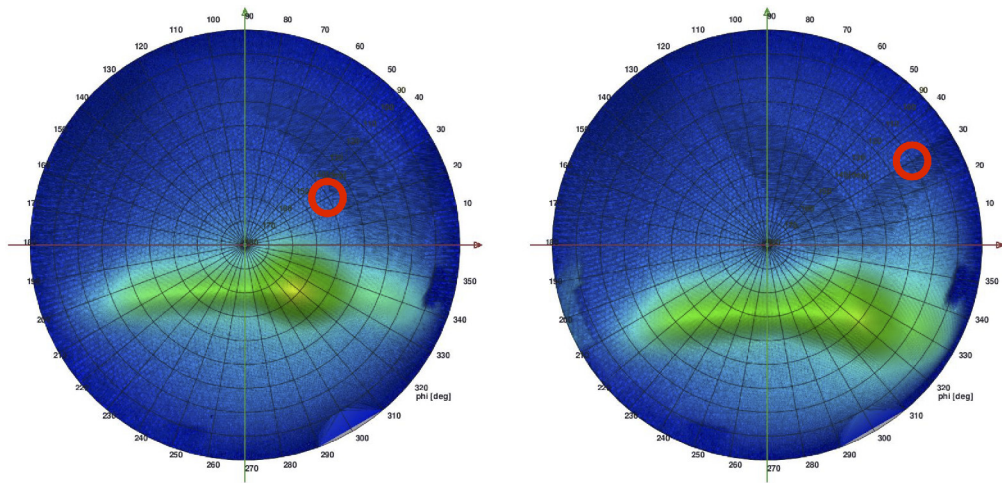


Figure 3.4: Measurement: DSFs of DRC1 for incident direction T1 (left, red) and T2 (right, red).

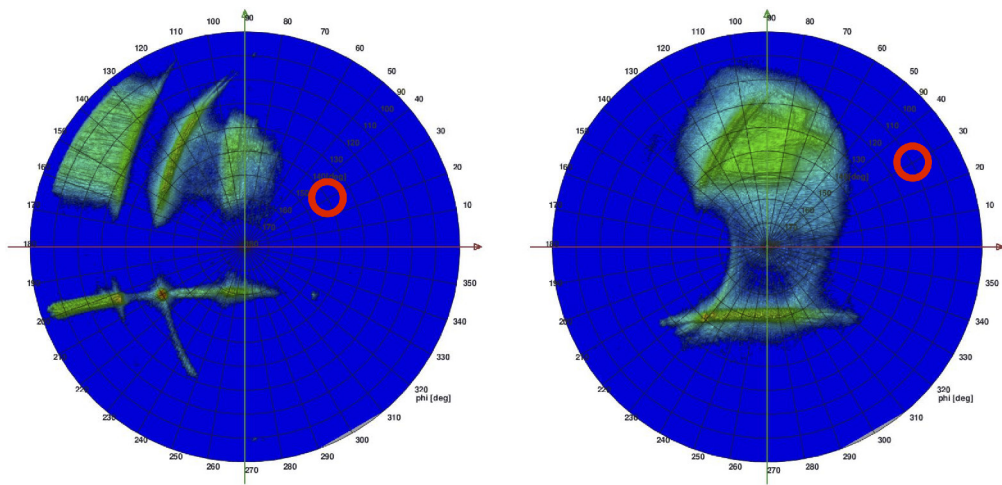


Figure 3.5: Measurement: DSFs of DRC2 for incident direction T1 (left, red) and T2 (right, red).

### 3.3.2 Interpolation effects

M1 and M2 lead to almost identical results for DRC1 but do not show the ridge as pronounced as measurements. Transmission to the downward direction (lower left quadrant) is underestimated by M1 when compared to M2 (Figure 3.6). For DRC2, M1 replicates the configuration of features found in the measurement, such as a strong peak due to direct transmission at  $\theta_s = 140^\circ, \phi_s = 210^\circ$  (Figure 3.7). The shape of other features, such as a secondary peak at  $\theta_s = 120^\circ, \phi_s = 200^\circ$ , and two parallel rims in the upper half of the plot, are not maintained by M1 but M2. The latter only differs from the measurement by less pronounced contours of its features, and a gradient toward grazing for which no measured data exists. The interpolation by M1 replicates the characteristic upward deflection of DRC1 as well as the distinct features of DRC2. The underestimation of downward transmission through DRC1 may however effect results in daylight simulation.

### 3.3.3 Extrapolation effects

As shown in Figure 3.8, the extrapolated DSF of DRC1 for T2 from M2 is almost flat in the deflected upward direction and lacks any peaks, which are present in the result from M3. Model M2 does not replicate the characteristic deflection of light toward the ceiling for high incident elevation directions, if these are not within the boundaries of the measurement. As no diffuse background is present in the DSF of DRC2, and no peaks in the complex DFS for T2 are extrapolated, M2 indicates almost zero transmission. This is contradicted by M3 (Figure 3.9), which closely matches the measured distribution. Due to the typical horizontal installation of DRC2, this corresponds to a significant underestimation of low sun angles e.g. in the morning and afternoon, if the boundaries of the measurement are not extended.

### 3.3.4 Effects of resolution and data-reduction

Figure 3.10 and Figure 3.11 show the DSFs for DRC1 and DRC2 at incident direction T1 at resolution  $k = 6$  without, and  $k = 7$  with 97% data-reduction applied. While the latter can better resolve the forward peak of DRC2 (Figure 3.11, right) data-reduction does not affect any important features for the two DRCs.

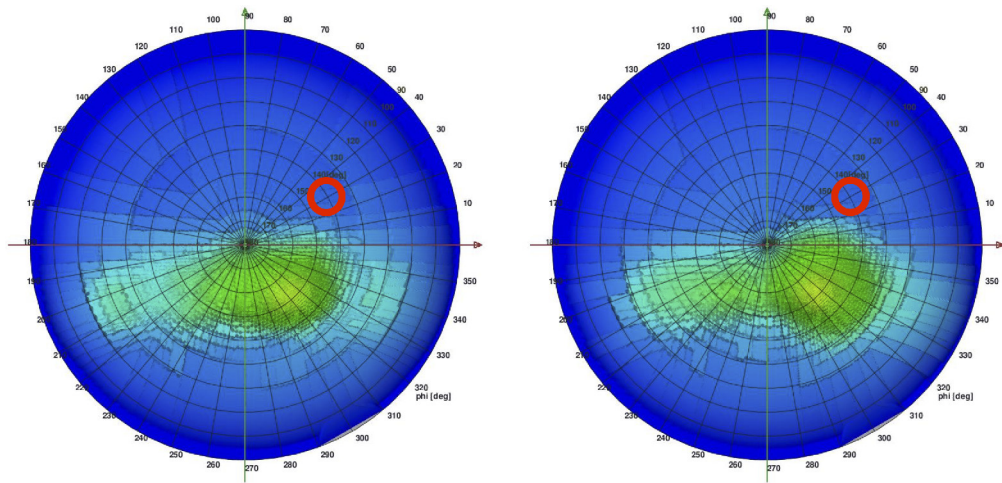


Figure 3.6: Predicted DSF of DRC1 for incident direction T1 (red) from interpolated M1 (left) and measured M2 (right).

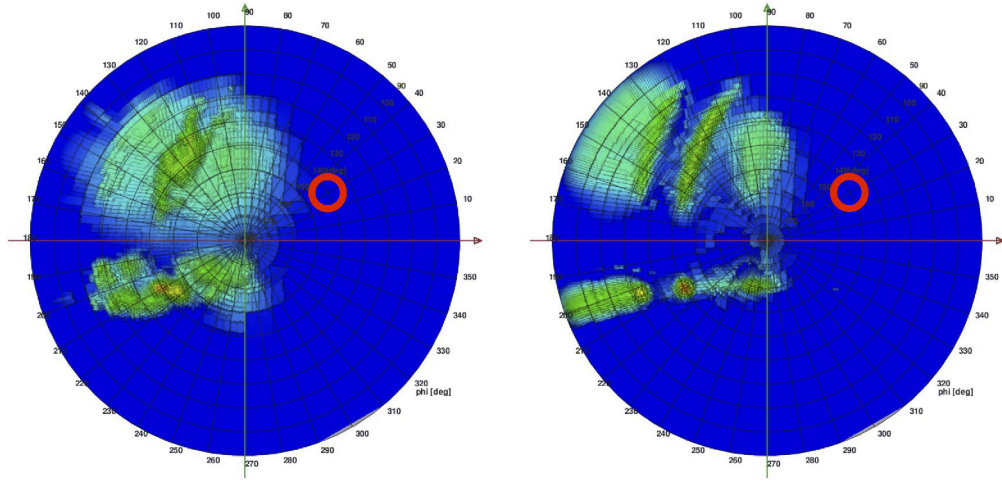


Figure 3.7: Predicted DSF of DRC2 for incident direction T1 (red) from interpolated M1 (left) and measured M2 (right).

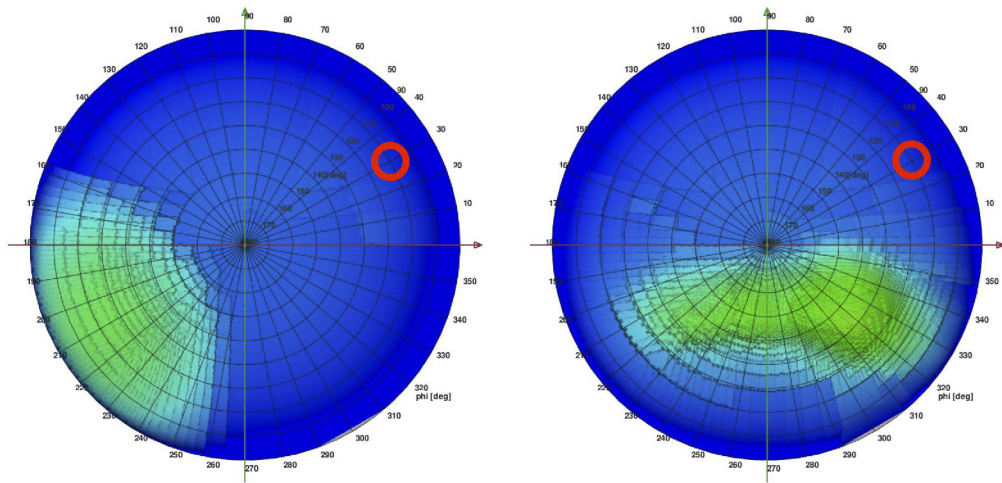


Figure 3.8: Predicted DSF of DRC1 for incident direction T2 (red) from extrapolation M2 (left) and measurement M3 (right).

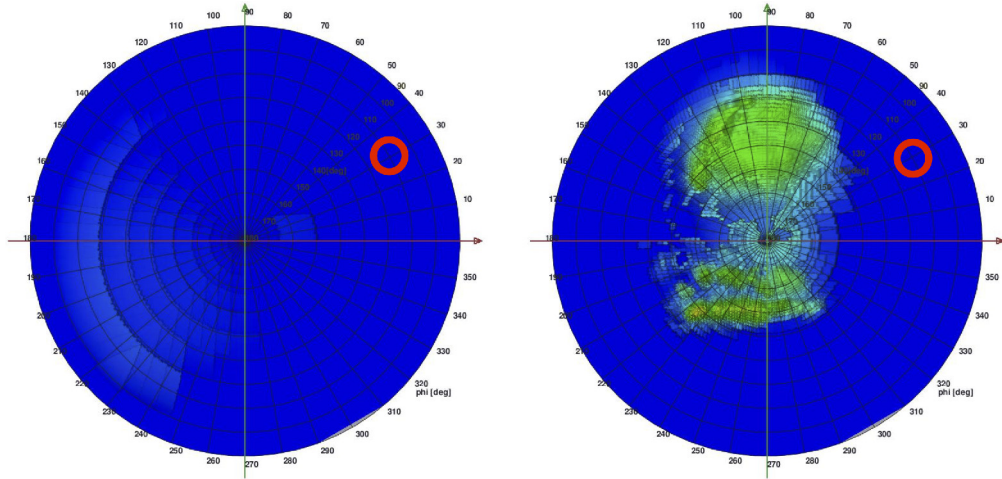


Figure 3.9: Predicted DSF of DRC2 for incident direction T2 (red) from extrapolation M2 (left) and measurement M3 (right).

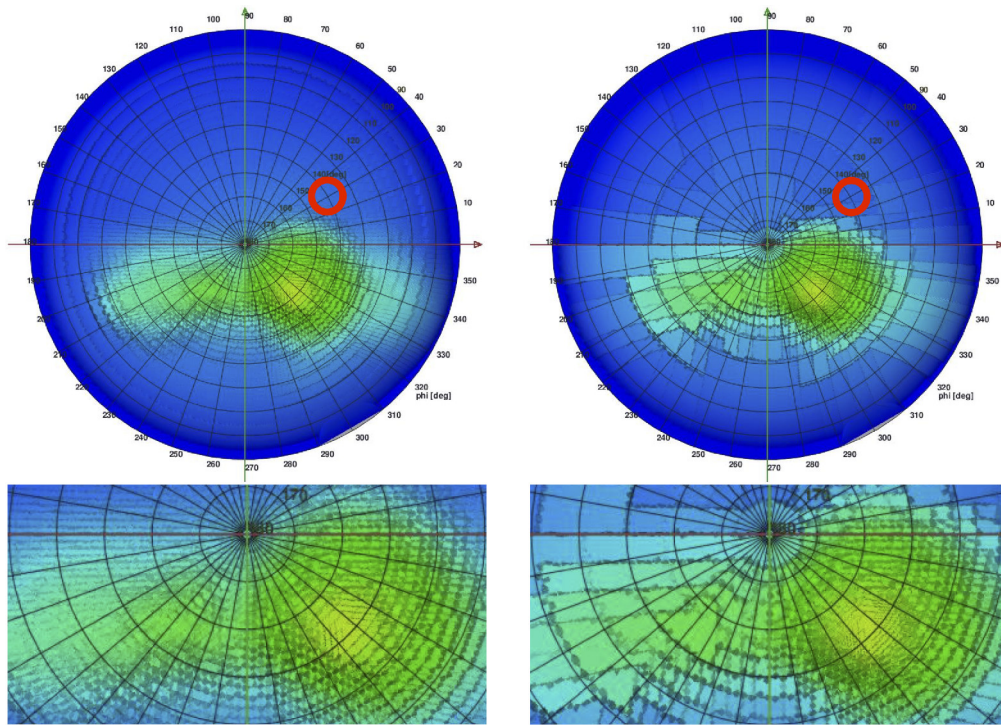


Figure 3.10: DSF of DRC1 for direction T1 (red). Left: Resolution  $k = 6$ , no data-reduction. Right:  $k = 7$ , data-reduction by  $pt = 97\%$ .

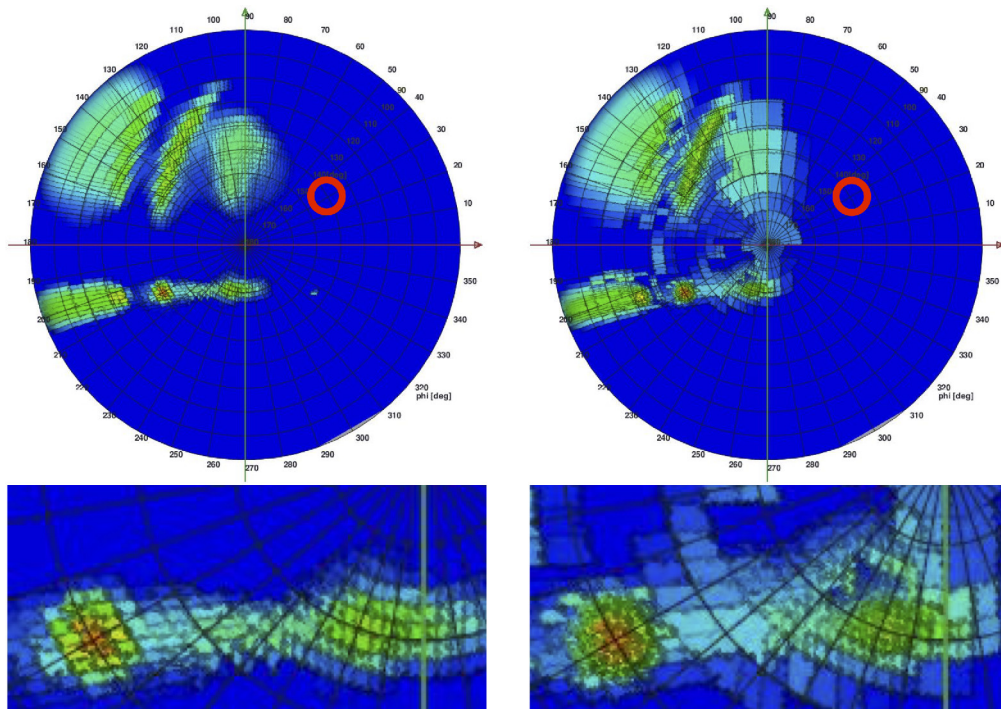


Figure 3.11: DSF of DRC2 for direction T1 (red). Left: Resolution  $k = 6$ , no data-reduction. Right:  $k = 7$ , data-reduction by  $pt = 97\%$ .

### 3.4 Conclusions and outlook

Data-driven models of two exemplary, micro-structured DRCs were generated based on measurements of their BSDF employing a gonio-photometer. The tensor-tree format of `RADIANCE` was employed, as it provides a generic means to model the irregular optical properties characterizing DRCs based on computation or measurement. Resulting models can be applied directly in daylight simulations with `RADIANCE`, or be efficiently combined with BSDF of other clear or non-scattering fenestration layers using an extended matrix formalism. The influence of interpolation and extrapolation, depending on the density of measurements as input for the model generation, was evaluated as well as the impact of model output parameters such as directional resolution and data-reduction.

While the data-driven model in `RADIANCE` is found capable to model the irregular BSDFs of both DRC1 and DRC2 by interpolation, less pronounced peaks such as the downward transmission through DRC1 can be underestimated. Resolution of measured incident directions is of particular importance for DRCs which abruptly change their properties between incident directions, such as DRC2, if details of the complex BSDF is to be maintained.

Extrapolation for complex BSDFs, which are characteristic for DRCs, is not reliable and did not lead to valid results for both assessed samples. Consequently models must be utilized only within the boundaries of measurements employed in model generation. Computational simulation to complement measurements even up to grazing have been demonstrated [83] but require detailed prior knowledge about the geometry and surface properties of DRCs. The extension of the geometrical boundaries to higher incident elevation angles imposes a challenge. The sampling aperture illuminated by a beam of circular diameter chosen to cover a representative amount of periodical features of a given DRC at normal incident tends to exceed the sample size at high elevation angles. While this can be addressed e.g. by shaping the beam employing elliptical or slit baffles, the resulting loss of beam power effects the signal to noise ratio of the measurement.

Data-reduction merges contiguous directions of low variance. This allows locally high resolution e.g. of distinct peaks at comparable file sizes, but effects less pronounced features such as ridges in the BSDF of DRC2.

The sensitivity of model accuracy to directional resolution and data-reduction depends on the complexity of the BSDF and shall be further studied for different classes of DRCs. Efficient configurations of the illumination system are currently investigated to limit the sampling aperture to the sample size even at very high incident directions.

The tensor-tree format and the routines for interpolation of measured BSDF implemented in `RADIANCE` provide a means to model DRCs characterized by high directional selectivity and highly directional, irregular transmission. Its variable resolution

promises higher accuracy in daylight simulation compared to the commonly used BSDF models of low directional resolution. To guide model generation and application employing the tensor-tree, a better understanding of the impact of directional resolution on assessments of different aspects of daylight performance, such as daylight supply, glare and energy-efficiency, is required.

### **3.5 Acknowledgments**

This research was supported by the Swiss Federal Office of Energy SFOE (#SI501427-01) as part of the project “High Resolution Complex Glazing Library (BIM-SOL)”. Sole responsibility for content and conclusions by the authors. DRC1 was provided by the Solar Energy and Building Physics Laboratory (LESO-PB) at École Polytechnique Fédérale de Lausanne (EPFL), its BSDF measured by Marek Krehel. Siteco Beleuchtungstechnik GmbH contributed DRC2. Thanks to Carsten Bauer for providing a photograph of DRC1 in Figure 3.1, and to Martin Vogel for Figure 4.4.

## CHAPTER 4

# MEASUREMENT AND DATA-DRIVEN MODELLING OF RETRO-REFLECTION

*This section was published as an article:*

“Characterization and data-driven modeling of a retro-reflective coating in Radiance”  
Grobe, L. O. *Energy and Buildings* **2018**, 162, 121–133

---

### 4.1 Introduction

The effective shading of direct sun-light is a key requirement for fenestration systems aiming for high thermal and visual performance. Solar gains shall be avoided at most times to prevent over-heating effects in well insulated buildings. Exposure to direct sun-light, while desirable to a certain degree in residential buildings,<sup>86</sup> can cause discomfort and veiling glare and severely affect the visual comfort e.g. in offices. Yet the supply of daylight and a view to the outside are essential performance criteria in facade design since they address energy efficiency targets as well as the comfort and well-being of occupants.<sup>7,19</sup>

Venetian blinds comprising profiles of often high geometric complexity address the dilemma to minimize the obstruction of view and daylight aperture, but exclude sun-light from being transmitted directly or by reflections in the fenestration.<sup>11,87</sup> However, the use of simple geometries appears to be desirable for at least two reasons. First, the manufacturing process to produce blinds with complex profiles is elaborate, if low tolerances shall be maintained. Second, any profile deviating from an ideal, flat slat occludes the view to the outside.

As an innovative approach to decouple shading performance from profile geometry, the application of a retro-reflective coating to the slats of Venetian blinds, and its effect on the daylight supply to an attached office, shall be tested.

### 4.1.1 Retro-reflection

Retro-reflection forms a special case of irregular light scattering by devices that “reflect incident light back toward the direction of the light source, operating over a wide range of angles of incidence”.<sup>88</sup> Standing out as the most prominent examples of retro-reflecting devices in optics are corner cubes and glass spheres, which retro-reflect light from any incident direction. The effect is utilized in a range of applications such as traffic signs and reflectors attached e.g. to clothes enhancing visibility.

When applied to Complex Fenestration Systems (CFSs), the term retro-reflection is often used in a broader sense, including devices that deflect light by altering only the elevation angle.<sup>89,90</sup> Since the horizontal azimuth angle is not affected by such CFSs, retro-reflection according to the formal definition given above occurs only for one given cardinal direction. Examples are retro-reflecting blinds, formed by extrusion of two-dimensional profiles. Such slats with configurable inclination angle are employed in CFSs to block direct sun-light. Complex profile geometries, combining sections that retro-reflect light from potential incident sun directions with sections that deflect light upward, allow to balance the daylight supply from direct sun-light with solar gains. The application of small-scale prismatic structures achieves retro-reflection even with simple geometries such as extruded arcs.<sup>13,91</sup>

The use of retro-reflective coatings comprising spherical and prismatic micro-structures in buildings has been proposed to mitigate urban heat islands effects.<sup>92,93</sup> A transparent window film applying such prismatic micro-structures has been demonstrated to selectively retro-reflect incident sun-light from high elevation.<sup>94</sup>

Applied on the surface of Venetian blinds, retro-reflective coatings have the potential to meet high visual and thermal comfort targets even with simple geometric profiles according to ray-tracing based assessments.<sup>95</sup> Empirical methods are however required to account for effects caused by imperfections in the composition and application of coatings,<sup>68</sup> and if the effective micor-structure is unknown or cannot be disclosed.

### 4.1.2 Measurement techniques

In typical configurations for reflection measurements, the retro-reflected fraction of scattered light is assumed to be negligible and excluded. An indirect measurement of this retro-reflected fraction by comparing absorption derived from calorimetric measurements with radiometric measurements of diffuse reflection has been proposed as an

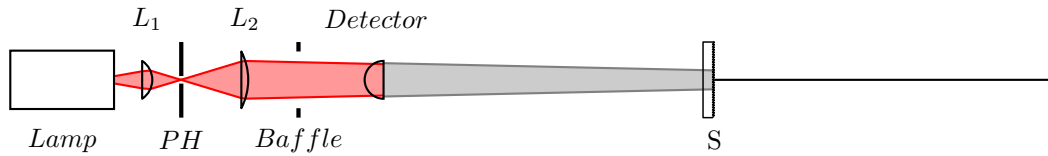


Figure 4.1: A naive approach to measure retro-reflection leads to shading by the detector.

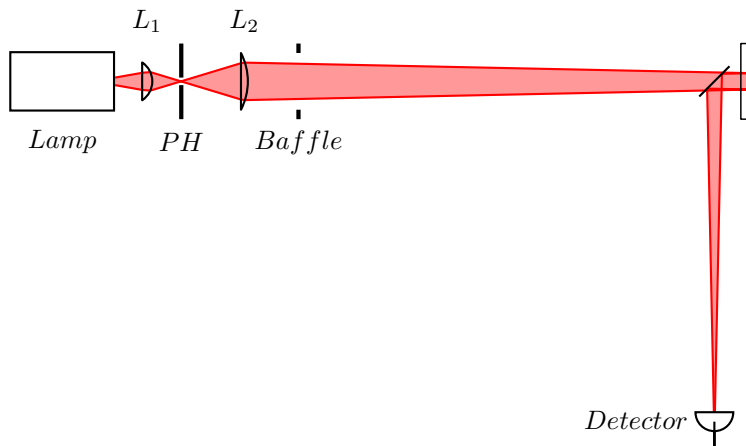


Figure 4.2: Configuration employing one beam-splitter.

approximation.<sup>96</sup>

A more comprehensive description of the directional distribution of retro-reflected light can be expressed by the Bidirectional Scattering Distribution Function (BSDF), describing the radiative flux between any pair of incident and outgoing scattered direction.<sup>60,97–99</sup> However, such directionally resolved characterization of retro-reflection employing goniophotometers is a particular challenge, since light source and detector occlude each other if incident and outgoing direction are close to equal (Figure 4.1). Only a very long distance between sample and detector allows to cover the peak region even of highly directional retro-reflection in such direct measurements.<sup>100</sup>

The introduction of a plate Beam Splitter (BS) between light source and sample allows the goniophotometric measurement of retro-reflection (Figure 4.2).<sup>101,102</sup> Light from the illuminator is partially transmitted by the BS to the sample. The retro-reflected light is then partially reflected by the BS to the detector. With an ideal BS, that transmits 50 % of the incident light and reflects the other 50 % without any absorptive losses, the detected signal would be attenuated to  $0.50 \cdot 0.50 = 0.25$ . The method relies on prior knowledge of the exact optical properties of the BS, which depend on the direction as well as the wavelength of light.

### 4.1.3 Modelling retro-reflection

To predict the retro-reflective effect caused by geometric structures, computational techniques for the simulation of light propagation such as ray-tracing can be employed with detailed geometric models.<sup>83,103</sup> However, due to the model complexity and size resulting from such approaches if applied to extended CFS, methods hiding the optically complex internal mechanisms are often preferred. Functional descriptions of the BSDF allow to hide the geometric complexity of retro-reflective structures. Numerous analytical,<sup>104</sup> numerical,<sup>105–107</sup> and empirical<sup>108</sup> models for particular cases of retro-reflection have been proposed but are of no general applicability.

Data-driven models are of general applicability but rely on huge data-sets. Basis functions such as wavelets or spherical harmonics provide a means to compress such data-sets at resolutions adequate to replicate characteristic features of BSDFs.<sup>109–111</sup> *RADIANCE* as a validated lighting simulation software for visual comfort assessment<sup>46</sup> implements a data-driven model based on adaptive data-reduction applied to a discrete representation of the BSDF as a four-dimensional tensor.<sup>51,82</sup> The dimensions of the tensor relate to incident and outgoing direction via an equal-area mapping algorithm between square and disk.<sup>57,112</sup> An interface to measured data is provided, featuring an advanced interpolation algorithm to reconstruct the full BSDF from sparse measurements for few incident directions.<sup>55,63,113</sup> The model is capable to replicate the characteristics of a retro-reflective coating.<sup>95</sup>

## 4.2 Materials and method

The data-driven BSDF in *RADIANCE* is employed to replicate retro-reflectivity of a coating measured by an extension to a scanning gonio-photometer.

### 4.2.1 Exemplary sample of a retro-reflective coating

For the measurement of its BSDF, the retro-reflective coating was applied to a metal sheet of 150 mm·150 mm (Figure 4.3). This sheet was subsequently laminated onto a flat glass pane. The glass as a rigid support prevents the sample from bending, which would affect the orientation of the measured surface region in the measurement. Surface imperfections are visible which are due to the prototype character of the specimen.

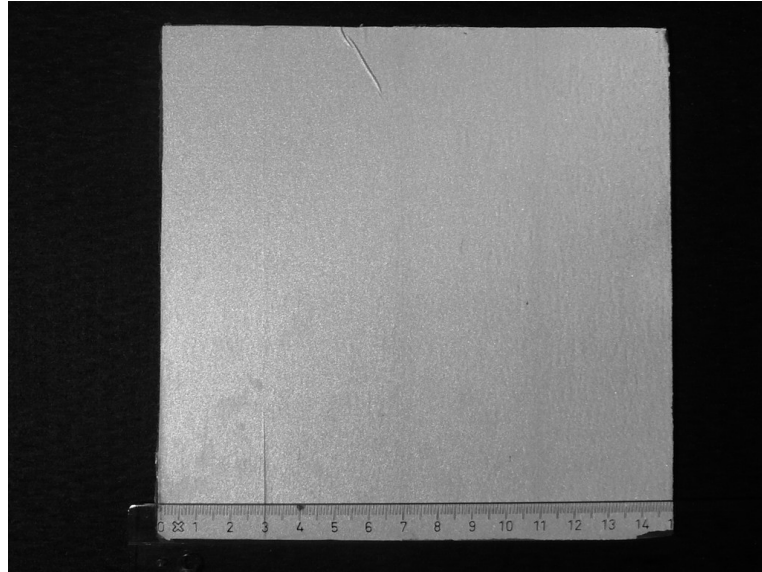


Figure 4.3: Sample for the measurement of the retro-reflective BSDF. The coating is applied on a 150 mm·150 mm metal sheet, which is laminated on a glass pane as rigid support.

## 4.2.2 Measurement of the BSDF

A scanning gonio-photometer is chosen for the measurement for two reasons. First, since measurements are performed sequentially and independently at each pair of incident and outgoing directions, a higher dynamic range is achieved when compared to image-based techniques. The dynamic range is crucial to capture the expected, highly directional reflection by the sample as well as features of the BSDF where its value is low. Second, the open design of the instrument supports modifications.

The gonio-photometer in its default configuration is illustrated by Figure 4.4. A light source with collimator is illuminating a spot on the sample from an invariant position. The size of this spot, which defines the sampling aperture over which the BSDF is averaged in the measurement, is adjusted to a diameter of  $\approx 10$  mm by slight focusing of the beam. The rotation of the sample over two axes defines the incident light direction. A detector mounted on a robotic arm is performing a continuous movement on a configurable path around the sample, varying the outgoing scattered light direction, and records irradiance at intervals of about  $1 \mu\text{s}$ . The use of different semi-conductor devices such as Silicon (Si) or Indium Gallium Arsenide (InGaAs), optionally coupled with filters, allows to match a given spectral target response.

The BSDF of a sample is acquired by two subsequent measurements. First, the effective power of the light source on the sample  $P_i$  is determined by integration of the unobstructed beam's intensity distribution. Second, under identical illumination conditions, light scattered by a sample introduced into the beam is recorded by the detector as

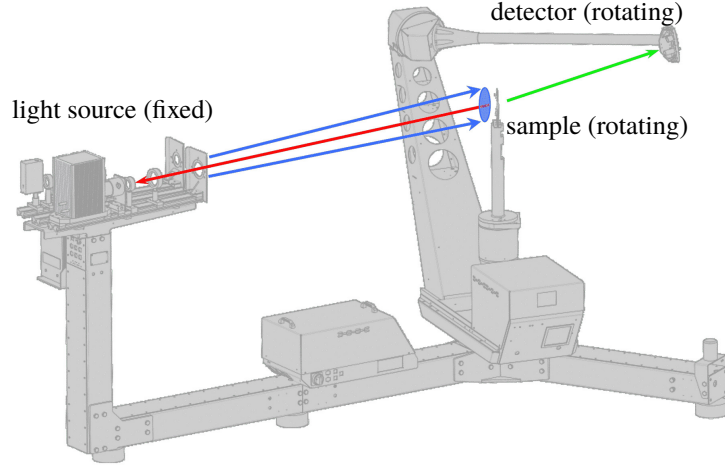


Figure 4.4: Gonio-photometer employed in this study. The incident direction (red) is set by two-axis rotation of the sample. Rotation of the detectors on a spherical path around the sample continuously varies the outgoing direction (green) in the course of the measurement. Illustration based on imagery by pab advanced technologies Ltd, Freiburg.

irradiance  $E$  at direction  $(\theta_i, \phi_i, \theta_s, \phi_s)$ . BSDF and Differential Scattering Function (DSF) are calculated<sup>60</sup> as:

$$\begin{aligned}
 BSDF(\theta_i, \phi_i, \theta_s, \phi_s) &= \frac{DSF(\theta_i, \phi_i, \theta_s, \phi_s)}{\cos \theta_s} \\
 &= \frac{E_s(\theta_i, \phi_i, \theta_s, \phi_s)}{P_i \cdot \cos \theta_s}
 \end{aligned} \tag{4.1}$$

### 4.2.3 Extension of the gonio-photometer to measure retro-reflection

To allow the measurement of the retro-reflected peak, the gonio-photometer is extended by two BSs as shown in Figure 4.5).

The first BS is located at the center of rotation of the detector. The sample is pressed against a rigid mounting plate from the back. This plate is installed at a distance of 105 mm behind the beam-splitter and can be manually rotated around its vertical axis to set the incident elevation angle  $\theta_i$ . As illustrated by the red beam, light is transmitted by the beam-splitter, is scattered by the sample back toward the incident direction, and then reflected from the BS to the detector at position *Detector*. This path is identical to the configuration in Figure 4.2.

The chosen BS features equal transmission and reflection  $\tau \approx 0.49$ ,  $\rho \approx 0.49$  for the

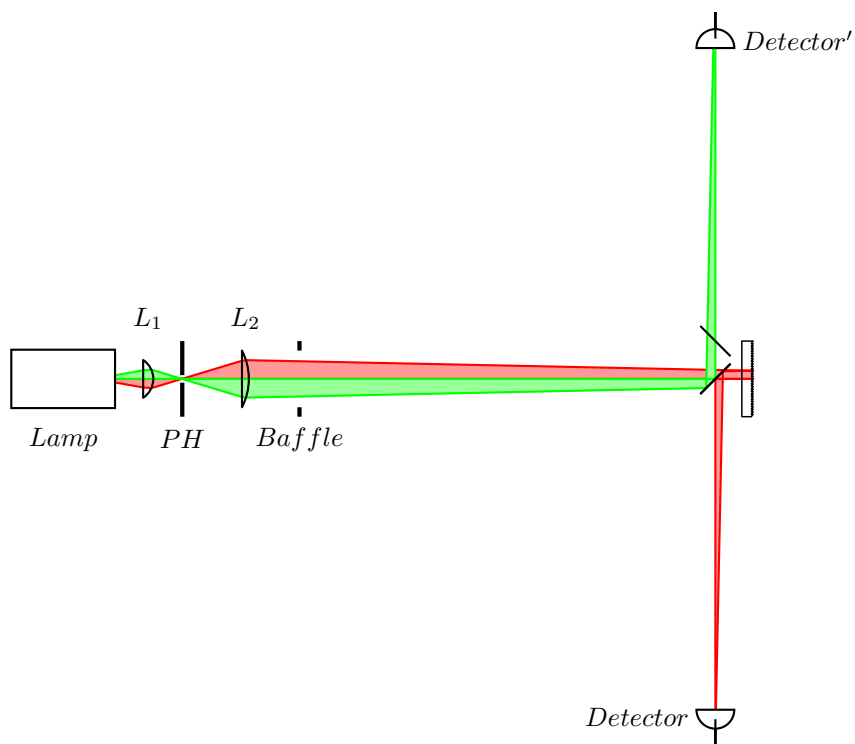


Figure 4.5: Modified configuration for retro-reflection employing two BSs. Green: reference measurement to characterize unobstructed beam. Ref: measurement of light scattered by sample.

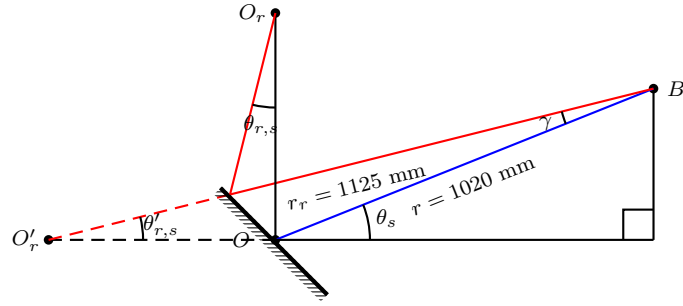


Figure 4.6: The introduction of BSs extends the optical path from the centre of the sample at  $O_r$  to the detector at  $B$ . The scatter direction relative to the mirror image of  $O'_r$  is calculated from the direction relative to the centre of the detector rotation  $O$ .

wavelength range of Visible light 380 nm to 780 nm (Vis) and angle of incidence  $\theta_{i,bs} = 45^\circ$ . However, to evaluate the shading performance of the coating, the entire solar spectrum including Vis and Near Infrared light 780 nm to 2500 nm (NIR) has to be accounted for. Transmission and reflection properties strongly depend on the wavelength and were e.g. measured as  $\tau \approx 0.26$ ,  $\rho \approx 0.72$  for NIR. An elaborate approach to account for this wavelength dependency would be to characterize the optical properties of the BS over the solar spectrum, and subsequently spectrally resolve the BSDF measurement. However, the high spectral resolution adds, in most cases of spectrally flat reflection unnecessary, complexity to the measurement and evaluation.

To compensate for the wavelength dependence of the BS's properties, a second, identical BS is placed next to the first at an angle of  $90^\circ$ . In analogy to the beam characterization in the BSDF measurements employing the gonio-photometer's default configuration, the unobstructed beam is measured at position *Detector'* via one reflection on the first, and one transmission by the second BS (green beam in Figure 4.5). Since both light paths (green and red) involve one reflection and one transmission event on identical BSs, exact a priori knowledge of their properties, which vary for different wavelength ranges, is not required. This assumes that the sample's reflection spectrum is flat within the wavelength range covered by one measurement and greatly simplifies the measurement.

Due to the location of the sample behind the detector's center of rotation, its optical distance to the detector (red in Figure 4.6) does not match the detector radius (blue in Figure 4.6). The effective scatter direction  $\theta_{r,s}$  according to the extended optical distance  $r_r$  can be found from the direction relative to the centre of the detector radius  $\theta_s$  as recorded by the instrument:

$$\sin \theta_{r,s} = \frac{r}{r_r} \cdot \sin \theta_s \quad (4.2)$$

The measured data-sets resulting from the measurement are rotated so that the angular offset of  $90^\circ$  caused by the BSs is compensated, and all data exceeding  $\pm 7.5^\circ$  from the direction of ideal retro-reflection is culled. The resulting BSDF, limited to the region of the peak that cannot be otherwise measured, is finally combined with a measurement on the unmodified gonio-photometer excluding the peak region.

#### 4.2.4 Testing of the extended gonio-photometer

To test the method, the BSDFs of a front-side mirror as measured with and without BSs are compared. For retro-reflection occurring at normal incidence ( $\theta_i = 0^\circ, \phi_i = 0^\circ$ ), a direct comparison with the gonio-photometer's default comparison is not possible due to the shading of the light source by the detector. Instead, the BSDF at scattered directions close to the peak region that can be measured with the default configuration and with the extended setup are compared. Any discontinuity of the BSDFs acquired by the two different setups is considered an artifact introduced by the method.

An important source of error in the peak region, characterized by a steep gradient, is misalignment of the sample in the measurements with and without beam-splitters. Alignment errors are expected to a certain degree due to the experimental nature of the instrument extension. To correct for this expected misalignment, the dataset resulting from the measurement employing BSs is rotated so that the maximum BSDF is located at  $\theta = 0^\circ$ .

A second measurement for one incident direction ( $\theta_i = 10^\circ, \phi_i = 0^\circ$ ), employing only the default configuration, shall allow to test the capability of the method to capture details in the BSDF at high directional resolution. The peak shape for adjacent incident directions is expected to change only gradually. A strong disagreement of the peak shape with the measurement employing BSs at ( $\theta_i = 0^\circ, \phi_i = 0^\circ$ ) would therefore indicate an error in the method.

#### 4.2.5 Measurement of the sample's BSDF

The characterization of the retro-reflective sample assumes isotropy and is performed for one invariant in-plane angle  $\phi_i = 0^\circ$  in NIR and Vis. The incident elevation angle is set to  $\theta_i = 5^\circ$  and  $\theta_i = 10^\circ$  to  $70^\circ$  in steps of  $10^\circ$ . Incident elevation angles above  $70^\circ$  are affected by shadowing due to the thickness of the plate holding the sample, and therefore not included in the measurement.

First, the BSDF of the entire reflection hemisphere (outgoing  $\theta_s = 0^\circ$  to  $90^\circ$ ,  $\phi_s = 0^\circ$  to  $360^\circ$ ) is scanned by the gonio-photometer in its default configuration. Directions close to retro-reflection, which are affected by the occlusion of the light source, are filtered from the datasets.

Second, the extended configuration with two BSs is employed to scan only the region of the retro-reflective peak (incident light direction  $\pm 7.5^\circ$ ). Since the outgoing directions are effectively mirrored over the first BS (Figure 4.5), post-processing has to transform the coordinates of the acquired data-points to match the coordinate system of the gonio-photometer in its default configuration. The measurement of the unobstructed peak is rotated from  $(\theta_s = 90^\circ, \phi_s = 180^\circ)$  to  $(\theta_s = 180^\circ, \phi_s = 0^\circ)$  and  $P_i$  is computed by integration. Distributions of light scattered by the retro-reflective sample are rotated from  $(\theta_s = 90^\circ, \phi_s = 0^\circ)$  to  $(\theta_s = 0^\circ, \phi_s = 0^\circ)$ . In a final transformation step, the rotation is adjusted so that the maximum recorded value is located at the ideal direction of retro-reflection, and the BSDF is computed applying Equation 5.1.

Data-points of the hemispherical scan and of the peak region are merged into one data-set per incident direction, covering the entire reflection hemisphere including the retro-reflected peak region.

Plots of the DSF in the scatter plane, defined as containing the incident direction  $(\theta_i, \phi_i)$  and the surface normal of the sample, illustrate the measured distributions. A logarithmic scale ensures visibility of the background scatter in distributions featuring strong peaks as expected for both the mirror and the retro-reflective sample.

#### 4.2.6 Generation of a data-driven model from the measured BSDF

For each measured incident direction and wavelength range, the `RADIANCE` command `pabopto2bsdf` generates a set of Gaussian basis functions approximating the BSDF over all outgoing directions. Between adjacent incident directions, a mass transport algorithm is employed by `bsdf2ttree` to interpolate and generate a discrete representation of the BSDF at chosen resolution. In the general case of anisotropic reflection, this results in a tensor of four dimensions relating to  $\theta_i, \phi_i$  and  $\theta_s, \phi_s$ . However in the case of isotropy, with invariant  $\phi_i$  in the measurement, the BSDF can be stored in a data cube of three dimensions. The resolution is parametrized as a power of 2 for each dimension, so that a resolution parameter  $k$  leads to  $2^{4 \cdot k}$  elements in the general case of anisotropy, or  $2^{3 \cdot k}$  for isotropy. In an optional, final pass, adjacent elements of the tensor with low variance are joined until a data-reduction target is met given. The resulting hierarchical representation as a compact, multi-dimensional tree structure is embedded into a Extensible Markup Language (XML)

```
pabopto2bsdf 05.dat 10.dat 20.dat \  
30.dat 40.dat 50.dat \  
60.dat 70.dat > sample.sir
```

```
bsdf2ttree -t3 -g 7 -t 95 \  
sample.sir > sample.xml
```

format that can be loaded into `RADIANCE` and applied to any geometric primitive via the `BSDF` material type.

The method is applied to the measured BSDFs of the retro-reflective sample to generate a data-driven model of high directional resolution for each wavelength range. The measured data-sets for NlR and Vis, each corresponding to one incident direction, are compiled into interpolants:

The resolution parameter  $k$  is set to 7, leading to a data-cube of  $2^{3 \cdot 7} = 2\,097\,152$  elements. The subsequent data-reduction pass with a reduction target of 95 % reduces the data-set to a compact model of  $\approx 104\,858$  elements:

The resulting XML file can be loaded by `RADIANCE` to define a material that can be assigned to any geometrical entity:

This defines a material description `retroreflectiveMat` referring to the data-driven model embedded in `sample.xml` as generated from the measurements. The second line of above example sets a zero thickness (second numerical value) and relates the in-plane reference, which is of no relevance for the case of isotropic reflection, toward the positive  $y$ -axis.

#### 4.2.7 Modeling the effect of retro-reflection in Venetian blinds

To assess the effect of the retro-reflective coating, it is compared to ideally diffuse and mirror-like slats of a Venetian blinds assembly embedded in a triple-glazing unit. The slats are flat and tilted horizontally. The depth and the vertical distance of the slats are equally set to 10 mm. Under the given sky condition, this prevents direct transmission of sun-light and thereby allows the evaluation of the effect of the reflection properties of the blinds. Perfectly flat slats are far from realistic components of Venetian blinds.

```
void BSDf retroreflectiveMat  
6 0 sample.xml 0 1 0 .  
0  
0
```

Table 4.1: Reflection properties of the slats in the comparison of the retro-reflective with ideally diffuse and specular coatings.

	<b>case A</b>	<b>case B</b>	<b>case C</b>
top	retro-reflective	specular $\rho = 0.8$	diffuse $\rho = 0.8$
bottom	diffuse $\rho = 0.8$	diffuse $\rho = 0.8$	diffuse $\rho = 0.8$

```

void metal mirrorMat
0
0
5      .8      .8      .8
      .9      0

void plastic diffuseMat
0
0
5      .8      .8      .8
      0      0

void glass exteriorMat
0
0
3      .99     .99     .99

void glass interiorMat
0
0
3      .775    .775    .775

```

Market-available CFS comprise slats featuring geometries that are highly optimized for visual comfort and control of solar gains. However, reducing the geometry of the slats to planar surfaces allows the isolated inspection of effects caused by the reflection properties in a shading device causing minimum view obstruction.

The retro-reflective coating is applied to the upper surface of the slats in case *A* with the bottom sides being ideally diffuse. The slats comprising case *B* feature a mirror-like top and ideally diffuse reflection on the bottom surface. In case *C*, both surfaces share the perfect diffuse reflection properties.

The blinds are embedded in a glazing assembly comprising an uncoated glass pane toward the exterior, and two coated glass panes toward the interior.

An overview of the reflection properties of the slats is given in Table 4.1.

The ideally diffuse and specular reflection properties of the blinds and glazing are modeled by the built-in material models in RADIANCE:

For the assessment of daylight performance in Vis, photometric data-driven models of the blinds assemblies for all three cases, including the glazing, are generated using

Table 4.2: genBSDF parameters to compute the BSDFs of Venetian blinds and glazing.

Parameter	Description	all cases	case A
-t4 $k$	Tensor resolution exponent, results in $2^{4 \cdot k}$ coefficients	6	
-c $n$	Sample rays per hemisphere	32768	
-ad $n$	Number of daughter rays at each ambient ray intersection	128	
-lw $w$	Maximum weight of single ray contribution	0.008	
-ss $n$	Number of specular samples		128

**genBSDF.** **genBSDF** is a ray-tracer for the computation of BSDFs from geometric models and distributed as part of RADIANCE. In analogy to the data-driven model of the retro-reflective coating, the BSDF of the fenestration system is a full description of the light scattering properties of blinds assembly and glazing. Other than the isotropic reflection model of the coating, the data-driven models of the fenestration replicate anisotropic transmission as well as reflection from front and back.

Parameters set in the generation of the fenestration BSDFs at high resolution in Vis are listed in Table 4.2. Prior to data-reduction, the tensors for all three fenestration BSDFs comprise  $2^{4 \cdot k} = 16\,777\,216$  elements for of the four BSDF components describing front and back reflection and transmission. This corresponds to 4096 incident and 4096 outgoing scattered directions for each component. The -c parameter, set to 32 768, determines the number of sampled rays for each incident direction. This ensures that, as an average,  $32\,768/4096=8$  rays are sent for each pair of incident and outgoing directions to random locations on the non-uniform surface of the fenestration system. The -ad and -lw parameters control the sampling on diffuse surfaces. Only for case A, an additional parameter -ss causes the generation of 64 rays at each specular reflection to sufficiently cover the width of the peak region as described by the data-driven reflection model.

A second set of BSDFs, both in Vis and NlR, is generated from the measurements of the coatings, and identical reflection values for Vis and NlR for all other surfaces. These BSDFs represent only the blinds assembly without glass layers. They are generated employing a fixed directional basis of 145 incident and 145 outgoing directions. The resulting BSDFs for each case are merged into one XML file, which consequently holds a description of light scattering in the entire solar spectrum.

For each case, the solar BSDF of the blinds assembly is combined with descriptions of the glazing layers in WINDOW.<sup>114</sup> The blinds are embedded in a glazing assembly comprising an uncoated pane to the outside, and two coated panes with 90 % Argon fill to the inside. Two variants of the coated panes are prepared for each case.

The first variant,  $L_e L_\tau$ , comprises panes of low emissivity and low solar transmission. Its properties in Vis correspond to the glazing description in the daylight performance evaluation.

Table 4.3: Solar-optical properties (visible, solar transmission  $\tau_{vis}, \tau_{sol}$  and front, back emissivity  $\epsilon_f, \epsilon_b$ ) as provided by the IGDB for glazings of given ID.

description	variant	ID	$\tau_{vis}$	$\tau_{sol}$	$\epsilon_f$	$\epsilon_b$
outer, uncoated pane	<i>both</i>	14706	0.912	0.905	0.840	0.840
inner, coated panes	$L_e L_\tau$	4407	0.858	0.522	0.053	0.841
	$L_e H_\tau$	21457	0.887	0.715	0.086	0.840

Variant  $L_e H_\tau$  combines low emissivity with high solar transmission. Selected optical properties of the glass layers, as provided by the International Glazing Database (IGDB) from within WINDOW, are listed in Table 4.3.

For each of the three cases and both variants, the Solar Heat Gain Coefficient (SHGC) and direct-hemispherical solar transmission  $\tau_{d,sol}$  are computed in WINDOW to assess the shading performance and, with variant  $L_e H_\tau$ , the potential to make controlled use of solar gains.

While  $\tau_{d,sol}$  is a purely optical property describing the transmission of radiation at short wavelengths, SHGC comprises of  $\tau_{d,sol}$  and the inward flowing fraction of radiation emitted by the fenestration layers. Both SHGC and  $\tau_{d,sol}$  are calculated for one incident elevation angle  $\theta = 50^\circ$ , when the blinds fully occlude direct sun-light and transmission through the assembly is limited to reflection on the slats.

#### 4.2.8 Testing the model in an exemplary test room

The effective daylight performance of the three glazing systems is tested for an exemplary cellular, South-oriented office (Figure 4.7). The office is directly exposed the sun in the South at an elevation of  $50^\circ$ . This sky condition agrees with the exemplary case chosen for the calculation of SHGC and  $\tau_{d,sol}$ , and ensures that direct sun-light is entirely occluded geometrically by the chosen horizontal orientation of the blinds.

The BSDFs in Vis representing the glazing systems of the three cases *A*, *B* and *C* are employed to invisible surfaces enclosing the fenestration geometry in the model. These BSDFs are queried only when the enclosing surfaces are hit by rays as part of the stochastic, indirect-diffuse calculation module of RADIANCE, geometrical ray-tracing within the fenestration does not take place. This use of the BSDF as a “black box” in the indirect-diffuse calculation simplifies the simulation, since complex light propagation within the fenestration is computed only once in the generation of the data-driven model. Furthermore, the data-driven model overcomes a limitation of the backward ray-tracing algorithm in the treatment of specular, redirecting systems, which would otherwise require

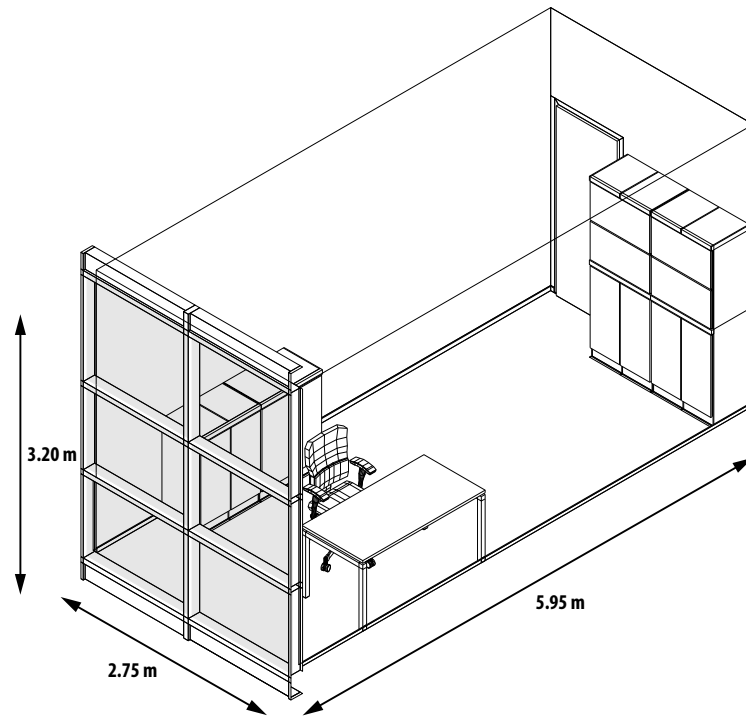


Figure 4.7: Cellular office<sup>57</sup> as a test case for the comparison of the retro-reflective coating with ideally diffuse and specular slats. The lowest zone of the fenestration is opaque.

techniques such as the introduction of virtual light sources or forward-tracing extensions.<sup>70</sup>

In the direct, deterministic calculation module of RADIANCE, rays pass the enclosing surfaces unaffected and take part of a full ray-tracing calculation through the fenestration system. This preserves visibility of the geometric detail, such as the slats, and pronounces shadow patterns due to direct sun-light.

For all cases A–C, illuminance on the interior surfaces of the office, as seen by an occupant facing the fenestration, is computed as a measure of shading by the flat blinds under ideal conditions for view-through.

For identical viewing conditions, luminance maps are generated. Other than the illuminance distribution, the luminance maps also reflect the reflection properties of the interior surfaces.

The glare evaluation software EVALGLARE is employed to compute Daylight Glare Probability (DGP) and Daylight Glare Index (DGI) as metrics for the evaluation of discomfort glare by daylight from the luminance maps.<sup>45,115</sup> The two metrics differ in that the formulation for DGP considers the vertical illuminance  $E_v$  reaching the eye of an observer as potential cause of discomfort glare, as well as to account for adaption effects which is accounted to background luminance  $L_b$  in the formulation of DGI.

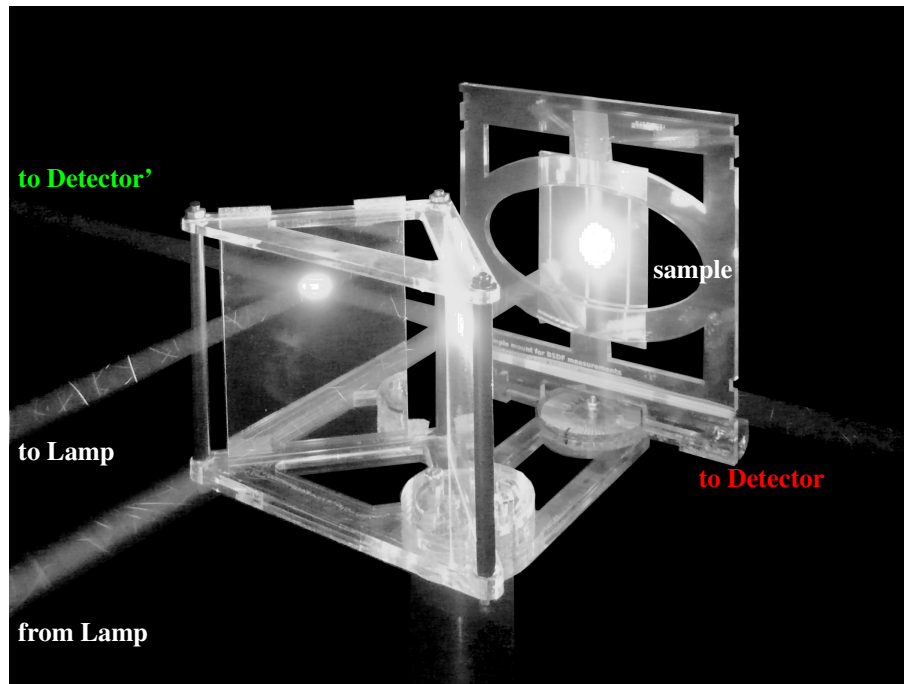


Figure 4.8: Prototype implementing the design outlined in Figure 4.5. Light reflected back to the lamp is discarded.

### 4.3 Results and discussion

The extended gonio-photometer allowed to measure the BSDF of the retro-reflecting coating, and to translate it into a data-driven model that was used in exemplary daylight simulations.

#### 4.3.1 Extension of the gonio-photometer

A prototype of the setup as illustrated in Figure 4.5 is shown in Figure 4.8. It comprises laser-cut acrylic parts holding two beam-splitters. The acrylic parts are held by PVC tubes and threaded rods. An additional baffle is attached to the mounting plate during measurements to prevent direct light scattering from the sample to the detector. The prototype replaces the sample mount of the default configuration. Since the beam-splitters orientation toward the light source must be kept fixed, the incident elevation angle  $\theta_i$  is manually set by rotation of the mounting plate.

### 4.3.2 Testing of the measurement method

Figure 4.9 shows the DSFs of the mirror close to the specular peak, as measured in the wavelength ranges of Vis and NIR for two incident directions. The data-set for  $\theta_i = 0^\circ$  comprises measurements with and without BSs. For  $\theta_i = 10^\circ$ , no BSs were employed and no reflection data is present in region around the incident direction.

For DSF values above 10, the widths of the peaks in both wavelength ranges match. The peak is wider in the range of Vis than NIR for values below 10. For values lower than 0.01, low frequency noise in NIR is apparent, which can be explained by a known drift mostly due to temperature effects at low signal levels. This effect does not occur in the range of Vis. These observations equally apply to the measurements with ( $\theta_i = 0^\circ$ ) and without BSs ( $\theta_i = 10^\circ$ ).

The measurement for  $\theta_i = 0^\circ$  without BSs shows artifacts caused by shading in the ranges  $\theta_s = -7.5^\circ$  to  $-2.5^\circ$  and  $\theta_s = 2.5^\circ$  to  $7.5^\circ$ . Data-points in this region are typically excluded and only shown here to illustrate the effect. The distributions for  $\theta_i = 0^\circ$  show a minor discontinuity at the joint data-sets for the hemisphere and the peak region at negative  $\theta$  in both wavelength ranges. The distributions agree at positive  $\theta$ .

The overall accordance between the measurements confirms the validity and the in-principal applicability of the method to the problem. The method is applicable for surfaces featuring strong peaks, leading to high signals in the entire peak region. This is the case for the sample that is to be evaluated in this study, and motivated the development of the instrument extension specifically for the peak region.

### 4.3.3 Measured BSDF of the coating

The DSFs of the sample, measured at eight incident directions in the wavelength ranges of Vis and NIR, are presented in Figure 4.10 and Figure 4.11.

The coating exhibits a strong directional peak toward the incident direction in both wavelength ranges. The heights of the peaks are approximately equal for incident directions in the range of  $\theta_i = 5^\circ$  to  $50^\circ$ , and then moderately decrease toward the highest measured  $\theta_i = 70^\circ$ . Lower, wide lobes are present in the forward direction. However, the magnitude of the retro-reflected peaks is about two orders of magnitude higher than the forward lobes.

Compared to the front-side mirror, a distinct diffuse background is visible but about three orders of magnitude lower than the peaks. The presence of this background can be confirmed visually since the sample does appear in a bright gray under directional

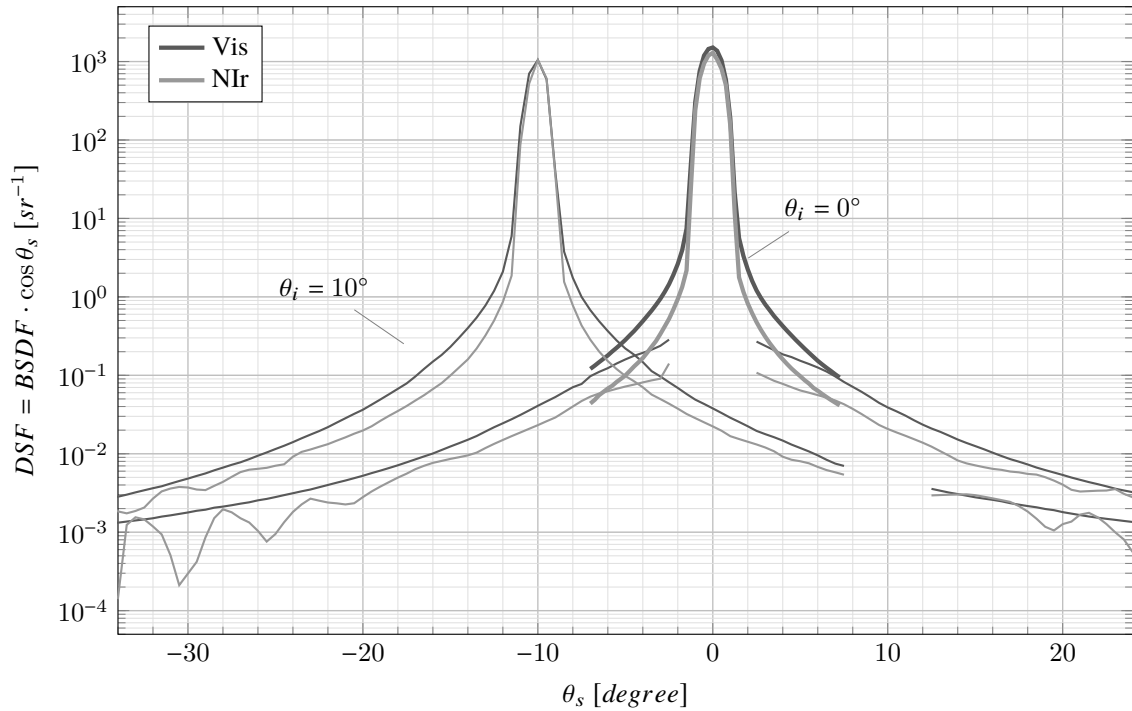


Figure 4.9: Profile of the mirror's DSF in the scatter plane, Vis and NIR. The peak-region measured through the BSs is indicated by an enhanced line-width.

illumination.

A discontinuity exists between the hemispherical measurements and the DSF of the peak region, which is measured employing the two BSs. In Vis, the peak is positively offset compared to the background, while a negative offset occurs in NIR.

Alignment errors can be excluded to cause this effect, since measurements in both wavelength ranges are conducted without change to the geometric setup.

One possible cause for the discontinuities are thermal effects at the detectors in particular when the measured signal is low. The gonio-photometer is operated in an environment with a temperature set to  $\approx 20^\circ\text{C}$ , but no direct cooling of the detectors. Thermal noise is compensated by subtraction of a fixed offset value from the signal. This offset is determined under stabilized thermal conditions. Setting of incident directions, when employing the BSs, is done manually by a person accessing the laboratory from the outside, and affects the temperature in the laboratory. Since the BSs decrease the overall signal range, the impact of thermal effects is high. On the other hand, for measurements of the reflection hemisphere excluding the peak, the incident direction is set automatically without manual intervention. The temperature in the lab thus remains stable and, furthermore, the impact of thermal effects is lower due to higher measured signals.

The role of thermal effects will be further investigated but, since they affect only the lower region of the peak measurements, are expected to have little effect on the validity of the results.

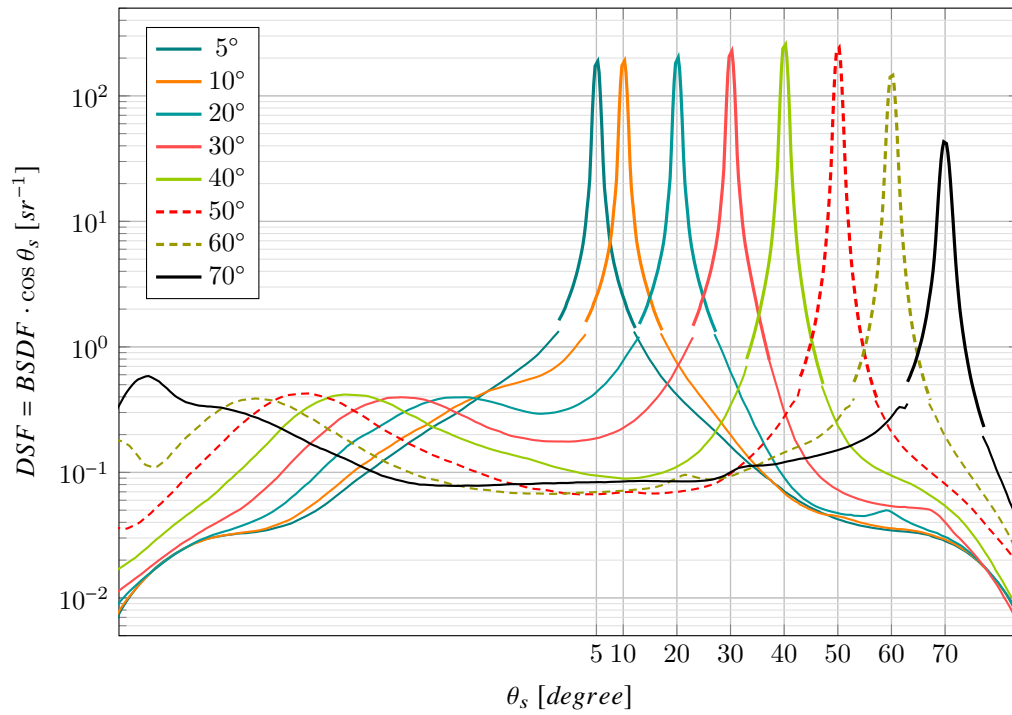


Figure 4.10: Profile of the retro-reflective sample's DSF in the scatter plane measured in the wavelength range of Vis.

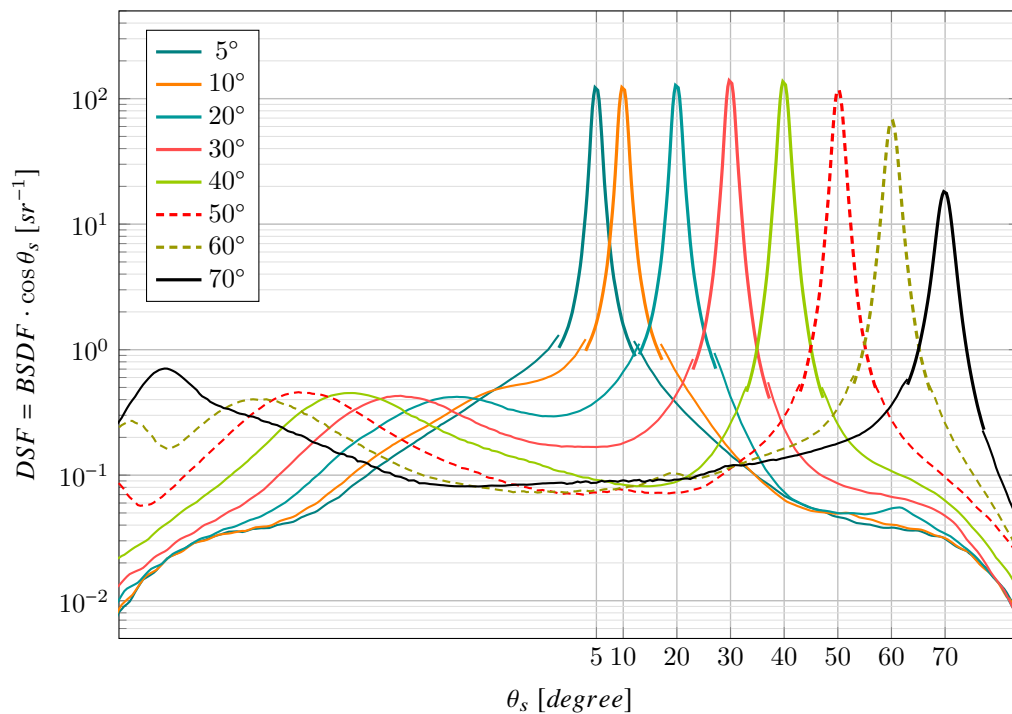


Figure 4.11: Profile of the retro-reflective sample's DSF in the scatter plane measured in the wavelength range of NIr.

#### 4.3.4 Data-driven reflection model from measured BSDF

The profiles of the DSF in the scatter plane, as predicted by the data-driven model for three exemplary incident directions  $\theta_i = 30^\circ, 45^\circ$  and  $60^\circ$ , are shown in Figure 4.12 (Vis) and Figure 4.13 (NIR). For two incident directions  $\theta_i = 30^\circ, 60^\circ$  the corresponding measurement data is underlaid. The distributions for  $\theta_i = 45^\circ$  are the result of interpolation.

In analogy to the measured DSF, the models show high accordance in both wavelength ranges.

The shape of the retro-reflected peaks are closely matched by the models for both measured directions. They also seem to be plausible for the third direction, where no direct comparison to measurements is possible. The resolution limit of the data-driven model ( $\approx 1.5^\circ$ ) results in a slightly flatter top of the peaks. The locally adaptive resolution is high in the peak region and closely matches the shape over several decades. The forward lobes of the distributions are present in the model output, but appear less pronounced and do not match the measurement as closely as the peaks. The interpolation algorithm seems to strongly favor peak regions when fitting the measured distributions. Note that the amplitude of the forward peak is low and pronounced in the plots by the logarithmic scale.

Step artifacts introduced by the local data-reduction are apparent at lower values of the DSF. However, due to the broadness of the forward peak, the reduced directional resolution in these regions does not lead to a stronger mismatch with the measurement.

The locally adaptive data-reduction appears to be well suited to maintain the sample's highly directional reflection characteristics, with most reflected power concentrated in a narrow peak region and a wide range of directions of little variance.

#### 4.3.5 Effects of retro-reflection in Venetian blinds

Figure 4.14 and Figure 4.15 show the photometric DSF for the fenestration systems, including glazing, in the scatter plane and for one incident elevation  $\theta_i = 130^\circ$ . Angular coordinates are relative to the fenestration plane, with  $\theta = 0^\circ$  corresponding to the inside. The shown distributions therefore correspond to a sun elevation of  $50^\circ$ .

Light transmitted through the system by upward reflection on the mirror blinds (case *B*) to  $\theta_s = 50^\circ$  is the most prominent feature in the transmission distributions. While all systems feature diffuse transmission downward due to identical reflection properties of the bottom surfaces of the slats, only for cases *A* and *C* a diffuse upward transmission occurs.

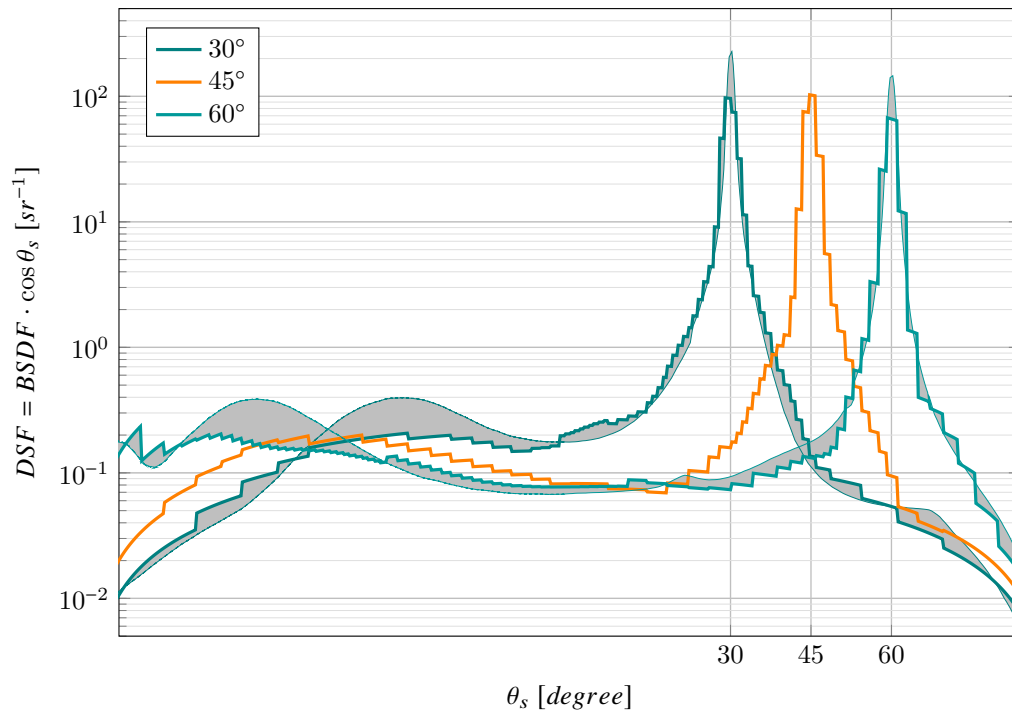


Figure 4.12: Profile of the retro-reflective sample's DSF in the scatter plane as returned by the data-driven model in the wavelength range of Vis. The deviations from measurements for  $\theta_i = 30^\circ$  and  $60^\circ$  are shaded.

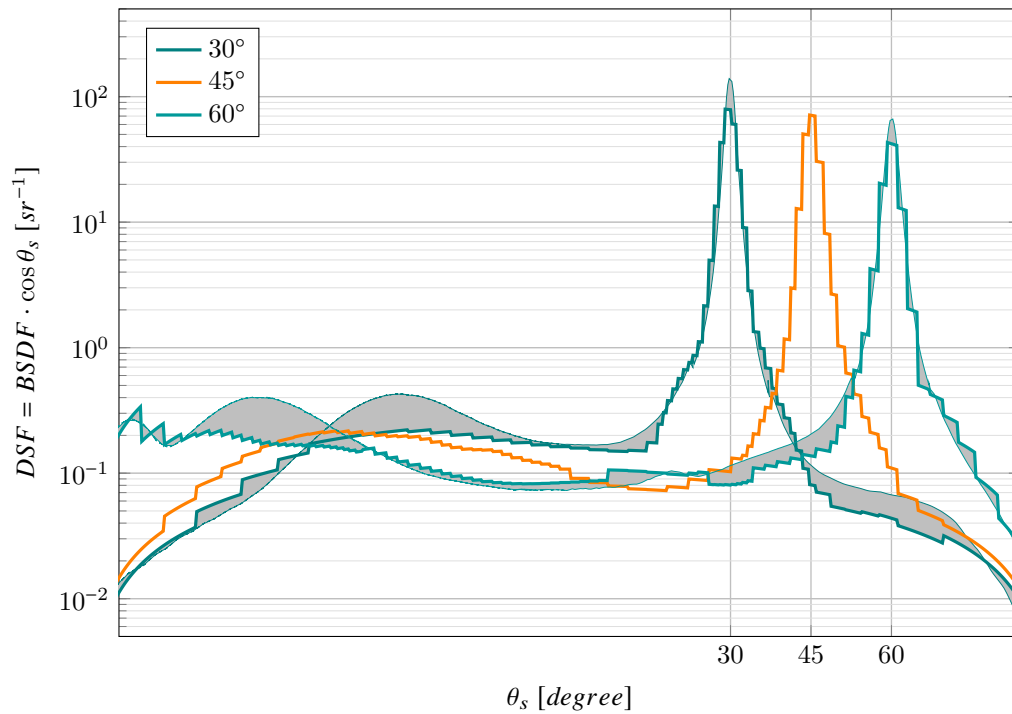


Figure 4.13: Profile of the retro-reflective sample's DSF in the scatter plane as returned by the data-driven model in the wavelength range of NlR. The deviations from measurements for  $\theta_i = 30^\circ$  and  $60^\circ$  are shaded.

Table 4.4: Solar gains through fenestration comprising two glazing variants and three cases for Venetian blinds as predicted by WINDOW for an exemplary incident elevation  $50^\circ$ .

<b>Variant</b>	<b>Case</b>	<b>SHGC</b>	<b><math>\tau_{d,sol}</math></b>
$L_e L_\tau$	<i>A</i>	0.2279	0.1024
	<i>B</i>	0.4484	0.2602
	<i>C</i>	0.2838	0.1356
$L_e H_\tau$	<i>A</i>	0.2803	0.1680
	<i>B</i>	0.5752	0.4197
	<i>C</i>	0.3540	0.2254

All systems show a pronounced peak at  $\theta_s = 230^\circ$  due to reflection on the outer glass surface, and diffuse downward reflection by the bottom surfaces of the slats. Retro-reflection causes a peak toward the incident direction for case *A*.

While light scattering by case *A* is characterized by the retro-reflection to the outside, and case *B* by the almost exclusive, directional transmission to the inside. Since the blinds assembly of case *C* scatters light equally to the inside and outside, the DSFs for transmission and reflection differ only due to the different transmission of the inner and outer glazing.

The solar gains for both glazing variants of all three cases as predicted by WINDOW are listed in Table 4.4.

For both variants, solar gains are highest if the mirror-like top surfaces reflect direct sun-light to the interior (case *B*).

Slats with diffuse reflection on top and bottom surface (case *C*) lead to a decrease of shortwave transmission by  $\approx 50\%$  when compared to the mirror blinds (case *B*). The decrease of SHGC is notably lower at  $\approx 40\%$ . This effect can be attributed to the longwave emission by the blinds, which are expected to have a higher temperature compared to case *B* due to multiple diffuse reflections within the system.

The retro-reflective coating (case *A*) achieves the lowest solar transmission and SHGC. Compared to case *B*, both solar transmission and SHGC are  $\approx 60\%$  lower. The coating combines minimal forward transmission due to its retro-reflective property, and low emission due to the high directionality of retro-reflection. It minimizes diffuse inter-reflection and thereby absorption within the blinds assembly, effectively limiting the emission toward the interior.

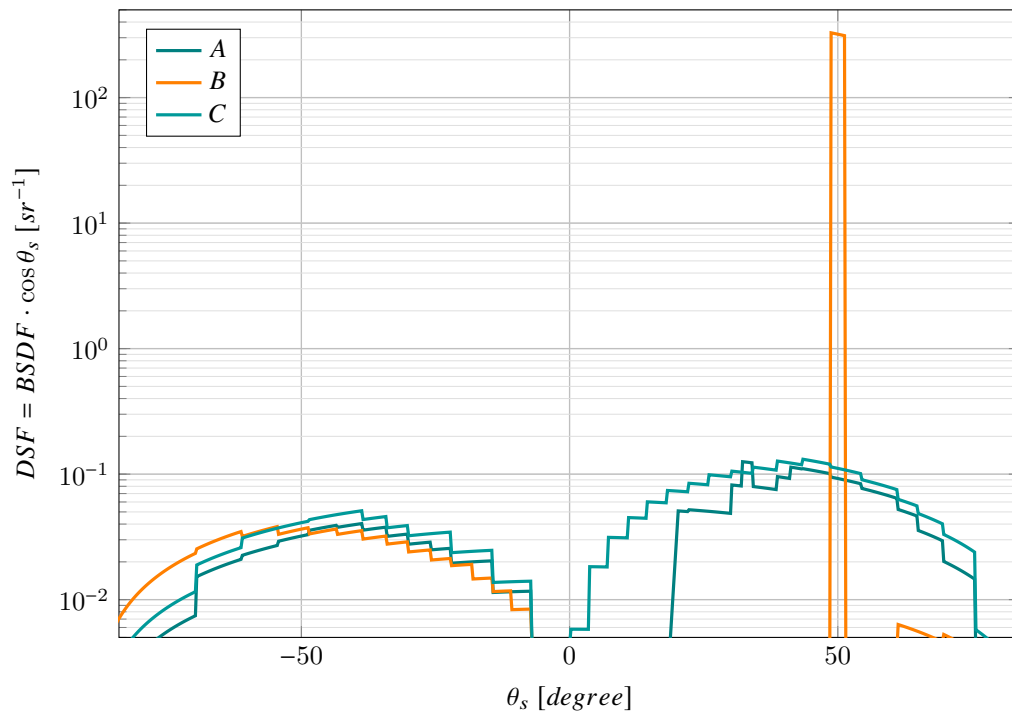


Figure 4.14: Profile of the fenestration system DSFs in the scatter plane for transmission in Vis. Coordinates are relative to the fenestration plane.  $\theta = 0^\circ$  points inward, positive  $\theta$  upward.

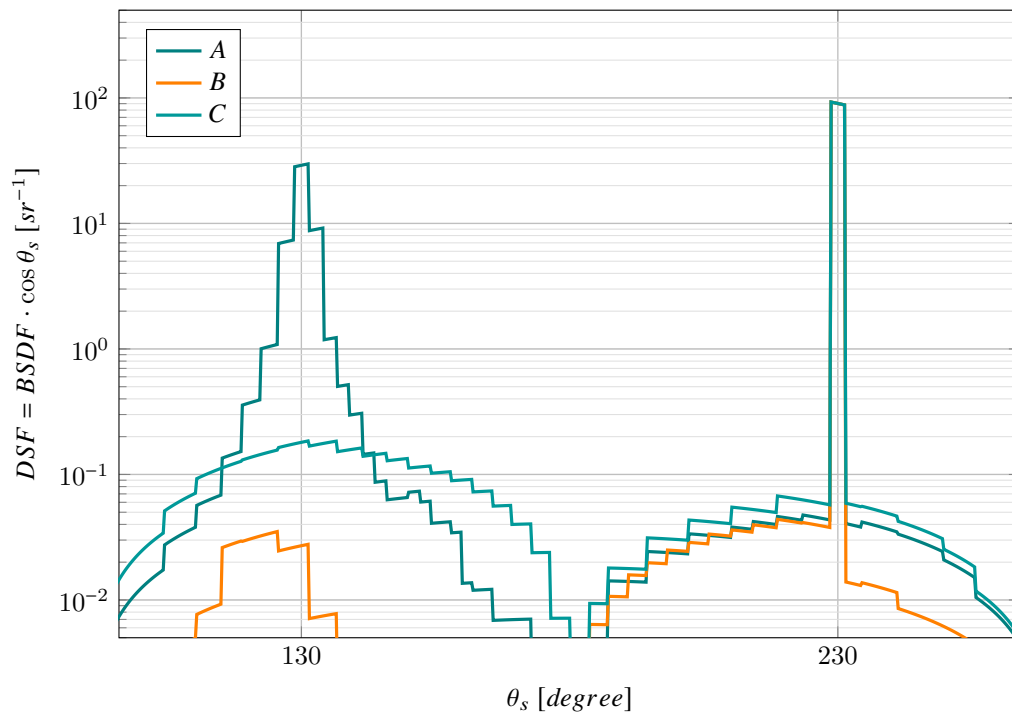


Figure 4.15: Profile of the fenestration system DSFs in the scatter plane for reflection in Vis.  $\theta = 180^\circ$  points outward.  $\theta = 90^\circ$  to  $180^\circ$  is above,  $\theta = 180^\circ$  to  $270^\circ$  below the horizon.

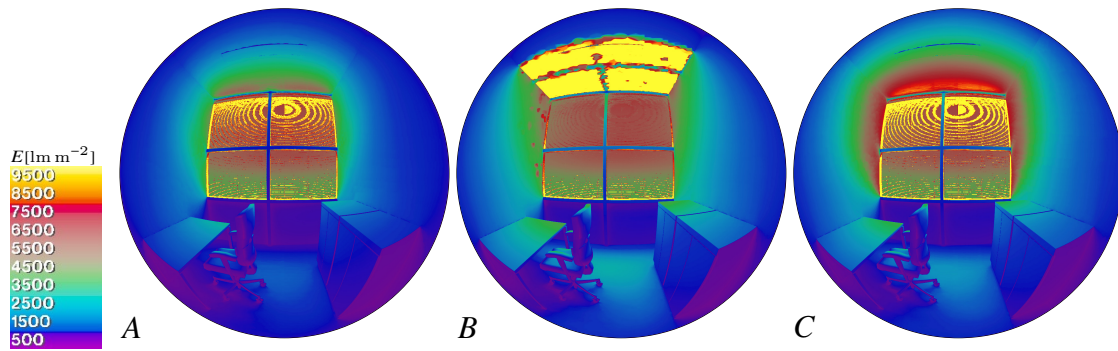


Figure 4.16: Distribution of illuminance  $E$  [ $\text{lm m}^{-2}$ ] on the surfaces of an exemplary, South-facing office with flat blinds featuring retro-reflective (case A), ideally mirror-like (B), and ideally diffuse (C) top surfaces. Sun elevation  $50^\circ$ , azimuth  $0^\circ$  (South).

### 4.3.6 Daylight performance with different coatings in an exemplary office

The illuminance distributions for the three cases are presented with a linear color-mapping in Figure 4.16. Due to the geometrical configuration of the blinds, sun-light for the given elevation angle of  $50^\circ$  is not directly transmitted through the window.

The retro-reflective coating as in case A achieves an effective shading by suppressing reflection to the interior. Illuminance is in the range of  $500 \text{ lm m}^{-2}$  to  $2000 \text{ lm m}^{-2}$  on all opaque surfaces but the side-walls and ceiling. On the walls in direct proximity to the window, a weak effect of diffuse skylight and scattering of sun-light by the slats is apparent and results in a higher illuminance of up to  $\approx 4000 \text{ lm m}^{-2}$ . Forward reflection causes a high illuminance on the ceiling close to the window up to  $\approx 5500 \text{ lm m}^{-2}$ . The mirror-like reflection of light from the slats comprising the blinds assembly in case B produces a projection of the window aperture to the ceiling. Consequently, illuminance reaches up to  $\approx 20\,000 \text{ lm m}^{-2}$  on the ceiling. Illuminance on the other opaque surfaces, illuminated mostly by light reflected from the ceiling ( $\rho = 0.8$ ), is in the range of  $500 \text{ lm m}^{-2}$  to  $4000 \text{ lm m}^{-2}$  and up to  $\approx 5000 \text{ lm m}^{-2}$  on the side-walls adjacent to the window. When compared to case B, the diffuse reflection by the slats in case C results in less extreme maximum illuminance of  $\approx 8000 \text{ lm m}^{-2}$ , which is limited to the ceiling in immediate proximity of the window. However, the illuminance on the opaque surfaces is consistently higher than in case A.

Figure 4.17 shows the luminance maps for the three cases. A logarithmic colormap is applied to cover the dynamic range of the imagery. As can be expected, the luminance on the diffuse surfaces is in accordance with the illuminance distributions in Figure 4.16. The specular reflection on the luminaire's surface at the ceiling produces a mirror image of the fenestration, and therefore high luminance values in all three cases. The highest pixel

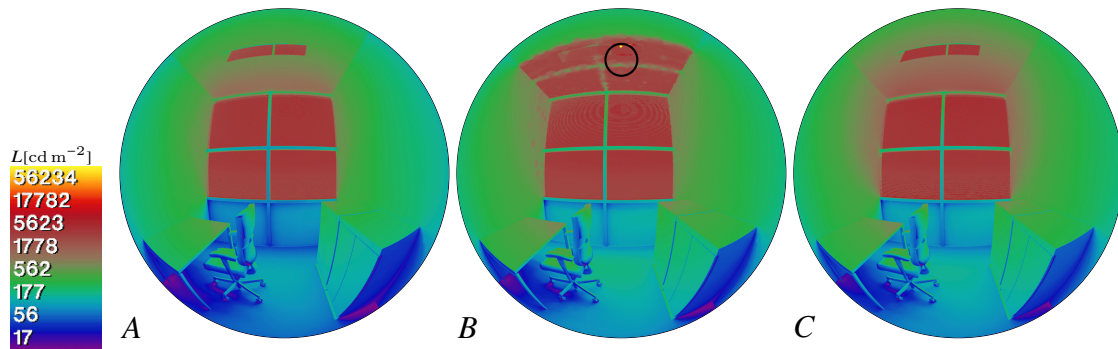


Figure 4.17: Luminance maps [ $\text{cd m}^{-2}$ ] for cases *A*, *B* and *C*. Note the reflection of the sun in the luminaire in case *B* marked by the black circle.

values are present in case *B*, where the reflected sun-disk is visible on the luminaire with a maximum luminance of  $\approx 850\,000 \text{ cd m}^{-2}$ .

The glare assessment of the three cases considers not only the opaque surfaces of the office interior, but also the sky as visible through the fenestration systems. Reflection by specular surfaces such as the luminaire in the suspended ceiling can contribute to glare if they reflect directional light. The results of the evaluation employing `EVALGLARE` are listed in Table 4.5. Detected glare sources are colored in Figure 4.18. Since a task area cannot be defined for the given view, a fixed threshold of  $2000 \text{ cd m}^{-2}$  was applied to the pixel values to identify glare sources, and a threshold of  $1\,000\,000 \text{ cd m}^{-2}$  to extract peaks such as reflections of the sun disk.

Discomfort glare as predicted by the DGP is extremely high for case *B*. The predicted value of 0.896 exceeds the defined range of the metric, and is clearly above the upper limit of tolerable glare defined as 0.45. For cases *A* and *C*, the computed DGPs are in the valid range of 0.2 to 0.8. The prediction for case *A* is below, case *C* just above the threshold of 0.35 for perceptible glare. According the DGP, good visual comfort conditions in terms of discomfort are maintained by both diffuse and the retro-reflective coating, but the latter is preferable.

The assessment based on DGI contradicts the predictions by the DGP metric. The result for cases *A* and *C* are in the acceptable range 22 to 24 with case *C* achieving a minimally better result. Case *B* is clearly higher and must be considered intolerable according to the metric. The disagreement of the two metrics in rating cases *A* and *C* can be explained by the role of  $E_v$  in DGP, and the background luminance  $L_b$  in DGI, to account for adaption effects. DGI models adaption based on background luminance  $L_b$ , which excludes the glare sources. This favors case *C* where  $L_b$  is more than three times higher than in case *A*. The approach is questionable in cases where the glare source covers a large fraction of the field of view, but is not considered to effect adaption. The formulation of DGP, driven by this short-coming, relies on  $E_v$  (including the potential glare sources) both as a factor for adaption and a source for discomfort glare.

Table 4.5: Results of glare assessments for the three cases of retro-reflective (*A*), specular (*B*), and diffuse (case *C*) blinds.

	case <i>A</i>	case <i>B</i>	case <i>C</i>
DGP	0.329	0.896	0.352
DGI	22.961	29.323	22.304
$E_v$ [ $\text{lm m}^{-2}$ ]	2233.655	8779.132	2705.902
$L_b$ [ $\text{cd m}^{-2}$ ]	211.082	250.898	312.609

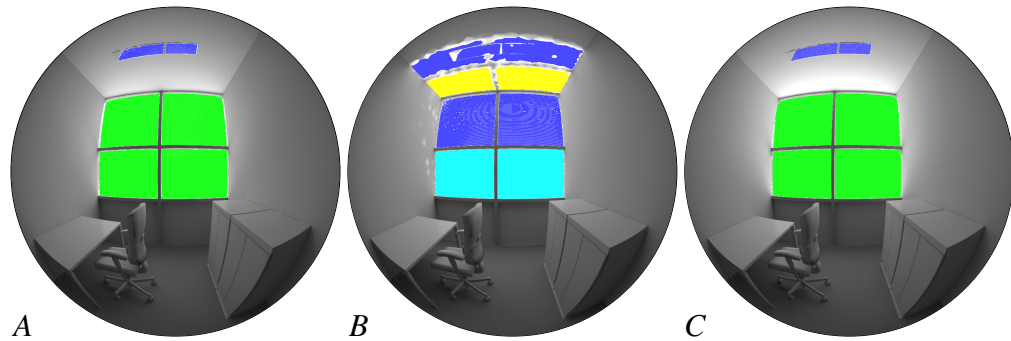


Figure 4.18: Potential glare sources for cases *A*, *B* and *C*.

#### 4.4 Conclusion

A novel extension to a scanning gonio-photometer for the measurement of retro-reflection has been developed. Applicability and validity of the approach, employing two beam-splitters to compensate for its wavelength dependent transmission and reflection properties, were demonstrated. Based on these initial tests, a fully functional setup shall be developed that reduces error due to misalignment compared to the presented prototype.

The evaluated coating achieves a highly directional, retro-reflective effect. This property is confirmed in both evaluated wavelength ranges Vis and NlR and over a wide range of incident directions  $\theta_i = 5^\circ$  to  $70^\circ$ .

Compiled from measured BSDF, the data-driven reflection model in RADIANCE is capable to accurately replicate all characteristic features of the sample. Since RADIANCE implements an advanced algorithm for interpolation, but has no means to extrapolate, the applicability of the model is limited to the range of measured incident directions. Based on the results of this work, the presented apparatus to measure retro-reflection shall be modified accordingly so that a wider range of incident directions can be covered. Yet, the measurement of reflection for incident directions close to grazing is inherently limited. The implementation of an extrapolation algorithm that predicts peaks either in the forward mirror direction or the direction of ideal retro-reflection based on a given set of measurements remains a challenge to overcome limitations of the data-driven model.

Since the retro-reflective effect is achieved independently from the profile geometry, the coating allows to develop Venetian blinds with low profile height. Effective sun-shading could be demonstrated in the comparison with diffuse and specular blinds even with flat, horizontal slats. Since most incident sun-light is directionally reflected toward the outside, visible light is blocked and solar gains are minimized. The application of the coating in future Venetian blinds assemblies promises to achieve high performance as a sun-shading device while maintaining view to the outside.

## **4.5 Acknowledgements**

I thank Tuğçe Kazanasmaz and Stephen Wittkopf, who, as supervisor and co-supervisor of my PhD research at Izmir Institute of Technology, were reviewing the work.

Further thanks to Peter Apian-Bennewitz and my colleague Marek Krehel for critical but always encouraging discussions, and to Jan Wienold for his patient support in the usage of EVALGLARE. Andreas Noback prepared Figure 4.7.

## **4.6 Role of the funding source**

This research was supported by the doctoral funding scheme of Lucerne University of Applied Sciences and Arts, and by the Swiss Federal Office of Energy SFOE (#SI501427-01) as part of the project “High Resolution Complex Glazing Library (BIMSOL)”. Sole responsibility for content and conclusions lies with the authors.

Pellini S.p.A. as a collaborator within the BIMSOL project provided the sample and funding to cover the measurements.

## CHAPTER 5

### COMBINING THE BSDFs OF FENESTRATION LAYERS AT HIGH DIRECTIONAL RESOLUTION

*This section has been published as an article:*

“Computational combination of the optical properties of fenestration layers at high directional resolution” Grobe, L. O. *Buildings* **2017**, 22

---

Complex Fenestration System (CFS) typically comprise co-planar, clear and scattering layers. As there are many ways to combine layers in fenestration systems, a common approach in building simulation is to store optical properties separate for each layer. System properties are then computed employing a fast matrix formalism, often based on a directional basis devised by JH Klems comprising 145 incident and 145 outgoing directions. While this low directional resolution is found sufficient to predict illuminance and solar gains, it is too coarse to replicate effects of directionality in the generation of imagery. For increased accuracy, a modification of the matrix formalism is proposed. The tensor-tree format of RADIANCE, employing an algorithm subdividing the hemisphere at variable resolution, replaces the directional basis. The utilization of the tensor-tree with interfaces to simulation software allows sharing and re-use of data. The light scattering properties of two exemplary fenestration systems as computed employing the matrix formalism at variable resolution show good accordance to the results of ray-tracing. Computation times are reduced to 0.4 % to 2.5 % compared to ray-tracing through co-planar layers. Imagery computed employing the method illustrates the effect of directional resolution. The method is supposed to foster research in the field of daylighting as well as applications in planning and design.

#### 5.1 Introduction

CFSs improve visual and thermal comfort by controlling the admission and distribution of daylight. They have a two-fold, beneficial effect on electrical energy demand.

Operation of artificial lighting can be minimized due to the increased supply of daylight and the reduced need to operate sun-shades. Demand for cooling decreases due to lower internal gains by lighting, and the control of solar gains.<sup>16-18</sup> Typical CFSs comprise a set of co-planar, clear and scattering layers. These layers are chosen from a range of coated and uncoated glazing, interior or exterior sun-shades and devices for glare control such as Venetian blinds or woven roller shades. The optical properties of a CFS result from the particular combination of its layers and includes the complex interreflection within the system.<sup>22</sup>

Daylight and building energy simulation are applied to predict the impact of CFSs on comfort conditions and energy demand.<sup>116,117</sup> For assessments of thermal comfort, models must accurately predict solar heat gain depending on the incident direction of solar irradiation.<sup>76</sup> Visual comfort assessments rely on models that replicate not only the total flux, but the distribution of light into the building interior, adding the outgoing direction as a second independent variable. Models fulfilling the requirements of thermal and visual comfort assessment are established for fenestration systems comprising clear layers, such as double or triple glazing, and implemented in simulation software. CFSs comprising scattering or re-directing layers impose a particular challenge due to their almost infinite variety and the characteristic irregularity of their optical properties.<sup>77</sup>

### 5.1.1 Modeling CFSs with BSDFs

The effect of CFSs on incident light can be expressed by their Bidirectional Scattering Distribution Functions (BSDFs). The BSDF describes light transport through a thin surface element, such as thin CFSs and their layers, for any pair of incident and scattered outgoing directions  $(\theta_i, \phi_i; \theta_s, \phi_s)$ .<sup>97,98</sup> The implicit definition of the BSDF is given by the rendering equation:<sup>118</sup>

$$L_s(\theta_s, \phi_s) = \int_{\theta_i, \phi_i}^{\omega_i=4\pi} BSDF(\theta_i, \phi_i; \theta_s, \phi_s) \cdot L_i(\theta_i, \phi_i) \cdot \cos(\theta_i) \cdot d\omega_i \quad , \quad (5.1)$$

where  $L_s(\theta_s, \phi_s)$  is the scattered outgoing,  $L_i(\theta_i, \phi_i)$  the incident radiance and  $\omega_i$  the solid angle of the light source seen from the surface. Equation 5.1 shows this simplest formulation of the BSDF depending only on incident and outgoing directions. Further variables may be introduced to resolve spatial non-uniformity or the dependence on wavelength.<sup>119</sup>

Analytical models for the BSDF of CFSs have been proposed, but share the limitation that they are applicable only to particular classes of systems.<sup>71,120</sup> The application of a directional basis, merging ranges of both incident and outgoing directions

Table 5.1: Matrix representation of BSDF components. Reflection  $\mathbf{R}$  occurs if incident and scattered light direction lie on the same side of a sample. Transmission  $\mathbf{T}$  is defined for incident and scattered light on opposite sides. Two-letter subscripts indicate the side of the sample where light is incident on (first subscript) and scattered to (second subscript).

				forward	backward
Reflection	front to front	$\theta_i = 0^\circ$ to $90^\circ$	$\theta_s = 0^\circ$ to $90^\circ$	$\mathbf{R}_{ff}$	
	back to back	$\theta_i = 90^\circ$ to $180^\circ$	$\theta_s = 90^\circ$ to $180^\circ$		$\mathbf{R}_{bb}$
Transmission	front to back	$\theta_i = 0^\circ$ to $90^\circ$	$\theta_s = 90^\circ$ to $180^\circ$	$\mathbf{T}_{fb}$	
	back to front	$\theta_i = 90^\circ$ to $180^\circ$	$\theta_s = 0^\circ$ to $90^\circ$		$\mathbf{T}_{bf}$

into patches, allows to replace the BSDF as a continuous function by a discrete set of luminous coefficients.<sup>81</sup> For each combination of one patch on the incident, and one on the outgoing hemisphere, this coefficient holds the average BSDF of all incident and outgoing directions contained by the patch. This average evaluates to the bi-conical transmission, an optical property that can be directly measured using gonio-photometers<sup>60,102</sup> or computed employing analytical models or Monte Carlo ray-tracing techniques.<sup>75,83,121</sup>

### 5.1.2 Computational combination of BSDFs

To leverage the fact that an almost infinite number of CFSs is formed by combining a limited set of available layers, measurements and the creation of libraries such as the Complex Glazing Database (CGDB)<sup>122</sup> typically aim to characterize individual layers rather than entire system assemblies. Computational methods to combine the BSDF of one fenestration layer or a subsystem ( $\text{BSDF}_L$ ) with that of adjacent layers into the effective BSDF of an entire fenestration system ( $\text{BSDF}_S$ ) are then applied to provide models for simulation. A matrix formalism is employed in analogy to the computation of scattering on stacks of clear layers.<sup>123</sup> Forward and backward reflection and transmission  $\mathbf{R}_{ff}, \mathbf{T}_{fb}, \mathbf{T}_{bf}, \mathbf{R}_{bb}$  form the four components of the BSDF (Table 5.1) and are each represented as a matrix of  $m$  incident and  $n$  outgoing directions.<sup>111,124</sup> In building sciences, the matrix formalism was proposed to evaluate the absorption of light on individual layers as part of the computation of solar heat gain through CFSs.<sup>125,126</sup> The luminous coefficients  $c_{m,n}$  for the four component matrices are ordered such that the columns  $m$  correspond to

145 incident, and rows  $n$  to 145 outgoing directions:

$$\mathbf{M} = \underset{out}{\downarrow} \begin{pmatrix} & \xrightarrow{in} & \\ c(\theta_{i,1}, \phi_{i,1}, \theta_{s,1}, \phi_{s,1}) & \dots & c(\theta_{i,145}, \phi_{i,145}, \theta_{s,1}, \phi_{s,1}) \\ \vdots & \ddots & \vdots \\ c(\theta_{i,1}, \phi_{i,1}, \theta_{s,145}, \phi_{s,145}) & \dots & c(\theta_{i,145}, \phi_{i,145}, \theta_{s,145}, \phi_{s,145}) \end{pmatrix} \quad (5.2)$$

The directional basis of 145 defined directions will be referred to as the *Klems basis* after its inventor and is illustrated in Figure 5.1 a). By convention, the forward direction corresponds to incident light from the building exterior. Purely specular transmission and reflection, defined by equal incident and outgoing direction, form a special case that can be described by diagonal matrices.

The coupling of the outgoing directions of one layer to the corresponding incident directions on the next adjacent layer is implemented by a diagonal propagation matrix  $\Lambda$ . Its coefficients are set to the projected solid angle of the patch represented by each coefficient  $c_m = \omega_m \cdot \cos \theta_m$ . The BSDF<sub>S</sub> of the entire system, including inter-reflection between layers, is then computed by iteratively repeating the combination of BSDF<sub>L</sub>S for pairs of layers or sub-systems  $L1$  and  $L2$ :

$$\begin{aligned} \mathbf{T}_{fb} &= \mathbf{T}_{fb,L2} \cdot (\mathbf{I} - \Lambda \cdot \mathbf{R}_{bb,L1} \cdot \Lambda \cdot \mathbf{R}_{ff,L2})^{-1} \cdot \Lambda \cdot \mathbf{T}_{fb,L1} & (5.3) \\ \mathbf{R}_{ff} &= \mathbf{R}_{ff,L1} + \mathbf{T}_{bf,L1} \cdot (\mathbf{I} - \Lambda \cdot \mathbf{R}_{ff,L2} \cdot \Lambda \cdot \mathbf{R}_{bb,L1})^{-1} \cdot \Lambda \cdot \mathbf{R}_{ff,L2} \cdot \Lambda \cdot \mathbf{T}_{fb,L1} \\ \mathbf{T}_{bf} &= \mathbf{T}_{bf,L1} \cdot (\mathbf{I} - \Lambda \cdot \mathbf{R}_{ff,L2} \cdot \Lambda \cdot \mathbf{R}_{bb,L1})^{-1} \cdot \Lambda \cdot \mathbf{T}_{bf,L2} \\ \mathbf{R}_{bb} &= \mathbf{R}_{bb,L2} + \mathbf{T}_{fb,L2} \cdot (\mathbf{I} - \Lambda \cdot \mathbf{R}_{bb,L1} \cdot \Lambda \cdot \mathbf{R}_{ff,L2})^{-1} \cdot \Lambda \cdot \mathbf{R}_{bb,L1} \cdot \Lambda \cdot \mathbf{T}_{bf,L2} \end{aligned}$$

To overcome effects of spectral averaging, the method can be applied to spectral channels and is as such implemented in WINDOW.<sup>114</sup> With its interfaces to various building energy simulation tools and the CGDB, this software is currently the de-facto standard for modelling of multi-layer CFSs.

### 5.1.3 Data-driven models of the BSDF in daylight simulation

Due to its general applicability, discrete representations of the BSDF have been employed in lighting simulation to model the irregular transmission through CFSs.

Distributed as part of the daylight simulation software RADIANCE, `mkillum` evaluates BSDF data during the pre-computation of light transport through fenestration. It replaces the CFS by a virtual light-source in the diffuse-indirect inter-reflection calculation.<sup>81</sup> The *Klems basis* comprising 145 patches is applied to both incident and outgoing directions. A modification of `mkillum` substitutes the *Klems basis* by 145 incident and 1297 outgoing directions, following a recommendation by the International Energy Agency (IEA).<sup>79,80,127</sup> Current versions of RADIANCE support the use of data-driven models not only in the pre-computation of virtual light sources. A data-driven reflection and transmission model allows to describe any CFS only by a surface and its BSDF<sub>S</sub> in all phases of the simulation. The support of the *Klems basis* provides an interface to the CGDB as a data provider, as well as to WINDOW to model glazing assemblies from chosen BSDF<sub>LS</sub>. The data-driven model is in wide use especially in Climate-Based Daylight Modelling (CBDM) work-flows such as the Three-Phase-Method (3PM). Shared among software tools such as WINDOW, ENERGYPLUS and RADIANCE, the *Klems basis* backs a consistent modelling approach in multi-domain simulation.<sup>34,128</sup>

The directional resolution of the *Klems basis* has been found to be sufficient in simulations aiming for illuminance-based performance metrics. However, its adequacy in the computation of imagery such as applied in the prediction of glare and visual comfort has been questioned.<sup>37</sup> RADIANCE addresses this limitation by a refined representation of the BSDF. Rather than applying a fixed directional basis, patches are defined by mapping regions of a sub-divided square to the hemisphere. A symmetric subdivision of both axes of the square by the base of 2 results in  $2^k \cdot 2^k$  patches, with typical  $k = 3 \rightarrow 7$ . An algorithm maps the boundaries of the sub-squares to directions  $\theta, \phi$  and leads to a set of patches of equal projected solid angle and configurable resolution  $2^{2 \cdot k} = 64 \rightarrow 16384$ . The resulting patches are shown for two exemplary resolutions ( $k = 3$  and  $k = 5$ ) in Figure 5.1 b) and c). A four-dimensional tensor (dimensions relating to  $\theta_i, \phi_i, \theta_s, \phi_s$ ) can consequently hold the  $2^{4 \cdot k}$  luminous coefficients for  $2^{2 \cdot k}$  incident and  $2^{2 \cdot k}$  outgoing directions of one BSDF component.<sup>82</sup> An optional data-reduction pass processes the coarse tensor into a hierarchical, four-dimensional tree structure by adapting its resolution according to the local variance of the initial set of coefficients. The adaptive resolution preserves important detail but drastically reduces the size of the model. An interface to load, cache and query the model is provided with *libBSDF* as part of the open source software RADIANCE. This approach to store the BSDF at configurable resolution will be referred to as *Shirley-Chiu algorithm*, after the inventors of the underlying disk-to-square mapping algorithm.<sup>112</sup>

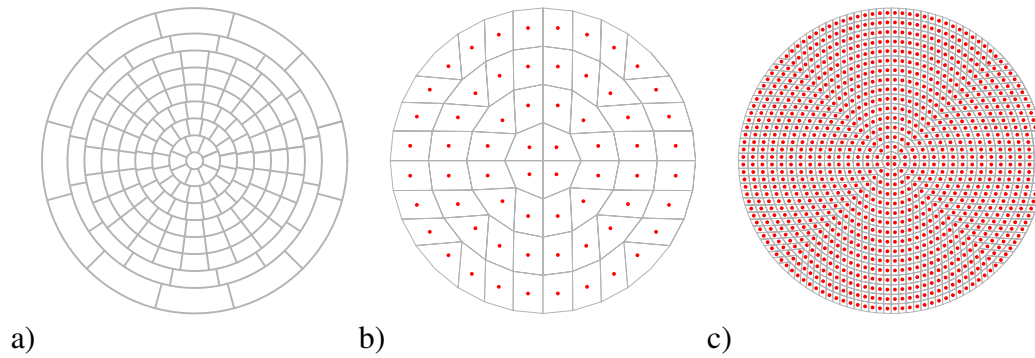


Figure 5.1: Fixed set of 145 patches comprising the *Klems basis* (a) and patches from square-to-disk mapping employing *Shirley-Chiu algorithm* at resolution  $k = 3$  (b) and  $k = 5$  (c).

While both the generation of BSDFs and its application in daylight simulation at high resolution are supported in *RADIANCE*, the combination of BSDF<sub>L</sub>s of adaptive resolution in analogy to the matrix formalism implemented in *WINDOW* is not possible. Modelling of CFSs by the data-driven model applied to co-planar surfaces is not feasible due to computational expense of ray-tracing. Horizontal research designs aiming to cover many different combinations of fenestration layers, as well as planners evaluating alternatives, are therefore currently limited to models of low resolution.

## 5.2 Objectives

An extension of the matrix formalism is proposed to support the combination of BSDF<sub>L</sub>s at variable resolution. Three criteria shall be fulfilled to match the requirements of daylight simulations:

1. BSDF<sub>L</sub>s of different directional resolution shall be combined. This reflects the fact that descriptions of layers with very different optical characteristics, often leading to different approaches in their characterization by measurement or simulation, have to be combined.
2. The directional resolution of the resulting BSDF<sub>S</sub> shall be configurable. The target resolution of the system's BSDF<sub>S</sub> depends on factors such as the characteristics of the CFS as well as the later application of the model in assessments requiring different degrees of accuracy.
3. Support for the data-driven reflection and transmission model in *RADIANCE* shall ensure the applicability of the method in visual comfort assessments, and leverage

the data-reduction algorithm implemented in RADIANCE. The compact representation allows to make use of libraries of BSDF<sub>L</sub> data in analogy to the CGDB, and is crucial to employ data-driven models in simulations with often complex and detailed architectural models.

The method shall be tested by applying it to two exemplary CFSs and comparing its results to Monte Carlo ray-tracing through geometric models. To illustrate the impact on computation time, the method is compared to ray-tracing through co-planar BSDF<sub>L</sub>s.

## 5.3 Method

The *Shirley-Chiu algorithm* is proposed to replace the *Klems basis* in the matrix formalism to combine BSDF<sub>L</sub>s. This extended matrix formalism employs the RADIANCE locally adaptive tensor-tree format to reduce the size of BSDF<sub>L</sub>s as input and BSDF<sub>S</sub>s as output. The implementation in C++ uses the EIGEN library<sup>129</sup> for matrix computations, and functions from RADIANCE to read, sample and write BSDF data. Exemplary CFSs are selected to test the method by comparing its results to those of ray-tracing through geometric models and stacks of BSDF<sub>L</sub>s. Down-sampling of BSDFs from high to lower resolution supports the combination of datasets with different resolution, and is employed to test the impact of resolution on direct-hemispherical optical properties.

### 5.3.1 Matrix formalism employing a subdivision algorithm of variable resolution

The *Klems basis* as originally proposed with the matrix formalism divides the hemisphere into patches of approximately equal solid angle. These patches, 1 to 145, allow to address a region containing any incident direction by its index  $m$ . Likewise, the outgoing direction is assigned to the index of its corresponding patch  $n$ . Ordering bi-conical transmission and reflection as coefficients by  $m, n$  allows to store each component of the BSDF in a matrix and to apply Equation 5.3.

The hardly parametrizable Klems basis is replaced in our method by the *Shirley-Chiu algorithm* to relate  $i \cdot j$  patches forming one hemisphere to cells of a square matrix  $\mathbf{H}$  of  $i$  rows and  $j$  columns. Subsequently, the cells of the matrix  $\mathbf{H}$  are re-ordered row-wise into one vector  $\mathbf{h}$  of  $i \cdot j$  elements so that any patch on the hemisphere can be addressed by

its vector-index in analogy to the *Klems basis*. Unlike the *Klems basis*, this vector is of configurable length depending on the chosen directional resolution.

Applying this method both to incident and outgoing directions, any incident direction  $\theta_i, \phi_i$  is related to its corresponding index  $m$ , and any outgoing direction  $\theta_s, \phi_s$  to index  $n$ . Similar to the component matrix based on the *Klems basis*, the indices  $m$  and  $n$  representing incident and outgoing direction become the position of the luminous coefficients in the component matrix  $\mathbf{M}$ . This allows to relate any coefficient  $c_{m,n}$  with indices  $m, n = 1$  to  $2^{2k}$ ,  $1$  to  $2^{2k}$  in a component square matrix  $\mathbf{M}$  of size  $m \cdot n$  to a corresponding pair of incident and outgoing directions  $\theta_i, \phi_i, \theta_s, \phi_s$ :

$$\mathbf{M} = \begin{matrix} & \xrightarrow{in} \\ \text{out} \downarrow & \begin{pmatrix} c(\theta_{i,1}, \phi_{i,1}, \theta_{s,1}, \phi_{s,1}) & \dots & c(\theta_{i,2^{2k}}, \phi_{i,2^{2k}}, \theta_{s,1}, \phi_{s,1}) \\ \vdots & \ddots & \vdots \\ c(\theta_{i,1}, \phi_{i,1}, \theta_{s,2^{2k}}, \phi_{s,2^{2k}}) & \dots & c(\theta_{i,2^{2k}}, \phi_{i,2^{2k}}, \theta_{s,2^{2k}}, \phi_{s,2^{2k}}) \end{pmatrix} \end{matrix} \quad (5.4)$$

The parameter  $k$  defines the directional resolution of the BSDF. Given that  $i = j = 2^k$  and  $k_{max} = 7$ , the method is applicable at directional resolutions of  $< 2^\circ$  or up to  $2^{2 \cdot k_{max}} = 16384$  incident and outgoing directions.

The resulting maximum size of the matrix is  $2^{4 \cdot k_{max}} = 268,435,456$  cells, corresponding to 1 GB per component assuming single precision floating point values. The *Shirley-Chiu algorithm* ensures that the disk is subdivided into regions of equal areas at any resolution. As this subdivision is projected to the hemisphere, the mapping of patches to matrix cells is cosine-weighted. The projected solid angle  $\Omega$  of all patches is equal and propagation matrix  $\mathbf{\Lambda}$ , relating outgoing and incident directions of adjacent layers, becomes a diagonal matrix with coefficients of equal value:

$$\mathbf{\Lambda} = \begin{matrix} & \xrightarrow{in} \\ \text{out} \downarrow & \begin{pmatrix} \Omega_1 & & \\ & \ddots & \\ & & \Omega_{2^{2k}} \end{pmatrix} \end{matrix} \quad \text{with all } \Omega = \frac{\pi}{2^{2k}} \quad (5.5)$$

### 5.3.2 Pair-wise combination of BSDFs at variable resolution

The computation of the  $\text{BSDF}_S$  of a CFS is implemented by a sequence of pair-wise combinations of layer  $\text{BSDF}_L$ s. The combinations are repeated to sequentially add  $\text{BSDF}_L$ s until all layers of the fenestration system have been merged into one data-driven model.

The tensor-tree representations of two layers are loaded calling functions of the *libBSDF* library as distributed with *RADIANCE*. As the convention in *RADIANCE*, being a backward ray-tracer, differs from that of the original matrix formalism in that it considers the interior to be the front surface, front and back components have to be flipped. For each layer, component matrices  $\mathbf{R}_{ff}, \mathbf{T}_{fb}, \mathbf{T}_{bf}, \mathbf{R}_{bb}$  of a size determined by the chosen target resolution are filled by sampling the tensor-tree for all pairs of incident and outgoing directions. The propagation matrix  $\mathbf{A}$  is initialized (see Equation 5.5) according to chosen resolution  $k$ . The components of the  $\text{BSDF}_S$  are calculated according to Equation 5.3. The resulting components are again flipped to match the different conventions of front and back side in *RADIANCE* and the Klems formalism. They are then sequentially passed to the command `rmtree_reduce`, generating a compact tensor-tree of each component, and merged into one file by `wrapBSDF`, adding the meta-data required to interpret the file by *libBSDF*. Both `rmtree_reduce` and `wrapBSDF` are distributed with *RADIANCE* and could be employed to integrate the method into the daylight simulation software.

### 5.3.3 Combination of BSDFs of different resolutions

The parametrizable directional basis allows to store discrete representations of BSDFs at different resolutions. However, the computational combination of  $\text{BSDF}_L$ s according to Equation 5.3 is only defined for matrices of identical size. A sampling strategy must be therefore chosen to combine  $\text{BSDF}_L$ s of different resolution and generate a  $\text{BSDF}_S$  of given target resolution. The size of all matrices employed in the calculation is set according to the desired resolution. The  $\text{BSDF}_L$  of each layer is down- or up-sampled accordingly when the matrices are created. For cases where the target resolution of  $\text{BSDF}_S$  is higher than the resolution of the input layer  $\text{BSDF}_L$ , clusters of neighbouring coefficients will share an identical value. If the resolution of  $\text{BSDF}_S$  is smaller than that of  $\text{BSDF}_L$ , proper sampling must ensure that e.g. sharp peaks in the input  $\text{BSDF}_L$  are not missed. In the current implementation, all coefficients of the high resolution dataset contained in one patch of the target dataset are sampled and averaged. Figure 5.2 shows the sampled directions, which equal the center points of the high resolution dataset, and the

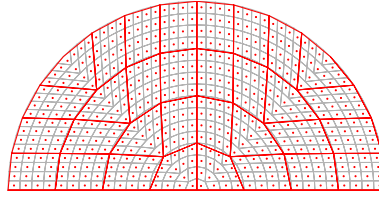


Figure 5.2: Re-sampling from higher ( $k_h = 5$ , red lines) to lower ( $k_l = 3$ , grey lines) directional resolution. For each patch at the target resolution,  $2^{2(k_h-k_l)}$  samples (red dots) are averaged.

low resolution patches of an exemplary target resolution. An adaptive sampling according to local variance in the input  $\text{BSDF}_L$  would promise to be computationally less expensive in many cases, but was not considered to reduce the complexity of the implementation.

### 5.3.4 Testing the method and its impact on the predicted performance of multilayer fenestration systems

Validity and performance of the method are tested by comparison to the combination of  $\text{BSDF}_L$ s by ray-tracing. Its applicability is evaluated for the case of modelling the fenestration of an exemplary office.

#### 5.3.4.1 Cases and computational generation of $\text{BSDF}$ s

To test the validity and impact of the method, it is applied to two exemplary CFSs:

**CFS1** Flat specular blinds embedded in a double glazing unit comprise a simple case of a CFS with predictable scattering properties.

**CFS2** Tilted light-shafts embedded in a triple glazing unit redirect light admitted from a range of given incident directions. The array of light shafts is highly directionally selective, aiming at a complete exclusion of direct sun-light in overhead applications.

Three sets of simulation models are prepared. These provide 1)  $\text{BSDF}_S$ s as input to the proposed method, 2) geometric models of the CFSs as input for ray-tracing as reference method to generate  $\text{BSDF}_S$ s, and 3) the input to combine  $\text{BSDF}_L$ s by ray-tracing as an alternative method.

First, simulation models of the scattering layers of both CFSs are prepared for the generation of  $\text{BSDF}_L$ s with **genBSDF**. Following the modelling convention in **RADIANCE**,

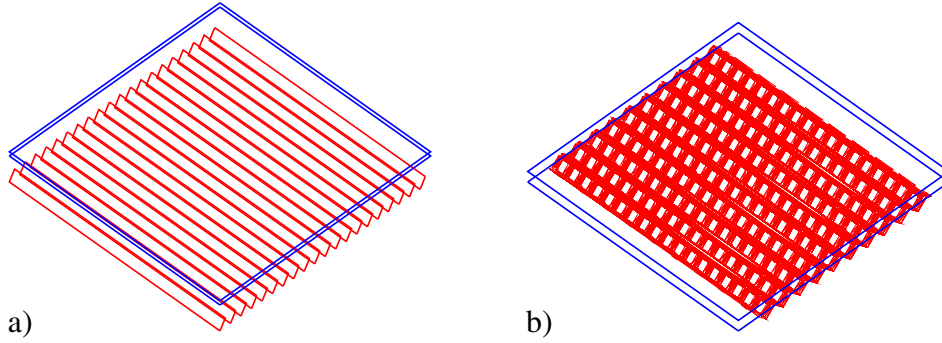


Figure 5.3: CFS1 (a): Flat mirror-blinds (red) in front of double-glazing (blue). CFS2 (b): Tilted light-shafts (red) embedded in double glazing (blue).

Table 5.2: Parameters for genBSDF in the generation of layer and system BSDFs from geometric models.

Parameter	Description	Value
-t4 $k$	Tensor resolution exponent, results in $2^{4 \cdot k}$ coefficients	7
-c $n$	Number of sample rays per hemisphere	163840
	Percentage of data reduction applied to tensor (set in genBSDF)	90

the inside surface points upward. The clear glass panes are modeled by the `RADIANCE` built-in `glass` material. The scattering layers are geometrically modelled, and their  $\text{BSDF}_{LS}$  computed by `genBSDF`. Parameters for `genBSDF` used in the generation of the layers'  $\text{BSDF}_{LS}$  are listed in Table 5.2. The generated tensor has four dimensions (-t4) corresponding to a mapping of  $\theta_i, \phi_i, \theta_o, \phi_o$  at resolution  $k = 7$ . From each incident direction, -c samples rays are sent. The chosen 163840 rays ensure that an average of  $163840/2^{2 \cdot 7} = 10$  rays for each pair of incident and outgoing directions are averaged over the model area to sample its non-uniform characteristics. The resulting  $\text{BSDF}_{LS}$  provide the input for our method.

A second set of geometric models is prepared for the entire assemblies *CFS1* and *CFS2*. The composition of the models is illustrated in Figure 5.3. The  $\text{BSDF}_{S}$  for both CFSs are computed by `genBSDF` with identical parameters as given in Table 5.2. The resulting  $\text{BSDF}_{S}$  are used as reference to test the validity of the extended matrix formalism. Finally, the CFSs are modelled as stacks of surfaces. Each surface with its associated  $\text{BSDF}_{L}$  represents one layer. The  $\text{BSDF}_{S}$  are computed using `genBSDF`. Ray-tracing through such stacks of  $\text{BSDF}_{L}$ s is a challenge for the sampling algorithm, and parameters are relaxed to achieve results in acceptable times as shown in Table 5.3. With the  $\text{BSDF}_{L}$ s being uniform over the layer surfaces, sampling parameter -c  $n$  is decreased. An additional parameter -ad  $n$  is set to reduce the number of rays spawned at each ray intersection of the diffuse-indirect calculation. The resulting  $\text{BSDF}_{S}$  should agree with the results of the proposed method, but significantly prolonged computation times are expected. This alternative approach shall illustrate the higher performance of the matrix formalism.

Table 5.3: Parameters for genBSDF in the generation of system BSDFs from stacked BSDF<sub>L</sub>s.

Parameter	Description	Value
-t4 $g$	Tensor resolution exponent, results in $2^{4g}$ coefficients	7
-c $n$	Number of sample rays per hemisphere	32768
-ad $n$	Number of daughter rays at each ambient ray intersection	128
	Percentage of data reduction applied to tensor (set in genBSDF)	90

### 5.3.4.2 Comparison of the results of the extended matrix formalism and ray-tracing

To test the validity of the extended matrix formalism employing the *Shirley-Chiu algorithm*, its results are compared with ray-tracing through the geometrical models. For one exemplary incident direction, the resulting BSDF<sub>S</sub>s of both CFSs are plotted in a cylindrical mapping of all directions of the transmission hemisphere. The plotted distributions are qualitatively compared to test the capability of the method to replicate the characteristic features in the BSDFs. For this evaluation of the method’s validity, the ray-traced BSDF<sub>S</sub>s is considered to be ground-truth, as the well-known ray-tracing algorithm in the computation of the BSDF<sub>S</sub>s is identical to the computation of the individual layers BSDF<sub>L</sub>s.

The cosine term  $\cos\theta_i$  in Equation 5.1 leads to an exaggeration of deviations in the BSDF at directions close to the grazing angle  $\theta_i = 90^\circ$ . The BSDF is therefore converted into its equivalent Differential Scattering Function (DSF) prior to quantitative comparisons according to Equation 5.6.

$$DSF(\theta_i, \phi_i; \theta_s, \phi_s) = BSDF(\theta_i, \phi_i; \theta_s, \phi_s) \cdot \cos(\theta_i) \quad (5.6)$$

Global Accordance (GA) and Local Accordance (LA) are applied to compare the two DSFs of a CFS for one given incident direction.<sup>68</sup> These metrics are based on the pair-wise comparison of values for identical directions. If a sharp peak is accurately predicted for a direction minimally offset from the peak direction in the reference, this good accordance would not be accounted for because of the mismatch of peak directions. To reduce the sensitivity of the comparison to such slight directional mismatches, the resolution of both distributions is reduced (from  $k = 7$  to  $k = 5$ ) before the application of

the metrics. This step merges 16 adjacent directions and thereby avoids artefacts due to sharp peaks and high frequency noise.

As defined in Equation 5.7, GA integrates the accordance  $f_{A,B}$  of DSF  $A$  with reference  $B$  for all outgoing direction indices  $j$  into one metric. For applications in the comparison of gonio-photometric measurements of luminaires assuming identical instrumentation, a range of 98 % to 99 % is considered good, 99 % to 100 % very good.<sup>130</sup> When different instruments or computational methods are employed, a lower degree of accordance can be expected.

$$f_{A,B} = 100 \left( 1 - \sqrt{\frac{\sum_{j=1}^n (DSF_{A,j} - DSF_{B,j})^2}{\sum_{j=1}^n (DSF_{A,j} + DSF_{B,j})^2}} \right) \quad (5.7)$$

LA as a directionally resolved metric is employed to localize deviations in the DSFs. For a distribution  $A$  and a given reference  $B$ , LA is defined for any directional index  $j$  by Equation 5.8.

$$f_{j,A,B} = 100 \left( 1 - \left| \frac{DSF_{A,j} - DSF_{B,j}}{DSF_{A,j} + DSF_{B,j}} \right| \right) \quad (5.8)$$

### 5.3.4.3 Comparing the performance of the matrix formalism to ray-tracing

The computation times of the extended matrix formalism and the application of **genBSDF** to combine  $BSDF_L$  is compared. Computation times are measured employing the **time** command, which is available on UNIX-like operating systems.<sup>131</sup> The *user time* is reported, accumulating the times spent by parallel processes to give an absolute measure of computational cost. To minimize the influence of input-output operations in the sampling routine of **genBSDF**, the model including its data-driven BSDFs was stored on a random-access memory (RAM) disk. In typical applications, access to the files containing the data-driven models would add up on the computation time for both techniques.

#### 5.3.4.4 Testing the down-sampling of BSDFs

To test the down-sampling from high to lower resolution, two BSDFs of *CFS2* are generated at directional resolutions of 1024 and 16384 directions per hemisphere ( $k = 7$  and  $k = 5$ ). The result of down-sampling the high resolution data-set to a resolution corresponding to the low-resolution data-set is compared to the latter for one incident direction.

#### 5.3.4.5 Impact of directional resolution on the predicted performance of fenestration systems

Direct-hemispherical transmission is computed from the  $\text{BSDF}_S$  of the two exemplary CFSs. As a measure of the total luminous flux through the system for one incident direction, it allows to test the impact of directional resolution on predicted supply of daylight and solar gains. As it is assumed that directional resolution can be low in building energy simulation and visual comfort assessments based on illuminance, a neglectable effect is expected.

To illustrate the impact of directional resolution on imagery rendered employing data-driven BSDF models, two variants of  $\text{BSDF}_S$  are employed to model *CFS1* in the context of a cellular office. One variant is based on the *Shirley-Chiu algorithm* and has a high directional resolution ( $k = 7$ ). The second variant employs the *Klems basis* and has a low directional resolution. The South oriented office is shown in Figure 4.7. It is exposed to direct sun-light, with sun altitude  $\theta_{sun} = 28.5^\circ$  and azimuth  $\phi_{sun} = 53.6^\circ$  West. Two views are considered, one facing the fenestration system, the other representing a typical position of an occupant. Images are rendered using the `RADIANCE rpict` command for two different views. The parameters for `rpict` are listed in Table 5.4.

### 5.4 Results

$\text{BSDF}_S$  were generate by the matrix-formalism and ray-tracing, and compared to test the validity and performance of the approach. Results of an exemplary application to an office model show the applicability, and the impact of the BSDF's resolution.

Table 5.4: Parameters for `rpict` in the generation of imagery.

<b>Parameter</b>	<b>Description</b>	<b>Value</b>
<code>-aa k</code>	Ambient accuracy, $k = 0$ disables ambient caching	0
<code>-ad n</code>	Ambient divisions, number of child rays in indirect-diffuse calculation	16384
<code>-lw w</code>	Limit weight, maximum contribution of one ray	5e-5
<code>-ss s</code>	Specular sampling, number of rays to send in indirect-specular calculation	1024
<code>-ps t</code>	Pixel sample spacing, $t = 1$ disables adaptive sampling	1

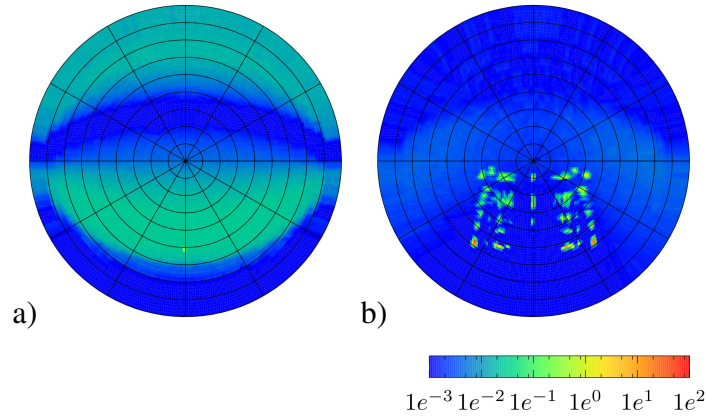


Figure 5.4: Transmission BSDF<sub>L</sub>s for incident direction  $\theta_i = 50^\circ$ ,  $\phi_i = 90^\circ$  of the scattering layers of CFS1 (a) and CFS2 (b). Please refer to Figure 5.3 for the positions of the scattering (red) layers within each CFS. Azimuth angle  $\phi = 90$  points up, referring to the up vector for *CFS1* and North for *CFS2*.

#### 5.4.1 Computed BSDFs of the fenestration layers

The BSDF<sub>L</sub>s of the two scattering fenestration layers as computed using genBSDF are shown in Figure 5.4. Only the distributions over the transmission hemisphere are plotted, although all four components of the BSDF<sub>L</sub>s are computed and required according to Equation 5.3. The scattering layer of *CFS1* shows no distinct peak in the transmission distribution as direct transmission is blocked at the high elevation angle  $\theta_i = 50^\circ$  (a). The complex structure contained in *CFS2* results in multiple distinct peaks (b).

#### 5.4.2 Re-sampling of the BSDF

The validity of the algorithm to sample a BSDF<sub>L</sub> to component matrices at variable resolution is of utter importance for the method, if BSDFs of different resolution shall be combined. Figure 5.5 shows three transmission distributions of *CFS3* for  $\theta_i = 30^\circ$ . Two distributions are generated by Monte Carlo ray-tracing at different directional resolutions ( $k = 7$  (a) and  $k = 5$  (b)). genBSDF was employed with the model of the assembly *CFS3* as shown in Figure 5.3 (b) and the parameters listed in Table 5.2. The third distribution (c) is the result of down-sampling from (a) to the lower resolution of (b).

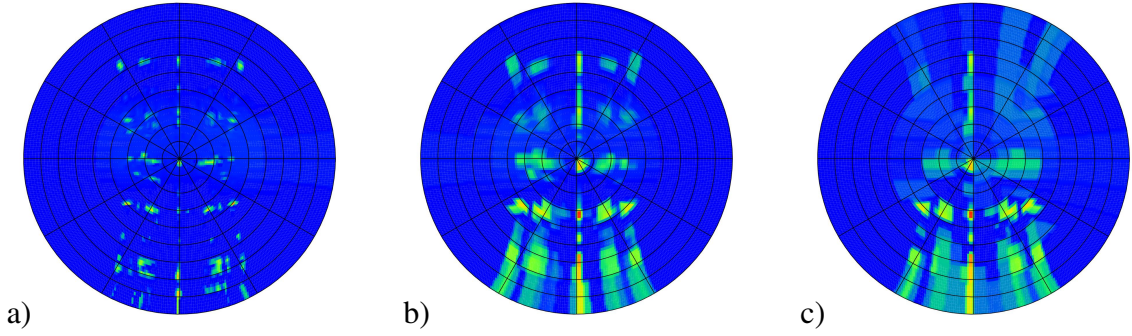


Figure 5.5: Comparison of ray-traced and down-sampled transmission distributions of CFS2 for incident direction  $\theta_i = 30^\circ, \phi_i = 90^\circ$ : a) Ray-traced at high resolution ( $k = 7$ ). b) Down-sampled from a) to moderate resolution ( $k = 5$ ). c) Ray-traced distribution with resolution as b).

Table 5.5: GA of results from matrix formalism with *Shirley-Chiu algorithm* and ray-tracing.

$\theta_i, \phi_i$	$65^\circ, 90^\circ$	$50^\circ, 90^\circ$	$45^\circ, 90^\circ$	$25^\circ, 90^\circ$	$45^\circ, 45^\circ$
<i>CFS1</i>	0.010	88.943	97.864	98.938	97.760
<i>CFS2</i>	67.677	95.410	97.992	96.361	98.738

### 5.4.3 Combined BSDFs and comparison to results of ray-tracing

The  $\text{BSDF}_S$  of each CFS was computed by ray-tracing from the geometric models as well as employing the extended matrix formalism. The data-reduction eliminated 90 % of the tensor in the final combination step.

The transmission distributions predicted by both methods for incident direction  $\theta_i = 50^\circ$  are shown in Figure 5.6. Their accordance is illustrated as  $1 - LA$  of their corresponding DSFs and emphasises regions of high deviation. While the distributions for *CFS1* appear to be identical in Figure 5.6 (a,c), a smearing out of the less distinct features can be observed for *CFS2* (b,d). The position and shape of the features in the distributions agree qualitatively.

GA as a quantitative metric of accordance is listed in Table 5.5. An extended set of distributions was evaluated and is illustrated in Figure 5.11 and Figure 5.12 in the appendix. Accordance between the results of the two methods is low for high incident elevation angles  $\theta_i$ . A particularly low GA is found for *CFS1* and incident direction  $\theta_i, \phi_i = 65^\circ, 90^\circ$  where all direct transmission is blocked.

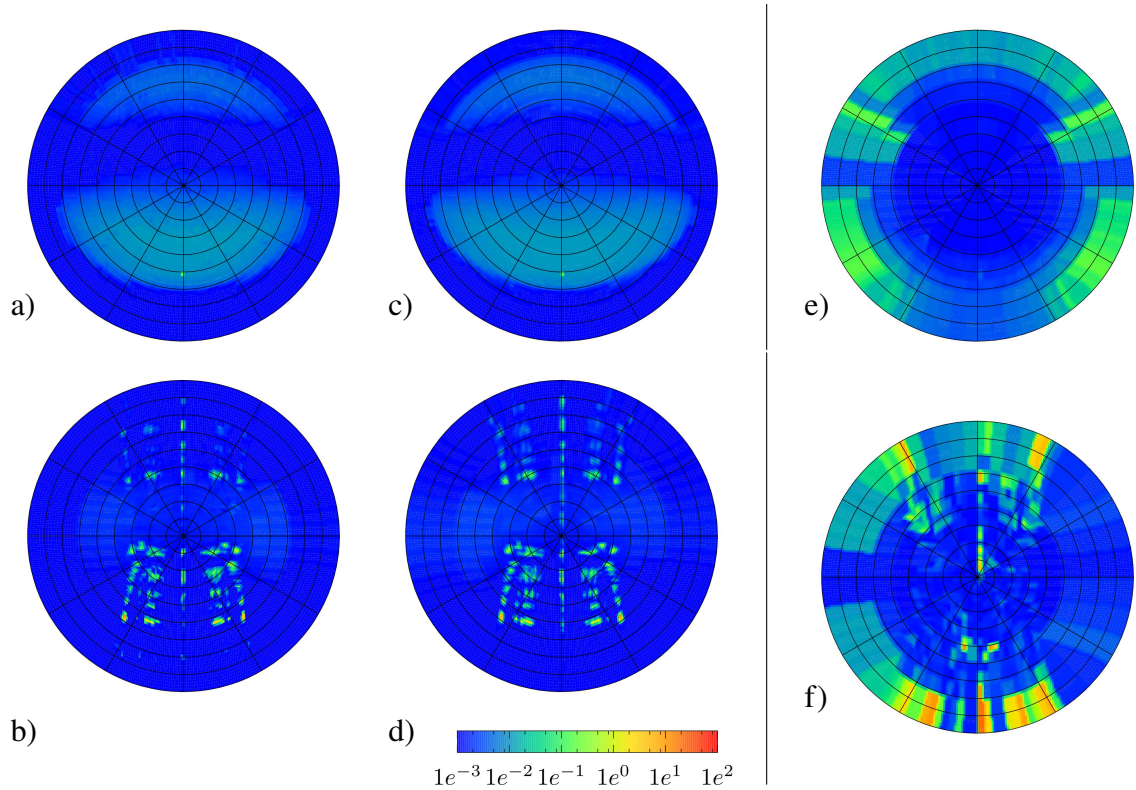


Figure 5.6:  $BPDF_S$  from geometrical ray-tracing (a,b) and matrix formalism (c,d).  $1 - LA$  (e,f) for  $\theta_i = 50^\circ, \phi_i = 90^\circ$ . Top to bottom:  $CFS1, CFS2$ .

#### 5.4.4 Evaluating the performance of the matrix formalism

Results from the computation of  $BPDF_{S5}$  by the matrix formalism employing the *Shirkey-Chiu algorithm* and by ray-tracing stacks of  $BPDF_{L5}$  using **genBSDF** are shown in Figure 5.7. The  $BPDF_{L5}$  as input for both methods were all of high directional resolution  $k = 7$ . GA of the resulting DSFs compared to ray-tracing with geometric models was 70.239 for  $CFS1$  and 82.636 for  $CFS2$ . Compared to the matrix formalism (Table 5.5), the accordance is low and affected by noise. Due to the already notable computation times, further increased sampling parameters to reduce noise and improve accordance were not investigated.

The combination of the three  $BPDF_{L5}$  comprising each CFS by Monte-Carlo ray-tracing and at high target resolution  $k = 7$  led to elapsed user times as shown in Table 5.6. Even if this computation time is distributed among e.g. 12 cores of a modern computer, this still leads to a computation time of about one day for  $CFS1$  and one week for  $CFS2$ . The durations of the ray-tracing approach for the two CFSs differ significantly.

Computation time of the matrix formalism at the same high target resolution as in the ray-tracing based approach is about 7 h without parallel processing. The duration is almost identical for both CFSs. Directional target resolution has a significant impact on the

Table 5.6: Elapsed user time for the combination of stacked  $\text{BSDF}_L$ s employing the extended matrix formalism at selected directional resolutions ( $k = 4$  to  $7$ ) and ray-tracing at high resolution ( $k = 7$ ).

CFS	$k = 4$	$k = 5$	$k = 6$	$k = 7$	genBSDF
<i>CFS1</i>	0.26 h	0.26 h	0.39 h	7.09 h	289 h
<i>CFS2</i>	0.26 h	0.26 h	0.40 h	7.07 h	1981 h

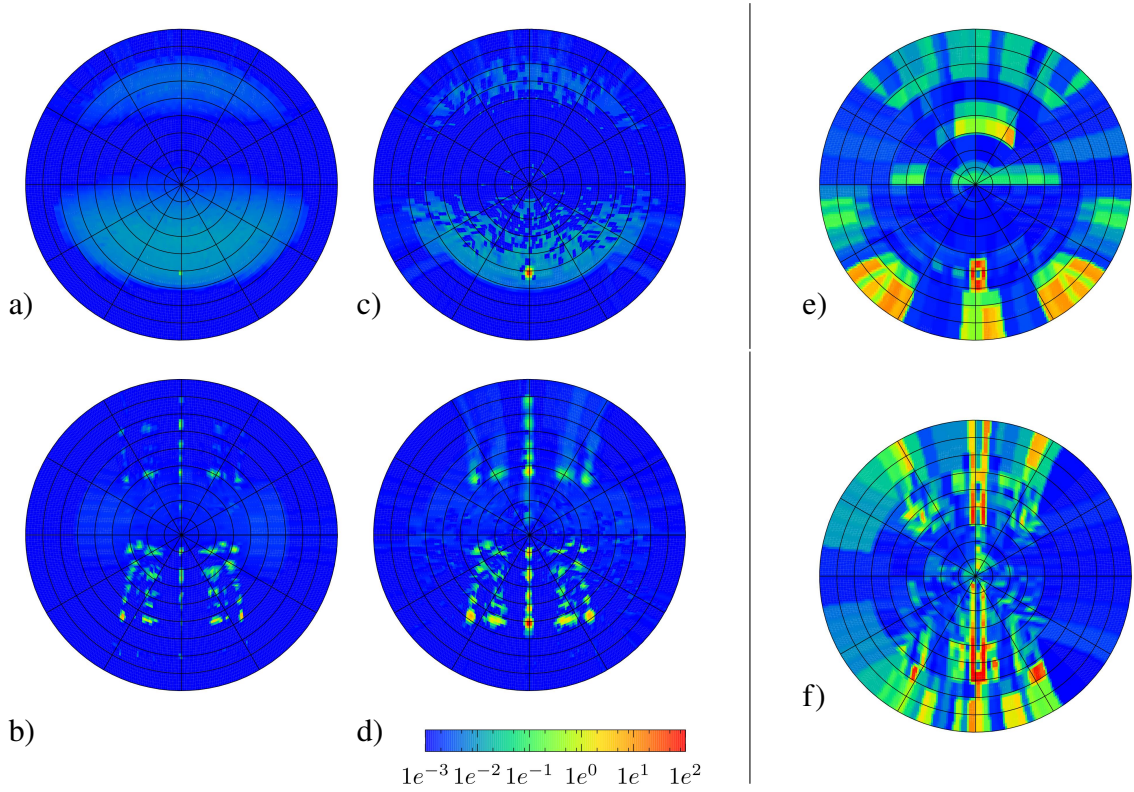


Figure 5.7:  $\text{BSDF}_S$  from ray-tracing geometrical models as shown in Figure 5.3 (a,b) and through stack of data-driven  $\text{BSDF}$  models (c,d).  $1 - LA$  (e,f) for  $\theta_i = 50^\circ, \phi_i = 90^\circ$ . Top to bottom: *CFS1*, *CFS2*.

computation time for resolutions higher than  $k = 5$ . For these resolutions, the extended matrix formalism leads to computation times in the range of approximately 0.25 h to 7 h for both CFSs. Resolutions below  $k = 5$  do not further reduce the computation time.

#### 5.4.5 Evaluating the impact of directional resolution

For both CFSs, the direct-hemispherical transmission calculated with different resolutions shows a high degree of accordance. The results are shown in Figure 5.8 for selected ranges of outgoing  $\theta_i$ . Ranges with possible direct sun-light exposure are underlaid

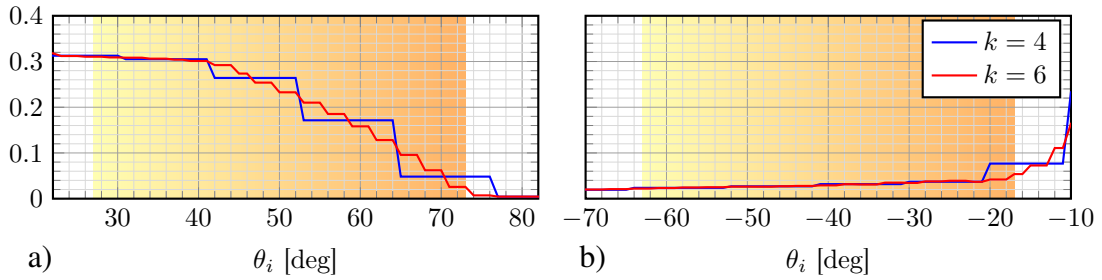


Figure 5.8: Direct-hemispherical transmission calculated with BSDFs of two different directional resolutions. The sun elevations for an application in a South facing fenestration are indicated for *CFS1* (a). For *CFS2* (b), an overhead installation is assumed. Sun elevations are chosen for Lucerne.

changing gradually from yellow (winter) to orange (summer) for typical orientations of the CFSs. The transmission through *CFS1* decreases with increasing  $\theta_i$ , corresponding to higher sun elevation angles as the CFS is typically installed vertically. *CFS2* is assumed in a horizontal orientation, with  $\phi_i = 90^\circ$  pointing North. For directions in the South, light is almost blocked up to sun altitudes of  $20^\circ$ , corresponding to  $\phi_i = -20^\circ$ . Transmission increases toward North. The step artefacts in all three curves match the angular diameter of the different resolution applied in the hemispherical sub-division.

Imagery generated employing the data-driven BSDF model at high resolution of  $k = 6$ , as well as of the *Klems directional base*, are shown in Figure 5.9 and Figure 5.10. The low resolution leads to a loss of the sharp contours of the shadow caused by the the shape of the windows and the dividing frames. While the difference is only marginally perceived when facing the fenestration (Figure 5.9), it dominates the field of view of an occupant facing the wall exposed to direct sun-light (Figure 5.10). Noise due to insufficient directional sampling of the high resolution BSDF is visible in views Figure 5.9 a) and Figure 5.10 b).

## 5.5 Discussion and conclusion

The proposed extension of the matrix formalism introduced by Klems allows to calculate optical properties of fenestration systems at higher and variable directional resolution. Utilization of the compact tensor-tree format supported by *RADIANCE* allows to build up libraries of layer data maintaining a high degree of detail at moderate file size, and provides a means to employ the generated system BSDFs in daylight simulation.

Accordance between results of the variable-resolution matrix formalism based on the *Shirley-Chiu algorithm* and ray-tracing as a reference is high for both tested CFSs and most incident directions. Artefacts occur for less distinct features if the directional

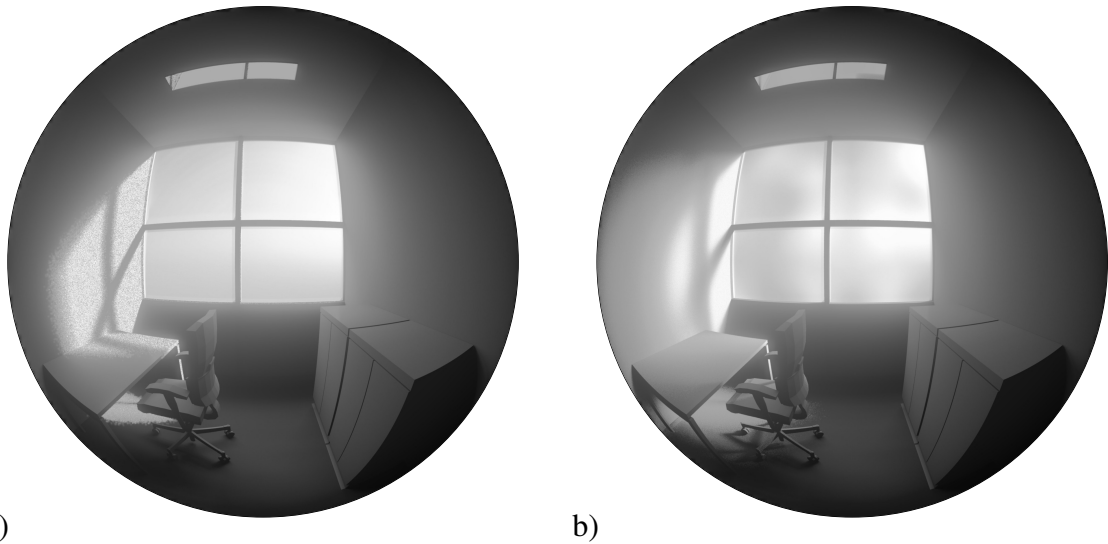


Figure 5.9: View toward fenestration. *CFSI* modelled by combining  $BSDF_L$ s based on *Shirley-Chiu algorithm* and high directional resolution  $k = 6$  (a) and *Klems basis* (b).

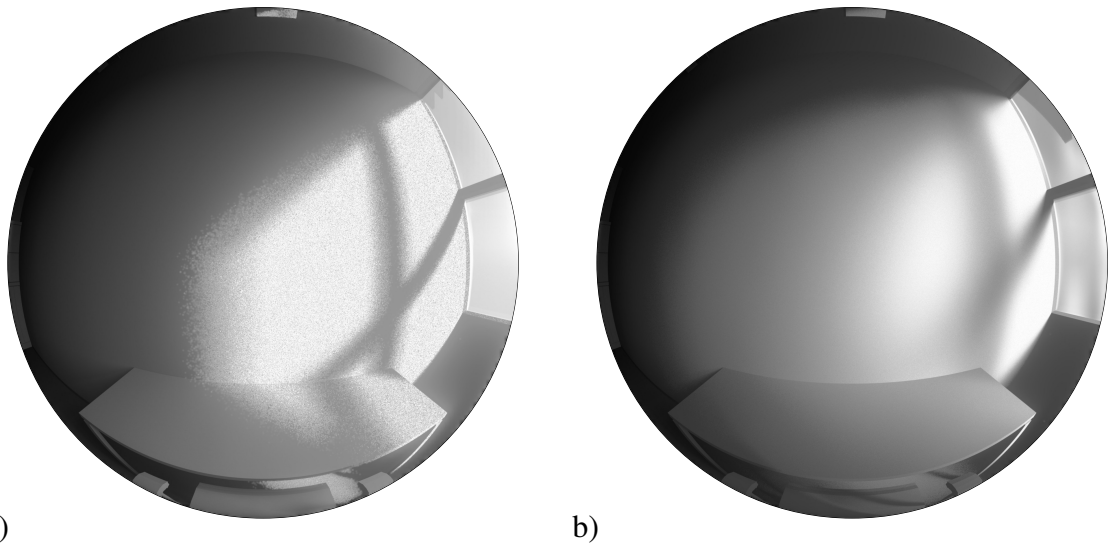


Figure 5.10: View of an occupant on his work desk, rendered with  $BSDF$  generated at high resolution  $k = 6$  (a) and with the original directional base by *Klems* (b). The different directional resolutions affect the luminance distribution within the field of view significantly.

resolution is reduced, but do not affect prominent features or the overall characteristics of the distribution. Low GA for incident directions where direct transmission is blocked can be explained with the higher impact of low values in the  $BSDF$ s. These are affected both by noise and the data-reduction algorithm. To ensure that accordance is not limited to distributions resulting from the one chosen incident direction, an extended set of distributions is shown in Figure 5.11 and Figure 5.12 in the appendix.

The dependency of direct-hemispherical transmission on the incident direction, which is characteristic for both assessed *CFS*s, is replicated by  $BSDF$ s of different

resolutions. While the slopes shown in Figure 5.8 are affected by step artefacts depending on directional resolution, these effects would be cancelled out by averaging if more than one incident direction is considered e.g. in annual assessments. Therefore one can expect that low resolution models, such as those supported by WINDOW, are applicable if the total flux entering a building through the CFS is to be evaluated based on annual simulations. This holds true especially for thermal comfort assessments. The results seem to confirm prior works<sup>37</sup> that also for assessments employing illuminance-based metrics, the impact of directional resolution can be neglected in the tested range of directional resolutions  $k = 4$  to  $k = 7$ . The difference in the imagery rendered employing BSDFs of different resolution asks for an in-depth study on the impact on luminance-based assessments of glare and visual comfort.

For the first time, BSDF<sub>S</sub>s fulfilling the requirements of such assessments can be efficiently computed from collections of layer properties. Combination of BSDF<sub>L</sub>s by ray-tracing is possible but impractical due to its inefficiency. The presented method is therefore expected to be an important support for practitioners, assessing variants such as different combinations of clear and scattering layers. In research, the extension of the matrix formalism to variable directional resolution opens a door to horizontal research design, aiming at the evaluation of not only few exemplary systems but huge numbers of possible combinations of fenestration components.

The current implementation does not allow to employ analytical models e.g. for clear layers. An extension to read in compact descriptions of the optical properties of clear glazing, which can be efficiently stored in diagonal matrices, shall be implemented. An optimization to process large data-sets in parallel beyond the already utilized optimizations in matrix computations would promise a significant speed-up and would allow to resolve the computation to spectral channels. Block-based algorithms in the multiplication of matrices shall be investigated to overcome memory constraints.

An open-source distribution is planned after revision of dependencies on software libraries, and further testing.

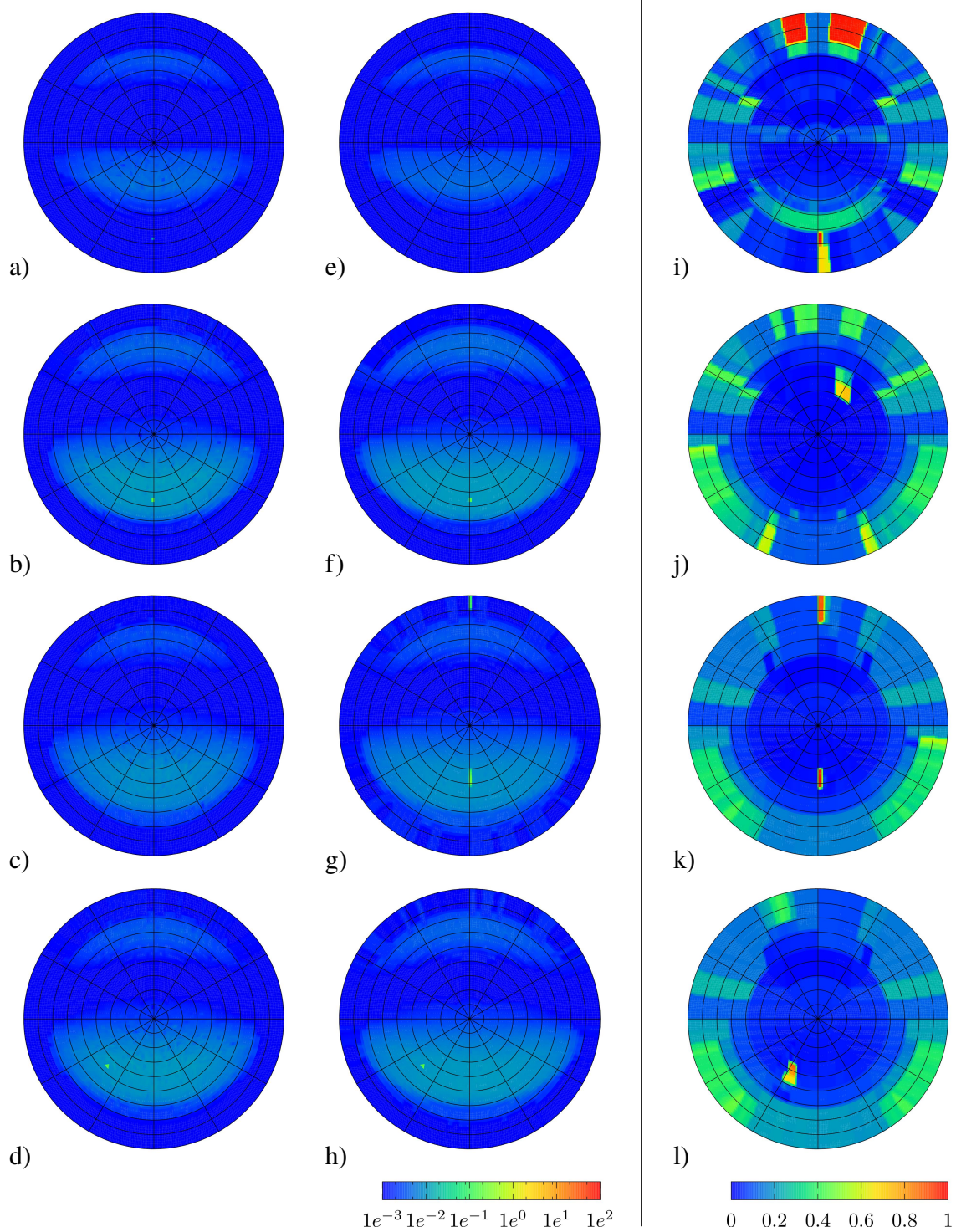


Figure 5.11: *CFSI*: Transmission based on ray-tracing (a-d) and matrix formalism (e-h).  $1 - LA$  of resulting distributions (i-l). Incident directions from top to bottom:  $\theta_i = 65^\circ, \phi_i = 0^\circ$  (a,e,i),  $\theta_i = 45^\circ, \phi_i = 0^\circ$  (b,f,j),  $\theta_i = 25^\circ, \phi_i = 0^\circ$  (c,g,k) and  $\theta_i = 45^\circ, \phi_i = 45^\circ$  (d,h,l).

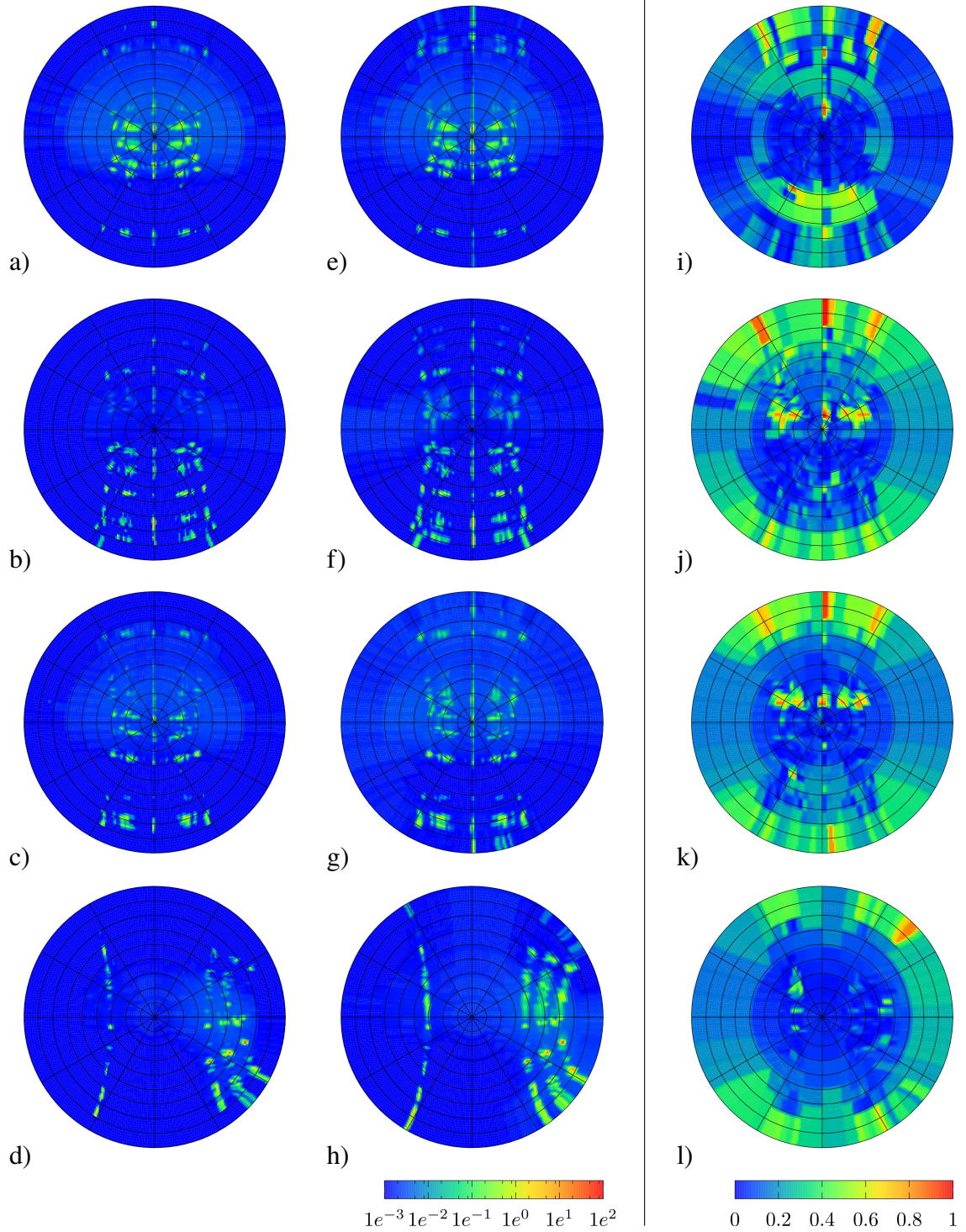


Figure 5.12: *CFS2*: Transmission based on ray-tracing (a-d) and matrix formalism (e-h).  $1 - LA$  of resulting distributions (i-l). Incident directions from top to bottom:  $\theta_i = 65^\circ, \phi_i = 0^\circ$  (a,e,i),  $\theta_i = 45^\circ, \phi_i = 0^\circ$  (b,f,j),  $\theta_i = 25^\circ, \phi_i = 0^\circ$  (c,g,k) and  $\theta_i = 45^\circ, \phi_i = 45^\circ$  (d,h,l).

## CHAPTER 6

# THE RADIANCE PHOTON MAP FOR IMAGE-BASED VISUAL COMFORT ASSESSMENTS WITH DATA-DRIVEN BSDF MODELS OF HIGH RESOLUTION

*A revised version of this section has been published as an article:*

“The Radiance Photon Map for image-based visual comfort assessments with data-driven BSDF models of high resolution” Grobe, L. O. *Journal of Building Performance Simulation* **2019**, DOI: 10.1080/19401493.2019.1653994

---

### 6.1 Introduction

The daylight simulation suite **RADIANCE** combines deterministic and stochastic algorithms into a hybrid implementation of Backward Ray-Tracing (BRT).<sup>132</sup> The deterministic testing of concentrated light-sources, such as the sun, as well as regular transmission and reflection are solved by deterministic ray-tracing.<sup>133</sup> Stochastic sampling by randomly distributed rays accounts for diffuse-indirect illumination.<sup>134</sup> **RADIANCE** provides physically plausible models for transmission and reflection, has been thoroughly validated,<sup>46,67,135–137</sup> and drives numerous front-ends (e.g. **DAYSIM / DIVA**, the **DIAL+SUITE**, **IDA ICE**, **ESP-R**, and **OPENSTUDIO**<sup>138</sup>) for applications in building simulation. **ACCELERAD** is a variant of **RADIANCE** that accelerates simulations by the massive parallelism of modern General Purpose Graphics Processing Unit (GPGPU) architectures, and allows for interactive visual comfort assessments.<sup>46,139</sup>

### 6.1.1 Daylight simulation with data-driven BSDF models in Radiance

To account for irregular light scattering, a data-driven model approximates arbitrary Bidirectional Scattering Distribution Functions (BSDFs)<sup>140</sup> by a set of coefficients.<sup>75,141</sup> Since assessments of visual comfort, and glare in particular, ask for image-based evaluation techniques<sup>38,41</sup> that are sensitive to the capability of the fenestration model to replicate directionality,<sup>37,142</sup> a data-structure of adaptive resolution is implemented in `RADIANCE`.<sup>51</sup> The *tensor tree* is compact by merging regions of low variance, yet it resolves features of the BSDF such as peaks caused by directional transmission and reflection. Models can be generated from measurements, and lend themselves in particular to micro-structures featuring complex light scattering properties, such as daylight redirecting films or coatings.<sup>51,55,56,84</sup>

The data-driven model also allows to model the irregular transmission characteristics of entire Complex Fenestration Systems (CFSs). These are otherwise not supported by the deterministic ray-tracing algorithm, which requires to know the sample directions leading toward the sun a priori, nor by stochastic backward sampling due to the impractically high amount of random rays required to sample a small source such as the sun. The software `genBSDF`, distributed with `RADIANCE`, pre-computes the BSDFs of such systems and compiles them into data-driven models supported by the backward algorithm.<sup>143,144</sup> To account for the geometric detail of macro-structured CFSs, e.g. Venetian blinds, the computationally generated, data-driven model can be evaluated only in the indirect-diffuse calculation, while an embedded geometric representation maintains visual detail and shadow patterns caused by the fenestration.<sup>82</sup>

One of the main challenges in the application of data-driven models even of moderate resolution in `RADIANCE` is their adequate sampling in the stochastic, indirect-diffuse calculation. The maximum resolution that can be achieved when modelling anisotropic reflection and transmission is currently limited to  $2^7 \times 2^7 = 16\,384$  outgoing (and, equally, incident) directions. To account for directional transmission through such models in the ambient calculation pass, an equal or higher number of random rays need to be spawned at each inter-reflection step in the building interior.<sup>145</sup> Acceleration by GPGPUs is currently not possible due to the lacking support for the data-driven model in `ACCELERAD`.

Climate-Based Daylight Modelling (CBDM) techniques such as the Five-Phase-Method (5PM) rely on dense stochastic sampling,<sup>36,146</sup> and mitigate computational effort by employing high resolution models only in the calculation of the direct sun contribution.<sup>53</sup> This approach is supported by a recently added modification of the data-driven model, `aBSDF`, that interprets distinct peaks in the BSDF as ideal direct transmission. Its implementation concentrates all light transmitted through a region defined by the model's resolution in its centre, and is therefore capable to model highly directional transmission of direct sun-light e.g. through fabric even with data-driven models of low or moderate resolution. The

technique has been demonstrated to achieve good results to model the visibility of the sun through shades, but effectively eliminates all information about the peak shape by reducing it to one direction.<sup>142</sup> This may be acceptable for cases where directional transmission is limited to one sharp peak, but is problematic with complex distributions comprising multiple peaks and other distinct features.

## 6.1.2 Daylight simulation with the Radiance Photon Map

The recursive simulation of light propagation in ray-tracing leads to a tree of rays. These are commonly classified by a formalized ray notation as listed in Table 6.1.<sup>147,148</sup> Hybrid BRT as implemented in `RADIANCE` replicates numerous mechanisms of light transport occurring in buildings, lending itself to applications in lighting design, daylighting and building design, in the form  $\boxed{\mathbf{E}(S^*) ([D|G]^*)L}$  for deterministic, and  $\boxed{\mathbf{E}(S^*) [D|G] ([D|G]^+)L}$  for stochastic ray-tracing. However, both algorithms are not capable to account for primary or secondary caustics  $\boxed{\mathbf{E}D ([S|G]^+) (D^*)L}$ .<sup>149</sup> Photon Mapping (PM) is a bi-directional algorithm that addresses this limitation and allows to simulate light transport in optically complex scenes.<sup>150</sup> Its integration in `RADIANCE` allows to model light redirection by non-planar reflectors and refracting structures that is not properly accounted for by BRT.<sup>69</sup> Light redirecting elements can be geometrically modelled as any other parts of the scene and, unlike the utilization of pre-computed BSDFs, do not require any pre-processing. Recent enhancements of the `RADIANCE PHOTON MAP`, such as its Out-of-Core (OoC) data-structure to store large amounts of photons, and the introduction of the `CONTRIBUTION PHOTON MAP` allow to employ the module in illuminance-based CBDM techniques.<sup>70,151–153</sup>

The `PHOTON MAP` module reflects the bidirectional nature of the algorithm by splitting the simulation into two separate passes.<sup>154</sup> The forward *photon distribution* from the light source is implemented by the program `mkpmap`. *Photon gathering* is integrated into the core simulation tools of `RADIANCE`, namely `rttrace` for computing single pixel values or sensor response, `rpict` for image generation, and `rcontrib` for the generation of contribution coefficients as required in CBDM.

In the distribution pass, light-sources emit photons that are reflected or transmitted by the scene geometry. After each collision with surfaces featuring a diffuse scattering component, photons are stored in the *global photon map* (dotted in Figure 6.1), or, for CBDM, in the contribution map for CBDM. Photons that collide with a diffuse surface after having been scattered by specular reflection or transmission are additionally stored in an optional *caustic photon map* (dashed and continuous lines in Figure 6.1). This photon

Table 6.1: Scattering phenomena defining the direction of subsequent rays with corresponding rtype values in RADIANCE, and the general notation of rays.<sup>149</sup>

Scattering	Direction	RADIANCE ray type	Symbol
none (primary)	from eye	PRIMARY	<b>E</b>
any	toward light source	SHADOW	<b>L</b>
regular reflection	mirrored incidence	REFLECTED	<b>S</b>
regular transmission	unchanged	TRANS	<b>S</b>
refraction	by Snell's law	REFRACTED	<b>S</b>
glossy reflection	perturbation of mirror	REFLECTED   SPECULAR	<b>G</b>
forward scatter	perturbation of incident	TRANS   SPECULAR	<b>G</b>
diffuse reflection	random	REFLECTED   AMBIENT	<b>D</b>
diffuse transmission	random	TRANS   AMBIENT	<b>D</b>

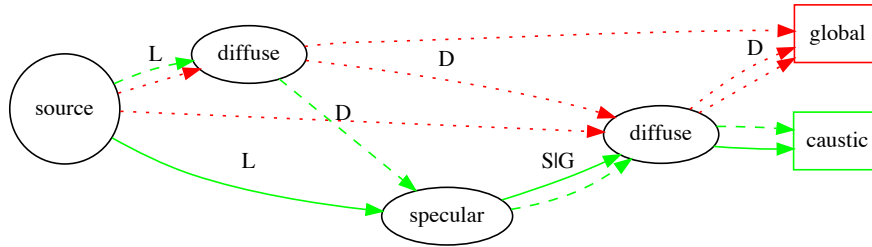


Figure 6.1: Exemplary paths of global (dotted) and caustic (continuous and dashed) photons. Note that directionally scattering (**G**) and regular transmission or reflection (**S**) are handled identically as specular in the original PHOTON MAP, but not in BRT by RADIANCE.

map refines the representation of the direct caustic path  $L([G|S]+)D$ . Note that the path is reversed, when compared to BRT, and starts with **L**. The primary eye ray **E** is not included in the distribution pass. Caustic photons are not only recorded after passing specular surfaces that are directly exposed to light sources, but also - as secondary caustics - if diffusely scattered photons are further scattered by specular reflection or transmission (e.g.  $L(D+)([G|S]+)D$ , dashed path in Figure 6.1).

In the photon gathering pass, the photon density is evaluated within an adaptive search radius. Other than caustic photons, the global photon density is by default not directly visualized. Instead, to reduce noise, local ambient illuminance is evaluated as the integral of the photon densities reached by one indirect-diffuse reflection by stochastic sampling. An alternative visualization mode directly computes illuminance from the local density. While this direct visualization is faster, it significantly increases noise and bias, and thereby impacts the appearance of the generated image.

With the local diffuse illumination being solved by gathering of global and caustic photons, the view ray toward diffusely reflecting surfaces and subsequent aimed shadow

rays  $\boxed{\text{E}(\text{S}^*)\text{DL}}$ , as well as the deterministic path  $\boxed{\text{E}(\text{S}^*)\text{L}}$  are traced backward during image generation. To avoid double-counting of rays already accounted for by the photon map, all ray sequences  $\boxed{\text{ED}(\text{S}+)\text{L}}$  must be eliminated in the stochastic backward sampling. This is implemented by the macro `srcRayInPmap(r)`. Unfortunately, since rays of types  $\boxed{\text{D}}$  and  $\boxed{\text{G}}$  are both handled by the stochastic scattering routines in `RADIANCE`, this effectively also suppresses the view-dependent ray sequence  $\boxed{\text{EG}(\text{S}+)\text{L}}$ , which is not represented by the photon map since photons are deposited only at  $\boxed{\text{D}}$  path segments. While this behaviour achieves correct results for local illuminance, it introduces an error in image generation when surface exhibit directional scattering, e.g. are specular-glossy or translucent.<sup>155</sup> Typical examples for this are the reflection of the sun on a glossy desk behind clear glazing (Figure 6.4), or forward-scattering by translucent objects toward the observer (Figure 6.5 and Figure 6.6). Consequently, the current implementation of the `PHOTON MAP`, while efficient in the sampling of data-driven models of high resolution, cannot be applied just to the problem where it could be most beneficial in current visual comfort research - the generation of imagery under sunny sky conditions.

### 6.1.3 Objectives

This research aims to enhance the applicability of the `RADIANCE PHOTON MAP` as a means to increase the efficiency of daylight simulation employing BSDF models of high directional resolution to image generation.

- The implementation is modified to account for directional transmission and reflection of scattered sun-light in image generation.
- Validity of the modified implementation is tested by comparison to BRT.
- The impact of the modification is evaluated by comparing glare ratings based on imagery, as generated by the original and the modified `PHOTON MAP`.
- A first benchmark compares the efficiency of the `PHOTON MAP` with that of BRT when data-driven models are employed.

The command-line interface of `RADIANCE` is not affected by the proposed modifications. Therefore, the presented method to increase efficiency and accuracy in image generation with data-driven models, in particular of CFSs, can be immediately applied by expert users familiar with `RADIANCE`, and could be easily implemented in future releases of front-ends.

## 6.2 Method

The implementation of the PHOTON MAP in RADIANCE is modified. The new implementation is tested against backward ray-tracing, and employed in glare assessment in an exemplary office.

### 6.2.1 Modification of the Photon Map implementation in Radiance

The modified implementation aims to employ deterministic BRT rather than PM for sources of known direction, e.g. when light sources are seen directly or through transparent layers, or by mirror-like reflection ( $\boxed{\text{E(S*)L}}$ ). Deterministic BRT is also applied when diffusely reflecting surfaces are lit directly, or through transparent surfaces without any intermediate scattering ( $\boxed{\text{ED(S*)L}}$ ) by non-extended light sources. Note that  $\boxed{\text{S}}$  applies only to regular transmission here. The shadow testing algorithm in RADIANCE would require *virtual light-sources* to account for regular reflection toward diffuse surfaces, therefore, the path ( $\boxed{\text{ED(S*)L}}$ ) leads to the deposition of a caustic photon in cases when  $\boxed{\text{S}}$  stands for regular reflection. BRT toward known source directions, but with randomly jittered rays, is employed to account for forward-scattering of light-sources within the field of view  $\boxed{\text{EGS*L}}$ , which is actively suppressed in the original implementation of the PHOTON MAP for RADIANCE.

In all other cases, PM is employed to solve for local illuminance on diffusely scattering surfaces. Furthermore, PM is extended to the diffuse reflection of light emerging from extended sources of type glow. The contribution of such sources was systematically underestimated in the original implementation of the PHOTON MAP.

To account for forwards-scattering toward the observer, the macro `srcRayInPmap(r)` in `src/rt/pmapmat.h` is disabled. Its functionality is replaced by refined criteria when photons are deposited, so that double-counting is avoided. Other than in the original implementation, regular and forward-scattered transmission are distinguished. In the case of regular transmission ( $\boxed{\text{LS*D}}$ ), indicated by `r->rtype&TRANS`) without any preceding deflection, no photons are deposited (Figure 6.2). All directional scattering ( $\boxed{\text{LG+D}}$ ) as `r->rtype&SPECULAR`, deflection by refraction ( $\boxed{\text{LS+D}}$  if `r->rtype&REFRACTED`), mirror-like reflection ( $\boxed{\text{LS+D}}$ ) if `r->rtype&REFLECTED`), or regular transmission either following prior deflection or emission from an extended source is accounted for by caustic photons. Consequently, the modified macro `ambRayInPmap(r)` disables Gaussian sampling when ambient rays pass hit directionally scattering surfaces. The criteria for deposition of caustic

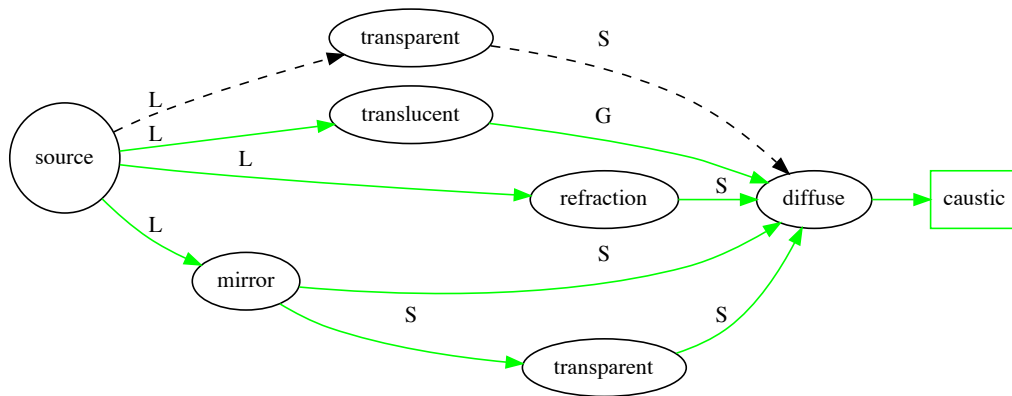


Figure 6.2: Exemplary paths leading to deposition of caustic photons in the modified PHOTON MAP (continuous lines). No photon is deposited after regular transmission without prior deflection (dashed lines).

photons are bundled in the new macro CAUSTICFLAGS(*r*) in `src/rt/pmapmat.h`.

To account for the illuminance by extended sources, e.g. the sky, *primary caustic photons* are introduced. These are deposited in the case  $\boxed{\text{LS*D}}$ , e.g. on diffusely transmitting glazing, or on diffusely reflecting surfaces that are exposed to the source either directly ( $\boxed{\text{LD}}$ ), or by regular transmission ( $\boxed{\text{LSD}}$ ).

A patch to apply the proposed modification to a current release of RADIANCE is provided with the supplementary materials.

## 6.2.2 Testing validity for image generation

Visual comfort is evaluated in architectural context, which is typically characterized by a high degree of geometric detail, as well as different optical properties of materials and finishes of interior room surfaces, furniture, glazing, and shading systems. To account for this complexity, a detailed model of an exemplary, South-oriented office is employed to test the modifications (Figure 6.3a).

The façade of the office features a CFS, comprising a Laser Cut Panel (LCP), which is embedded in the glazing of the upper window zone. Clear glazing is applied to the remaining, lower windows zones.

The LCP is expected to deflect incident sun-light toward the ceiling, and thereby to increase the depth of the daylighted zone. Figure 6.3b, right shows a sample provided for characterization and modelling. A data-driven model of the LCP is compiled from measurements on a scanning gonio-photometer. The tensor-tree with 16 384 incident and

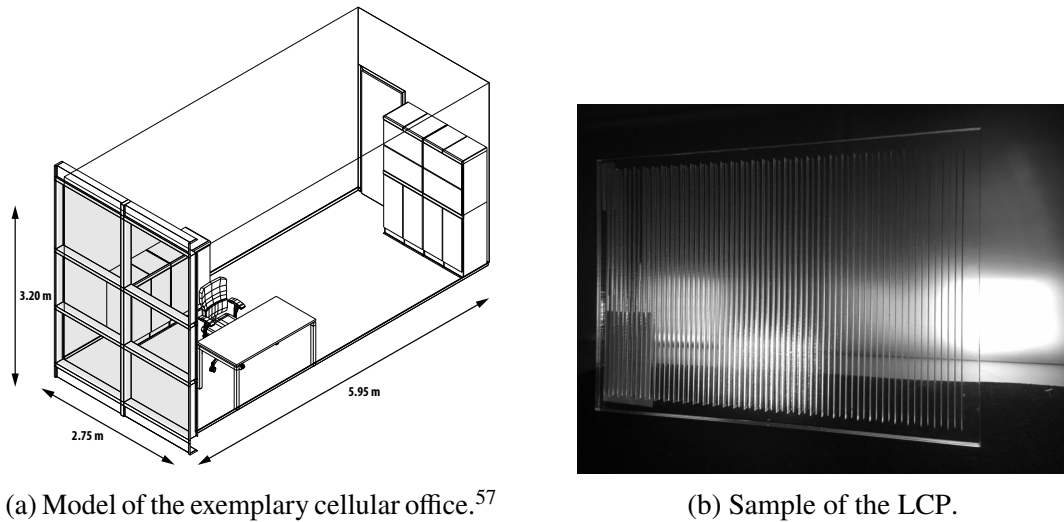


Figure 6.3: Office model and CFS as an exemplary test-case.

16 384 outgoing directions before data-reduction by 98 % achieves a maximum resolution of  $\approx 1.4^\circ$ . The model is available as part of the supplementary material. The lower window areas are covered with clear glazing and are modelled by the `glass` model in `RADIANCE`.

Imagery for two exemplary views is computed. View `v1` takes the perspective of a standing occupant facing the façade. View `v2` corresponds to an occupant seated at a desk facing the Eastern side-wall of the office. The modified and the original implementation of the `PHOTON MAP` are employed for image generation, as well as `BRT` as a reference. For each simulation technique, approaches to accelerate the calculation are investigated.

For `BRT`, the CFS is modelled with and without *peak extraction*. This technique (enabled by the use of the `aBSDF` transmission model) partially replaces the computationally demanding stochastic sampling of the transmission peak by deterministic shadow-testing. This may reduce artefacts of the ambient cache without increasing the stochastic sampling density. However, since the technique assumes regular transmission without any forward-scattering, it is expected that peak extraction will introduce an error in the image generation. `BRT` employing the data-driven model without peak-extraction (type `BSDF`) is therefore considered ground-truth in the scope of this work.

The `PHOTON MAP` supports two visualization modes of global photons. *Indirect photon visualization* estimates local illuminance by the evaluation of the global photon density at the first diffuse reflection of randomly distributed backward rays. This helps to reduce photon noise and bias as two typical artefacts of `PM`. *Direct photon visualization* skips the intermediary stochastic sampling and is therefore faster, but at the expense of more pronounced artefacts in the resulting imagery. Both visualization modes are tested for their impact on the appearance of the generated images, and on the results of visual comfort assessments.

Table 6.2: Parameters for image generation by BRT and PM.

Description	Parameter	BRT	PM
<b>mkpmap:</b>			
photon port modifier	<i>-apo</i> < <i>s</i> >		portMat
global photon map, photon count target	<i>-apg</i> < <i>s</i> > < <i>N</i> >		g.pm, 1M
caustic photon map, photon count target	<i>-apc</i> < <i>s</i> > < <i>N</i> >		c.pm, 1M
inter-reflections	<i>-lr</i> < <i>N</i> >		3
<b>rt pict:</b>			
reflections	<i>-lr</i> < <i>N</i> >	4	4
ambient reflections	<i>-ab</i> < <i>N</i> >	4	1 or -1
ambient accuracy	<i>-aa</i> < <i>k</i> >	0.15	0.15
ambient divisions	<i>-ad</i> < <i>N</i> >	1024	256
ambient subdivisions	<i>-as</i> < <i>N</i> >	512	64
ambient resolution	<i>-ar</i> < <i>N</i> >	64	48
maximum ray weight	<i>-lw</i> < <i>k</i> >	$2 \times 10^{-5}$	$8 \times 10^{-4}$
specular super-samples	<i>-ss</i> < <i>N</i> >	4	4
specularity threshold	<i>-st</i> < <i>k</i> >	0.0	0
photon map, bandwidth	<i>-ap</i> < <i>s</i> > < <i>N</i> >		g.pm, 80
photon map, bandwidth min max	<i>-ap</i> < <i>s</i> > < <i>M</i> > < <i>N</i> >		c.pm, 40, 400
pixel resolution	<i>-x</i> < <i>M</i> > <i>-y</i> < <i>N</i> >	2048, 2048	2048, 2048

To accelerate the simulations, the parallel image-generation program `rt pict` is extended to support PM, and is employed with PM as well as with BRT. The parameters for the generation of the reference imagery are listed in Table 6.2 (column BRT).

Light simulation with the `PHOTON MAP` comprises two passes. Parameters for the photon distribution with `mkpmap`, and the subsequent photon-gathering and image generation by `rt pict`, are listed in Table 6.2 (column PM). Note that, compared to BRT, the parameters of the indirect-diffuse, or ambient, calculation are relaxed, and that at most one indirect-diffuse scattering event (`-ab 1`) is accounted for in the backward-pass. Setting this parameter to a negative value (`-ab -1`) effectively suppresses the indirect-diffuse calculation entirely and triggers the direct visualization of global photons. A variable bandwidth of 40 to 400 photons is applied in the gathering of caustic photons to reduce bias in image regions where the illuminance gradient is steep.

For the quantitative comparison of the results of the `PHOTON MAP` calculations with the reference images, relative luminance difference is computed pixel-wise:

$$\Delta_r = \frac{|L_1 - L_2|}{L_1 + L_2} \cdot 2 \quad (6.1)$$

Table 6.3: Glare classification based on thresholds applied to DGP and DGI.

	<b>Classification</b>	<b>DGP</b>	<b>DGI</b>
•	imperceptible	< 0.35	< 0.18
•	Perceptible	< 0.40	< 0.24
•	Disturbing	< 0.45	< 0.31
•	Intolerable	> 0.45	> 0.31

Table 6.4: Photometric quantities computed from the imagery by evalglare.

<b>Symbol</b>	<b>Unit</b>	<b>Description</b>
$\bar{L}$	$\text{cd m}^{-2} \text{sr}^{-1}$	Average luminance of all pixels.
$\tilde{L}$	$\text{cd m}^{-2} \text{sr}^{-1}$	Median of the pixel values.
$E_v$	$\text{cd m}^{-2}$	Eye illuminance, cosine-weighted integral of pixel values.
$\bar{L}_{src}$	$\text{cd m}^{-2} \text{sr}^{-1}$	Average luminance of the detected glare sources.
$\Omega_{src}$	sr	Solid angle of the glare sources.
$\bar{L}_b$	$\text{cd m}^{-2} \text{sr}^{-1}$	Average luminance of the background.

### 6.2.3 Exemplary glare assessments

To assess the accordance of the modified PHOTON MAP with the reference, and to estimate the impact of the limitations in the original PM implementation when employed in image-based visual comfort assessments, glare metrics are calculated by evalglare<sup>45</sup> from the results of all three implementations. The glare metrics Daylight Glare Probability (DGP) and Daylight Glare Index (DGI), as well as the underlying photometric quantities (Table 6.4), are reported.<sup>156</sup> Glare sources are detected according to a fixed luminance threshold of  $2000 \text{ cd m}^{-2} \text{sr}^{-1}$ .<sup>157</sup> The metrics are classified according to a set of thresholds listed in Table 6.3.<sup>115</sup>

Due to the chosen solar geometry, the view to the sun is obstructed by the LCP. Sun-light cannot directly reach the view-point by transmission through the clear glazing, but by forward-scattering through the LCP and on the glossy surface of an office desk. It is expected that the resulting highlights are accounted for in the glare evaluations based on BRT as well as by the modified PHOTON MAP, but not by its original implementation.

## 6.3 Results

Imagery created by the PM and BRT, and the analysis with `evalglare` are presented to allow the qualitative and quantitative evaluation of the method.

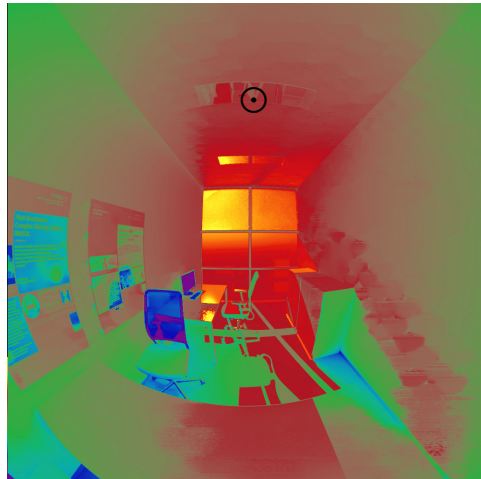
### 6.3.1 Visual inspection and comparison of imagery

Luminance maps corresponding to views  $v1$  and  $v2$ , are shown in Figure 6.4 and Figure 6.5. A logarithmic scale is applied to account for the high dynamic range of the images. The position of the pixel of highest luminance is marked in each image.

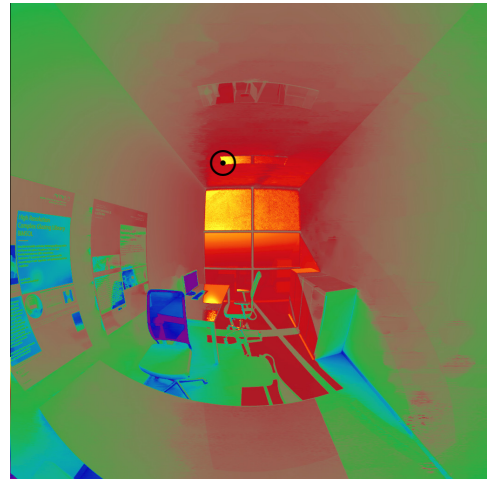
The results by BRT with and without peak-extraction achieve high accordance. The brightest pixel in  $v1$  is located on the specular luminaire in the foreground in imagery by BRT (Figure 6.4a), but on the distant luminaire according to BRT with peak extraction (Figure 6.4b). For  $v2$ , the brightest values are identified in the image area of the LCP (Figure 6.5a and Figure 6.5a). The stochastic sampling of the indirect-diffuse calculation introduces noise, and leads to the visible cloud-like artefacts of the ambient cache along the right side-wall in  $v1$  (Figure 6.4a). This artefact is less apparent in  $v2$  (Figure 6.5a). The effect of the concentration of the peak region in one singular direction becomes obvious in Figure 6.6, which shows a part of the upper window zone in  $v2$ . The forward-scattered light in a circular region centred at the direction toward the sun is assumed to be non-scattered and concentrated in few, very bright pixels, leading to a visible artefact.

The `PHOTON MAP` introduces visible noise in all generated images. Noise is more apparent when global photons are directly visualized, and in the case of the original `PHOTON MAP`, in image regions receiving sun-light through the clear glazing (e.g. parts of the desk in  $v2$ , Figure 6.5d and Figure 6.5d). Even with the indirect visualization of global photons, noise on the ceiling and the side-wall in the right half of the image is visible in  $v1$  (Figure 6.4c Figure 6.4e). This is due to the high contribution of caustic photons triggered by directional transmission through the LCP. These photons are always directly visualized, and the resulting noise is not modulated by the reflective pass in the gathering of global photons.

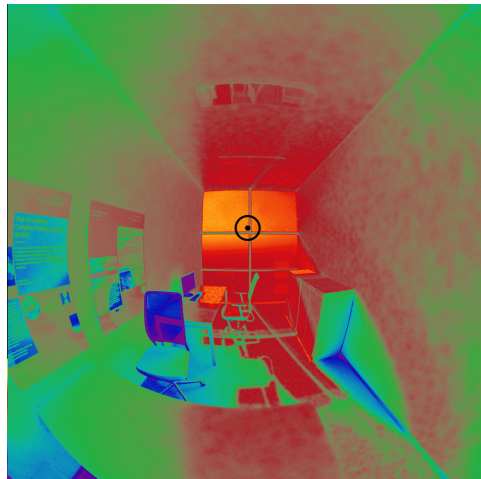
As expected, Figure 6.4c, Figure 6.4d, Figure 6.5c and Figure 6.5d show that the original `PHOTON MAP` does not account for the forward-scattering toward the observer, and thereby misses the most pronounced highlights. This applies to both views  $v1$  and  $v2$ , and to both modes of photon visualization (indirect and direct). The missing visibility of the sun through the LCP is shown in detail in Figure 6.6. Due to the lack of pronounced



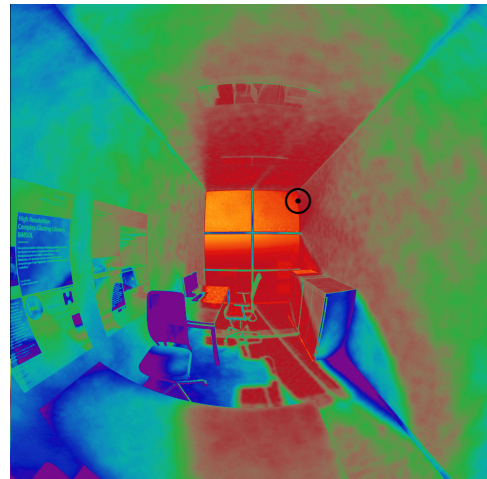
(a) BRT as reference.



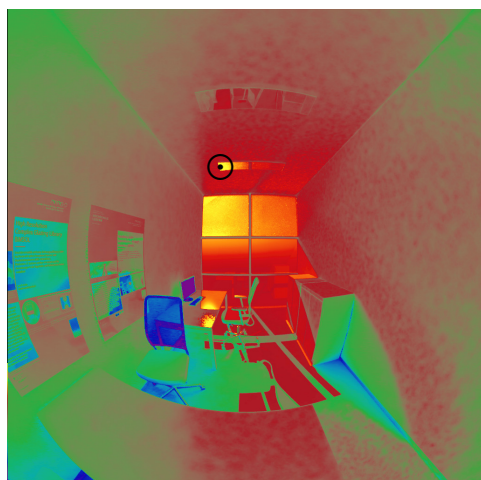
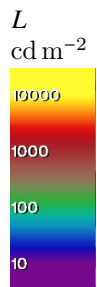
(b) BRT with peak-extraction.



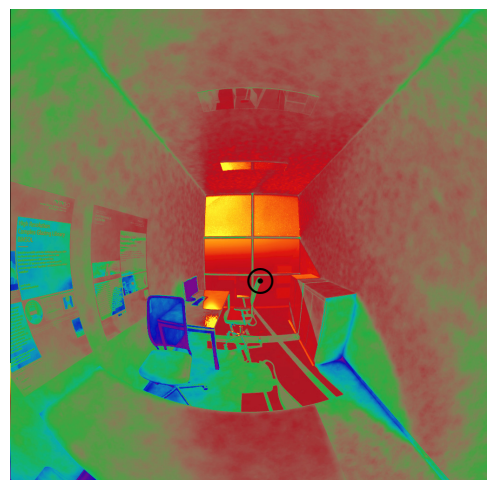
(c) Original PM, indirect photon visualization.



(d) Original PM, direct photon visualization.

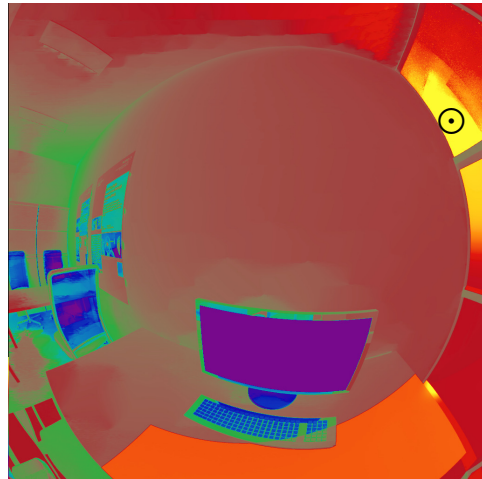


(e) Modified PM, indirect photon visualization.

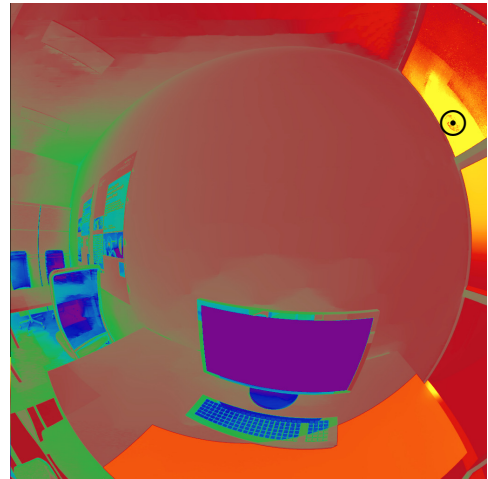


(f) Modified PM, direct photon visualization.

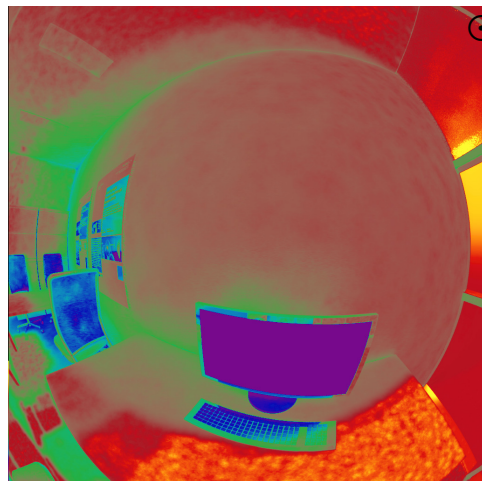
Figure 6.4: Luminance maps for view  $v1$ .



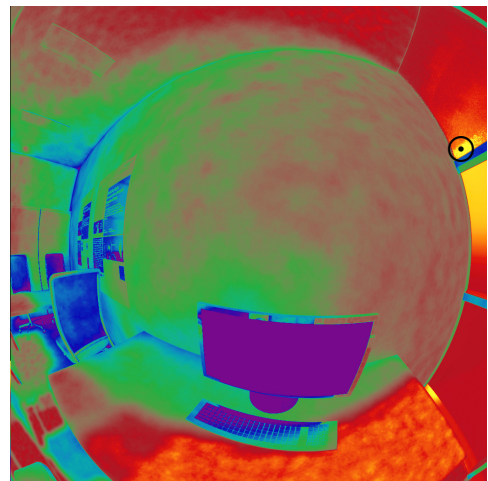
(a) BRT as reference.



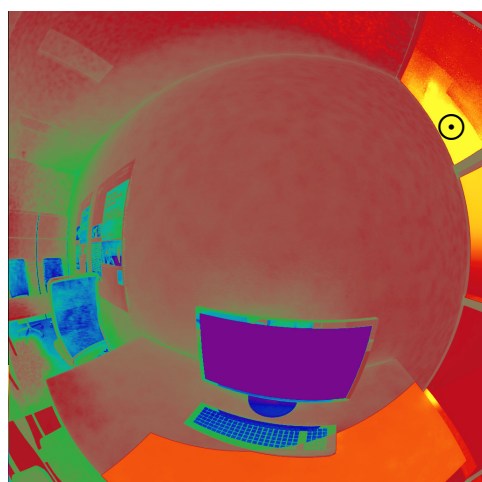
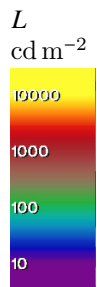
(b) BRT with peak-extraction.



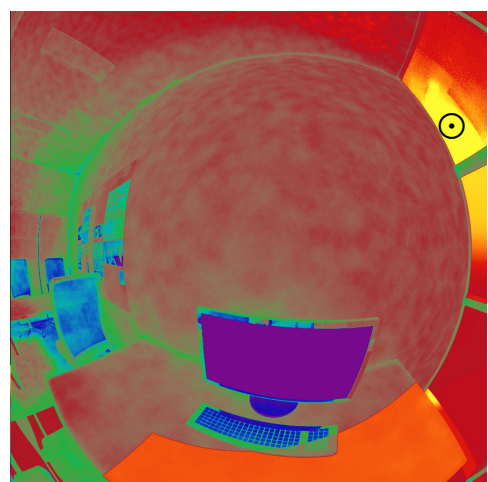
(c) Original PM, indirect photon visualization.



(d) Original PM, direct photon visualization.



(e) Modified PM, indirect photon visualization.



(f) Modified PM, direct photon visualization.

Figure 6.5: Luminance maps for view  $v_2$ .

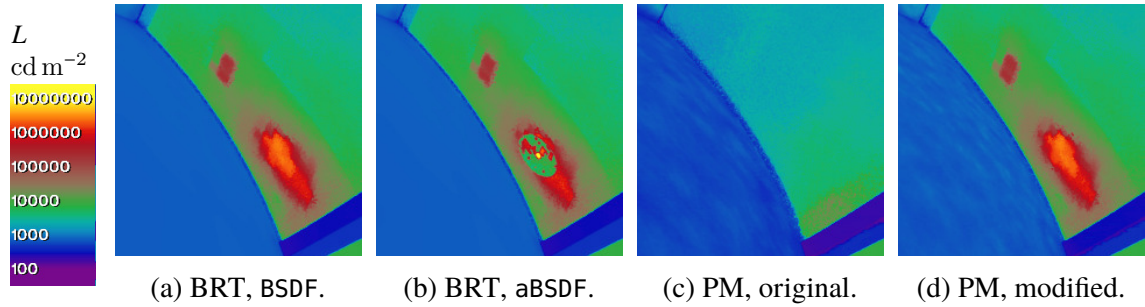


Figure 6.6: Sun seen through LCP in view  $v2$ . Note the concentration of forward scattered transmission to one direction due to peak extraction (b), and its absence with the original `PHOTON MAP` implementation (c).

highlights, the coordinates of pixels with highest  $L_{max}$  are inconsistent between Figure 6.4c and Figure 6.4d in  $v1$ , and between Figure 6.5c and Figure 6.5d in view  $v2$ . When global photons are directly visualized with the original implementations (Figure 6.4d and Figure 6.5d), regions not receiving sun-light are darker than in all other results. This can be explained by the missing contribution of diffuse sky-light, which is modelled as an extended source of type `glow` and is not accounted for in the original implementation, when indirect-diffuse sampling is suppressed in favour of the direct visualization of global photons.

The modified `PHOTON MAP` generally achieves good agreement with BRT. Figure 6.4f shows that the highest luminance in  $v1$  is found in a highlight due to reflection on the furniture when global photons are directly visualized. This is inconsistent with BRT and indirect photon visualization. Other than the original implementation, the modified `PHOTON MAP` maintains sharp boundaries of the brightly illuminated regions of the desk in  $v2$  (Figure 6.5e and Figure 6.5f). Due to the introduction of primary photons, the diffuse sky-light is accounted for. The highlight caused by the sun seen through the LCP agrees with the result of backward ray-tracing (Figure 6.6).

### 6.3.2 Quantitative comparison of imagery

The relative luminance (pixel) differences between imagery generated by the modified `PHOTON MAP` and BRT are shown in Figure 6.7 and Figure 6.8. Low-frequency photon noise is present in both views. If global photons are visualized indirectly, noise is reduced in regions with mostly diffuse illuminance (e.g. left side-wall in  $v1$ , Figure 6.7, which covers most of the background in view  $v2$ ). Noise by caustic photons (e.g. right side-wall in  $v1$ ) is not affected by the mode of photon visualization. Besides noise, bias is introduced by direct visualization of global photons, leading to linear edge-artefacts along

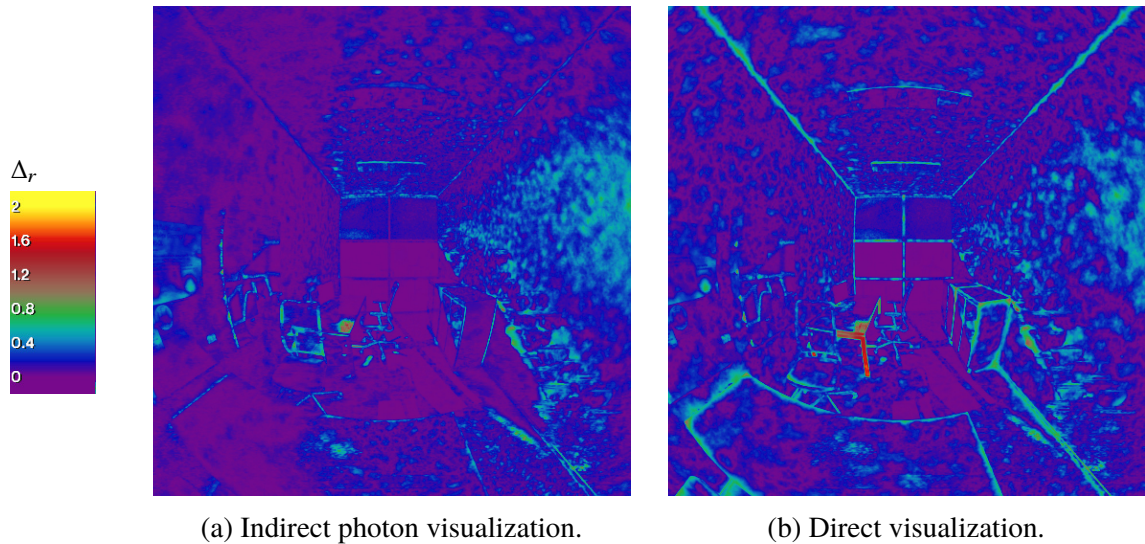


Figure 6.7: View  $v1$ : Relative differences of results by modified PHOTON MAP and BRT.

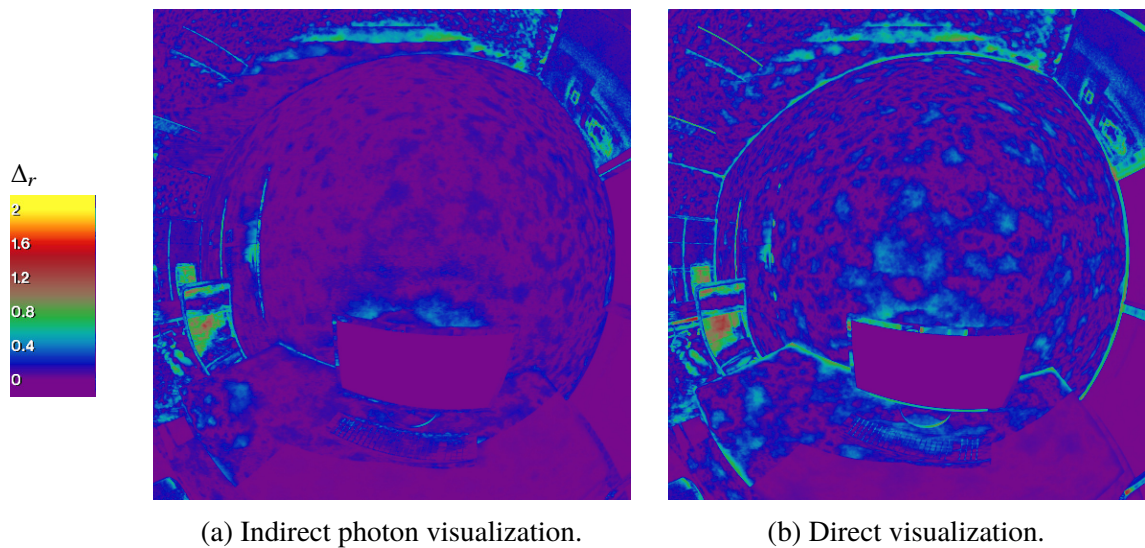


Figure 6.8: View  $v2$ : Relative differences of results by modified PHOTON MAP and BRT.

the junctions of the inner surfaces of the room (Figure 6.7b and Figure 6.8b).

The differences between the results of the two PHOTON MAP implementations are reflected by the photometric quantities calculated from the imagery (Table 6.5).

For  $v1$ , Table 6.5 shows a high degree of accordance between the photometric characteristics calculated from imagery as generated by BRT and the modified PHOTON MAP.  $L_{max}$  is identical for BRT with peak extraction and the PHOTON MAP, but lower than that by BRT without peak extraction, as could be expected since it is measured at different pixel coordinates. The original implementation of the PHOTON MAP underestimates  $L_{max}$ , which is in fact attributed to arbitrary locations on the LCP due to the omission of specular reflections of the sun, as well as all other values. Yet, the deviation in terms of eye illuminance, average luminance and solid angle of glare sources, and background

Table 6.5: Photometric quantities computed for views  $v1$  and  $v2$ . Results employing peak extraction are given in brackets. The reference (BRT) is highlighted.

Implementation	$\bar{L}$	$\tilde{L}$	$E_v$	$\bar{L}_{src}$	$\Omega_{src}$	$\bar{L}_b$	$L_{max}$
<b>View <math>v1</math> :</b>							
BRT	774	368	3471	3393	0.622	476	137114
	(716)	(336)	(3273)	(3229)	(0.620)	(445)	(107042)
PM, original	644	327	2872	2844	0.539	453	90395
PM, modified	786	413	3482	3387	0.607	495	107042
<b>View <math>v2</math> :</b>							
BRT	1786	547	1693	17530	0.478	455	3168300
	(1196)	(538)	(1625)	(9862)	(0.476)	(453)	(15358200)
PM, original	591	427	1236	3408	0.408	355	71421
PM, modified	1764	530	1634	19074	0.436	438	3168300

illuminance in  $v1$  is only moderate.

The results for  $v2$  in Table 6.5 confirm the good agreement of the modified PHOTON MAP and BRT without peak extraction. Since the  $L_{max}$  is attributed to identical coordinates here, and the visibility of the sun through the LCP is exclusively covered by BRT in both implementations, identical values for  $L_{max}$  are returned. The effect of the concentration of forward-scattered sun-light by the peak extraction algorithm leads to an extreme overestimate for  $L_{max}$ . The unmodified PHOTON MAP fails short to predict any of the listed photometric quantities. This can be explained by the predominant role of forward-scattering of sun-light in  $v2$ , which is known to be not accounted for by this implementation.

The similar values of  $\Omega_{src}$  predicted by BRT with and without peak extraction, and by the modified PHOTON MAP, indicate that the size of glare sources, which is – due to the moderate luminance threshold of  $2000 \text{ cd m}^{-2}$  – not limited to the highlights caused by specular transmission and reflection, is only moderately affected by the rendering techniques. The original PHOTON MAP underestimates the size of the glare sources in particular in  $v1$ , since it does not account for glossy reflections of the sun in  $v1$ .

### 6.3.3 Results of exemplary glare assessments

The chosen glare metrics DGP and DGI extend the photometric quantities listed in Table 6.5 to models of human response. Results for views  $v1$  and  $v2$  are listed in Table 6.6.

For  $v1$ , the modified PHOTON MAP and BRT show a very high degree of accordance. This applies to both glare metrics, and includes the faster direct visualization

Table 6.6: Glare evaluation, views  $v1$  and  $v2$ . Results with acceleration techniques (aBSDF model, direct visualization of global photons) are listed in brackets.

Implementation	$v1$		$v2$	
	DGP	DGI	DGP	DGI
BRT	• 0.40	• 22.68	• 0.38	• 18.76
(peak-extraction)	• (0.38)	• (22.37)	• (0.33)	• (17.34)
PM, original	• 0.36	• 21.85	• 0.24	• 11.87
(direct visualization)	• (0.35)	• (22.08)	• (0.22)	• (13.12)
PM, modified	• 0.40	• 22.51	• 0.38	• 18.82
(direct visualization)	• (0.39)	• (22.67)	• (0.38)	• (18.92)

of global photons. Peak extraction has a minor impact. The unmodified PHOTON MAP significantly underestimates DGP, but achieves good agreement for DGI.

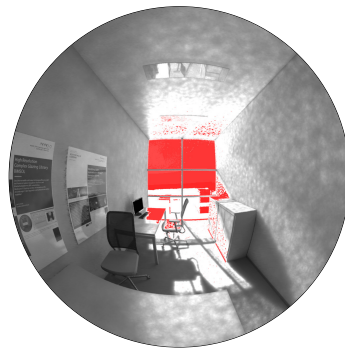
The presence of the forward-scattered image of the sun in the field of view in  $v2$  leads to almost identical results, when the glare metrics are calculated from imager by BRT and the modified PHOTON MAP. The mode of global photon visualization has no effect. The original PHOTON MAP fails to predict glare by omitting the predominant source. The impact on the luminance-driven DGI is higher than on DGP, a consequence of the drastic underestimation of the average luminance of glare sources as indicated by Table 6.5.

The application of a luminance threshold of  $2000 \text{ cd m}^{-2} \text{ sr}^{-1}$  to the images identifies approximately identical image areas as glare sources, marked red in Figure 6.9 and Figure 6.10. Note that this spatial attribution is solely based on the threshold of  $2000 \text{ cd m}^{-2}$ , and does not quantify the luminance further. The exposure to direct sun-light causes the entire upper window areas in  $v1$ , as well as the lit area of the desk to exceed the threshold, so that specular scatter is not further distinguished from the diffuse transmission and reflection background. The deflection of light toward the ceiling is above the threshold in the results of backward ray-tracing and the modified PHOTON MAP, but not the original PHOTON MAP.

The exemplary application of glare metrics gives differentiated ratings for DGP and DGI in the view toward the façade  $v1$ . According to DGP, when based on the reference as well as the modified PHOTON MAP with indirect visualization of global photons, disturbing glare is expected. Based on DGI and identical imagery, on the other hand, glare is just perceptible. When peak extraction (with BRT) or direct visualization of global photons (with the modified PHOTON MAP) are employed, both metrics indicate perceptible but not disturbing glare. This inconsistency illustrates a problem of the application of thresholds – the seemingly contradicting ratings are based on values for DGP that are almost identical, but just in the range of the threshold. The original implementation, not accounting for the highlights, gives results at the lower threshold of the perceptible but not disturbing range, thereby giving the same rating as BRT with peak-extraction and the modified PHOTON



(a) BRT.



(b) PM, original.

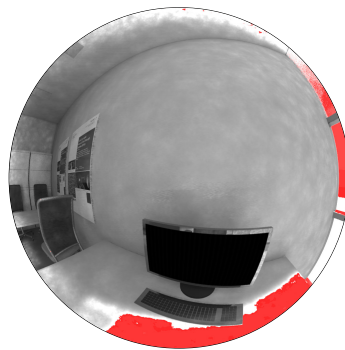


(c) PM, modified.

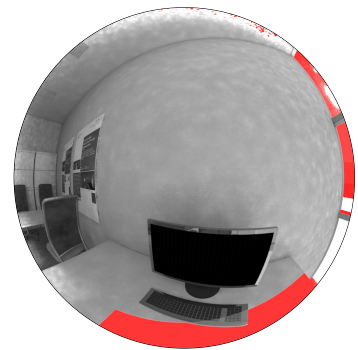
Figure 6.9: Glare sources in  $v1$  as detected by evalglare.



(a) BRT.



(b) PM, original.



(c) PM, modified.

Figure 6.10: Glare sources in  $v2$  as detected by evalglare.

Table 6.7: Duration of the simulation passes for the different simulation techniques, view  $v1$ . Results with acceleration techniques (aBSDF model, direct visualization of global photons) are listed in brackets.

Implementation	Pass 1	Pass 2	Total
<b>BRT</b>	NA	52 800 s	52 800 s
(with peak extraction)	NA	(49 320 s)	(49 320 s)
PM, original	552 s	1692 s	2244 s
(direct photon visualization)	(552 s)	(1284 s)	(1836 s)
PM, modified	696 s	1824 s	2520 s
(direct photon visualization)	(696 s)	(1332 s)	(2028 s)

MAP with direct photon visualization, although the absolute difference of the predicted DGP values is much higher. The rating for DGI is consistent for all generated imagery, indicating a low impact of the highlights in this particular view configuration.

The wall-facing view  $v2$ , with the forward-scattered sun covering an extended image region, shows a distinct difference between the reference and the modified PHOTON MAP on the one, and the original PHOTON MAP as well as BRT with peak extraction on the other hand. The former give practically identical results and predict perceptible, but non-disturbing glare. Peak-extraction leads to a clear underestimate of glare by both DGP and DGI – a surprising result, since the artefact due to the concentration of the peak leads to very high pixel values toward the sun, but reduces the average luminance of the detected light source. The original PHOTON MAP clearly underestimates glare in  $v2$ , as expected, since it does not account for the predominant glare source by forward-scattering from the sun in  $v2$ .

### 6.3.4 Initial benchmark

Table 6.7 shows the simulation times for the office scene and the BSDF model ( $v1$  as in Figure 6.4). BRT without peak-extraction requires a very high amount of sample rays in the stochastic computation to sample the transmission peak. Consequently, the computation time is  $\approx 20$  times higher than that of the modified PHOTON MAP.

The additional code triggering the disposal of caustic photons only after scattering events only slightly increases the duration of the photon distribution pass when compared to the original implementation. The purely stochastic sampling through the BSDF, on the other hand, results in strong artefacts caused by the interpolation from the ambient cache (Figure 6.4a). Peak extraction, while incapable to replicate forward-scattering, achieves a notable acceleration and reduces artefacts in the case of ideally regular scattering (Figure 6.4b).

## 6.4 Discussion

In view of the increasing interest in luminance-based metrics for visual comfort, as well as the need to visualize the effect of CFSs beyond their functional aspects, the PHOTON MAP is a promising means to leverage the benefits of data-driven models in research as well as design and planning practice. The modification of the PHOTON MAP implementation for RADIANCE allows to employ the data-driven BSDF model in the rapid synthesis of imagery that is not only visually appealing – and lacking the typical artefacts due to indirect-diffuse sampling – but also valid for the evaluated case. This is considered a crucial step toward the wider acceptance of data-driven models as a general means to replicate the irregular optical properties of CFSs.

Forward-scattering, that is not properly reflected by the original implementation of the PHOTON MAP but can contribute significantly to glare, is accurately replicated, e.g. when the sun or its specular reflections are in the field of view. This allows to employ the bidirectional algorithm to generate imagery for visual comfort and glare assessments. The original implementation, on the other hand, should not be applied in image-based visual comfort assessments, if any forward scattering may occur. Peak extraction to accelerate BRT or PM should be applied only with great care, and if the underlying assumption of ideal regular transmission holds true.

The modified PHOTON MAP achieves a high degree of accordance with BRT in glare assessments, but reduces simulation times to  $\approx 5\%$  in an exemplary single point-in-time simulation. The direct visualization of global photons promises only minor acceleration compared to the indirect visualization by one reflection, but causes artefacts that may affect not the results of visual comfort assessments, but the perceived image quality and evaluations of aesthetic aspects of CFSs. Progressive PM<sup>69</sup> can leverage the presented modification of the PHOTON MAP and may further improve image quality with data-driven models.

The PHOTON MAP lends itself not only to the simulation of light transport through geometrically modelled CFSs, but also to the efficient sampling of data-driven BSDF models showing strong directional behaviour. With the BRT algorithm of RADIANCE, such models can be only efficiently modelled if peak extraction reduces the directional peak to one direction. This technique successfully reduces computation times, but effectively loses information of the close-to-peak distribution and can lead to wrong results if non-ideal forward-scattering occurs.

A potential future application of the PHOTON MAP is to replace the calculation of the direct sun component in the 5PM to reduce the complexity of the method. This would also allow to account for non-Lambertian reflection, that may contribute to visual discomfort but is currently omitted in typical CBDM evaluations. A manuscript presenting

such a CBDM method is currently under preparation. Another potential application of the PHOTON MAP is the generation of imagery of models with static illumination, but for varying view positions and directions, since the result of the forward-distribution of photons is view-independent and can be reused.

The scalability of PM is limited since the required number of photons increases with the spatial dimensions of the model, when average photon density is kept constant. The OoC data-structure addresses this, but is not efficient with the indirect visualization of global photons. Progressive PM appears to be fields for future research to widen the scope of potential applications in daylight simulation.

## **6.5 Acknowledgements**

Thanks to my colleague Roland Schregle for his advice and guidance through the PHOTON MAP code, and to Greg Ward for discussing its modifications. Andreas Noback prepared Figure 6.3a. I am grateful to Tuğçe Kazanasmaz and Stephen Wittkopf for their valuable feed-back on my PhD research at Izmir Institute of Technology. The LCP was kindly provided by Ian Edmonds and Chantal Basurto-Dàvila.

## **6.6 Funding**

This research was supported by the Swiss Innovation Agency Innosuisse under grant #1155000149 as part of the Swiss Competence Center for Energy Research SCCER FEEB&D.

## CHAPTER 7

# PHOTON-MAPPING IN CBDM WITH HIGH-RESOLUTION BSDFs

*This section is identical to the author's revised manuscript, which has been conditionally accepted (subject to minor revisions) for publication.*

“Photon-Mapping in Climate-Based Daylight Modelling with High-Resolution BSDFs”  
Grobe, L. O. *Energy and Buildings* **accepted**

---

### 7.1 Introduction

The new European standard for daylight in buildings<sup>23</sup> sets requirements for *daylight provision, view, sunlight exposure, and glare protection* as the key aspects of daylight performance. The aim of daylighting is thereby extended from supplementing electrical lighting as a means to reduce demand of electrical energy, to the reconciliation of daylight utilization as a resource, and the moderation of its negative effects on visual comfort. The latter is directly related to the operation of glare controls and artificial lighting, and therefore the electrical energy demand of buildings.<sup>7</sup> Consequently, planning and assessing the utilization of daylight in buildings cannot solely rely on measures of daylight provision by illuminance-based performance metrics.<sup>27,33</sup> The holistic assessment of daylight performance, including visual comfort and glare, rather calls for luminance-based performance metrics.<sup>38,41,158</sup>

#### 7.1.1 Climate-Based Daylight Modelling in visual comfort assessments

The increase of efficiency, model variability, and accuracy are objectives that drive the ongoing evolution of Climate-Based Daylight Modelling (CBDM) techniques.<sup>54,159</sup>

The *efficiency* of Daylight Coefficient (DC) calculations in the generation of time-series data in daylight simulation is a fundamental premise for the application of CBDM.<sup>32</sup> The computationally elaborate simulation of light propagation, e.g. by ray-tracing, solved not for absolute quantities such as luminance  $L$  or illuminance  $E$ , but rather the contribution of a defined region of the sky dome to the quantity. The partition of the continuous sky hemisphere into a discrete set of sky regions is defined by a directional basis. The Scaling and summation of the individual contributions allows the simulation of different sky conditions. The isolation of variable sky conditions, which can be rapidly calculated from few measured parameters, and light transport in a building model, which is invariant but elaborate to simulate, allows to compute sensor data as well as images at any temporal resolution. The light simulation suite `RADIANCE` supports DC calculations with the dedicated ray-tracing program `rcontrib`.

*Variability* in terms of fenestration models is increased by the Three-Phase-Method (3PM). It splits the simulation of light transport before and after transmission through an interchangeable, data-driven fenestration model.<sup>35</sup> The 3PM aims at the efficient modelling of multiple states (e.g. open – closed, horizontal – tilted, clear – tinted) of a fenestration system, or at modelling design variants with different Complex Fenestration Systems (CFSs) that can then be compared. The 3PM has been integrated in building performance simulation, such as `OPENSTUDIO`<sup>160</sup> or `IDA ICE`.<sup>161</sup>

The 3PM models the distribution of light transmitted by the fenestration, as well as the distribution of light emitted by the sky, at low directional resolution of  $\approx 10^\circ$ . This leads to an accuracy that is considered sufficient to predict daylight supply, but cannot accurately model sun-light in image-based visual comfort assessments.<sup>36,37</sup> `DAYSIM` employs a refined model of sun-light by interpolation between 65 sparse, but narrow sun arranged along sun-paths that depend on the location, or a refined solar model of 2305 positions.<sup>162</sup> A similar separation of sky- and sun-light is achieved by the *Four Component Method*.<sup>163</sup> Its directional basis is agnostic to the particular sun-path for a given location, but denser with 2056 or 5035 positions.<sup>164</sup>

The Five-Phase-Method (5PM) aims to maximize accuracy by combining a 3PM calculation of diffuse sky-light and indirect sun-light with a refined DC calculation of the direct solar component.<sup>52,53</sup> A sky model comprising typically 5185 distant, narrow sources mimics the high directionality of the sun since it agrees with its apparent angular diameter ( $\approx 0.5^\circ$ ). Interpolation error is minimized due to the density of the model. The fenestration is represented either by a detailed geometric model, or by a refined data-driven model that achieves high directional resolution of  $\approx 1.4^\circ$ . Light propagation from the sun (not the diffuse sky) through the fenestration to the first intersection with a diffusely reflecting, interior surface is computed employing this refined model. Accordingly, this segment is removed from the results of the 3PM by subtraction of the result of a second 3PM run with only one inter-reflection and a sun-only sky model.

While removal of this segment – ”direct“ if light propagation prior to transmission through the fenestration is not considered – is easily achieved, the computation of its refined replacement with RADIANCE is problematic. Since deterministic ray-tracing through the fenestration would account only for regular transmission, the backward ray-tracing algorithm has to generate random samples that intersect with the fenestration, and then spawn shadow rays toward the light sources. Unfortunately, the implementation in RADIANCE does not allow to restrict the generation of such ”secondary shadow rays“ to intersections with the fenestration, but also applied it to reflective interior surfaces that are equally reached by the random rays. The 5PM avoids this unwanted inter-reflection by a work-around, that requires to modify the model. Light propagation between fenestration and first subsequent intersection is computed indirectly by multiplication of the illuminance distribution in a model where all surfaces have zero reflectance, with a Lambertian *reflectance map*. As outlined in 7.5, this leads to a complex sequence of 3PM and DC simulations, intermediate model modifications, and pixel-wise image operations that comprise image generation with the 5PM. Unfortunately, this complexity of the 5PM has so far hindered its wider adoption as well as its integration in front-ends.

While the aforementioned approaches aim to increase the general accuracy of imagery, enhanced simplified Daylight Glare Probability (DGP) aims at matching image generation to the particular sensitivity of one particular glare metric, DGP.<sup>49</sup> DGP depends on four input variables, the eye illuminance  $E_v$ , and the luminance, solid angles and position indices of all  $n$  detected glare sources  $L_{s,n}$ ,  $\omega_{s,n}$ ,  $P_{s,n}$ .<sup>45</sup> Illuminance, in particular by diffuse sky-light, can be efficiently solved by the 3PM.<sup>36,37</sup> All but  $E_v$  and to some extent  $P_{s,n}$  are sensitive to the directional resolution of sky and fenestration models, but can be attributed to specular reflection and regular transmission in a typical architectural context, and lend themselves to fast deterministic ray-tracing. While constrained to the DGP metric, the method allows for fast glare assessments including multiple view points and directions.<sup>165</sup> A similar separation of diffusely scattered and regularly transmitted light in daylight simulation coupling radiosity with ray-tracing has been proposed for quasi real-time glare assessments for the control of Venetian blinds.<sup>166</sup>

### 7.1.2 Data-driven modeling of CFSs

Matrix-based daylight simulation techniques share a general, data-driven model of the fenestration’s Bidirectional Scattering Distribution Function (BSDF), that can be populated either by measurements or by computational means.<sup>55,141,143,167</sup> Such models act as a “black box”, rather than describing the often complex optical mechanisms causing an

effect on light scattering, they externalize this complexity and just look up and interpolate the contained data. Similar to the partition of the sky in CBDM, a directional basis is required to translate the continuous distribution into a set of coefficients. The fenestration model of the 3PM emerged from solar heat gain calculations and has a low directional resolution of 145 incident and 145 outgoing directions as defined by the *Klems basis*.<sup>34</sup> An asymmetric directional basis combining 145 incident with 1297 outgoing directions was proposed by the International Energy Agency for daylighting applications<sup>16</sup> and has been implemented in RADIANCE.<sup>80</sup> Since further refinement of the directional basis leads to an exponential increase of model size, RADIANCE implements the *tensor tree* of locally adaptive resolution. This compact data-structure achieves a high directional resolution of  $\approx 1.5^\circ$  for anisotropic, and even higher resolution for isotropic scattering.<sup>51</sup>

The calculation of the direct solar component in the 5PM relies on stochastic backward sampling.<sup>168</sup> Only a high density of random rays, originating from the receiver surface and reaching the data-driven model of the CFS, ensures that the narrow solar angle of the sun is reached. The *BSDF proxy* not only adds visual detail such as shadow-patterns and the fenestration geometry, but moves regular transmission through CFS, into the domain of fast deterministic ray-tracing.<sup>169</sup> *Peak extraction* triggers deterministic ray-tracing if regular transmission is identified as a distinct peak in the distribution<sup>142</sup> and achieves good results even with low-resolution BSDF, but is limited to the case of regular transmission with no significant forward scattering.

### 7.1.3 Daylight simulation with the PHOTON MAP

The PHOTON MAP extension of RADIANCE primarily targets modelling of reflective and refractive devices that deflect or concentrate light.<sup>154</sup> The bidirectional algorithm distributes particles forward – originating from the light sources – in a geometric model, and records their collisions with diffusely scattering surfaces. The density of photons is then evaluated as an estimate of local illuminance to solve for diffuse reflection and transmission. As any forward rendering technique, the algorithm is efficient in accounting for small or highly directional light sources. To reduce visible artefacts due to the inherent bias and noise introduced by photon mapping, illuminance can be evaluated indirectly by one indirect-diffuse reflection. Full support for data-driven BSDF models has been implemented in the PHOTON MAP in recent releases of RADIANCE.<sup>152</sup>

*Contribution photons* are linked to their original light source and allow applications of the PHOTON MAP in DC calculations. To account for each light source, for which a coefficient shall be generated, by a sufficient number of photons, the total amount of photons

in the contribution photon map has to increase with the directional resolution of the sky model. The resulting photon map therefore grows significantly when refined sky-models of high resolution are employed. An Out-of-Core (OoC) data-structure allows to exceed the limits of installed memory. Efficient evaluation of local illuminance is provided by a *photon cache*. It employs a spatial data-structure and loads photons in blocks representing voxels of an octree, efficiently reducing storage access when photons are gathered for a sequence of adjacent locations.<sup>70</sup>

DC calculations with the PHOTON MAP and data-driven BSDF have been employed in daylight performance assessments by the illuminance-based metrics spatial Daylight Autonomy and Annual Sunlight Exposure.<sup>27,84,153</sup> Based on a recent modification of the PHOTON MAP,<sup>58</sup> the presented work extends the application of the PHOTON MAP in CBDM to image synthesis for visual comfort assessments employing luminance-based metrics.

#### 7.1.4 Objectives

A CBDM technique for image synthesis is developed, tested, and demonstrated. The method shall

- allow efficient sampling of arbitrary data-driven BSDF as well as geometric models of CFSs,
- reduce complexity when compared to the 5PM to support its applicability, yet
- achieve the high accuracy of the 5PM.

To test the validity of the method, its result shall be compared to backward ray-tracing for one exemplary time-step (with `rt race`) as well as the annual results of the 5PM (employing `r contrib`). Effects of data-driven modelling shall be tested by comparison of results achieved by the new method with data-driven BSDF models, and geometric models of an exemplary CFS.

Finally, the simulation technique is demonstrated in an exemplary comparative performance assessments of two CFSs employing the glare metrics Daylight Glare Index (DGI) and DGP.

## 7.2 Method

Photon mapping is particularly efficient in the simulation of light propagation constrained either by the size or the directionality of light sources. In these cases, relatively few samples emitted from the source account for the bulk of the luminous flux. Sending random rays backward, on the other hand, requires a very high sampling resolution to ensure that such sources are accounted for. This is the reason why the solar component in the 5PM is computed without internal inter-reflections, and with a modified model of the evaluated space comprising – besides the fenestration – only Lambertian surfaces. The computation of the solar component employing the `PHOTON MAP`, on the other hand, can rely on the unmodified model.

### 7.2.1 Refined computation of the solar component

Sky and fenestration are modelled just as for the 5PM. The refined sky model comprises distant sources with the true angular diameter of the sun ( $\approx 0.5^\circ$ ). A *Reinhart sky* discretization with  $6 \times 6$  subdivisions is chosen, leading to 5184 sun positions. The fenestration is represented by a data-driven BSDF model<sup>1</sup>. The BSDF is stored in a tensor-tree structure with the initial resolution set to the current maximum of  $128 \times 128$  incident, and equal number of outgoing directions.

*Photon emission* is performed by the `RADIANCE` program `mkpmap`. Due to the high number of light sources, a high target of *4G contribution photons*<sup>2</sup> is set. For the given sky model, this results in a theoretical average of  $4G/5184 \approx 772K$  photons per light source. The effective number of photons per light source will be higher, since sun positions that are not visible from the fenestration do not contribute and increase the weight of the other sun positions. Since the memory required to store 4G photons exceeds the resources on typical hardware, the OoC implementation of the `PHOTON MAP` is applied<sup>3</sup>. Photons are visualized directly to make efficient use of the *photon cache*.

---

<sup>1</sup>Although not in the focus of this work, the `PHOTON MAP` supports geometric modelling of CFSs just as well.

<sup>2</sup>In this text, *G* stands for 1 000 000 000, *M* for 1 000 000, and *K* for 1000.

<sup>3</sup>This requires to set the switch `-DPMAP_OOC` at compile-time.<sup>170</sup>

Following photon emission, a DC calculation is performed. Hourly imagery  $\mathbf{I}_{sun}$  is generated by folding daylight coefficients  $\mathbf{DC}_{sun}$  with custom sky vectors  $\mathbf{S}_{sun}$ , as generated with genskyvec<sup>4</sup>:

$$\mathbf{I}_{sun} = \mathbf{DC}_{sun} \times \mathbf{S}_{sun} \quad (7.1)$$

Parameters for `mkpmap` and `rcontrib` are listed in Table 7.8 in 7.7.

This approach maintains the high directional resolution, that is achieved by the 5PM only for the first two segments of light propagation between sky model and fenestration, and between fenestration and first interior surface, along the entire path of light propagation over multiple reflection and transmission steps.

### 7.2.2 Three-Phase Method calculation of diffuse sky

The luminance distribution of the sky hemisphere, excluding the sun and the circumsolar region, is characterized by a low gradient. This allows, just like in the 5PM, to employ the 3PM in the computation of the diffuse sky component without loss of accuracy. Light paths are split and stored in separate matrices:

**V**, the view matrix connecting view point and fenestration,

**T**, the transmission matrix representing the fenestration by its low-resolution BSDF,

**D**, the daylight matrix accounting for exterior inter-reflections and shading, and relating the fenestration BSDF to the sky discretization, and

**S<sub>sky</sub>**, the diffuse sky matrix, comprising the hourly luminance averages of sky elements, excluding the sun, for one year.

The diffuse sky component is then computed by multiplication of the four matrices, leading to a matrix of positions and time-steps  $\mathbf{E}_{sky}$  in the case of sensor signals, or pixel-indices and times-steps  $\mathbf{I}_{sky}$ , stored as a sequence of images in the case of image-generation:

$$\mathbf{I}_{sky} = \mathbf{V} \times \mathbf{T} \times \mathbf{D} \times \mathbf{S}_{sky} \quad (7.2)$$

---

<sup>4</sup>The diffuse sky is excluded (switch -d), the subdivision of the sky refined (-m 6), and the luminance of the sky element is scaled according to the angular diameter of the sun (-s - .533).

Note that diffuse sky-light can be computed directly in one pass and without model modifications, while the 5PM requires the sum of diffuse sky-light and reflected sun-light.

In cases when the evaluated space is illuminated by fenestration comprising zones of different configurations, or apertures that are oriented toward different directions, these are grouped into *window groups* and calculated separately, just as common practice in applications of the 3PM. The 3PM calculation of diffuse sky-light is implemented by backward ray-tracing with the RADIANCE programs `rfluxmtx`, `gendaymtx`, and `dctimestep`.

### 7.2.3 Adding fenestration's visual detail

Under perfectly diffuse illumination, the fenestration would be represented only by the result of the 3PM, which is solely based on the low-resolution data-driven BSDF. Even with diffuse sky conditions, visible geometry of the system may contribute significantly to the visual information and potentially affect visual comfort. A separate DC calculation is therefore performed in analogy to Equation 7.1, but employing backward ray-tracing and sky vectors excluding the direct sun component, only for the image region covered by the fenestration. If available, a geometric model of the fenestration is used with a moderately refined model of the diffuse sky. The resulting imagery  $\mathbf{I}_{sky, fen}$  is masked, and replaces the visible fenestration resulting from the 3PM simulation of the diffuse sky component.

### 7.2.4 Composition of hourly images

Hourly imagery is composed by simple summation of the component imagery  $\mathbf{I}_{sun}$ , and  $\mathbf{I}_{sky}$  or  $\mathbf{I}_{sky, fen}$  for each time-step  $n$ :

$$\mathbf{I}_n = \mathbf{I}_{sun, n} + \begin{cases} \mathbf{I}_{sky, n} & \text{non-fenestration} \\ \mathbf{I}_{sky, fen, n} & \text{within fenestration} \end{cases} \quad (7.3)$$

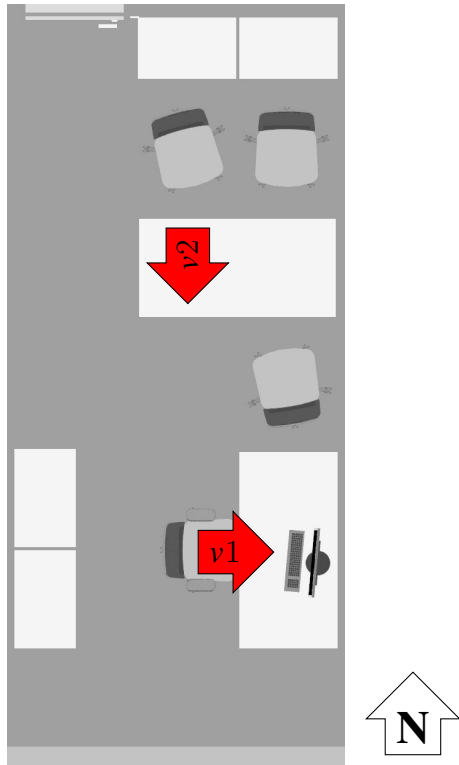


Figure 7.1: Cellular office and view points  $v1$ ,  $v2$  employed in the exemplary evaluation of the proposed CBDM technique.<sup>57</sup>

Table 7.1: Configurations of fenestration systems  $FS1$  and  $FS2$ .

	$FS1$	$FS2$
$wg1$	$CFS1$ deflecting blinds	$CFS3$ redirecting film
$wg2$	$CFS2$ retro-reflecting blinds	$CFS4$ glass, shading
$wg3$	$CFS2$ retro-reflecting blinds	$CFS4$ glass, shading

## 7.2.5 Cases to test and demonstrate the method

The proposed CBDM technique is applied to the model of an exemplary, South-facing cellular office (Figure 7.1).<sup>57</sup> The simulations are performed based on weather data of a representative meteorological year for Izmir, Turkey, at hourly intervals. The façade is vertically divided into three window zones (Table 7.1). The upper zone, later on referred to as window group  $wg1$ , is located above the eye level of a sitting or standing occupant and assumed to be most effective in the admission of daylight.  $wg2$  is supposed to provide a view to the outside, but to be less important for daylight supply.  $wg3$  is below the work plane level and therefore does not significantly contribute to daylight illumination. Depending on the building context, it may provide a visual connection to the outside, and it has to be accounted for in glare evaluations due to possible reflections.

Two fenestration systems  $FS1$  and  $FS2$ , featuring typical properties of CFSs such as directional selectivity irregular transmission, are evaluated in the exemplary application of the proposed CBDM.

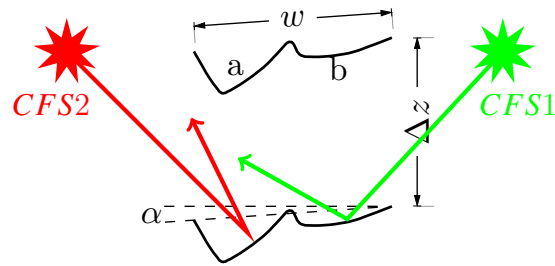


Figure 7.2: Profiles of *FS1*. In *CFS1*, segment *b* points outward and deflect sun-light upward. In *CFS2*, segment *a* of the flipped profile retro-reflects sun-light in summer.

### 7.2.5.1 FS1: Static retro-reflecting fenestration

Fenestration system *FS1* features highly specular slats featuring a complex geometric profile illustrated by Figure 7.2<sup>5</sup>. The slats of width  $w = 12$  mm have a vertical distance of  $\Delta z = 10$  mm, and are tilted toward the outside by  $\alpha = 4^\circ$ . They comprise a retro-reflection component (*a*) and an attached light-shelf (*b* in Figure 7.2). The configuration of the system in *wg1*, *CFS1*, deflects incident sun-light upward. In *wg2* and *wg3*, configuration *CFS2* retro-reflects sun-light to reduce glare and solar gains. It maintains a view to the outside due to the particular profile of the slats allowing an almost horizontal orientation.<sup>68,171</sup> The system is chosen as an example that allows both geometric and data-driven modelling.

Geometric models of *CFS1* and *CFS2* are set up by extrusion of the slats' profiles. The upper surface is assumed to act as an almost perfect mirror (reflectance  $\rho = 0.94$ , specular reflectance  $\rho_s = 0.85$ ). Semi-specular reflection is attributed to the lower side ( $\rho = 0.85$ ,  $\rho_s = 0.17$ ). To ensure equivalency of geometric and data-driven models, latter are derived from former by genBSDF. For maximum accuracy of the data-driven model, the initial resolution of the tensor tree before data-reduction is set to  $128 \times 128$  incident and outgoing directions (Table 7.6 in section 7.6).

### 7.2.5.2 FS2: Redirecting film with operated shading

Fenestration system *FS2* employs an adhesive prismatic film on a clear glass substrate, *CFS3*, that is applied only to *wg1*. Its micro-structure redirects incident light upward toward the ceiling. The lower window zones *wg2* and *wg3* are equipped with a retractable roller-shade, *CFS4*, that is assumed to be operated according to the visual comfort conditions in the attached room. Figure 7.3 shows the dense structure of the fabric.

<sup>5</sup>RetroLuxTherm 12 mm louvers for daylight control, patent Helmut Köster.

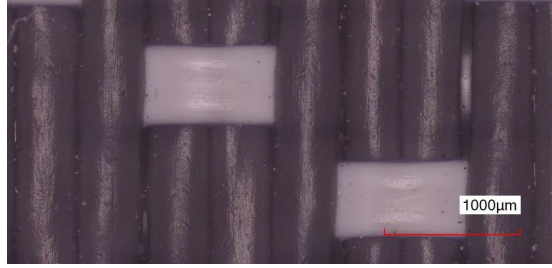


Figure 7.3: Dense fabric of *CFS4* as employed in *FS2*.

Its normal-hemispherical transmission  $\tau_{nh}$  and reflection  $\rho_{nh}$  for the inside (subscript *int*) and outside (subscript *ext*) are listed in Table 7.2<sup>6</sup>. Note that these properties refer to visible light (subscript *v*).

The BSDFs of *CFS3* and *CFS4*, are gonio-photometrically measured and compiled into RADIANCE tensor-tree models. The maximum directional resolution for anisotropic models of  $128 \times 128$  incident and outgoing directions is applied to *CFS3*. For *CFS4*, an isotropic representation is chosen to further increase the directional resolution to  $512 \times 512$  directions (Table 7.7 in section 7.6).

## 7.2.6 Testing the validity of the method with geometric and data-driven fenestration models

Testing the validity of the proposed CBDM technique aims to identify and explain deviations in the results of glare assessments. To account for the particular sensitivity of such assessments to different kinds of errors introduced by the modelling and image generation techniques, not only the imagery is compared but also the results of glare assessments for an exemplary view (*v1* in Figure 7.1). The test aims at different aspects of the modelling and simulation method:

1. The general applicability of data-driven modelling, effectively replacing geometrical detail and non-uniformity of the CFS by its average transmission characteristics, is verified. This test is implemented by the comparison of annual glare assessments employing the geometric model of *FS1* with that employing a data-driven model generated from the geometric model.
2. From the results of annual simulations with geometric and data-driven models of *FS1*, the time-step with the highest disagreement in terms of DGP is identified. The images

<sup>6</sup>The reflection properties are derived from measurements of the BSDF under an oblique incident angle  $\theta_i = 30^\circ$ , to avoid partial shadowing of the reflected peak by the detector.

Table 7.2: Optical properties of the fabric employed in *CFS4*.

$\tau_{v,nh}$	$\rho_{v,nh,ext}$	$\rho_{v,nh,int}$
0.014	0.438	0.241

Table 7.3: Thresholds applied to DGP and DGI.

Rating	DGP	DGI
• Imperceptible	< 0.35	< 0.18
• Perceptible	< 0.40	< 0.24
• Disturbing	< 0.45	< 0.31
• Intolerable	> 0.45	> 0.31

generated from geometric and data-driven models for this time-step are compared, and possible reasons for deviations are investigated.

3. For the same time-step, that is considered to represent a problematic sky condition, the results achieved by the proposed CBDM technique – employing the PHOTON MAP – is compared to reference imagery generated by backward ray-tracing, which is considered ground truth. The images are quantitatively analyzed using *evalglare*<sup>7</sup> and *pextreme*. This test is performed with the geometric and data-driven models of *FS1*, as well as data-driven modelling of *FS2*.

## 7.2.7 Demonstration of the method

The applicability of the method is demonstrated in an exemplary glare study for a cellular office. The generated annual imager is compared to the results of the 5PM.

### 7.2.7.1 Exemplary glare assessment

The results of the annual simulations with *FS1* and *FS2* are evaluated and compared. For *FS1*, the annual results of both geometric and data-driven models are presented. For *FS2*, the effective annual glare probability is quantified by combining the results of the fenestration with clear glazing in *wg2* and *wg3* if  $DGP < 0.40$ , and otherwise assuming a closed shading. The annual frequency of glare conditions and 95 percentile<sup>8</sup> DGI and DGP are analysed by histograms. The thresholds reported in Table 7.3<sup>115</sup> are applied to rate the exemplary cases according to the calculated glare metrics<sup>9</sup>.

<sup>7</sup>A fixed luminance threshold of  $2000 \text{ cd m}^{-2}$  is set in the detection of glare sources.<sup>44</sup>

<sup>8</sup>The comparison of percentiles follows standard procedures for the evaluation of glare by daylight<sup>23</sup>

<sup>9</sup>DGP thresholds, referenced by,<sup>23</sup> have been adjusted recently.<sup>172</sup>

### 7.2.7.2 Comparison with the Five Phase Method

The results of the PHOTON MAP based annual simulation are contrasted with those of the 5PM. The office model with *FS2*, but a view point facing the façade is chosen (*v2* in Figure 7.1). The sun, when at low altitudes in the South, is expected to cause a highlight on the glossy surface of the desk. Hourly imagery is generated employing CBDM with the PHOTON MAP and the established 5PM. DGP is applied to the results, and the time-step showing the highest deviation is analysed in detail.

## 7.3 Results and discussion

After testing the validity of the proposed method applied to geometric and data-driven modelling of the fenestration, the result of an exemplary application of CBDM employing Photon Mapping (PM) are presented and discussed.

### 7.3.1 Results of CBDM with geometric modelling for one time-step

Figure 7.4 a-c show imagery  $\mathbf{I}_{sky,wg}$  for one time-step (January 1st, 1:30 p.m.), representing the diffuse sky component as admitted through the three window groups of *FS1*. The images are technically generated employing the 3PM with a diffuse-only sky vector. Their sum is the combined sky component image  $\mathbf{I}_{sky}$  (Figure 7.4 d). Note that the patches of the coarse directional basis as employed in the 3PM are visible in the image region covered by the fenestration. These artefacts do not occur in  $\mathbf{I}_{sky,fen}$  (Figure 7.4 e), the result of a refined DC calculation constrained to the directly visible fenestration.

The direct solar image component  $\mathbf{I}_{sun}$  for the time-step is shown in Figure 7.4 f). Due to the direct visualization of contribution photons, low-frequency photon noise is apparent in regions not exposed to directionally transmitted sun-light. High-frequency pixel noise occurs in image regions where direct sun-light, accounted for by backward ray-tracing, reaches diffuse surfaces. Deflected sun-light causes visible caustics along the wall adjacent to the fenestration, as well as on the ceiling.

The time-step image  $\mathbf{I}$  (Figure 7.6 a), composed from  $\mathbf{I}_{sky}$ , and  $\mathbf{I}_{sky,fen}$  or  $\mathbf{I}_{sun}$ , is contrasted with the results of backward ray-tracing in Figure 7.6. While Figure 7.6 a) and c) show a good overall accordance, artefacts are apparent. Figure 7.6 a) inherits the

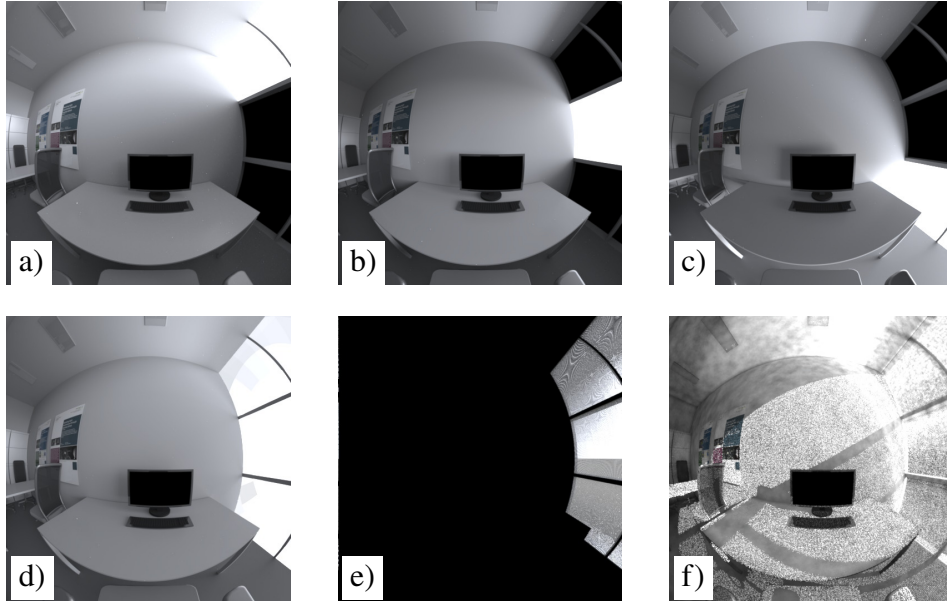


Figure 7.4: Top: Diffuse sky components  $I_{sky,0}$ ,  $I_{sky,1}$ ,  $I_{sky,2}$  contributed by three window groups of  $FS1$  (a-c). Bottom: Combined diffuse sky component  $I_{sky} = I_{sky,0} + I_{sky,1} + I_{sky,2}$  (d), refined DC computation of the fenestration under diffuse sky-light  $I_{sky, fen}$  (e), and solar component  $I_{sun}$  (f). Only  $I_{sun}$  (f) is computed by photon-mapping.

low-frequency photon noise and high-frequency pixel noise from Figure 7.4 f). Figure 7.6 c), on the other hand, shows the cloud-alike artefacts of the ambient cache in regions where the illuminance gradient is high, e.g. the ceiling adjacent to the fenestration. Since Figure 7.6 c) is down-sampled from a higher pixel resolution, high-frequency pixel noise is reduced. Consequently, the shadow pattern of the slats of the CFS is clearly pronounced.

### 7.3.2 Results of CBDM with data-driven modelling for one time-step

The diffuse sky component in Figure 7.5 a) is identical to that in Figure 7.4 d). The fenestration component  $I_{sky, fen}$  in Figure 7.5 b) lacks the linear structures caused by the slats comprising  $FS1$ , but otherwise agrees with the fenestration component resulting from the geometric model Figure 7.4 e).

The direct solar component Figure 7.5 c) differs from that by geometric modelling (Figure 7.4 f) in that the high-frequency pixel noise on the wall is replaced by low-frequency photon noise. This can be explained by the fact that the directional transmission through the data-driven BSDF, other than the geometric model, is accounted for by contribution photons. Since photon density is relatively low in this image region, due to the shading effect of the CFS, noise becomes apparent. Consequently, on surfaces with high photon density, such as the caustics on the wall close to the fenestration and the ceiling, photon

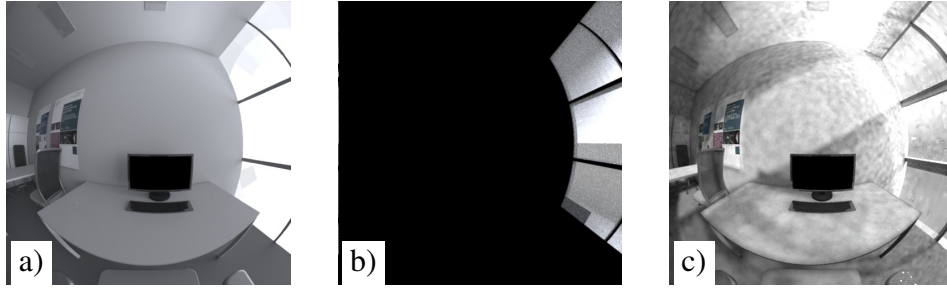


Figure 7.5: Combined diffuse sky contribution  $I_{sky}$  (a), backward DC computation of the fenestration  $I_{sky, fen}$  (b), and photon-mapping computation of the solar component  $I_{sun}$  through  $FS1$  (c). While a) is identical with Figure 7.4 d), the latter two are based on data-driven modelling.

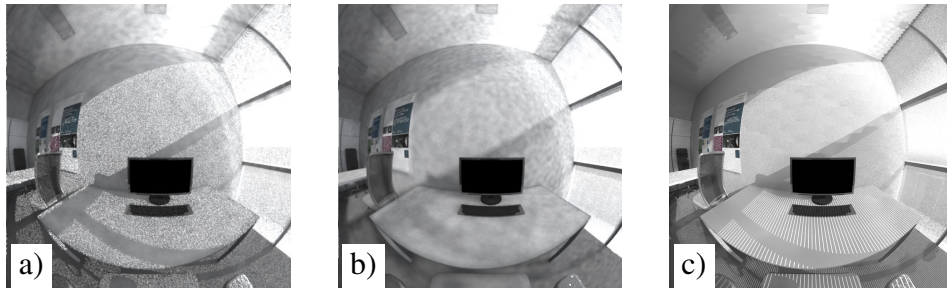


Figure 7.6: Results of the proposed CBDM technique employing the PHOTON MAP with geometric (a) and data-driven (b) models of  $FS1$ , compared to the reference by backward ray-tracing (c). Corresponding solid angles of potential glare sources ( $L \geq 2000 \text{ lm m}^{-2} \text{ sr}^{-1}$ ) are 1.29 sr (a), 0.94 sr (b), and 1.94 sr (c).

noise decreases. The distinct shadow of the framing on the desk, as in Figure 7.6 a) and c), is less pronounced in Figure 7.6 b) due to bias. This can be attributed to the low photon density on surfaces where the sun is effectively blocked by the CFS configuration of the lower window zones.

### 7.3.3 Testing validity for one time-step

Testing the validity of the proposed CBDM technique for visual comfort assessments has to distinguish errors introduced by the method from those related to the modelling technique.

First, the impact of the data-driven modelling is assessed by comparing the results of data-driven and geometric modelling of  $FS1$  for the time-step showing the highest deviation of DGP (subsubsection 7.3.3.1). Second, the results of the proposed CBDM technique for this time-step (subsubsection 7.3.3.2, subsubsection 7.3.3.3 and subsubsection 7.3.3.4) are compared in detail to backward ray-tracing to test the simulation technique. Third,

extending the test from one time-step to annual simulation, the results of a comparison of CBDM employing the PHOTON MAP with the 5PM are presented in subsubsection 7.3.3.5.

All presented tests aim at an annual rating of glare, measured by DGI and DGP according to the classification listed in Table 7.3. These metrics rely on the accurate detection and quantification of glare sources, characterized by high luminance, and the integration over the field of view evaluating to eye illuminance  $E_v$ . Artefacts such as photon noise, which may be problematic e.g. in visualizations, are expected to have minor effect on the selected metrics since they affect mostly darker image regions<sup>10</sup>. Consequently, the presented results do not allow conclusions on the applicability of the method for any applications other than glare assessments.

### 7.3.3.1 Identification of a problematic time-step

The DGP metric is applied to the results of annual simulations employing both modelling techniques with *FS1*. The annual distributions of DGP, based on the geometric and data-driven models, are illustrated as heat-maps in Figure 7.7 and Figure 7.8. While these show a high degree of accordance over most of the evaluation period, the two modelling techniques lead to obvious differences for late morning hours in March (marked by white frames on the heat-maps).

Hourly values of DGP and  $E_v$  on March 12th, which has the highest deviation between geometric and data-driven models, are shown in Figure 7.9. The two curves, labelled *geo* for geometric, and *dd* for data-driven modelling, illustrate the impact of the modelling technique on the results of the new CBDM technique for one day. The significant mismatch with the reference (labelled *ref*) for the given day is limited to one time-step at 11:30 am.<sup>11</sup> The record of the weather file that corresponds to this time-step, shown in Figure 7.4, indicates sunny sky conditions. The sun, although shaded by the CFSs, is in the field of view. The luminance distribution of the sky for this time-step is calculated by `gendaylit`. Reference images are rendered for both CFSs by backward ray-tracing. Oversampling in the image domain, and the use of proxy geometry complementing the data-driven BSDF model of *FS1*, aim to reduce rendering artefacts. A linear false-color scale is applied to illustrate the luminance values. The reference images are shown in Figure 7.10 (a) for *FS1*, and Figure 7.13 (a) for *FS2*. Average  $\bar{L}$ , median  $\tilde{L}$ , and maximum luminance  $L_{max}$ , eye illuminance  $E_v$ , glare metrics DGP and DGI, and the sum the solid angles of the detect glare sources  $\omega_s$  of the reference images are reported in rows 1 and 5 of Table 7.5.

<sup>10</sup>This assumption may not hold true in cases when the average luminance of such regions would reach the threshold of  $2000 \text{ lm m}^{-2} \text{ sr}^{-1}$

<sup>11</sup>The refined approach leading to curve *geo+os* is explained in subsubsection 7.3.3.2.

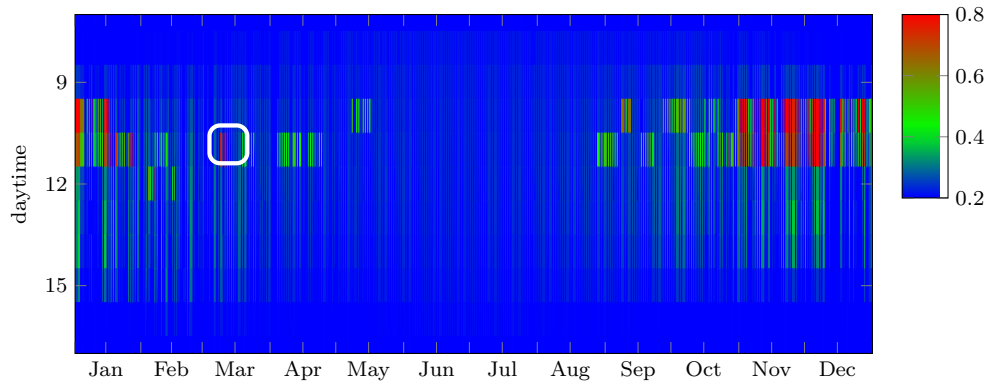


Figure 7.7: Annual distribution of DGP by geometric modeling of *FS1*.

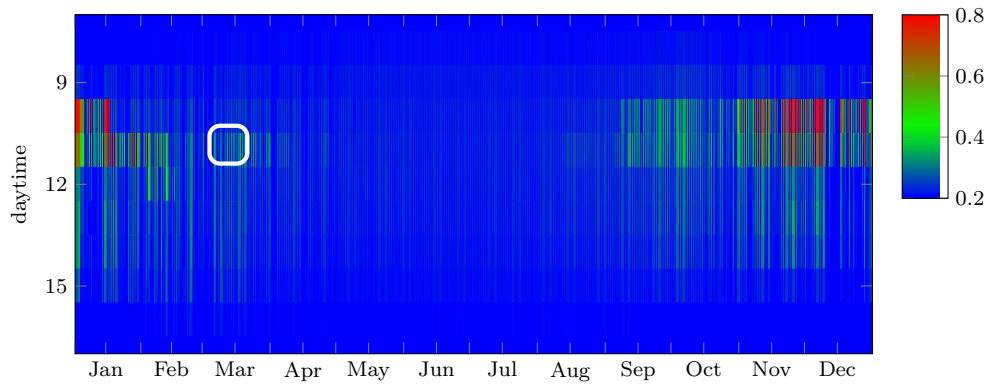


Figure 7.8: Annual distribution of DGP by data-driven modeling of *FS1*.

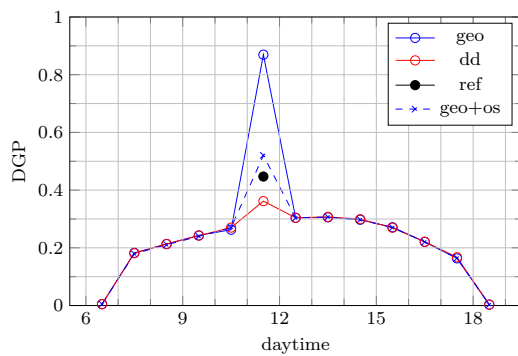


Figure 7.9: Hourly values of DGP on March 12th by geometric (geo, geo+os) and data-driven modelling of *FS1*.

Table 7.4: Sky conditions on 12th of March, 11:30, according to the weather file for Izmir. The azimuth angle is given from South to East.

Solar altitude	45.8°
Azimuth	18.8°
Direct-normal irradiance	901 W m <sup>-2</sup>
Diffuse-horizontal irradiance	101 W m <sup>-2</sup>

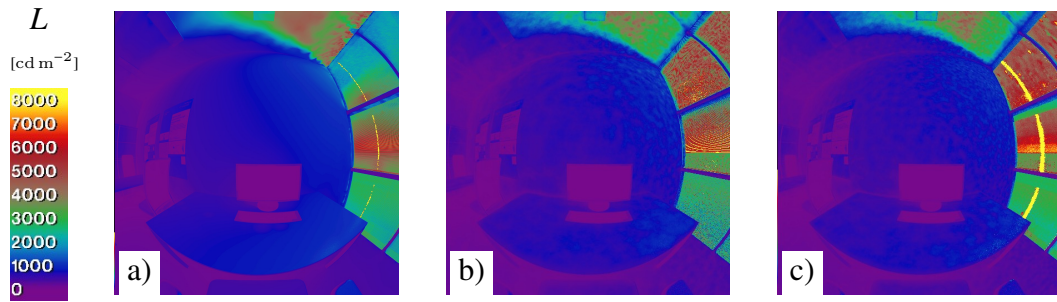


Figure 7.10: Reference for  $FS1$  (a), and results of the proposed CBDM technique employing the PHOTON MAP with geometric (b) and data-driven (c) models.

Figure 7.10 shows the imagery corresponding to the problematic time-step and  $FS1$ . Visual inspection reveals that a distinct vertical highlight, due to deflection on the curved slats of  $FS1$ , is replicated by the reference (a) and the data-driven model (c), but not by the geometric model (b). Compared to the reference (a), the data-driven model – due to its limited directional resolution – spreads the directional transmission and thereby widens the vertical highlight (c).

Table 7.5 reveals the poor agreement of the image statistics as well as the glare metrics based on the geometric model of  $FS1$  (row 2) with the reference (row 1). The geometric model leads to maximum pixel values that are more than three decades higher than those of the reference. Since only few, isolated pixels in Figure 7.10 a) contribute these extremely high luminance values due to direct transmission of sun-light, this disagreement is not apparent in a visual inspection. Impact on the glare metrics is, however, significant.  $E_v$  is over-estimated by a factor of 2. While only DGP directly accounts for the high  $E_v$  predicted by the geometric model, both glare metrics are affected by the bright concentrated pixels, which are detected as glare sources. Consequently, glare is drastically overestimated by the results of CBDM with the geometric model.

Data-driven modelling of  $FS1$ , on the other hand, achieves good agreement with backward ray-tracing in terms of all image statistics but  $\tilde{L}$  and  $L_{max}$  (row 4 in Table 7.5). The latter effects the glare metrics. In terms of DGP and DGI, the reference is closer to the results by data-driven than geometric modelling, but – due to the proximity to the DGP threshold of 0.40 (according to Table 7.3) – leads to a different rating.

### 7.3.3.2 CBDM with geometric modelling of $FS1$

The attribution of directional transmission to few isolated, but extremely bright pixels (reflected by the high  $L_{max}$  in row 2 of Table 7.5) can be explained as an artefact of pixel sampling. The resolution of images generated by the CBDM technique is set to

Table 7.5: Results of single time-step analysis by evalglare.

#	Modeling method	$E_v$ [lm/m <sup>2</sup> ]	$\bar{L}$ [cd m <sup>-2</sup> ]	$\tilde{L}$ [cd m <sup>-2</sup> ]	$L_{\max}$ [cd m <sup>-2</sup> ]	DGP [-]	DGI [-]	$\omega_s$ [sr]
<b>FS1, view <math>v_1</math>, Mar. 12th</b>								
1	backward ray-tracing, geometric	2550.9	1135.3	675.2	2.66e+03	0.447	26.1	0.782
2	PHOTON MAP CBDM, geometric	4243.7	2519.6	548.8	4.06e+06	0.869	40.7	0.685
3	geometric, oversampling	2319.1	1091.5	554.6	1.02e+05	0.520	29.0	0.773
4	data-driven	2405.2	1162.9	551.6	1.38e+03	0.379	23.1	0.782
<b>FS2, view <math>v_1</math>, March 12th</b>								
5	backward ray-tracing, data-driven	3075.9	1412.8	754.4	2.24e+02	0.354	16.1	0.766
6	PHOTON MAP CBDM, data-driven	3184.3	1517.8	739.3	2.63e+03	0.363	17.1	0.812
<b>FS2, view <math>v_2</math>, Sep. 29th</b>								
7	PHOTON MAP CBDM, data-driven	10640.4	2043.3	602.0	3.22e+05	0.882	32.7	0.551
8	5PM, data-driven	9311.9	1807.5	513.0	1.86e+05	0.796	32.1	0.564
9	3PM, data-driven	11537.8	2145.5	548.3	1.13e+05	0.920	32.2	0.539

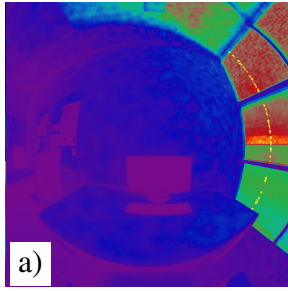


Figure 7.11: Geometric model, oversampling.

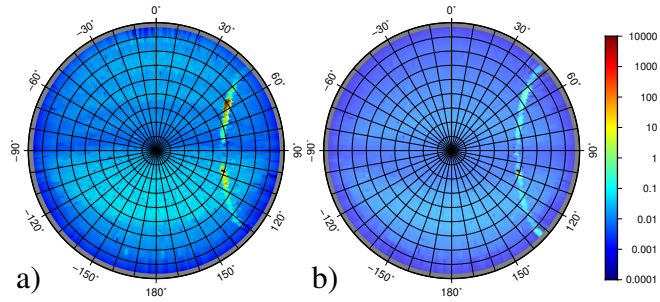


Figure 7.12: DSF of *CFS1* (a) and *CFS2* (b) for incident sun direction according to Figure 7.4.

$1024 \times 1024$  pixels<sup>2</sup>. Given the view point and the narrow distance of the slats comprising *FS1*, each image pixel represents a range of view directions that includes a fraction hitting the reflective slats, as well as unobstructed directions missing them. Parts of the view directions reaching the slats form a bright mirror-image of the sun, while others, due to the bend profile, are reflected to other sky directions and are missing the sun. The effect is eliminated in the reference, which is rendered at a higher pixel resolution of  $8192 \times 8192$  pixels<sup>2</sup> and subsequently down-sampled, effectively averaging 64 rays into one pixel value.

To verify this explanation of the differences between CBDM with the `PHOTON MAP` and the reference, employing the same geometric model, a second CBDM simulation with geometric modelling and pixel oversampling by a factor of 40, is performed<sup>12</sup>. The effect is a pronounced highlight shown in Figure 7.11, which closely matches that of the reference (Figure 7.10 a). The quantitative evaluation leads to results (row 3 in Table 7.5) that are close to the reference (row 1) and the results of data-driven modelling (row 4) in terms of  $E_v$ ,  $\bar{L}$ ,  $\tilde{L}$ , and at least closer in the case of  $L_{max}$ . The latter is still almost two decades higher when compared to the reference. Consequently, the agreement in terms of DGP and DGI is better than without oversampling, yet, it leads to an overestimation of glare (Figure 7.9, label `geo+os`).

### 7.3.3.3 CBDM with data-driven modelling of *FS1*

CBDM with data-driven models shows good agreement with the reference in terms of  $E_v$  and  $\bar{L}$  (rows 1 and 4 in Table 7.5). Yet,  $L_{max}$  is significantly lower than with backward ray-tracing. This can be attributed to the widened high-light on the fenestration. Since the latter exceeds the threshold of  $2000 \text{ cd m}^{-2}$ , it is detected as a glare-source. Consequently, DGI and DGP are moderately (compared to geometric modelling) overestimated.

<sup>12</sup>Note that this approach is not generally applicable due to the computational effort – it took two weeks to arrive at the results. Eight `rcontrib` processes were running in parallel on a 2.2 GHz Intel Xeon E5-2660.

The disagreement is a systematic shortcoming of the data-driven model and its maximum directional resolution of  $\approx 1.5^\circ$  (in the case of anisotropic scattering), which cannot accurately replicate the apparent angular diameter of the sun of  $\approx 0.5^\circ$ . Figure 7.12 shows the distribution of transmitted light for the incident direction corresponding to the sun according to Figure 7.4. The distribution is illustrated by the Differential Scattering Function (DSF) =  $B SDF \times \cos \theta_s$  to avoid the exaggeration of values at directions close to  $\theta_s = 90^\circ$ . For both configurations, the redirecting *CFS1* applied to *wg0*, and the retro-reflecting *CFS2* of *wg1* and *wg2*, direct transmission is indicated by a peak in the distribution at  $\theta_s \approx 131^\circ$ ,  $\phi_s \approx 107^\circ$ , in line with the incident direction  $\theta_s = 49^\circ$ ,  $\phi_s = -73^\circ$ . The low sun elevation, less than  $20^\circ$  above the horizon, reduces the shading effect of the CFS and leads to partial visibility of the sun through the gaps between the slats. The direct transmission of sun-light is complemented by a pronounced linear feature, caused by vertical deflection of incident light reflected upward – by the mirror-like top surfaces of the slats – or downward by multiple reflections. For *CFS1*, the upward deflection is intended, while for *CFS2* it constitutes a potential source of glare.

#### 7.3.3.4 CBDM with data-driven modelling of FS2

Figure 7.13 confirms good agreement of the results of the proposed CBDM technique (a) with backward ray-tracing (b). Since the images are based on the same data-driven model here, any differences can be accounted either to the employed simulation algorithms, or to the discretization of the sky model by CBDM. The latter is apparent in the shape of the highlight caused by forward-scattered sun-light passing *CFS3*, and the sky gradient toward the horizon. Compared to the reference (Figure 7.13 a), which employs the continuous sky luminance distribution by `gendaylit`, the highlight in Figure 7.13 b) is enlarged. This can be explained by the interpolation of the eventual sun direction between the fixed 5185 sun positions of the Reinhart sky employed in the computation of the solar component  $\mathbf{I}_{sun}$ . The coarser subdivision of  $\mathbf{I}_{sky, fen}$  causes patch-artefacts that are visible through the clear glazing of *wg1* and *wg2*.

Table 7.5 rows 5 and 6 show good agreement of all image statistics with the reference. The one notable deviation is  $L_{max}$ , which is  $\approx 12$  times higher in the results of the CBDM technique. A closer inspection of the highlight in *CFS3* reveals considerable pixel noise in the latter (Figure 7.13 d). Since `evalglare` considers the entire area of *CFS3* as one glare source, the noise is effectively eliminated by averaging in the glare evaluation. This is reflected by the accordance of the glare evaluation by DGP and DGI.

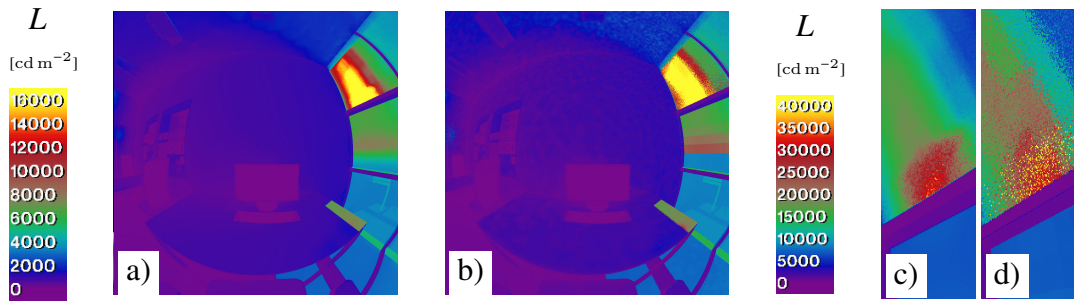


Figure 7.13: Reference image for *FS2* (a) and results of CBDM employing the `PHOTON MAP` with data-driven modelling (b). Forward-scattered sun-light by reference (c) and CBDM (d).

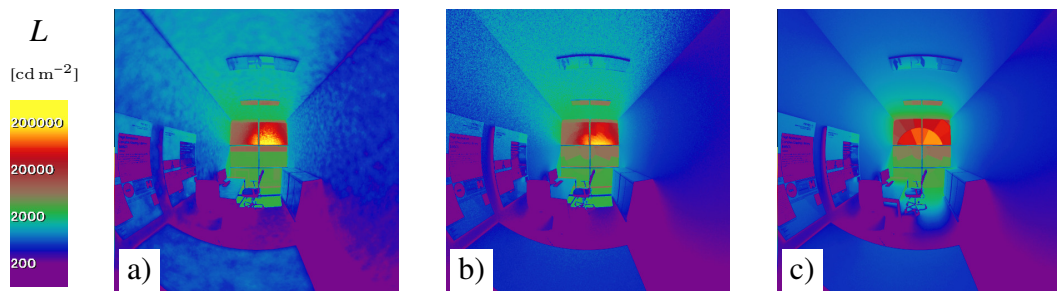


Figure 7.14: View toward *FS2*, September 29th. Result of CBDM employing the `PHOTON MAP` (a), 5PM (b), and 3PM(c).

### 7.3.3.5 Comparison with 3PM and 5PM

Figure 7.14 shows corresponding time-step imagery generated by the proposed CBDM method employing the `PHOTON MAP`, and by the 5PM based on backward ray-tracing. September 29th shows the strongest disagreements in terms of DGP for the two CBDM methods – 0.882 for the `PHOTON MAP`, and 0.795 for the 5PM. The low-resolution 3PM leads to an even higher DGP of 0.920. Due to the very high eye illuminance characterizing this time-step, the results of DGP metric are governed by the  $E_v$  term in this case, so that the 5PM cannot show its strengths in the accurate representation of glare sources. However, since the fenestration covers only a small fraction of the field of view, this effect is limited to relatively few time-steps. This is reflected by the good agreement of CBDM employing the `PHOTON MAP`, 5PM, and 3PM in terms of 95 percentile DGP (Figure 7.15).

Closer visual inspection of the imagery reveals the characteristic low-frequency photon noise in Figure 7.14 a), and the high-frequency pixel-noise in Figure 7.14 b). While the former can be explained by the insufficient density of photons on surfaces not reached by directly transmitted or directionally deflected sun-light, the latter is due to the insufficient density of stochastic rays sent toward the sun.

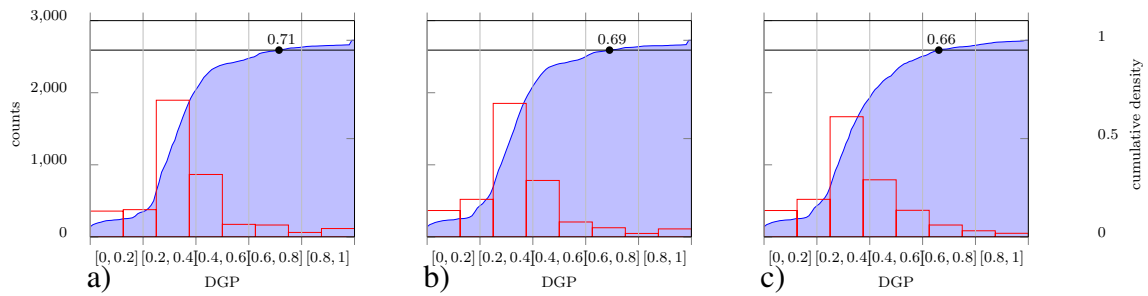


Figure 7.15: Histograms (bars), cumulative density (filled curve), and 95 percentile DGP. Result of CBDM employing the PHOTON MAP (a), 5PM (b), and 3PM(c) for view as in Figure 7.14.

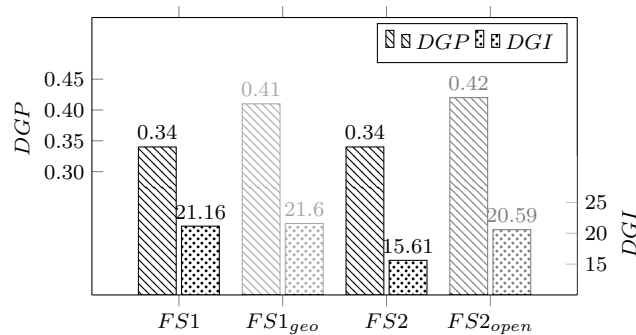


Figure 7.16: 95 percentile DGP and DGI achieved by FS1 and FS2. The less reliable results of geometric modelling of FS1, and the unrealistic case of FS2 with constantly open shade, are given for completeness in dimmer color.

### 7.3.4 Exemplary application of the method in the comparison of FS1 and FS2

The comparison of the two CFSs addresses glare conditions experienced by the seated occupant ( $v_1$  in Figure 7.1). 95 percentile DGP and DGI for the two CFSs are illustrated in Figure 7.16. Results for FS2, but without shading, are included (FS2<sub>open</sub>). The 95 percentiles are computed from the frequencies of annual DGP and DGI, based on the proposed CBDM technique with data-driven modelling of FS1 and FS2. For DGP, these are illustrated by histograms and cumulative density curves as shown in Figure 7.18 a) and c). For completeness, the results based on geometric modelling of FS1 with pixel oversampling are reported in Figure 7.18 b) and included in Figure 7.16 (FS1<sub>geo</sub>), although they have to be considered less robust, as discussed in subsection 7.3.3.2.

For FS1, the 95 percentile DGI based on geometric modelling (21.60, 25.2 with pixel oversampling) is higher than based on the data-driven model (21.16). However, both modelling techniques lead to a consistent rating of perceptible, not disturbing glare

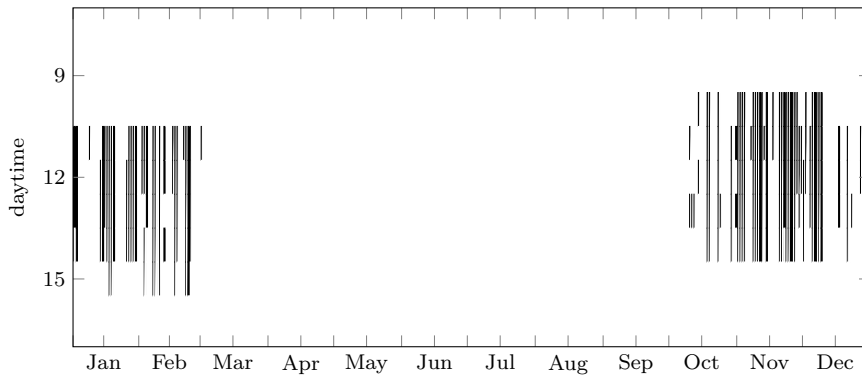


Figure 7.17: Operation of sun-shade with *FS2* (black: closed).

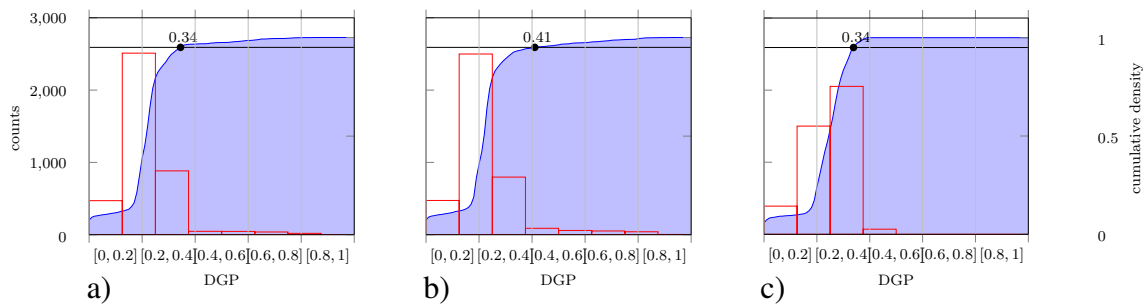


Figure 7.18: Histograms (bars), cumulative density (filled curve), and 95 percentile DGP. Data-driven (a) and geometric (b) models of *FS1*, and data-driven model of *FS2* (c).

according to Table 7.3. This agrees with the 95 percentile DGP based on data-driven modelling (0.34). Geometric modelling, which is considered problematic as discussed before, predicts disturbing glare (0.41, 0.43 with pixel oversampling).

*FS2*, when compared to *FS1*, achieves significantly better glare ratings in terms of 95 percentile DGI (15.61 for *FS2*, 21.16 for *FS1*). DGP, on the other hand, a metric that has been explicitly developed for cases with extended fenestration, leads to identical 95 percentile results for *FS1* (0.34) and *FS2* (0.34), just below the threshold between imperceptible and perceptible (but not disturbing) glare.

The reported 95 percentile DGP and DGI for *FS2* rely on the operation of a sun-shade, occluding the lower window groups *wg1* and *wg2* and thereby significantly affecting the view to the outside. The assumed operation schedule, based on a set-point of  $DGP \geq 0.40$  and hourly evaluation, is illustrated by Figure 7.17.

## 7.4 Conclusions

A method for the generation of imagery for visual comfort assessments, namely glare evaluations, is presented. It extends a prior approach that applied the `PHOTON MAP` to quantify daylight provision.<sup>153</sup>

The presented CBDM technique is similar to the 5PM in that it allows for accurate annual simulations with data-driven BSDF models. Other than the 5PM, it does not require scene modifications. The method is particularly efficient in cases when techniques to limit the impact of stochastic sampling in backward ray-tracing, such as the BSDF proxy or peak extraction are unavailable. While the method matches the 5PM in terms of accuracy, the complexity of the simulation process is drastically reduced to one 3PM step, and one DC calculation comprising photon distribution and gathering passes.

The results of the proposed CBDM technique show a high degree of accordance with backward ray-tracing. This holds true not only in the visual and quantitative comparison of images, but also in terms of the tested glare metrics DGP and DGI for individual time-steps as well as annual evaluations.

As with any method employing average BSDF to model CFSs, non-uniformity over the fenestration area e.g. due to visible geometric detail is not accounted for. However, for the evaluated case of *FS1*, spatial averaging over the fenestration area and the limited directional resolution of the data-driven model were found to impact the glare evaluations less than the sampling resolution in the image domain with geometric modelling. Even 40× oversampling of image pixels could not fully eliminate this effect, when geometric modelling is applied. The impact of spatial averaging over the fenestration area occurring with data-driven, and of pixel sampling artefacts with geometric modelling on glare assessment asks for more research covering a wider range of CFSs.

Even with a high number of 4G photons, possible only due to the OoC data-structure, the `PHOTON MAP` algorithm introduces visible photon noise and bias since only a small fraction of photons contributes to each daylight coefficient. The artefacts may be perceived as unpleasant, but do not effect typical visual comfort assessments, e.g. glare evaluations employing DGP and DGI. The effect on appearance may be even more severe if the spatial extent of the model increases, since the same number of photons would be distributed over a larger space. A possible approach to reduce the visibility of photon noise and bias would be the indirect visualization of photons by one inter-reflection step, which is the default behaviour of the `PHOTON MAP` module for `RADIANCE`. However, this renders the photon cache ineffective, which is a prerequisite for the efficient utilization of the OoC data-structure. The scalability of the method, and its capability to provide not only valid but visually pleasant results, are considered to be worthwhile to be further investigated.

It is hoped that the simplicity of the presented simulation process will allow its future integration into building performance simulation software. This would contribute to research in the field of daylighting, and provide practitioners with a new tool supporting planning decisions in the design of high performance buildings.

The comparison of the two CFSs illustrates the need to balance different aspects of visual comfort in daylighting. While *FS2* outperforms *FS1* in terms of DGI, in the light of identical 95 percentile DGP the continuous provision of an almost unobstructed view through *FS1* is a strong argument for optimized, static CFSs. Based on the results of this exemplary application of the presented CBDM technique, the reconcilability of view and glare control in the appropriate window zones is considered a major and rewarding objective in daylighting, that deserves closer attention in research as well as in the practice of architects and engineers.

## **Acknowledgements**

Thanks to my colleague Roland Schregle for his advice and guidance through the `PHOTON MAP` code, and to Tuğçe Kazanasmaz and Stephen Wittkopf for their valuable support during my PhD research at Izmir Institute of Technology.

## **Funding**

This research was funded by the Swiss Innovation Agency Innosuisse, contract #1155000149, and is part of the Swiss Competence Center for Energy Research SCCER FEEB&D.

## 7.5 Sequence of simulation steps comprising the 5PM

The 5PM is an established, yet elaborate CBDM method for accurate image generation. It comprises a sequence of simulation steps, and operations on the resulting imagery to effectively replace the direct solar component from the 3PM by a more accurate simulation:

1. Standard 3PM image generation,  $N$  inter-reflections, 145 sky regions, and Klems-basis fenestration model:  $\mathbf{I}_{145,-ab N} = \mathbf{V}_{145,-ab N} \cdot \mathbf{T} \cdot \mathbf{D} \cdot \mathbf{S}$ .
2. Generation of a reflection map for the given view:  $\rho$ .
3. Model modification so that interior surface reflectance  $\rho = 0$ , and computation of illuminance view matrix, one inter-reflection:  $\mathbf{V}_{E,145,-ab 1}$ .
4. Pixel-wise multiplication of illuminance view matrix with the reflection map to solve direct solar view matrix:  $\mathbf{V}_{145,-ab 1} = \mathbf{V}_{E,145,-ab 1} \cdot \rho$ .
5. 3PM image generation from direct solar view matrix with sun-only sky matrix:  $\mathbf{I}_{sun,145,-ab 1} = \mathbf{V}_{145,-ab 1} \cdot \mathbf{T} \cdot \mathbf{D} \cdot \mathbf{S}_{sun,145}$ .
6. Preparation of the refined solar model (5185 light sources):  $\mathbf{S}_{sun,5185}$ .
7. Computation of illuminance DCs with black interior surfaces and refined solar model, one inter-reflection:  $\mathbf{C}_{E,5185,-ab 1}$ .
8. Multiplication of illuminance DCs with the reflection map to calculate solar luminance DCs for room surfaces:  $\mathbf{C}_{r,5185,-ab 1} = \mathbf{C}_{E,5185,-ab 1} \cdot \rho$ .
9. Computation of luminance DCs with black interior surfaces and refined solar model to account for visible fenestration detail:  $\mathbf{C}_{f,5185,-ab N}$ .
10. Generation of “direct solar” imagery by folding the sum of the resulting DCs for room and fenestration with a refined sun-only sky matrix:  $\mathbf{I}_{sun,5185,-ab 1} = (\mathbf{C}_{r,5185,-ab 1} + \mathbf{C}_{f,5185,-ab N}) \cdot \mathbf{S}_{sun,5185}$ .
11. Replacement of the 3PM’s “direct solar” component by the result of the DC calculation:  $\mathbf{I}_{5PM} = \mathbf{I}_{145,-ab N} - \mathbf{I}_{sun,145,-ab 1} + \mathbf{I}_{sun,5185,-ab 1}$ .

## 7.6 Model generation parameters

Data-driven models are generated from geometric descriptions of *CFS1* and *CFS2* by genBSDF with the parameters reported in Table 7.6.

Table 7.6: Parameters for model generation by genBSDF.

<b>Description</b>	<b>Parameter</b>	<b>Value</b>
tensor rank, initial resolution $2^N$	$-t \langle M \rangle \langle N \rangle$	4, 7
ray accumulation (averaging)	$-c \langle N \rangle$	163840
compute front scatter	$\langle - + \rangle f$	+
compute back scatter	$\langle - + \rangle b$	+
include geometry, unit	$\langle - + \rangle geo \langle s \rangle$	-, meter
rttrace arguments	$-r \langle s \rangle$	listed below
diffuse inter-reflections	$-ab \langle N \rangle$	5
ambient divisions	$-ad \langle N \rangle$	2
maximum ray weight	$-lw \langle k \rangle$	0.2

Data-driven models are generated from interpolants, which represent front- and back-scattering by sets of radial basis functions, employing the command `bsdf2tree` with the parameters reported in Table 7.7.

Table 7.7: Parameters for model generation by `bsdf2tree`.

<b>Description</b>	<b>Parameter</b>	<b><i>CFS3</i></b>	<b><i>CFS4</i></b>
initial resolution $2^N$	$-g \langle N \rangle$	7	9
data-reduction by %	$-t \langle N \rangle$	98	98

## 7.7 Image generation parameters

The direct solar component is calculated by folding  $DC_{sun}$ , computed with the parameters listed in Table 7.8, with sky vectors for each time-step.

Table 7.8: Parameters for photon distribution and image synthesis in the computation of the solar component  $DC_{sun}$ .

Description	Parameter	Value
<b>mkpmap:</b>		
photon-port modifier	<i>-apo</i> < <i>s</i> >	outerGlass
file and target count of contribution photons	<i>-apC</i> < <i>s</i> > < <i>N</i> >	C.pm 4G
<b>rcontrib:</b>		
ambient reflections, -1 for direct photon visualization	<i>-ab</i> < <i>N</i> >	-1
maximum ray weight	<i>-lw</i> < <i>k</i> >	$2 \times 10^{-4}$
specular threshold	<i>-st</i> < <i>k</i> >	0.0
list of source modifiers	<i>-M</i> < <i>s</i> >	mods.lst
contribution photons file, bandwidth	<i>-ap</i> < <i>s</i> > < <i>N</i> >	C.pm 108 030
photon cache size	<i>-aC</i> < <i>N</i> >	16M
photon cache page size	<i>-ac</i> < <i>N</i> >	16
image resolution in pixels	<i>-x</i> < <i>M</i> > <i>-y</i> < <i>N</i> >	1024, 1024

## CHAPTER 8

### CONCLUSIONS AND FUTURE RESEARCH DIRECTIONS

#### 8.1 Main research questions and objectives

Methods for the data-driven modelling of Daylight Redirecting Fenestration (DRF) in daylight simulation for visual comfort assessment have been developed, tested, and applied. Within this scope, the five articles forming the core chapters of this thesis present particular aspects that address the main research questions that were stated in section 1.6 of the introduction:

**Parametrization of measurement and model generation:** Chapter 3 demonstrates that the interpolation technique implemented to compile measured Bidirectional Scattering Distribution Function (BSDF) to data-driven models is applicable to DRF. To maintain the distinct features of complex BSDFs, e.g. featuring multiple peaks, a refined measurement in terms of incident resolution is required. Due to the lack of a generally applicable extrapolation algorithm, the resulting models are valid only within the range of measured incident directions. Adaptive data-reduction is effective in cases where pronounced peaks are accompanied by large regions of low variance in the distributions. However, the model resolution was governed by the measurement, due to the strong diffusing effect of the first evaluated Daylight Redirecting Component (DRC), and the widened sampling aperture required for the measurement of the second.

**Measuring and modelling retro-reflection:** A novel extension of a scanning gonio-photometer was presented in chapter 4, that allows to measure retro-reflection by an innovative coating at high resolution by two beam-splitters. The acquired data, representing the peak region, could be assembled with the results of hemispherical scans into a complete reflection model. This model allowed to compare the daylight performance of Venetian blinds featuring the retro-reflective coating with blinds exhibiting specular and diffuse reflection. The comparison indicates the potential that blinds, due to the distinct retro-reflection achieved by the coating, can effectively block sun-light, even when they are not fully closed. The effect is similar to that achieved by the complex profiles of another retro-reflective system presented in chapter 7.

**Efficient combination of layer properties:** The matrix-calculation of system properties from the BSDFs of fenestration layers, as commonly applied to models of low resolution, could be adapted to variable resolution. The technique was applied to exemplary DRF and allows to model e.g. different states of DRF, or static DRF that are combined with retractable shading. Please note that the efficiency depends on the layer properties – Backward Ray-Tracing (BRT) through layers (e.g. by genBSDF) is typically outperformed if the latter requires dense stochastic sampling, e.g. if more than one scattering layer is present.

**Sampling of data-driven models:** Chapter 6 introduces a modification of the bidirectional Photon Mapping (PM) implemented in RADIANCE. In the case of an exemplary office model, featuring Laser Cut Panels (LCPs) under sunny sky conditions, simulation times decreased by  $\approx 95\%$ . The comparison with BRT showed good agreement besides the expected artefacts that are characteristic to each rendering technique. The reverse sampling of the BSDF from the light source rather than the receiver allows to employ data-driven models in image synthesis, without peak extraction or the utilization of proxy geometry.

**Reducing complexity in Climate-Based Daylight Modelling:** The PHOTON MAP implementation introduced in chapter 6 was applied to the calculation of the solar component in Climate-Based Daylight Modelling (CBDM) in chapter 7. This allows image synthesis achieving the same accuracy in visual comfort assessments as the Five-Phase-Method (5PM), but with a drastically reduced complexity.

**Retro-reflecting micro-structures:** The method is subsequently applied to annual glare assessments of two types of DRF. One combines a redirecting film with clear glazing, that is equipped with retractable shading. The other is a static DRF featuring redirecting and retro-reflecting mirror-blinds. The application of Daylight Glare Probability (DGP) shows that both DRF achieve the same protection from glare over the year. While the retractable shading switches between a perfectly unobstructed view and almost opaque states, the static system permanently maintains a visual connection to the outside through the flat profiles of the retro-reflective slats. The results show the potential of retro-reflection to reconcile the conflicting target of view and glare protections, and opens the question on how to account for the gradual obstruction of view.

Data-driven modelling could be applied to a wide range of DRF, as summarised by Table 8.1. It provides a unified interface between daylight simulation, and different BSDF acquisition techniques, e.g. gonio-photometric measurement and ray-tracing.

Table 8.1: DRF modelled as part of the research presented in chapters 3 to 7. For models employing the tensor tree as data-structure, the tensor size before adaptive data-reduction is indicated.

Chapter	Fenestration system or component	Model based on	Directional basis
3	Prismatic film	Measured BSDF <sub>S</sub> (transparent, diffusing layers)	Tensors $2^{6.4}, 2^{7.4}$
3	Micro-grid of tilted light shafts	Measured BSDF <sub>L</sub> of the light redirecting inlet	Tensors $2^{6.4}, 2^{7.4}$
4	Retro-reflective coating	Measured BSDF of the coating (Vis, NIR)	Tensor $2^{7.4}$
4	Venetian blinds, mirror-like reflection	Geometric model	Klems
4	Venetian blinds, diffuse reflection	Geometric model	Klems
4	Venetian blinds, retro-reflection	Geometric model	Klems
5	Venetian blinds, mirror-like reflection	Geometric model of the blinds	Tensor $2^{7.4}$
5	Micro-grid of tilted light shafts	Geometric model of the light redirecting inlet	Tensor $2^{7.4}$
5	Clear glass	Geometric models of the clear glass layers	Tensor $2^{7.4}$
5	Venetian blinds, mirror-like reflection	Matrix-combination of BSDF <sub>L</sub> s (blinds, glazing)	Klems, Tensors $2^{4.4}, 2^{6.4}, 2^{7.4}$
5	Micro-grid of tilted light shafts	Matrix-combination of BSDF <sub>L</sub> s (inlet, glazing)	Klems, Tensors $2^{4.4}, 2^{6.4}, 2^{7.4}$
6	LCP	Measured BSDF of the LCP	Tensor $2^{7.4}$
7	Light redirecting Venetian blinds	Geometric model of the blinds	Klems, Tensor $2^{7.4}$
7	Retro-reflecting Venetian blinds	Geometric model of the blinds	Klems, Tensor $2^{7.4}$
7	Light redirecting film	Measured BSDF <sub>L</sub> of the film (on glass)	Klems, Tensor $2^{7.4}$
7	Dense fabric for glare control	Measured BSDF <sub>L</sub>	Klems, Tensor $2^{9.3}$

## 8.2 Limitations of this research

The presented research includes the modification of the `PHOTON MAP` module, that is part of the daylight simulation suite `RADIANCE`. This modification is validated by comparison to the results of the unmodified BRT algorithm, which is the default in `RADIANCE`. No validation against other computational techniques or experimental results was performed. Consequently, this research relies on the validity of the core routines of `RADIANCE`. The methods are applied to exemplary cases, combining few DRFs with an office model. Weather data for Izmir is used in the CBDM calculations. This research can therefore not aim at representative results that could be generalized to applications of DRF in arbitrary building contexts or at other locations.

## 8.3 Recommendations

The generation of data-driven models from measurements allows to accurately replicate the daylight scattering properties of uniform, micro-structured DRF and its components. With the illuminator focused on the sample or the detector, the resolution of the measurement slightly exceeds that of the anisotropic model ( $\approx 1.4^\circ$ ). Since the sampling aperture required to cover a representative area on the DRF increases with the size of its periodical structures, the directional resolution degrades when macro-structured DRF is characterised. If the illuminated sampling aperture exceeds a size of  $\approx 100$  mm, far-field conditions are not met with the device used in this research, and would require a significantly larger instrument. On the other hand, the geometry of such large structures can usually be reliably acquired. Consequently, it is recommended to generate models from measured BSDF of micro-structures, and to apply computational methods such as `genBSDF` to macro-structured DRF.

The `PHOTON MAP` has been demonstrated to significantly accelerate simulations with data-driven models of DRF for single time-steps. In CBDM, the typical artefacts become more apparent due to the typically lower number of photons per light source. While these artefacts did not affect the visual comfort assessments presented in chapter 7, they may have an impact on other luminance-based metrics. However, the use of the bidirectional `PHOTON MAP` can be recommended for visual comfort assessments, in particular when techniques such as peak extraction or the use of BSDF proxies are not applicable. This holds true to most micro-structured DRF featuring directional transmission that cannot be easily accounted to an idealised peak shape.

## 8.4 Main contributions

The presented research offers a new method to combine data-driven models of variable resolution by adapting matrix-computations as previously applied to BSDF models of moderate resolution. This makes it feasible to build up libraries of high-resolution BSDFs, that can be combined to model and compare different configurations of DRF.

A technique to accurately characterise retro-reflection in the wavelength ranges of Vis and NIR was developed. The method has proven its usefulness in the testing of optical properties achieved by coating processes, and in assessing the effect of a retro-reflecting coating, applied blinds, on visual comfort prior to the availability of prototypes. This assessment applied, to the author's knowledge for the first time, the generation of simulation models to retro-reflection in daylight simulation.

The PHOTON MAP in RADIANCE has been modified for the synthesis of valid imagery with data-driven models. The initial tests reveal the potential of the bidirectional algorithm to increase rendering speed not only with geometric, but also with data-driven modelling, or with combinations of both. The application of the PHOTON MAP to Climate-Based Daylight Modelling promises a potential to simplify image synthesis for annual glare assessments. This shall encourage researchers and practitioners to assess visual comfort by robust, luminance-based visual comfort metrics rather than potentially invalid approximations based on e.g. vertical or horizontal illuminance. Ultimately, it is hoped that an efficient and simplified image generation technique can lead to the integration of visual comfort assessments in general Building Performance Simulation (BPS).

## 8.5 Scientific and non-scientific impact

Data-driven modelling based on measured BSDF, and the modified PHOTON MAP developed in this research immediately provided valuable data in research on the effects of Roman glass on the illumination of lost architecture.<sup>173–175</sup>

The presented methods also support the development of DRF in the ongoing collaboration with two industry partners. The modified PHOTON MAP in conjunction with data-driven models compiled from measured BSDF has been applied by an international architectural firm in detailed visual comfort assessments, after several failed attempts to achieve results by BRT. While the results from non-scientific collaboration can typically not be disclosed, it is important to note that these collaborations play an important role in guiding and testing research and development.

Most measured BSDF and data-driven models of DRF have been made available to practitioners as well as for research.<sup>176</sup>

## 8.6 Further research directions

The methods developed in the course of this research were applied only in exemplary studies of selected DRF in the context of one cellular office. The vast amount of different DRF, and the dependency of its performance on exterior conditions and the attached space, ask for a systematic assessment of visual comfort by combining DRFs with varying office types, locations, and orientations. The methodological contributions of this research could provide the foundations for such a study.

While the geometric modelling of macro-structured DRF is feasible, a means to measure light scattering by such systems at high resolution would allow to validate the computationally generated BSDFs and probably disclose yet unexpected effects.<sup>68</sup> The extension of the gonio-photometry to allow near-field measurements would overcome this limitation. Furthermore, it would allow to characterise non-uniformity of DRF, and, in analogy to current practice in the characterisation of luminaires, may lead to data-driven modelling approaches that spatially resolve the fenestration area.

The annual assessment of visual comfort and glare by luminance-based metrics, as demonstrated e.g. in chapter 7, is a big step forward compared to approaches based on vertical or, worse, horizontal illuminance. However, the current practice of glare evaluations employing the DGP metric contradicts the zonal performance assessments, that are established in BPS, and that have been addressed with spatio-temporal metrics for daylight provision and sun exposure. Research on the spatio-temporal assessment of glare has just been started and shall advance visual comfort assessment to develop into a representative evaluation in line with other criteria of building performance.<sup>177</sup>

## BIBLIOGRAPHY

- (1) Corbusier), C.-É. J. (, *Precisions on the present state of architecture and city planning: With an American prologue, a Brazilian corollary followed by The temperature of Paris and The atmosphere of Moscow*;  
MIT Press: Cambridge, 1991 (cit. on p. 1).
- (2) Selkowitz, S. In *Daylighting'98 Conference*, Ottawa, 1998 (cit. on p. 1).
- (3) Boyce, P.; Hunter, C.; Howlett, O.  
*The benefits of daylight through windows*; tech. rep.;  
New York: Rensselaer Polytechnic Institute, 2003 (cit. on p. 2).
- (4) Leslie, R. *Building and Environment* **2003**, 38, 381–385 (cit. on p. 2).
- (5) Mardaljevic, J. In *Sustainable built environments*, Loftness, V., Haase, D., Eds.;  
Springer New York: 2013, pp 69–111 (cit. on p. 2).
- (6) Baker, N. V.; Fanchiotti, A.; Steemers, K. In;  
Routledge: 2013; Chapter Daylighting evolution and analysis (cit. on p. 2).
- (7) Hoffmann, S.; Lee, E. S.; McNeil, A.; Fernandes, L.; Vidanovic, D.;  
Thanachareonkit, A. *Energy and Buildings* **2016**, 112, 279–298  
(cit. on pp. 2, 29, 43, 115).
- (8) DiLaura, D. L.; Houser, K. W.; Mistrick, R. G.; Steffy, G. R.,  
*The lighting handbook*; Illuminating Engineering Society: 2011 (cit. on pp. 2, 7).
- (9) Dave, S.; Andersen, M.  
In *27th Conference on Passive and Low Energy Architecture (PLEA)*, 2011  
(cit. on p. 2).
- (10) Dave, S.; Andersen, M. In *Proceedings of CISBAT 11: CleanTech for Sustainable Buildings-From Nano to Urban Scale*, 2011 (cit. on p. 2).
- (11) Kolås, T. Performance of daylight redirecting Venetian blinds for sidelighted spaces at high latitudes., Ph.D. Thesis, Norges Teknisk-Naturvitenskapelige Universitet, Fakultet for Arkitektur og Billedkunst, 2013 (cit. on pp. 2, 3, 43).
- (12) Deroisy, B.; Deneyer, A.; Lethé, G.; Flamant, G. In *Lux Europa 2013*, 2013  
(cit. on p. 2).
- (13) Kuhn, T. E. *Solar Energy* **2017**, - (cit. on pp. 2, 44).
- (14) Andresen, I. A multi-criteria decision-making method for solar building design., Ph.D. Thesis, Fakultet for arkitektur og billedkunst, 2000 (cit. on p. 2).
- (15) Konis, K. *Energy and Buildings* **2014**, 77, 67–79 (cit. on p. 3).

- (16) Ruck, N.; Aschehoug, Ø.; Aydinli, S.; Christoffersen, J.; Courret, G.; Edmonds, I.; Jakobiak, R.; Kischkoweit-Lopin, M.; Klinger, M.; Lee, E.; Michel, L.; Scartezzini, J.-L.; Selkowitz, S.,  
*Daylight in Buildings - A source-book on daylighting systems and components*; Aschehoug, Ø., Christoffersen, J., Jakobiak, R., Johnsen, K., Lee, E., Ruck, N., Selkowitz, S., Eds.; Lawrence Berkeley National Laboratory: 2000  
(cit. on pp. 4, 29, 71, 118).
- (17) Gago, E.; Muneer, T.; Knez, M.; Köster, H.  
*Renewable and Sustainable Energy Reviews* **2015**, *41*, 1–13 (cit. on pp. 4, 29, 71).
- (18) Nair, M.; Ramamurthy, K.; Ganesan, A.  
*Lighting Research and Technology* **2014**, *46*, 245–267 (cit. on pp. 4, 29, 71).
- (19) Konis, K.; Selkowitz, S.,  
*Effective daylighting with high-performance facades: emerging design practices*; Springer: 2017 (cit. on pp. 4, 43).
- (20) Selkowitz, S.; Lee, E. S. In *Daylighting '98 Conference*, Ottawa, 1998  
(cit. on p. 4).
- (21) Bueno, B. Integrated simulation of complex fenestration systems., [https://www.ise.fraunhofer.de/content/dam/ise/en/documents/information-material/Building-Energy-Technology/15e\\_ISE\\_Flyer\\_Complex\\_Fenestration.pdf](https://www.ise.fraunhofer.de/content/dam/ise/en/documents/information-material/Building-Energy-Technology/15e_ISE_Flyer_Complex_Fenestration.pdf), 2015 (cit. on p. 4).
- (22) Papamichael, K.; Winkelmann, F.  
In *International Daylighting Conference Proceedings*, 1986; Vol. 1  
(cit. on pp. 4, 71).
- (23) *Daylight in buildings*; Standard EN 17037:2018; CEN / TC 169, 2019  
(cit. on pp. 6, 115, 126).
- (24) Stiller, M., *Quality lighting for high performance buildings*; Fairmont Press: 2012  
(cit. on p. 7).
- (25) Of Oregon Lighting Design Lab, E. T. Footcandle light guide., [https://www.lightingdesignlab.com/sites/default/files/pdf/Footcandle\\_LightingGuide\\_Rev.072013.pdf](https://www.lightingdesignlab.com/sites/default/files/pdf/Footcandle_LightingGuide_Rev.072013.pdf), Last accessed June 2017, 2013  
(cit. on p. 7).
- (26) *Light and lighting - Lighting of work places - Part 1: Indoor work places*; Standard EN 12464-1:2011; CEN / TC 169, 2011 (cit. on p. 7).
- (27) Heschong, L.; Wymelenberg, V. D.; Andersen, M.; Digert, N.; Fernandes, L.; Keller, A.; Loveland, J.; McKay, H.; Mistrick, R.; Mosher, B., et al.  
*Approved method: IES spatial Daylight Autonomy (sDA) and Annual Sunlight Exposure (ASE)*; tech. rep.; IES-Illuminating Engineering Society, 2012  
(cit. on pp. 7, 115, 119).

- (28) Reinhart, C. F.; Weissman, D. A. *Building and environment* **2012**, *50*, 155–164 (cit. on p. 7).
- (29) Nezamdoost, A.; Wymelenberg, K. G. V. D. *LEUKOS* **2017**, *13*, 107–123 (cit. on p. 7).
- (30) Nabil, A.; Mardaljevic, J. *Energy and Buildings* **2006**, *38*, 905–913 (cit. on p. 8).
- (31) Mardaljevic, J. In *CIBSE National Conference*, 2006 (cit. on p. 8).
- (32) Mardaljevic, J. In; De Montfort University: 1999; Chapter Daylight Coefficients: Formulation, validation and application, pp 210–280 (cit. on pp. 8, 116).
- (33) Brembilla, E.; Mardaljevic, J. *Building and Environment* **2019**, *158*, 151–164 (cit. on pp. 8, 115).
- (34) Klems, J. H. In *EnergyPlus engineering reference*; Ernest Orlando Lawrence Berkeley National Laboratory: 2013; Chapter Window calculation module (cit. on pp. 8, 30, 74, 118).
- (35) Saxena, M.; Ward, G.; Perry, T.; Heschong, L.; Higa, R. In *SimBuild*, New York, NY, US, 2010; Vol. 4, pp 402–409 (cit. on pp. 8, 116).
- (36) McNeil, A.; Lee, E. *Journal of Building Performance Simulation* **2013**, *6*, 24–37 (cit. on pp. 8, 9, 95, 116, 117).
- (37) McNeil, A.  
*On the sensitivity of daylight simulations to the resolution of the hemispherical basis used to define bidirectional scattering distribution functions*; tech. rep.; DOE Technical Memo, 2011 (cit. on pp. 8, 9, 74, 91, 95, 116, 117).
- (38) Wymelenberg, K. V. D.; Inanici, M. *Leukos* **2014**, *10*, 145–164 (cit. on pp. 8, 95, 115).
- (39) Bellia, L.; Fragliasso, F.; Stefanizzi, E.  
*Building and Environment* **2016**, *106*, 301–312 (cit. on p. 8).
- (40) Dutra de Vasconcellos, G.  
Evaluation of Annual Sunlight Exposure (ASE) as a proxy to glare: A field study in a NZEB and LEED certified office in San Francisco., MA thesis, Berkeley, CA, US: University of California, 2017 (cit. on p. 8).
- (41) Wymelenberg, K. V. D.; Inanici, M. *Leukos* **2016**, *12*, 113–138 (cit. on pp. 8, 95, 115).
- (42) Vos, J. J. *Lighting Research & Technology* **2003**, *35*, 163–176 (cit. on p. 8).
- (43) Osterhaus, W. K. E. *Solar Energy* **2005**, *79*, 140–158 (cit. on p. 8).
- (44) Pierson, C.; Wienold, J.; Bodart, M. *Leukos* **2018**, 1–38 (cit. on pp. 8, 126).

- (45) Wienold, J.; Christoffersen, J. *Energy and Buildings* **2006**, *38*, 743–757 (cit. on pp. 8, 57, 103, 117).
- (46) Jones, N. L.; Reinhart, C. F. *Building and Environment* **2017**, *113*, 131–150 (cit. on pp. 8, 46, 94).
- (47) Jones, N. L.; Reinhart, C. F. In *Building Simulation 2015: 14th Conference of the International Building Performance Simulation Association*, Hyderabad, IN, 2015 (cit. on p. 8).
- (48) Jones, N. L.; Reinhart, C. F. In *Building Simulation 2015: 14th Conference of the International Building Performance Simulation Association*, Hyderabad, IN, 2015 (cit. on p. 8).
- (49) Wienold, J. In *Proceedings of Building Simulation*, Glasgow, Scotland, 2009, pp 944–951 (cit. on pp. 8, 117).
- (50) *Blinds and shutters - Thermal and visual comfort - Performance characteristics and classification*; Standard EN 14501:2005; CEN / TC 33, 2006 (cit. on p. 8).
- (51) Ward, G.; Kurt, M.; Bonneel, N. In *Eurographics Workshop on Material Appearance Modeling*, ed. by Klein, R.; Rushmeier, H., The Eurographics Association: 2014 (cit. on pp. 9, 46, 95, 118).
- (52) Lee, E. S.; Geisler-Moroder, D.; Ward, G. *Solar Energy* **2018**, *160*, 380–395 (cit. on pp. 9, 116).
- (53) Geisler-Moroder, D.; Lee, E. S.; Ward, G. In *Building Simulation*, 2017 (cit. on pp. 9, 95, 116).
- (54) Subramaniam, S. *Daylighting simulations with Radiance using matrix-based methods*; tech. rep.; Lawrence Berkeley National Laboratory, 2017 (cit. on pp. 9, 115).
- (55) Grobe, L. O.; Wittkopf, S.; Kazanasmaz, Z. T. *Journal of Facade Design and Engineering* **2017**, *5*, 101–113 (cit. on pp. 12, 28, 46, 95, 117).
- (56) Grobe, L. O. *Energy and Buildings* **2018**, *162*, 121–133 (cit. on pp. 12, 43, 95).
- (57) Grobe, L. O. *Buildings* **2017**, *22* (cit. on pp. 12, 30, 46, 57, 70, 101, 123).
- (58) Grobe, L. O. *Journal of Building Performance Simulation* **2019**, DOI: 10.1080/19401493.2019.1653994 (cit. on pp. 12, 13, 94, 119).
- (59) Grobe, L. O. *Energy and Buildings* **accepted** (cit. on pp. 13, 115).
- (60) Apian-Bennewitz, P. In *Proceedings SPIE*, Brussels, 2010; Vol. 7792 Reflection, Scattering, and Diffraction from Surfaces II, 779200–779200 (cit. on pp. 14, 32, 45, 48, 72).

- (61) Grobe, L. O.; Wittkopf, S.; Apian-Bennewitz, P.; Jonsson, J. C.; Rubin, M. *Proceedings SPIE* **2010**, *7725 Photonics for Solar Energy Systems III*, 772510–772510 (cit. on pp. 14, 162).
- (62) Apian-Bennewitz, P. Goniophotometer pab-pgII user manual.; pab advanced technologies Ltd, 2014 (cit. on pp. 14, 26).
- (63) Apian-Bennewitz, P. In *Eurographics 2014 Workshop on Material Appearance Modeling: Issues and Acquisition*, Eurographics Association: Lyon, France, 2014, pp 1–4 (cit. on pp. 14, 33, 46).
- (64) Apian-Bennewitz, P. Messung und Modellierung von lichtstreuenden Materialien zur Computer-Simulation von Tageslichtbeleuchtung., Ph.D. Thesis, Albert-Ludwigs-Universität, Freiburg, 1995 (cit. on pp. 14, 26).
- (65) Delaunay, B. *Izv. Akad. Nauk SSSR, Otdelenie Matematicheskii i Estestvennyka Nauk* **1934**, 7, 1–2 (cit. on p. 27).
- (66) Grobe, L. O.; Wittkopf, S.; Kazanasmaz, Z. T. In *ICBEST Istanbul: Interdisciplinary perspectives for future building envelopes*, ed. by Tavil, A.; Çelik, O. C., Istanbul Technical University: Istanbul, 2017, pp 84–93 (cit. on p. 28).
- (67) Ward, G.; Shakespeare, R., *Rendering with Radiance*; Morgan Kaufmann Publishers: San Francisco, CA, 1998 (cit. on pp. 29, 94).
- (68) Noback, A.; Grobe, L. O.; Wittkopf, S. *Buildings* **2016**, 6, 30 (cit. on pp. 29, 44, 81, 124, 149, 162).
- (69) Schregle, R.; Grobe, L. O.; Wittkopf, S. K. *Solar Energy* **2015**, 114, 327–336 (cit. on pp. 29, 96, 113).
- (70) Schregle, R.; Grobe, L. O.; Wittkopf, S. *Journal of Building Performance Simulation* **2016**, 9, 620–632 (cit. on pp. 29, 57, 96, 119).
- (71) Greenup, P.; Edmonds, I.; Compagnon, R. *Lighting Research and Technology* **2000**, 32, 49–54 (cit. on pp. 29, 71).
- (72) Maamari, F.; Andersen, M.; de Boer, J.; Carroll, W. L.; Dumortier, D.; Greenup, P. *Energy and Buildings* **2006**, 38, 878–889 (cit. on p. 29).
- (73) Laouadi, A.; Parekh, A. *Lighting Research and Technology* **2007**, 39, 109–122 (cit. on p. 29).
- (74) Mohanty, L.; Yang, X.; Wittkopf, S. K. *Solar Energy* **2012**, 86, 505–519 (cit. on p. 29).
- (75) McNeil, A.; Lee, E. S.; Jonsson, J. C. *Building and Environment* **2017**, 113, 280–297 (cit. on pp. 29, 31, 72, 95).

- (76) Kuhn, T. E.; Herkel, S.; Frontini, F.; Strachan, P.; Kokogiannakis, G. *Energy and Buildings* **2011**, *43*, 19–27 (cit. on pp. 29, 71).
- (77) Appelfeld, D.; McNeil, A.; Svendsen, S. *Energy and Buildings* **2012**, *50*, 166–176 (cit. on pp. 29, 71).
- (78) McNeil, A.; Lee, E. S. *Simulated daylight performance of a new prototype prismatic window film in deep open plan offices*; DOE/ CEC PIER; Lawrence Berkeley National Laboratory, 2013 (cit. on p. 30).
- (79) De Boer, J. *Modelling indoor illumination by CFS based on bidirectional photometric data*; tech. rep.; International Energy Agency Task 31, 2005 (cit. on pp. 30, 74).
- (80) Kämpf, J. H.; Scartezzini, J.-L. In *CISBAT 2011*, Lausanne, 2011, pp 349–354 (cit. on pp. 30, 74, 118).
- (81) Ward, G.; McNeil, A. A variable-resolution BSDF implementation., 10th International Radiance Workshop, 2011 (cit. on pp. 30, 72, 74).
- (82) Ward, G.; Kurt, M.; Bonneel, N. *A practical framework for sharing and rendering real-world Bidirectional Scattering Distribution Functions*; tech. rep.; Lawrence Berkeley National Laboratory, 2012 (cit. on pp. 30, 46, 74, 95).
- (83) Krehel, M.; Grobe, L. O.; Wittkopf, S. *Journal of Facade Design and Engineering* **2016**, *4*, 79–89 (cit. on pp. 30, 41, 46, 72).
- (84) Kazanasmaz, T.; Grobe, L. O.; Bauer, C.; Krehel, M.; Wittkopf, S. *Building and Environment* **2016**, *102*, 243–256 (cit. on pp. 31, 95, 119, 162).
- (85) Grobe, L. O.; Noback, A.; Wittkopf S. K., S.; Kazanasmaz, Z. T. In *Proceedings of International Conference CISBAT 2015 Future Buildings and Districts Sustainability from Nano to Urban Scale*, 2015, pp 205–210 (cit. on p. 31).
- (86) Darula, S.; Christoffersen, J.; Malikova, M. *Energy Procedia* **2015**, *78*, 1245–1250 (cit. on p. 43).
- (87) Köster, H., *Daylight modulation*; Witag-Verlag: 2015 (cit. on p. 43).
- (88) Arecchi, A. V.; Messadi, T.; Koshel, R. J., *Field guide to illumination*; SPIE Optical Engineering Press: Bellingham, WA, 2007 (cit. on p. 44).
- (89) Tsangrassoulis, A. In *Energy performance of buildings: Energy efficiency and built environment in temperate climates*, Boemi, S.-N., Irulegi, O., Santamouris, M., Eds.; Springer International Publishing: Cham, 2016, pp 437–466 (cit. on p. 44).
- (90) Wong, I. L. *Renewable and Sustainable Energy Reviews* **2017**, *74*, 959–968 (cit. on p. 44).

- (91) Köster, H., *Dynamic daylighting architecture: basics, systems, projects*; Springer Science & Business Media: 2004 (cit. on p. 44).
- (92) Rossi, F.; Pisello, A. L.; Nicolini, A.; Filipponi, M.; Palombo, M. *Applied Energy* **2014**, *114*, 621–631 (cit. on p. 44).
- (93) Sakai, H.; Iyota, H. *International Journal of Thermophysics* **2017**, *38*, 131 (cit. on p. 44).
- (94) Ichinose, M.; Inoue, T.; Nagahama, T. *Energy and Buildings* **in press**, DOI: 10.1016/j.enbuild.2017.01.051 (cit. on p. 44).
- (95) Papaiz, L.; Grobe, L. O.; De Michele, G. Modeling and measuring of solar shading with retro-reflection microstructure., 15th International Radiance Workshop, Padua, 2016 (cit. on pp. 44, 46).
- (96) Yuan, J.; Emura, K.; Farnham, C. *Journal of Building Physics* **2015**, *38*, 500–516 (cit. on p. 45).
- (97) Nicodemus, F. E.; Richmond, J. C.; Hsia, J. J.; Ginsberg, I. W.; Limperis, T. *Geometrical considerations and nomenclature for reflectance*; tech. rep.; Washington, DC, USA: US Department of Commerce, National Bureau of Standards, 1977 (cit. on pp. 45, 71).
- (98) *Standard practice for goniometric optical scatter measurements*; Standard ASTM E2387-05; ASTM / SC E12.03, 2005 (cit. on pp. 45, 71).
- (99) Karamata, B.; Andersen, M. *Journal of the Optical Society of America A* **2014**, *31*, 1040–1048 (cit. on p. 45).
- (100) Sametoglu, F.; Celikel, O. *Measurement* **2009**, *42*, 757–763 (cit. on p. 45).
- (101) Rabal, A.; Ferrero, A.; Campos, J.; Fontecha, J.; Pons, A.; Rubiño, A.; Corróns, A. *Metrologia* **2012**, *49*, 213 (cit. on p. 45).
- (102) Stover, J. C., *Optical scattering: Measurement and analysis*, 2nd ed.; SPIE Optical Engineering Press Bellingham, WA: 1995 (cit. on pp. 45, 72).
- (103) Luo, H.; Yuan, C. *Optik - International Journal for Light and Electron Optics* **2015**, *126*, 4272–4277 (cit. on p. 46).
- (104) Yoo, K. M.; Tang, G. C.; Alfano, R. R. *Applied Optics* **1990**, *29*, 3237–3239 (cit. on p. 46).
- (105) Grosjes, T. *Optical Materials* **2008**, *30*, 1549–1554 (cit. on p. 46).
- (106) Bourlier, C.; Berginc, G. *Waves in Random Media* **2004**, *14*, 229–252 (cit. on p. 46).

- (107) Bourlier, C.; Berginc, G. *Waves in Random Media* **2004**, *14*, 253–276 (cit. on p. 46).
- (108) Belcour, L.; Pacanowski, R.; Delahaie, M.; Laville-Geay, A.; Eupherte, L. *Journal of the Optical Society of America A: Optics, Image Science, and Vision* **2014**, *31*, 2561–2572 (cit. on p. 46).
- (109) Pacanowski, R.; Celis, O. S.; Schlick, C.; Granier, X.; Poulin, P.; Cuyt, A. *IEEE Transactions on Visualization and Computer Graphics* **2012**, *18*, 1824–1835 (cit. on p. 46).
- (110) Claustres, L.; Boucher, Y.; Paulin, M. *Optical Engineering* **2004**, *43*, 2327–2339 (cit. on p. 46).
- (111) Jakob, W.; D'Eon, E.; Jakob, O.; Marschner, S. *ACM Trans. Graph.* **2014**, *33*, 118:1–118:14 (cit. on pp. 46, 72).
- (112) Shirley, P.; Chiu, K. *Journal of Graphics Tools* **1997**, *2*, 45–52 (cit. on pp. 46, 74).
- (113) Bonneel, N.; Van De Panne, M.; Paris, S.; Heidrich, W. In *ACM Transactions on Graphics (TOG)*, 2011; Vol. 30, p 158 (cit. on p. 46).
- (114) Mitchell, R.; Kohler, C.; Klems, J.; Rubin, M.; Arasteh, D.; Huizenga, C.; Yu, T.; Curcija, D. *Window 6.2 / Therm 6.2 research version user manual*; tech. rep. LBNL-941; Berkeley, CA: Lawrence Berkeley National Laboratory, 2008 (cit. on pp. 55, 73).
- (115) Jakubiec, J. A.; Reinhart, C. F. *Lighting Research and Technology* **2012**, *44*, 149–170 (cit. on pp. 57, 103, 126).
- (116) Janak, M. In *Proceedings of the fifth International IPBSA Conference*, 1997, pp 8–10 (cit. on p. 71).
- (117) Bueno, B.; Wienold, J.; Katsifaraki, A.; Kuhn, T. E. *Energy and Buildings* **2015**, *94*, 10–20 (cit. on p. 71).
- (118) Kajiya, J. T. In *Proceedings of the 13th Annual Conference on Computer Graphics and Interactive Techniques*, ACM: New York, NY, USA, 1986, pp 143–150 (cit. on p. 71).
- (119) Lawrence, J.; Ben-Artzi, A.; DeCoro, C.; Matusik, W.; Pfister, H.; Ramamoorthi, R.; Rusinkiewicz, S. In *ACM Transactions on Graphics*, 2006; Vol. 25, pp 735–745 (cit. on p. 71).
- (120) Kaempf, J. H.; Scartezzini, J. *Integration of BT(R)DF data into Radiance lighting simulation programme*; tech. rep.; Ecole Polytechnique Federale de Lausanne, 2004 (cit. on p. 71).
- (121) Kostro, A.; Scartezzini, J.-L.; Schueler, A. In *Proceedings of CISBAT 2013 Cleantech for Smart Cities and Buildings*, 2013; Vol. 2, pp 1115–1120 (cit. on p. 72).

- (122) Lawrence Berkeley National Laboratory Complex Glazing Database., <https://windows.lbl.gov/software/CGDB/>, 2016 (cit. on p. 72).
- (123) Stokes, G. G. In *Proceedings of the Royal Society of London*, 1860, pp 545–556 (cit. on p. 72).
- (124) Eisenlohr, J.; Tucher, N.; Höhn, O.; Hauser, H.; Peters, M.; Kiefel, P.; Goldschmidt, J. C.; Bläsi, B. *Optics express* **2015**, *23*, A502–A518 (cit. on p. 72).
- (125) Klems, J. H. *ASHRAE Transactions* **1994**, *100*, 1065–1072 (cit. on p. 72).
- (126) Klems, J. H. *ASHRAE Transactions* **1994**, *100*, 1073–1086 (cit. on p. 72).
- (127) Aydinli, S.; Kaase, H. *Measurement of luminous characteristics of daylighting materials*; tech. rep.; International Energy Agency Task 21, 1999 (cit. on p. 74).
- (128) Basurto Dávila, C. On advanced daylighting simulations and integrated performance assessment of complex fenestration systems for sunny climates., Ph.D. Thesis, École Polytechnique Fédérale de Lausanne, 2014 (cit. on p. 74).
- (129) Guennebaud, G.; Jacob, B., et al. Eigen v3., <http://eigen.tuxfamily.org>, (accessed on 03/2017) (cit. on p. 76).
- (130) Bergen, A. S. J. *Lighting Research and Technology* **2012**, *44*, 27–36 (cit. on p. 82).
- (131) time(1) Linux User’s Manual.; The Linux man-pages project, (last accessed 3/2017) (cit. on p. 82).
- (132) Ward, G. J. In *Proceedings of the 21st Annual Conference on Computer Graphics and Interactive Techniques*, ACM: New York, NY, USA, 1994, pp 459–472 (cit. on p. 94).
- (133) Whitted, T. *Communications of the ACM* **1980**, *23*, 343–349 (cit. on p. 94).
- (134) Cook, R. L.; Porter, T.; Carpenter, L. In, ACM: 1984; Vol. 18, pp 137–145 (cit. on p. 94).
- (135) Grynberg, A. *Validation of Radiance*; tech. rep.; Lawrence Berkeley Laboratory, Berkeley LBID, 1989 (cit. on p. 94).
- (136) Schregle, R.; Wienold, J. In *Computer Graphics Forum*, 2004; Vol. 23, pp 761–781 (cit. on p. 94).
- (137) Geisler-Moroder, D.; Dür, A. Validation of Radiance against CIE 171:2006 and improved adaptive subdivision of circular light sources., 7th international Radiance Workshop, 2008 (cit. on p. 94).
- (138) Jakica, N. *Renewable and Sustainable Energy Reviews* **2018**, *81*, 1296–1328 (cit. on p. 94).

- (139) Jones, N. L.; Reinhart, C. F.  
*Journal of Building Performance Simulation* **2019**, *12*, 343–361 (cit. on p. 94).
- (140) Heckbert, P. S. Simulating global illumination using adaptive meshing.,  
Ph.D. Thesis, Berkeley, CA, USA: University of California, 1991 (cit. on p. 95).
- (141) Ward, G.; Mistrick, R.; Lee, E.; McNeil, A.; Jonsson, J. *Leukos* **2011**, *7*, 241–261  
(cit. on pp. 95, 117).
- (142) Lee, E.; Wang, T.; Jonsson, J. C.; Ward, G.; Grobe, L. O.; Wienold, J.;  
Geisler-Moroder, D.  
Generating high-resolution BSDFs for the direct beam component.,  
International Radiance Workshop, 2018 (cit. on pp. 95, 96, 118).
- (143) Molina, G.; Bustamante, W.; Rao, J.; Fazio, P.; Vera, S.  
*Journal of Building Performance Simulation* **2015**, *8*, 216–225  
(cit. on pp. 95, 117).
- (144) Mainini, A. G.; Zani, A.; De Michele, G.; Speroni, A.; Poli, T.; Zinzi, M.;  
Gasparella, A. *Energy and Buildings* **2019**, *190*, 202–215 (cit. on p. 95).
- (145) Rogers, Z.; Thanachareonkit, A.; Fernandes, L.  
*Enhanced skylight modeling and validation*; tech. rep.;  
California Energy Commission, 2013 (cit. on p. 95).
- (146) Brembilla, E.; Chi Pool, D. A.; Hopfe, C. J.; Mardaljevic, J.  
In *Building Simulation Conference BS2017*, Aug. 7, 2017,  
IBPSA: San Francisco, CA, US, 2017, pp 1047–1056 (cit. on p. 95).
- (147) Heckbert, P. S. *SIGGRAPH Computer Graphics* **1990**, *24*, 145–154 (cit. on p. 96).
- (148) Veach, E. Robust Monte Carlo methods for light transport simulation.,  
Ph.D. Thesis, Stanford, CA, US: Stanford University, 1997 (cit. on p. 96).
- (149) Arvo, J.; Fajardo, M.; Hanrahan, P.; Wann Jensen, H.; Mitchell, D.; Pharr, M.;  
Shirley, P. State of the art in Monte Carlo ray tracing for realistic image synthesis.,  
ed. by Wann Jensen, H., Los Angeles, US, 2001 (cit. on pp. 96, 97).
- (150) Jensen, H. W., *Realistic image synthesis using photon mapping*;  
AK Peters / CRC Press: 2001 (cit. on p. 96).
- (151) Schregle, R.; Bauer, C.; Grobe, L. O.; Wittkopf, S. K. In *CISBAT 2015 Future  
Buildings and Districts Sustainability from Nano to Urban Scale*,  
Lausanne, 2015, pp 217–222 (cit. on p. 96).
- (152) Schregle, R.  
*Development and integration of the Radiance photon map extension*; tech. rep.;  
Lucerne University of Applied Sciences and Arts, 2015 (cit. on pp. 96, 118).

- (153) Bauer, C.; Wittkopf, S.  
*Journal of Facade Design and Engineering* **2016**, *3*, 253–272  
(cit. on pp. 96, 119, 139).
- (154) Schregle, R. Daylight simulation with photon maps.,  
Ph.D. Thesis, Universitaet des Saarlandes, 2004 (cit. on pp. 96, 118).
- (155) Schregle, R. Memorandum: Known bug in the Radiance photon map., 2016  
(cit. on p. 98).
- (156) Bellia, L.; Cesarano, A.; Iuliano, G. F.; Spada, G.  
In *Visual quality and energy efficiency in indoor lighting: today for tomorrow*,  
Visual quality and energy efficiency in indoor lighting: today for tomorrow,  
Rome, IT, 2008 (cit. on p. 103).
- (157) Pierson, C.; Wienold, J.; Bodart, M.  
*Buildings* **2018**, *8*, DOI: 10.3390/buildings8080094 (cit. on p. 103).
- (158) Rockcastle, S.; Amundadottir, M.; Andersen, M.  
*Lighting Research & Technology* **2017**, *49*, 882–903 (cit. on p. 115).
- (159) Wang, T.; Ward, G.; Lee, E. S. *Energy and Buildings* **2018**, *174*, 464–483  
(cit. on p. 115).
- (160) Guglielmetti, R. Integrated building simulation - Linking EnergyPlus and  
Radiance using OpenStudio.,  
presentation at EPRI National Energy Efficiency Technology Summit, 2012  
(cit. on p. 116).
- (161) Karlsen, L.; Grozman, G.; Heiselberg, P.; Bryn, I.  
In *7. Passivhus Norden – Sustainable Cities and Buildings*, Copenhagen, DK, 2015  
(cit. on p. 116).
- (162) Bourgeois, D.; Reinhart, C. F.; Ward, G.  
*Building Research & Information* **2008**, *36*, 68–82 (cit. on p. 116).
- (163) Brembilla, E.; Hopfe, C. J.; Mardaljevic, J.  
*Journal of Building Performance Simulation* **2018**, *11*, 333–349 (cit. on p. 116).
- (164) Brembilla, E.; Chi Pool, D. A.; Hopfe, C. J.; Mardaljevic, J.  
*Energy and Buildings* **2019**, DOI: 10.1016/j.enbuild.2019.109454  
(cit. on p. 116).
- (165) Abravesh, M.; Bueno, B.; Heidari, S.; Kuhn, T. E. *Building and Environment* **2019**,  
in press, DOI: 10.1016/j.buildenv.2019.106213 (cit. on p. 117).
- (166) Xiong, J.; Tzempelikos, A. *Solar Energy* **2016**, *134*, 416–428 (cit. on p. 117).
- (167) Tzempelikos, A.; Chan, Y.-C. *Energy and Buildings* **2016**, *126*, 396–407  
(cit. on p. 117).

- (168) McNeil, A. BSDFs, matrices and phases., 13th International Radiance Workshop, London, UK, 2014 (cit. on p. 118).
- (169) Ward, G. *Computing and applying variable-resolution data for Bidirectional Scattering Distribution Functions*; tech. rep.; Berkeley, CA, US: Anywhere Software, 2011 (cit. on p. 118).
- (170) Schregle, R. *The Radiance out-of-core photon map*; tech. rep.; Horw, CH: Lucerne University of Applied Sciences and Arts, 2016 (cit. on p. 120).
- (171) Aydınli, S.; Gramm, S.; Kaase, H.; Köster, H. *Bauphysik* **2015**, *37*, 257–262 (cit. on p. 124).
- (172) Wienold, J.; Iwata, T.; Sarey Khanie, M.; Erell, E.; Kaftan, E.; Rodriguez, R. G.; Yamin Garreton, J. A.; Tzempelikos, T.; Konstantzos, I.; Christoffersen, J.; Kuhn, T. E.; Pierson, C. M. A.; Andersen, M. *Lighting Research & Technology* **2019**, DOI: 10.1177/1477153519826003 (cit. on p. 126).
- (173) Noback, A.; Grobe, L. O.; Lang, F., 21st Congress of the Association Internationale pour l’Histoire du Verre, Istanbul, TR, 2018 (cit. on p. 148).
- (174) Grobe, L. O.; Noback, A.; Lang, F. *ACM Journal on Computing and Cultural Heritage* **in press**, DOI: 10.1145/3350428 (cit. on pp. 148, 162).
- (175) Grobe, L. O.; Noback, A. Light scattering by Roman window glass., Digital data-set, 2019 (cit. on p. 148).
- (176) Grobe, L. O. Daylighting in the antique., 2017 (cit. on p. 149).
- (177) Light fields in climate-based daylight modeling for spatio-temporal glare assessment., Last accessed 20. August 2019 (cit. on p. 149).
- (178) Grobe, L. O. *Journal of Physics: Conference Series* **in press**, *CISBAT 2019* (cit. on p. 162).
- (179) Wittkopf, S.; Grobe, L. O.; Geisler-Moroder, D.; Compagnon, R.; Kämpf, J.; Linhart, F.; Scartezzini, J.-L. *Solar Energy* **2010**, *84*, 986–996 (cit. on p. 162).
- (180) Grobe, L.; Wittkopf, S.; Pandey, A. R.; Xiaoming, Y.; Seng, A. K.; Scartezzini, J.-L.; Selkowitz, S. In *International Conference on Applied Energy*, 2010 (cit. on p. 162).

**Lars O. GROBE.** Born 23. December 1974 in Bonn, Germany.

### **Education**

Mr. Grobe received his degree in architecture (German Diplom-Ingenieur, equivalent to Masters degree) from Technische Universität Darmstadt in 2005. He had the opportunity to study at Istanbul Technical University from 2003 to 2004.

### **Appointments in research and development**

Mr. Grobe was invited as a visiting scholar to the National University of Singapore in 2008. This was followed by an appointment as research associate at the Solar Energy Research Institute of Singapore, where he contributed to the BCA Zero Energy Building in the fields of daylighting, and to the set-up and operation of the gonio-photometer laboratory, which he led until leaving Singapore in 2010. In 2011, Mr. Grobe was awarded the *Singapore Minister for National Development Research & Development Award*.

In 2012, Mr. Grobe rejoined academia as a senior research associate at Lucerne University of Applied Sciences and Arts. He prepared and led a research project on the “Modeling and simulation of daylight redirecting systems” (2013 – 2016, funded by the Swiss National Science Foundation SNSF#147053, with Stephen Wittkopf being the main applicant), the measurement campaign “High Resolution Complex Glazing Library BIMSOL” (2016 – 2018, supported by the Swiss Federal Office for Energy SFOE #SI501427-01). Recently he initiated a research project on “Light fields in climate-based daylight modelling for spatio-temporal glare assessment” (2019 – 2023, SNSF#179067). Besides these projects, he is applying the gonio-photometer of the Competence Center Building Envelopes in research collaborations with industry, planners and research partners.

### **Selected publications** (excluding chapters of this thesis)

“Data-Driven Modelling of Daylight Scattering by Roman Window Glass” Grobe, L. O. et al. *ACM Journal on Computing and Cultural Heritage* **in press**, DOI: 10.1145/3350428

“Photon mapping to accelerate daylight simulation with high resolution, data-driven fenestration models” Grobe, L. O. *Journal of Physics: Conference Series* **in press**, *CISBAT 2019*

“Three approaches to optimize optical properties and size of a South-facing window for spatial Daylight Autonomy” Kazanasmaz, T. et al. *Building and Environment* **2016**, *102*, 243–256

“Accordance of light scattering from design and de-facto variants of a daylight redirecting component” Noback, A. et al. *Buildings* **2016**, *6*, 30

“Ray tracing study for non- imaging daylight collectors” Wittkopf, S. et al. *Solar Energy* **2010**, *84*, 986–996

“Experimental validation of bidirectional reflection and transmission distribution measurements of specular and scattering materials” Grobe, L. O. et al. *Proceedings SPIE* **2010**, *7725 Photonics for Solar Energy Systems III*, 772510–772510

“Singapore’s Zero-Energy Building’s daylight monitoring system” Grobe, L. et al. In *International Conference on Applied Energy*, 2010